

**A STUDY OF THE WHITE LIGHT FLARE RATES OF M AND L  
DWARFS**

by  
Rishi Paudel

A dissertation submitted to the Faculty of the University of Delaware in partial fulfillment of the requirements for the degree of Doctor of Philosophy in Physics

Spring 2019

© 2019 Rishi Paudel  
All Rights Reserved

**A STUDY OF THE WHITE LIGHT FLARE RATES OF M AND L  
DWARFS**

by

Rishi Paudel

Approved: \_\_\_\_\_  
Edmund R. Nowak, Ph.D.  
Chair of the Department of Physics and Astronomy

Approved: \_\_\_\_\_  
John Pelesko, Ph.D.  
Interim Dean of the College of Arts and Sciences

Approved: \_\_\_\_\_  
Douglas J. Doren, Ph.D.  
Interim Vice Provost for Graduate and Professional Education

I certify that I have read this dissertation and that in my opinion it meets the academic and professional standard required by the University as a dissertation for the degree of Doctor of Philosophy.

Signed: \_\_\_\_\_

Prof. John E. Gizis, Ph.D.  
Professor in charge of dissertation

I certify that I have read this dissertation and that in my opinion it meets the academic and professional standard required by the University as a dissertation for the degree of Doctor of Philosophy.

Signed: \_\_\_\_\_

Prof. Dermott Mullan, Ph.D.  
Member of dissertation committee

I certify that I have read this dissertation and that in my opinion it meets the academic and professional standard required by the University as a dissertation for the degree of Doctor of Philosophy.

Signed: \_\_\_\_\_

Prof. George C. Hadjipanayis, Ph.D.  
Member of dissertation committee

I certify that I have read this dissertation and that in my opinion it meets the academic and professional standard required by the University as a dissertation for the degree of Doctor of Philosophy.

Signed: \_\_\_\_\_

Rachel Osten, Ph.D.  
Member of dissertation committee

## ACKNOWLEDGEMENTS

I consider myself fortunate to have had the opportunity to work under the supervision of Prof. John Gizis. I cannot express how grateful I am to him for my achievement in my research. I am greatly indebted to Prof. Gizis for giving me the freedom to work in the way I wanted and to explore new research ideas, and for encouraging me in all stages of my research. His positive feedback in every meeting were very helpful to motivate me and to grow as a scientist. I greatly value his contribution and effort in teaching research skills and his kindness in helping me to correct even the most minor errors with great patience.

I would like to express my deepest gratitude to all the members of my dissertation committee: Prof. Dermott Mullan, Dr. Rachel Osten and Prof. George Hadjipanayis for generously providing their time and valuable feedback in making my dissertation better. Their suggestions were extremely helpful in giving a good direction to my research path. I am especially thankful to Dr. Osten for coming all the way from Baltimore during my oral candidacy exam and Ph.D. dissertation defense despite her busy schedule.

I greatly appreciate the support and contributions of my collaborators Prof. Dermott Mullan, Prof. Adam Burgasser, Dr. Sarah Schmidt, Dr. Peter Williams, Dr. Allison Youngblood and Dr. Keivan Stassun, which were very important in finishing my project and helped to lead to publication of the results. I benefited greatly from their expertise in their respective fields.

I am deeply indebted to Prof. Dermott Mullan for teaching me the physics of the Sun as well as the flares. I am very grateful to him for the time he spent with me, teaching me the physical concepts which increased my understanding of the results of

my project. His teaching was very important for increasing my confidence in the subject matter. In addition, I am also thankful to him for helping me correct the language errors in my papers and dissertation.

This work would not have been possible without support from the Department of Physics and Astronomy (DPA), University of Delaware. I am very thankful to the DPA for granting me admission and allowing me to use all the resources necessary for my research. My work would have been impossible without the financial support from the DPA. I am also thankful to the DPA for waiving the Physics-GRE requirement for my admission. My especial thanks to Prof. James MacDonald, the Chair of Graduate Admissions Committee, who had an important role for granting me admission. I gratefully acknowledge University of Delaware Dissertation Fellowship which helped me to complete my dissertation on time, and also provided time for writing job applications.

My sincere thanks also go to the staffs in the DPA IT department: Sola Johnson, Sansern Somboonsong and Daniel De Marco who helped me solve many problems related to software and hardware. They were very friendly whenever I went to ask for help.

My deep appreciation goes out to all my friends in the DPA and all also to all the members of UD Nepalese Student Association who were with me during the moments of my successes and failures. Their loving and caring company helped to boost my confidence when I had success, and remain strong even in the most difficult situation when I had a foot injury and had limited mobility for about three months in the summer of 2018. The coffee meetings we used to have in Brew Ha Ha are especially unforgettable, when we used to share our stories regarding research as well as life.

I express my heart-felt gratitude to Prof. Binil Aryal, advisor of my Master's thesis, who showed me the initial direction to conduct research in astronomy. It is because of him I changed my mind away from becoming a condensed matter physicist, and was inspired to become involved in astronomy.

Some of the results presented in this dissertation have already been published in two journals: the *Astrophysical Journal* (ApJ) and the *Monthly Notices of the*

Royal Astronomical Society (MNRAS). The material in this dissertation is based upon work supported by NASA under award Nos. NNX15AV64G, NNX16AE55G and NNX16AJ22G. Some/all of the data presented in this dissertation were obtained from the Mikulski Archive for Space Telescopes (MAST). STScI is operated by the Association of Universities for Research in Astronomy, Inc., under NASA contract NAS5-26555. This dissertation includes data collected by the Kepler mission. Funding for the Kepler mission is provided by the NASA Science Mission directorate. This work has made use of data from the European Space Agency (ESA) mission *Gaia* (<https://www.cosmos.esa.int/gaia>), processed by the *Gaia* Data Processing and Analysis Consortium (DPAC, <https://www.cosmos.esa.int/web/gaia/dpac/consortium>). Funding for the DPAC has been provided by national institutions, in particular the institutions participating in the *Gaia* Multilateral Agreement. This research has made use of the VizieR catalogue access tool, CDS, Strasbourg, France. The original description of the VizieR service was published in A&AS 143, 23. This work made use of the <http://gaia-kepler.fun> crossmatch database created by Megan Bedell.

I am beyond words to express my gratitude to my *buba*, my *ama* and my *saano mama* whose love, support and inspiration brought me to this stage of my life. My work would be incomplete without the support and love of my *jeevan-sangini* Nisha and my *chhori* Arinshu. I am extremely grateful to Nisha for her sacrifice, patience and company during the ups and downs of my life. Nisha had a very great role in encouraging me as well as taking care of Arinshu and me when I was busy in my research.

## DEDICATION

To my *ama*, Devi Paudel,  
my *buba*, Mitralal Paudel,  
my *mama*, Durga Datta Dhungana,  
my *jeevan-sangini*, Nisha Ghimire,  
and my *chhori*, Arinshu Paudel

## TABLE OF CONTENTS

LIST OF TABLES . . . . .	xiii
LIST OF FIGURES . . . . .	xvi
ABSTRACT . . . . .	xxvi

### Chapter

<b>1 INTRODUCTION . . . . .</b>	<b>1</b>
1.1 A brief history of study of flares on M and L dwarfs . . . . .	1
1.2 Stellar classification system . . . . .	2
1.3 M dwarfs . . . . .	3
1.4 L dwarfs . . . . .	4
1.5 Brown Dwarfs . . . . .	4
1.6 Ultracool dwarfs . . . . .	5
1.7 Flares . . . . .	6
1.7.1 Flares on M/L dwarfs . . . . .	7
1.8 Flare frequency distribution (FFDs) . . . . .	9
1.9 Importance of studying flares . . . . .	13
1.9.1 Nature of the magnetic dynamo . . . . .	13
1.9.2 Rotation-activity relations . . . . .	14
1.9.3 Motivation for studying flares on UCDS . . . . .	16
1.10 M dwarf flares in the context of planet habitability . . . . .	20
1.11 The <i>Kepler</i> mission . . . . .	23
1.12 The <i>K2</i> mission . . . . .	24
1.12.1 <i>Kepler</i> and <i>K2</i> data . . . . .	26
1.13 Dissertation Outline . . . . .	26

<b>2</b>	<b>WHITE LIGHT FLARE RATES OF M/L DWARFS USING <i>K2</i> SHORT CADENCE DATA</b>	<b>30</b>
2.1	White light flares	30
2.2	Sample	33
2.3	Data Reduction and Computations	46
2.3.1	<i>K2</i> photometry	46
2.3.2	Flare detection	49
2.3.3	Calibration of equivalent duration and calculation of flare energy	51
2.4	Artificial flare injection and estimation of lowest detectable flare energy	56
2.5	Flare statistics and Flare energy spectrum of target UCDs	58
2.5.1	Possibility of a broken power-law or a power-law with exponential cutoff in the FFD of some UCDs	72
2.6	Superflares observed on two UCDs	75
2.6.1	Photometry of superflare observed on L0 dwarf 2MASS J12321827-0951502	76
2.6.2	Photometry of a superflare observed on M7 dwarf 2MASS J08352366+1029318	77
2.7	Discussion and conclusions	79
2.7.1	Variation of the power-law slope $\beta$ according to spectral type	81
2.7.2	Effect of H $\alpha$ luminosity on flare rates	83
2.7.3	Comparison of flare rates of L dwarfs with earlier spectral types	85
2.7.4	Energies and timescales associated with two superflares of largest amplitudes observed on two UCDs	88
2.7.5	Variation of power-law index $\beta$ as a function of kinematic age	89
2.7.6	Do FFDs always follow a single power law distribution?	92
<b>3</b>	<b>WHITE LIGHT FLARES OBSERVED ON M6-M9 DWARFS USING <i>K2</i> LONG CADENCE DATA</b>	<b>94</b>
3.1	Data reduction	94
3.2	Flare search and estimation of energies	95
3.3	Results	95

<b>4</b>	<b>A STUDY OF FLARES ON L/T DWARFS USING <i>K2</i> LONG CADENCE DATA</b>	<b>102</b>
4.1	Introduction	102
4.1.1	Previous studies: H $\alpha$ emission	102
4.1.2	Previous studies: X-ray and radio emission	103
4.1.3	Flares on L and T dwarfs	105
4.1.4	Sample of L/T dwarfs observed by <i>K2</i>	106
4.2	Data reduction, flare search and flare energy estimation	110
4.2.1	Flare on 2MASS J08585891+1804463	110
4.2.2	Flares on an L5 dwarf VVV BD001	111
4.3	Results	113
4.3.1	FFD of L dwarfs using long cadence data	115
<b>5</b>	<b>MONSTER FLARES OBSERVED ON THE YOUNG BROWN DWARF CFHT-BD-TAU 4</b>	<b>117</b>
5.1	INTRODUCTION	117
5.2	TARGET CHARACTERISTICS	118
5.3	DATA REDUCTION AND COMPUTATIONS	120
5.3.1	<i>K2</i> photometry	120
5.3.2	Computation of Flare Energies	122
5.3.3	Flare photometry	123
5.4	Discussion	125
<b>6</b>	<b>HIGH SUPERFLARE RATES ON RAPIDLY ROTATING LATE-M DWARFS</b>	<b>131</b>
6.1	Introduction	131
6.2	Target Characteristics	131
6.3	Data reduction and computations	134
6.3.1	<i>K2</i> photometry	134
6.3.2	Flare detection and estimation of flare energies	135

6.3.3	Comparison of flare rates with TRAPPIST-1 . . . . .	136
6.3.4	X-ray energy emitted during the largest flare on 2M0837+2050 . . . . .	142
6.4	Summary and Discussion . . . . .	142
6.4.1	Flare rates of $\sim 700$ Myr TRAPPIST-1 like objects . . . . .	144
6.4.2	Particle flux associated with the largest superflare on 2M0837+2050 . . . . .	145
6.4.3	Estimation of CME masses associated with the superflares on 2M0837+2050 . . . . .	146
6.4.4	Comparison of superflare on 2M0837+2050 with that on M2 dwarf GSC 8056-0482 for possible UV flux estimates . . . . .	147
6.4.5	Timescales of planet formation and life on Earth . . . . .	148
6.4.6	How can the superflares be beneficial to studies regarding CMEs associated with stellar flares? . . . . .	149
6.4.7	Possible benefits of superflares to the planets in the HZ of M dwarfs . . . . .	150
<b>7</b>	<b>2MASS J10274572+0629104: THE VERY SHORT PERIOD YOUNG M6 DWARF BINARY SYSTEM IDENTIFIED IN <i>K2</i> DATA</b> . . . . .	<b>151</b>
7.1	INTRODUCTION . . . . .	151
7.2	OBSERVATIONS . . . . .	152
7.2.1	<i>K2</i> photometry . . . . .	152
7.2.2	<i>Gaia</i> Astrometry and photometry . . . . .	153
7.2.3	Spectroscopy . . . . .	156
7.2.4	Flares . . . . .	158
7.3	Discussion and Conclusion . . . . .	158
<b>8</b>	<b>CHANDRA MONITORING OF A FLARING L1 DWARF WISEP J190648.47+401106.8</b> . . . . .	<b>161</b>
8.1	WISEP J190648.47+401106.8 . . . . .	161
8.2	OBSERVATIONS AND DATA REDUCTION . . . . .	162
8.2.1	<i>Chandra</i> Observations . . . . .	162
8.2.2	<i>CIAO</i> Data Reduction . . . . .	162
8.2.3	<i>Astrometry</i> . . . . .	163
8.3	RESULTS . . . . .	164

<b>9 CONCLUSIONS AND FUTURE WORK . . . . .</b>	<b>166</b>
9.1 FFDs of mid-to-late M and L dwarfs using <i>K2</i> short cadence data . .	166
9.2 Effect of H $\alpha$ luminosity in the flare rates . . . . .	167
9.3 Variation of power-law index $\beta$ as a function of kinematic age . . . .	168
9.4 Maximum flare energies observed in each spectral type . . . . .	169
9.5 Timescales associated with the superflares on UCDS . . . . .	171
9.6 Summary of additional works . . . . .	171
9.7 FUTURE WORK . . . . .	173
<b>BIBLIOGRAPHY . . . . .</b>	<b>176</b>
<b>Appendix</b>	
<b>A PROPERTIES OF FLARES IDENTIFIED USING <i>K2</i> SHORT CADENCE DATA . . . . .</b>	<b>204</b>
<b>B M6-M8 DWARFS OBSERVED IN <i>K2</i> LONG CADENCE MODE</b>	<b>224</b>
<b>C PROPERTIES OF WL FLARES OBSERVED ON M6 - M9 DWARFS BY <i>K2</i> . . . . .</b>	<b>235</b>
<b>D COPYRIGHT POLICY OF JOURNALS . . . . .</b>	<b>240</b>

## LIST OF TABLES

2.1	Name and EPIC ID of flaring targets . . . . .	38
2.2	Physical properties of flaring targets . . . . .	39
2.3	Photometric properties of flaring targets . . . . .	40
2.4	Kinematic properties of flaring targets . . . . .	41
2.5	Activity indicators (I) of flaring targets . . . . .	42
2.6	Activity indicators (II) of flaring targets . . . . .	43
2.7	List of targets with non-detection of flares by <i>K2</i> . . . . .	44
2.8	PS1 and <i>Gaia</i> measurements of non-flaring objects . . . . .	45
2.9	Median fluxes and <i>Kepler</i> magnitudes of flaring targets . . . . .	48
2.10	Minimum energies of injected and detected artificial flares . . . . .	57
2.11	Flare statistics . . . . .	63
2.12	Power law fits to FFDs of targets . . . . .	67
2.13	Average values of $\beta$ and $\alpha_o$ . . . . .	82
2.14	Average slopes of FFDs of targets classified by kinematic age . . . . .	89
3.1	Flare statistics of M6 - M9 dwarfs. I. . . . .	97
3.2	Flare statistics of M6 - M9 dwarfs. II. . . . .	97
3.3	Obs. time and ED1 of flaring M6 dwarfs . . . . .	98
3.4	Obs. time and ED1 of flaring M7 dwarfs . . . . .	99

3.5	Obs. time and ED1 of flaring M8 dwarfs . . . . .	100
3.6	Obs. time and ED1 of flaring M9 dwarfs . . . . .	101
4.1	Total observation time by campaign . . . . .	107
4.2	List of L and T dwarfs observed by <i>K2</i> . . . . .	108
4.3	Values of ED1 for each flaring L dwarf . . . . .	111
4.4	Properties of VVV BD001 . . . . .	113
4.5	Properties of flares on L dwarfs . . . . .	115
4.6	Properties of flaring L dwarfs . . . . .	116
5.1	Properties of CFHT-BD-Tau 4 . . . . .	121
5.2	Flare properties . . . . .	125
6.1	Properties of targets . . . . .	133
6.2	Properties of superflares . . . . .	141
7.1	Properties of 2M1027+0629 . . . . .	154
A.1	Flare properties of GJ 3631 . . . . .	204
A.2	Flare properties of GJ 3636 . . . . .	207
A.3	Flare properties of Wolf 359 . . . . .	209
A.4	Flare properties of LHS 2090 . . . . .	212
A.5	Flare properties of 2M1507-2000 . . . . .	215
A.6	Flare properties of 2M0825+2021 . . . . .	216
A.7	Flare properties of 2M1330-0453 . . . . .	216
A.8	Flare properties of 2M2353-0833 . . . . .	216
A.9	Flare properties of 2M1055+0808 . . . . .	217

A.10	Flare properties of 2M1048+0111 . . . . .	217
A.11	Flare properties of 2M2228-1325 . . . . .	217
A.12	Flare properties of 2M2202-1109 . . . . .	218
A.13	Flare properties of 2M0835+1029 . . . . .	219
A.14	Flare properties of 2M2214-1319 . . . . .	219
A.15	Flare properties of 2M1332-0441 . . . . .	220
A.16	Flare properties of TRAPPIST-1 . . . . .	221
A.17	Flare properties of 2M1221-0843 . . . . .	221
A.18	Flare properties of 2M0326+1919 . . . . .	222
A.19	Flare properties of 2M1221-0257 . . . . .	222
A.20	Flare properties of 2M1232-0951 . . . . .	223
B.1	List of M6 dwarfs . . . . .	225
B.2	List of M7 dwarfs . . . . .	227
B.3	List of M8 dwarfs . . . . .	232
B.4	List of M9 dwarfs observed by <i>K2</i> . . . . .	234
C.1	Flare properties of M6 dwarfs . . . . .	235
C.2	Energies of flares on M7 dwarfs . . . . .	236
C.3	Energies of flares on M8 dwarfs . . . . .	238
C.4	Energies of flares on M9 dwarfs . . . . .	239

## LIST OF FIGURES

1.1	An example of the FFD of a late-M dwarf: TRAPPIST-1. Along the $X$ -axis are log values of observed flare energies and along the $Y$ -axis are log values of cumulative frequencies. The blue dots represent the observed flares and the red line represents the fitted line using a power-law model. . . . .	11
1.2	Artist’s conception of the <i>Kepler</i> mission. Credit: NASA . . . . .	27
1.3	The shape of the <i>Kepler</i> bandpass which covers most of the optical spectrum. Credit: NASA . . . . .	27
1.4	This image shows the <i>K2</i> mission’s different FOVs as it orbited around the Sun. The FOV of the primary <i>Kepler</i> mission is also shown. Credit: NASA . . . . .	28
1.5	This cartoon summarizes the various research areas of astronomy and astrophysics, which can be studied by using the <i>Kepler</i> and <i>K2</i> data. Reproduced with permission from Ann Marie Cody/NASA Ames. . . . .	28
1.6	A cartoon showing the field of view in <i>K2</i> Campaign 18 which started on 12 May, 2018 and ended on 2 August, 2018. Reproduced with permission from Ann Marie Cody/NASA Ames. . . . .	29
1.7	The ‘last light’ image taken by <i>K2</i> mission on 9/25/2018. It represents the end of <i>Kepler</i> ’s 9+ year journey of data collection. Credit:NASA <i>Kepler</i> . . . . .	29
2.1	Examples of WLFs observed by <i>K2</i> on a flaring star GJ 3631 during Campaign 14. The flare on the left is also called a classical flare and the one on left is a complex flare. The two dashed vertical lines in each plot mark the start and end times of the flare. The time mentioned on the top of each time is the <i>Kepler</i> mission time at which the peak of the flare was observed. The time along $X$ -axis is centered around the peak flare time and the flux along $Y$ -axis is normalized by the median counts of the continuum. . . . .	32

2.2	Bar chart showing the total number of targets in each spectral type. The total number of targets in the sample is 42. . . . .	36
2.3	Bar chart comparing the number of flaring targets with those of all targets in each spectral type. The blue bars correspond to the total number of targets in each spectral type and the red bars correspond to the flaring targets. The numbers of all targets and of those which were observed to flare is indicated for each spectral type. . . . .	36
2.4	Color magnitude diagram of all targets in the sample. The $X$ -axis corresponds to the color-difference of $i$ and $z$ magnitudes measured by PS1 survey (whenever available) and the $Y$ -axis corresponds to absolute magnitudes $M_i$ . The red dots correspond to flaring targets and the blue dots correspond to the non-flaring targets. . . . .	37
2.5	Tangential velocity distribution of all targets in the sample. The red dots represent the flaring targets and the blue dots represent the non-flaring targets. It should be noted here that I have not plotted $V_{\text{tan}}$ as a function of any other physical quantity since the main idea is to show only the distribution of velocities. . . . .	37
2.6	<b>Left:</b> Target pixel level data of M5 dwarf GJ 3636 in a randomly chosen cadence. <b>Right:</b> Target pixel level data of L0 dwarf 2M1232-0951 in a randomly chosen cadence. . . . .	47
2.7	The $K2$ light curve of the M5 dwarf GJ 3631 obtained by using a 3-pixel radius aperture from its TPF. The time along the $X$ -axis is measured relative to the time when the <i>Kepler</i> mission began observation in 2009. The flux along the $Y$ -axis is given in units of counts $\text{s}^{-1}$ which were registered on the pixels considered. . . . .	49
2.8	Examples of two large flares observed on the M5 dwarf GJ 3631. The black vertical dashed lines in both plots represent the start and end times of the flares. The red horizontal dashed line represents the continuum (photospheric) level. All fluxes above the continuum level in between the start and the end times are considered to be flare fluxes. The time mentioned above each plot is the peak flux time and is given in terms of <i>Kepler</i> mission time. The time along the $X$ -axis is centered around the peak flux time. The flux along the $Y$ -axis is normalized by the continuum level. . . . .	52

2.9	Examples of two small flares observed on the M5 dwarf GJ 3631. Though both have comparable amplitudes, the flare in the right side, being a complex flare, has greater energy. . . . .	52
2.10	The optical and near-infrared spectral energy distribution of TRAPPIST-1 (red) and a hypothetical 10,000 K blackbody (blue). The wavelength range in between vertical dashed lines is the <i>Kepler</i> band. Using the distance of 12.3 pc, the bolometric luminosity of TRAPPIST-1 is $2.0 \times 10^{30}$ erg s <sup>-1</sup> and that of 10,000 K flare is $2.8 \times 10^{29}$ erg s <sup>-1</sup> . . . . .	55
2.11	An example of artificial flare injection in 2M2228-1325 light curve. The upper plot is a detrended light curve with 1- $\sigma$ noise and the lower plot is the light curve with artificial flares injected at random times.	58
2.12	Bar chart showing the distribution of flare energies in each spectral types. Different colors refer to the flares with certain range of energies. . . . .	60
2.13	Average number of flares observed per day per target in each spectral type, except L2-L9. This plot includes only the flaring targets. . .	60
2.14	Bar chart showing the total time of observation (in units of days) of the flaring targets in each spectral type, except L2-L9. . . . .	61
2.15	Average number of flares observed per day per target in each spectral type, except L2-L9. This plot includes all flaring and non-flaring targets observed in short cadence mode. . . . .	61
2.16	Bar chart showing the total time of observation (in units of days) of all targets in each spectral type, except L2-L9, which were observed in short cadence mode. . . . .	62
2.17	An example showing how a lower limit on flare energy was chosen for fitting in the case of targets with flattened distribution at low energy. The dashed vertical line corresponds to the lowest energy which was considered for fitting. . . . .	65
2.18	Individual FFD of M5 and M6 dwarfs in the sample. In each panel, the blue dots represent the observed data and the red solid line represents the fitted model. The FFDs of other targets with spectral types M5 and M6 are also plotted in the background for comparison.	69

2.19	Individual FFD of M7 dwarfs in the sample. In each panel, the blue dots represent the observed data and the red solid line represents the fitted model. The FFDs of other targets with spectral type M7 are also plotted in the background for comparison. . . . .	70
2.20	Individual FFD of M8, M9 and L dwarfs in the sample. In each panel, the blue dots represent the observed data and the red solid line represents the fitted model. The FFDs of other targets with spectral type M8, M9 and L are also plotted in the background for comparison.	71
2.21	<b>Left:</b> Fitted FFDs of M5-M6 dwarfs in the sample. <b>Right:</b> This plot is similar to that in the left except that the flare energies are replaced by the corresponding EDs of the flares. . . . .	72
2.22	<b>Left:</b> Fitted FFDs of M7-M8 dwarfs in the sample. <b>Right:</b> This plot is similar to that in the left except that the flare energies are replaced by the corresponding EDs of the flares. . . . .	73
2.23	<b>Left:</b> Fitted FFDs of M8, M9 and L0 dwarfs in the sample. <b>Right:</b> This plot is similar to that in the left except that the flare energies are replaced by the corresponding EDs of the flares. . . . .	73
2.24	Comparison of the FFD of a young brown dwarf 2M0335+2342 (red) with that of an L0 dwarf 2M1232-0951 (purple). The dots represent observed data and solid lines represent the fitted power law model. This plot suggests that the L0 dwarf has a flare rate that is comparable to that of a 24 Myr old brown dwarf as regards high energy flares, despite the L0 dwarf having a cooler atmosphere. . .	74
2.25	<b>Left:</b> Comparison between broken power law and power law with cutoff in case of 2M2228-1325. <b>Right:</b> Comparison between broken power law and power law with cutoff in case of 2M0326+1919. . . .	75
2.26	(a) Superflare observed on 2M1232-0951. The blue dots represent the observed flux and the red curve represents the fitted flux using slightly different parameters in the D14 model. The time is zero centered at peak flare time and scaled by $t_{1/2}$ . The vertical dashed lines represent the flare start and end times. (b) This plot is a log-log version of plot shown in (a). . . . .	78

2.27	(a) Superflare observed on 2M0835+1029. The blue dots represent the observed flux and the red curve represents the fitted flux using slightly different parameters in D14 model. The vertical dashed lines represent the start and stop times of flare. The time is zero centered at peak flare time and scaled by $t_{1/2}$ . (b) This plot is log-log version of plot shown in (a). . . . .	79
2.28	Comparison of average flare rates of each spectral type in our sample. The flare rates of GJ 1243 (M4) are taken from <a href="#">Hawley et al. [2014]</a> . There is only one flaring M9 dwarf, so the flare rate of this spectral type is not plotted in this figure. . . . .	83
2.29	The FFDs of 10 targets on which $\geq 20$ flares were observed and for which we have information of both $H\alpha$ and bolometric luminosity. . . . .	85
2.30	The flare rates of same targets used in Figure 2.29, with the flare energies normalized by the corresponding bolometric luminosities of the targets. . . . .	86
2.31	The flare rates of same targets used in Figure 2.29, with the flare energies normalized by the corresponding $H\alpha$ luminosities of the targets. . . . .	86
2.32	The flare rates of targets with ST of M5 and M6, with the flare energies normalized by the corresponding $H\alpha$ luminosities of the targets. . . . .	87
2.33	<b>Left:</b> Tangential velocity distribution of flaring targets. Since no physical quantity is plotted along the $X$ -axis, spread of the velocities in horizontal direction has no meaning at all. <b>Right:</b> Plot showing the relation between tangential velocities and slopes of FFDs ( $\beta$ ) of the flaring targets whose fitted flare energies span a range $>1$ order of magnitude. . . . .	89
2.34	Plot showing the variation of slopes of FFDS ( $\beta$ ) and the tangential velocity for each flaring target. In each panel, the tangential velocity is plotted along $Y$ -axis and the values of $\beta$ are indicated above each blue bar. To make it easy for comparison, the $\beta$ values of objects are given in the increasing order of tangential velocities. . . . .	90
3.1	Bar chart comparing the number of flaring targets with the total number of targets for spectral types: M6 - M9, observed by $K2$ in long cadence mode. . . . .	96

4.1	The distribution of L/T dwarfs by spectral type. There are only two T dwarfs in our sample, so their distribution is shown in only one bin.	110
4.2	The flare observed on L2 dwarf 2MASS J08585891+1804463. . . .	112
4.3	<b>Left:</b> Position of V01 as shown by VizieR Photometry Viewer with center at $\alpha = 17^h 26' 40''.20$ $\delta = -27^\circ 38' 3''.00$ . <b>Right:</b> Pixel data of V01. The centroid is located at (660,229) inside the circled pixel. . .	114
4.4	Flares observed on V01. The time along the $X$ -axis is centered at peak flare time mentioned above each plot. The flux along the $Y$ -axis is normalized by the median flux which corresponds to photospheric level. . . . .	114
4.5	The FFD estimated by using the energies of all flares identified on L dwarfs observed by $K2$ long cadence mode. . . . .	116
5.1	The $K2$ light curve of CT4. The two superflares are not shown in full scale to focus the periodic nature of the curve. Using Lomb-Scargle periodogram, the dominant period of the light curve is 2.98 day. The two dashed vertical lines mark the peak flux times of the superflares.	122
5.2	Optical spectral energy distribution (SED) of CT4 (black solid curve). The three dashed lines represent the SEDs of hypothetical blackbody flares of temperature 10,000 K, 6,500 K and 10,000 K which produce the same counts through $Kepler$ filter, corresponding to $A_V = 6.37$ , 6.37 and 3.0 respectively. The upper plot is the reddened version of SEDs, and the lower plot is the dereddened version of SEDs. . . . .	123
5.3	The strongest superflare observed on CT4. The blue dots represent the observed data. The dashed vertical lines represent the start and end times of flare. . . . .	124
5.4	Next superflare observed on CT4. The blue dots represent the observed data. The dashed vertical lines represent the start and end times of flare. . . . .	124
6.1	The phase folded $K2$ Campaign 5 light curve of M7 dwarf 2M0831+2042 corresponding to period of 0.556 d. The LSP is also shown inside. The second peak in the LSP corresponds to instrumental noise of $\sim 0.25$ d. . . . .	136

6.2	The phase folded <i>K2</i> Campaign 18 light curve of M8 dwarf 2M0837+2050 corresponding to period of 0.193 d. The LSP is also shown inside. . . . .	137
6.3	The phase folded <i>K2</i> Campaign 18 light curve of M9 dwarf 2M0831+2244 corresponding to period of 0.292 d. The LSP is also shown inside. . . . .	137
6.4	The superflare observed on M7 dwarf 2M0831+2042. The blue dots represent the observed data, and the vertical dashed lines represent the start and end times of the flare. The time along the <i>X</i> -axis is centered at the peak flare time. . . . .	138
6.5	The largest superflare observed on M8 dwarf 2M0837+2050. The blue dots represent the observed data, and the vertical dashed lines represent the start and end times of the flare. The time along the <i>X</i> -axis is centered at the peak flare time. . . . .	138
6.6	The largest superflare observed on M9 dwarf 2M0831+2244. The blue dots represent the observed data, and the vertical dashed lines represent the start and end times of the flare. The time along the <i>X</i> -axis is centered at the peak flare time. . . . .	139
6.7	Other superflares observed on 2M0837+2050 in Campaign 5 data. The blue dots represent the observed data and the time is centered at peak flare time. Though the second and the third plots are similar, the only difference is the peak flare time mentioned on the top of them, corresponding to each flare. . . . .	139
6.8	Other superflares observed on 2M0831+2244. The blue dots represent the observed data and the time is centered at peak flare time. . . .	140
6.9	<b>Left:</b> Comparison of flare frequency distribution of TRAPPIST-1 with 2M0837+2050 and 2M0831+2244. The solid black line plotted over TRAPPIST-1 flare energies is fitted line using parameters from [Paudel et al., 2018a] and the dashed black line represents extrapolation to energy $\log E$ (erg) = 35. <b>Right:</b> Same as the figure in left. The flare energies are replaced by corresponding EDs. . . .	140
7.1	The <i>K2</i> light curve of 2M1027+0629, in Campaign 14. Only a portion of the light curve is shown to focus on the beat patterns which are produced as a result of two closely separated periods 0.2114 days and 0.2199 days. . . . .	153

7.2	Phase folded lightcurves of 2MJ1027+0629. The blue lightcurve corresponds to period of 0.2114 day and the red lightcurve corresponds to period of 0.2199 day. Both lightcurves were binned using phase bin width = 0.005. . . . .	155
7.3	Lomb-Scargle periodogram of 2MJ1027+0629. The two peaks correspond to periods of 0.2114 and 0.2199 day. . . . .	155
7.4	Color magnitude diagram of M6-M9 dwarfs using <i>Gaia</i> DR2. 2M1027+0629 is marked in red and lies at the upper edge of the main sequence. . . . .	156
7.5	NIRSPEC spectrum of 2M1027+0629 obtained on UT 2018 April 26 (black line). The red line represents BT-Settl Solar-metallicity spectral model from [Allard et al., 2012]. The best fit parameters are $T_{\text{eff}} = 3110 \pm 40$ K, $\log g = 5.2 \pm 0.2$ , $RV = -9.8 \pm 0.6$ km s <sup>-1</sup> and $v \sin i = 21.5 \pm 1.1$ km s <sup>-1</sup> . The difference between data and model (O-C) is shown in black at the bottom of the plot; the $\pm 1\sigma$ uncertainty spectrum is indicated in gray. . . . .	157
7.6	The three strong flares observed on 2M1027+0629. The blue dots represent the observed data. The time along the X-axis of each panel is centered at peak flare time mentioned above each panel. . . . .	159
8.1	Circle of radius 2.5 arcsec, encircling the position of W1906+40 in its center at R.A.=19 <sup>h</sup> 06 <sup>m</sup> 48 <sup>s</sup> .63 and Dec.=+40°11'05".90. We can see two dots inside the circle, representing X-ray sources but <i>Chandra</i> detected only 1 photon from each of them, meaning that they are equally probable to be background noise. . . . .	164
9.1	Maximum flare energies observed on targets of various spectral types using both <i>K2</i> short and long cadence data. . . . .	170
D.1	Permission from Oxford University Press. . . . .	241

## ABBREVIATIONS

**2MASS** Two Micron All-Sky Survey

**ASASSN** All-Sky Automated Survey for Supernovae

**ASCA** Advanced Satellite for Cosmology and Astrophysics

**BD** brown dwarf

**DENIS** Deep Near Infrared Survey of the Southern Sky

**EPIC** Ecliptic Plane Input Catalog

**EXOSAT** European X-ray Observatory Satellite

**FFD** flare frequency distribution

**FUSE** Far Ultraviolet Spectroscopy Explorer

**GBR** Güdel-Benz relation

**HSC** Harvard stellar classification

**HST** Hubble Space Telescope

**IUE** International Ultraviolet Explorer

**JWST** James Webb Space Telescope

**KPNO** Kitt Peak National Observatory

**MAST** Mikulski Archive for Space Telescopes

**NASA** National Aeronautics and Space Administration

**PS1** Pan-STARRS1

**ROSAT** Roentgen Satellite

**SDSS** Sloan Digital Sky Survey

**ST** spectral type

**Swift-XRT** Swift X-ray Telescope

**TPF** Target Pixel File

**TESS** Transiting Exoplanet Survey Satellite

**UCD** ultracool dwarf

**UV** ultraviolet

**V01** VVV BD001

**VLA** Very Large Antenna

**WISE** Wide-field Infrared Survey Explorer

**WLF** white light flare

## ABSTRACT

We have used the NASA *Kepler K2* mission short cadence ( $\sim 1$  minute) and long cadence ( $\sim 30$  minutes) data to study the white light flare (WLF) rates of (sub)stellar objects with spectral types later than M4. Most of our targets are ultracool dwarfs. We analyzed WLFs of 42 targets using short cadence data and  $\sim 350$  targets using long cadence data. We identified a total of 1105 WLFs on 22 targets which were observed in short cadence mode. We observe a higher flare rate in the mid-M dwarfs where the stars are believed to become fully convective. The total estimated (UV/visible/IR) energies of flares observed in short and long cadence mode are in the range of  $\log E$  (erg)  $\sim (29.5-36)$ . The flare rate decreases as the effective temperature decreases. In an energy range of  $10^{29.8} - 10^{33.8}$  erg, the flare energy distributions follow a power law with slopes  $-\alpha$  in range  $-(1.3 - 2.0)$ . The cooler targets tend to have shallower slopes. We suggest that such shallower slopes can be attributed to the reduced electrical conductivity of the atmospheres in the cooler targets. We find that the slopes are independent of the kinematic ages of the targets, and have a mean value of  $-\alpha$  equal to  $-1.7 \pm 0.2$ . Comparing our results with those in literature, we find that the flare energy distributions of ultracool dwarfs have similar properties to those of flares in the Sun and also in stars with spectral types earlier than M5. This is a strong indication that solar and (sub)stellar flares are caused by a universal phenomenon presumably related to the magnetic field strength  $B$  in active regions on each star: the total flare energy involves the product of magnetic energy density  $B^2/8\pi$  and a volume. We find that there is no significant difference in the maximum energies of flares produced by targets of various spectral types in our sample. This suggests that the upper limit to the flare energy is independent of the effective temperature of the targets.

We find that targets with spectral type as late as L5 can produce white light

flares. We observed one large flare on 2MASS J08585891+1804463 (L2) and two superflares (flares with energy in excess of  $10^{33}$  erg) on VVV BD001 (L5). The largest flare on VVV BD001 had an amplitude  $>300$  times the quiescent photospheric level: this was the largest amplitude event among all the flares studied here. The estimated energy of this flare is equal to  $10^{34.7}$  erg. The occurrence of superflares on targets with spectral types as late as L5 also suggests that either they have strong magnetic fields comparable to those in the warmer targets or the volumes associated with flares are larger on cooler targets, or a combination thereof. For the superflares observed on an M7 and an L0 dwarf using short cadence data, we find that they have very short full-width-half-maximum (FWHM) timescales of  $\sim 2$  minutes.

## Chapter 1

### INTRODUCTION

#### 1.1 A brief history of study of flares on M and L dwarfs

The history of observation of flares on faint stars dates back to the year 1924 when Ejnar Hertzsprung, a Danish chemist and astronomer, first noticed a brightening of a faint star on one of the photographic plates used to study the star. [Gershberg \[2005\]](#) argues that this brightening is apparently the first recorded stellar flare. WX UMa (M6.0e) is the first known M dwarf on which a huge flare was recorded in 1940 by using photographic plates. It brightened by  $1\text{-}2^m$  on a photographic plate [[van Maanen, 1940](#)]. Similar phenomena were observed again on YZ CMi (dM4.5e) in 1945 [[van Maanen, 1945](#)] and on L 726-8 (M5.5e+M6.0e; also known as GJ 65 AB) in 1948 [[Joy and Humason, 1949](#); [Luyten, 1949](#)]. One of the members of L 726-8 binary system was later named as UV Cet and is an M6.0e star. Nowadays, the flaring M dwarfs are commonly known as UV Ceti type stars and are a special category of variable stars as recognized by the General Assembly of the International Astronomical Union [[Gershberg, 2005](#)]. In addition to the flaring M dwarfs mentioned above, some other famous nearby flaring M dwarfs are AD Leo (M3.5e), EV Lac (M3.5e), Barnard's star (M4.0), Proxima Centauri (M5.5e) and Wolf 359 (M6.5e).

More flaring M dwarfs were identified during the 1950s by various monitoring programs performed at various observatories. The increase in data also enabled a statistical analysis of flare activity of such stars (see for e.g., [Gershberg 1972](#); [Moffett 1974](#); [Lacy et al. 1976](#)). Flare stars were mainly studied by using photographic plates until the late-1970s. The launch of various space satellites including IUE, *Einstein* Observatory, EUVE, EXOSAT, ROSAT, ASCA, *Chandra*, Swift-XRT, XMM-*Newton*, HST

and FUSE in the 1980s and 1990s broadened the horizon of the study of flaring stars. Such facilities in combination with several ground based facilities including KPNO, VLA, made possible the (simultaneous) multiwavelength studies of flaring M dwarfs in the X-ray, FUV, UV, visible and radio wavelengths. This helped to study the amount of flux emitted in both quiescent and flaring state in various wavelengths and the corresponding correlations (see for e.g., [Hawley and Pettersen 1991](#); [Osten et al. 2005, 2006, 2010, 2016](#)). However, most of such studies were done on M1 - M6 dwarfs. Before the *KeplerK2* mission started observing ultracool dwarfs (UCDs; defined below), only a very few late-M dwarfs were known to produce flares in various wavelengths including  $H\alpha$ , X-ray and white light continuum (see for e.g., [Liebert et al. 1999](#); [Rutledge et al. 2000](#); [Martín and Ardila 2001](#); [Rockenfeller et al. 2006](#); [Schmidt et al. 2007](#)). [Gizis et al. \[2000\]](#) and [Schmidt et al. \[2007\]](#) reported that the flaring late-M dwarfs (M7-M9) had  $\sim 5\%$ - $7\%$   $H\alpha$  flare duty cycle. Likewise, [Liebert et al. \[2003\]](#) and [Schmidt et al. \[2007\]](#) reported that L dwarfs had  $H\alpha$  flare duty cycle of  $\sim 1\%$ - $2\%$ . One L dwarf (2MASS J01443536-0716142; L5.0) was known to produce an  $H\alpha$  flare [[Liebert et al., 2003](#)] and one T dwarf (2MASS J10475385+2124234; T6.5) was known to produce a radio flare [[Route and Wolszczan, 2012](#)]. Also prior to *K2*, [Hilton \[2011\]](#) used ground based telescopes to observe 4 M6-M9 dwarfs for 60.27 hr and detected 29 flares. It was the *K2* mission which provided a major opportunity to study the flares on UCDs in greater detail. The importance of studying flares on UCDs is discussed in [Section 1.9.3](#).

## 1.2 Stellar classification system

The stellar and substellar objects are classified into various spectral types on the basis of their surface effective temperatures ( $T_{\text{eff}}$ ). According to the Harvard stellar classification (HSC) system, they are classified as O, B, A, F, G, K, M, L, T and Y spectral types. Among these, the objects with O spectral types are the hottest and most massive and those with Y spectral types are the coolest and least massive. Each spectral type is further divided into various subclasses. Each subclass is denoted by a

spectral class followed by a number in between 0 and 9, for e.g. G1, G2.5 etc. This classification does not give proper information regarding the luminosity class. Such information was later incorporated in a new classification system known as Morgan-Keenan (MK) system in which Roman numerals are also used in addition to HSC to denote whether if the objects are supergiants, giants, main sequence stars, sub-dwarfs or white dwarfs. For example, the numeral V denotes that the star is in main sequence. Our Sun has a spectral type of G2V with  $T_{\text{eff}} \approx 5800$  K [Karttunen et al., 2017].

### 1.3 M dwarfs

M dwarfs are objects with  $T_{\text{eff}}$  in the range  $\sim (3800 - 2400)$  K and are also commonly known as red dwarfs. They make up  $\sim 75\%$  of all main sequence stars in the local stellar population [Clements et al., 2017]. They are smaller, cooler and less luminous than the Sun. M dwarfs with spectral types of M7 or later are a mixture of both low mass stars and young brown dwarfs. Thus if an M dwarf is a star, it has mass in the range  $\sim (0.5 - 0.075) M_{\odot}$  and if it is a brown dwarf, it has mass less than  $\sim 0.075 M_{\odot}$  which is the hydrogen burning limit [Burrows et al., 2001]. According to stellar models, the M dwarfs with mass  $\lesssim 0.35 M_{\odot}$  are fully convective [Chabrier and Baraffe, 1997]. However, this mass limit of fully convective stars also depends on metallicity and age. For e.g., Mullan et al. [2015] claim the limit is  $0.32 - 0.33 M_{\odot}$  or  $0.33 - 0.34 M_{\odot}$  depending on various model assumptions.

The optical spectra (6300 to 9000 Å) of M dwarfs are mainly dominated by titanium oxide (TiO), vanadium oxide (VO) and carbon monoxide (CO) absorption bands. In particular, the TiO bands are stronger in the case of M0-M6 dwarfs and become weaker in the later types in which the VO bands are stronger. Likewise, in the near-infrared spectra (0.95 to 2.35  $\mu\text{m}$ ), the H<sub>2</sub>O bands as well as the absorption lines of neutral alkali metals (Na, K) and FeH appear to be stronger in the late-M dwarfs [Kirkpatrick et al., 1991, 1995].

## 1.4 L dwarfs

L dwarfs are objects with  $T_{\text{eff}}$  in the range  $\sim (2400 - 1300)$  K. They are also a mixture of both old low mass stars and brown dwarfs. They have average radii of  $0.1 R_{\odot}$ . Theoretically, all the L dwarfs with spectral types later than L4 are brown dwarfs (see for e.g., [Chabrier et al. 2000](#); [Saumon and Marley 2008](#)). Because of cooler atmospheric temperatures, the spectra of early L dwarfs are dominated by many atomic and molecular bands. In the spectra of early-L dwarfs, the most prominent atomic lines are those of neutral alkali metals (Na I, K I, Rb I, Cs I) and the most prominent molecular lines are the oxide bands TiO and VO, and the hydride bands CrH, FeH and CaOH. The TiO and VO bands are both weaker in comparison to the late-M dwarfs and disappear by mid-L dwarfs in which the neutral alkali metal lines (mostly Na I and K I) are very strong. Likewise, the hydrides MgH, CaH, CrH and FeH also become stronger than in early-L dwarfs. In the case of late-L dwarfs, the H<sub>2</sub>O absorption bands are the the most prominent features along with the neutral alkali metal lines, while the hydrides are somewhat reduced [[Kirkpatrick et al., 1999](#)].

It should be noted here that three surveys, the Two Micron All Sky Survey (2MASS; [Skrutskie et al. 2006](#)), the Deep Near-infrared Sky Survey (DENIS; [Epchtein et al. 1999](#)) and the Sloan Digital Sky Survey (SDSS; [York et al. 2000](#)), played a very important role in discovering and characterizing many M and L dwarfs.

## 1.5 Brown Dwarfs

Brown dwarfs (hereafter BDs) are substellar objects with masses lower than  $\sim 0.075 M_{\odot}$  which is the minimum mass required for hydrogen fusion in the core of object. This mass limit depends on metallicity. Work by [Chabrier and Baraffe \[1997\]](#) find a “minimum mass” for hydrogen burning (which they define as that mass where hydrogen burning can supply the star’s luminosity after 1 billion years) is about  $0.072 M_{\odot}$  for a star with solar metallicity, but rises to about  $0.083 M_{\odot}$  for stars which have

less than a tenth of the solar metallicity. Earlier work by [Baraffe et al. \[1995\]](#) determined a limit of  $0.09 M_{\odot}$  for a metallicity 30 times less than the Sun. The review of [Burrows et al. \[2001\]](#) says that the minimum mass for a “zero metallicity” population III star is  $0.092 M_{\odot}$ . This limit originates from modeling work performed by [Saumon et al. \[1994\]](#). In summary, the value of  $M_{\min}$ , i.e. the minimum stellar mass for H fusion to occur, ranges from  $0.072 M_{\odot}$  up to  $0.092 M_{\odot}$ , depending on the metallicity: lower metallicity drives  $M_{\min}$  to larger masses.

The BDs can fuse deuterium and have masses as low as  $\sim 13 M_J$  which is the minimum mass required for deuterium burning and also depends on various factors like the helium abundance, the initial deuterium abundance, the metallicity [[Spiegel et al., 2011](#)]. In general, they have masses in the range  $\sim (75 - 13) M_J$ , which covers the gap between planetary mass and stellar mass. Hence, they are also sometimes called failed stars or giant Jupiters. The existence of brown dwarfs was first predicted theoretically by [Kumar \[1962\]](#). It took about 33 years for the first reliable identification of a brown dwarf because of lack of proper observing instruments. Teide 1 [[Rebolo et al., 1995](#)] was the first observationally confirmed BD. In the same year, another BD (G1229B) was discovered by [Nakajima et al. \[1995\]](#). Originally BDs were also called “black dwarfs” as they were predicted to have very low luminosity and hence might be undetectable. The same term was also used to refer very old white dwarfs. In order to avoid the confusion, the name “brown dwarfs” was first coined by [Tarter \[1976\]](#) for such objects. However, this name doesn’t describe their true color which is more close to purple.

## 1.6 Ultracool dwarfs

Ultracool dwarfs refers to all the (sub)stellar objects with spectral types  $\gtrsim M7$ . The late-M dwarfs and early-L dwarfs may be old low mass stars or brown dwarfs; T and Y dwarfs are all brown dwarfs. They have effective temperatures  $\lesssim 2700$  K [[Kirkpatrick et al., 1999](#); [Martín et al., 1999](#)].

## 1.7 Flares

Stellar flares are transient events which are caused by sudden releases of magnetic energy in the atmosphere of a star (e.g., [Mullan 1977](#)). Flares are the most prominent manifestation of magnetic activity on the surface of the Sun and on low-mass stars. During a flare, the magnetic structure of a loop or active region is altered in some way by convection (e.g., [Mullan and Paudel 2018](#)), with the result that some energy previously stored in the non-force-free field is released rapidly, on time-scales of seconds or less. The rapid release of energy in a small region with linear dimension  $l$  is believed to be due to magnetic reconnection of the loops which extend from the active regions to the corona. It occurs on a time-scale related to the ratio  $l/V_A$ , where  $V_A$  is the Alfvén speed. In the case of the Sun, observed values of  $V_A$  in solar active regions are in the range 1,900 to 37,000 km/s [[Schmelz et al., 1994](#)]: therefore magnetic energy can be released on time scales of seconds or less provided that the size of the reconnection region is smaller than roughly 40,000 km. In fact, the length scales associated with electrons propagating from an acceleration region in solar flares to a region of hard X-ray emission (i.e., time of flight information) have been narrowed down to have linear sizes of no more than a few thousand km [[Aschwanden et al., 1996](#)]. Moreover, the linear size of the acceleration region itself may be even smaller (e.g., [Cassak et al. 2008](#)).

Our understanding of the flares is mainly based on the observations of solar flares. Multiwavelength studies of various stellar flares (for e.g., [Mullan 1977](#); [Hawley and Pettersen 1991](#); [Osten et al. 2005, 2006, 2010, 2016](#)) suggest that a common physical process gives rise to the flares on the Sun and other stars. During magnetic reconnection, energy which was originally stored in magnetic fields is mainly converted to kinetic energy of the particles (ions and electrons) which are accelerated up to MeV energies, bulk plasma motion and thermal emission mostly in the form of soft X-rays. Some of the bulk plasma motion leads to ejection from the star in the form of coronal mass ejections (CMEs). Some of the non-thermal particles propagate towards the loop

footpoints. Electromagnetic radiations of various wavelengths are emitted as a consequence of the energetic particles impacting the denser gas in the lower atmosphere of the star. Nonthermal radio emission is produced as a result of gyrosynchrotron of the highly energetic electrons. The downward moving particles deposit a large amount of their energies in the lower atmosphere via thick target bremsstrahlung producing nonthermal hard X-rays/gamma rays. As a consequence of this heating, some chromospheric material evaporates and hence injects soft X-ray emitting material into the flaring loops. This leads to the production of thermal soft X-rays. After losing their energies, the particles precipitate and form hot condensations in the lower chromosphere or the upper photosphere and emit white light continuum. More details regarding physical processes involved during the production of flares and the corresponding references can be found in the review paper by [Benz and Güdel \[2010\]](#).

### 1.7.1 Flares on M/L dwarfs

In addition to having low values of luminosity, M dwarfs have another important characteristic: they are also known to be the sites of strong magnetic fields [[Saar, 1996](#); [Reiners et al., 2009a](#)], with surface field strengths up to as much as 7 kG [[Shulyak et al., 2017](#)]. These fields, when perturbed by convective flows in the envelope of the M dwarfs, lead to magnetic activity. One of the prominent signatures of such activity is that the  $H\alpha$  line (which in the photosphere of a dwarf is present only weakly in absorption) is driven into emission if the supply of mechanical energy entering the chromosphere is sufficiently large [[Cram and Mullan, 1979](#)]: magnetic fields, in view of their large energy density ( $B^2/8\pi$  ergs  $\text{cm}^{-3}$ ) can, in the presence of convection, supply mechanical energy in abundance to a stellar chromosphere. The observed fraction of M dwarfs which have the  $H\alpha$  line in emission rises until it reaches  $\sim 90\%$  at spectral type L0 [[Schmidt et al., 2015](#)].

Now that we know that strong magnetic fields are also present on the surfaces of M dwarfs, and M dwarfs also possess convective envelopes, it is plausible to expect

that phenomena analogous to solar flares occur when magnetic energy is released during flares on M dwarfs. Is there any support for this expectation? Yes. The white light flares on the Sun have clear analogs in the flares reported by the ground-based study of [Hawley and Pettersen \[1991\]](#), and also in the space-based study of the many (almost 1 million!) flares detected by the broad-band filter on *Kepler* [[Davenport, 2016](#)]. Flare-related emissions extending across the electromagnetic spectrum from radio to X-ray have been reported for some flare stars like EV Lacertae (dM 4.5e) and DG CVn (GJ 3789; M dwarf binary system) [[Osten et al., 2005, 2016](#)]. Likewise, the observation of 21 white light flares on an L1 dwarf WISEP J190648.47+401106.8 by the *Kepler* mission [[Gizis et al., 2013](#)] provides strong evidence that flares can be produced by such cool objects. Further discussion about flares on L dwarfs will be presented in other chapters. Observations suggest that there is no significant difference in white light flares on M dwarfs and L dwarfs. The only differences are the flare energies and flare rates. The overlaps in observational signatures strengthen the plausibility that flares on M/L dwarfs are analogs of the energetic phenomena which we see (in much more spatial detail) on the Sun. In contrast to the analogy between stellar and solar flares, [Pineda et al. \[2017\]](#) have suggested a very different interpretation for flares on brown dwarfs: they might result from planet-like auroral emissions produced by large-scale magnetospheric currents.

The amount of energy which is released in flares on M/L dwarfs ranges from  $\log E$  (ergs)  $\sim 26$  -  $\log E$  (ergs)  $> 36$  [[Lacy et al., 1976](#); [Kowalski et al., 2010](#); [Davenport, 2016](#); [Paudel et al., 2018a,b](#)]. Flares occur on M dwarfs even when they are very young [[Hilton, 2011](#); [Paudel et al., 2018b](#)]. CFHT BD Tau 4 is an example of a very young ( $\sim 1 - 2$  Myr) M7 dwarf on which one of the biggest superflares (defined as flares with energies in excess of  $10^{33}$  ergs) was observed using *K2* long cadence data. This flare has a total energy in excess of  $10^{36}$  erg. However, it is not merely young stars that undergo flares: the star Trappist-1 has been observed to flare multiple times [[Vida et al., 2017](#); [Paudel et al., 2018a](#)], and the star is definitely old, with an age of  $7.6 \pm 2.2$  gigayears

[Burgasser and Mamajek, 2017]. Thus, flares can occur on M dwarfs over a wide range of ages, indicating that either (i) the star can hold onto its magnetic fields for many gigayears, or else (ii) the fields are actively generated by dynamo activity even when the stars are older than the Sun.

### 1.8 Flare frequency distribution (FFDs)

The flare frequency distribution (FFD) of a flaring star is observed to have a shape which can be fitted with a power law. A log-log plot between the flare energy  $E$  and cumulative frequency (number of flares with energy  $> E$ ), can in many cases be fitted (over a finite range of energies) by a straight line. The data suggest that the FFD has some well defined characteristics (e.g. Lacy et al. 1976):

i) At the lowest energies, flares cannot be confidently distinguished from the detector noise: as a result, the detector noise in effect sets a lower limit  $E_{\min}$  on the energy of a reliably identifiable flare event on any particular star.

ii) At the largest energies, there appears to be a saturation such that even after long intervals of observing time, the energy of an individual flare in any particular star appears to have great difficulty in rising above a certain limit. In other words, there appears to be an upper limit  $E_{\max}$  on the energy of flares which can occur on that star.

iii) At energies which are intermediate between  $E_{\max}$  and  $E_{\min}$ , the FFD can be fitted by a power law of the form [Gershberg, 1972; Lacy et al., 1976]:

$$\log \tilde{\nu} = \alpha_o - \beta \log E \quad (1.1)$$

where  $\tilde{\nu}$  is the cumulative (or integrated) flare frequency, i.e. the number of flares with energies of  $\geq E$  which were detected per unit observation time. The constant  $\alpha_o$

represents the cumulative frequency intercept at zero energy, and the constant  $\beta$  represents the slope of the FFD.  $\beta$  is a very important parameter which gives information regarding the number of flares with energies in a given range and observation time. If the  $\beta$  value of FFD of the flaring star is steep, this signifies that for a given observation time and an energy range, more flares can be observed on this star than on another star with a shallower value of  $\beta$ .

The FFD can also be expressed in a differential form as:

$$dN/dE = AE^{-\alpha} \quad (1.2)$$

where  $dN$  is the differential number of flares occurring on a given star per unit time with total energy between  $E$  and  $E+dE$ , and  $A$  is some constant. The indices in Eq. 1.1 and Eq. 1.2 are related by  $\alpha = \beta + 1$ . In stars which are found to have spectral index  $\beta > 1$  (i.e.,  $\alpha > 2$ ), the weakest flares contribute most to the total energy emitted by flares. In the stars with  $\beta < 1$  (i.e.,  $\alpha < 2$ ), the strongest flares contribute most to the total energy emitted by flares. Here, the phrase “total energy emitted by flares” refers to the energy released in all flares which were detected on a particular star during a given observation time.

Assuming that all the flares with energy in the range from  $E_{\min}$  to  $E_{\max}$  follow a FFD with a uniform power law, the total energy of all such flares during an observation time  $T$  can be computed by using the spectral index  $\beta$ . This total energy is expressed as [Gershberg and Shakhovskaia, 1983]:

$$\varepsilon = T \times 10^\alpha \beta (E_{\max}^{1-\beta} - E_{\min}^{1-\beta}) / (1 - \beta) \quad (1.3)$$

Figure 1.1 shows the FFD of one famous late-M dwarf: TRAPPIST-1. This FFD was estimated by using the *K2* mission data and will be discussed in more detail in

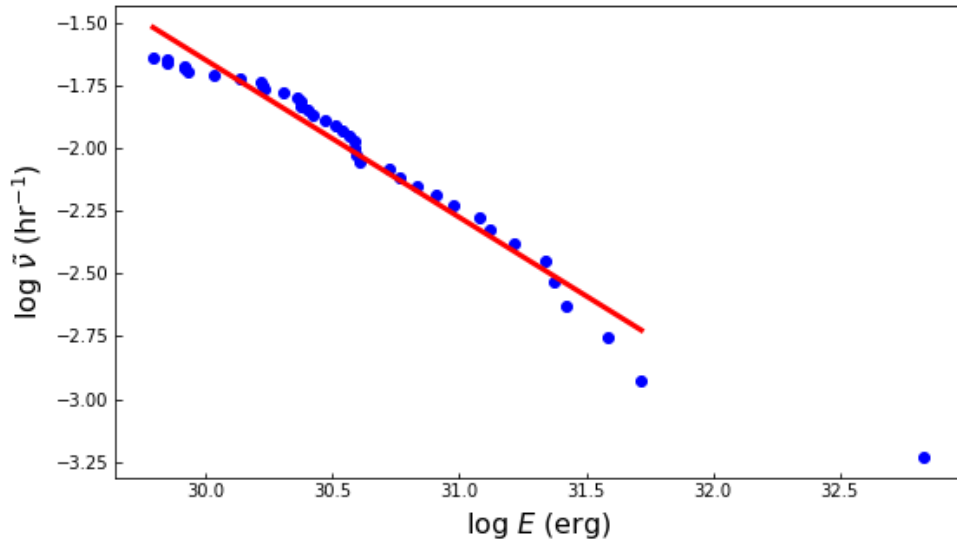


**Figure 1.1:** An example of the FFD of a late-M dwarf: TRAPPIST-1. Along the  $X$ -axis are log values of observed flare energies and along the  $Y$ -axis are log values of cumulative frequencies. The blue dots represent the observed flares and the red line represents the fitted line using a power-law model.

## Chapter 2.

There is some information contained in the value of  $E_{\max}$ , above which no flares are observed. In the Sun, when radiation in the ultraviolet can be measured,  $E_{\max}$  is found to be of order  $5 \times 10^{32}$  erg [Kopp et al., 2005]. What is the physical significance of this result? To interpret it, we also note that the Sun experiences another kind of magnetically driven energy release (CMEs) where the energy is in the form of bulk kinetic energy, with no significant contribution from radiant energy. Jackson and Howard [1993] report that during the time of solar maximum around 1980, the numbers of CMEs  $N$  as a function of mass had an exponential form:  $N = 370 \exp(M/M_c)$  where  $M_c$  has a numerical value of  $1.06 \times 10^{16}$  gm. Using this value of  $M_c$  as the upper limit of mass, and the upper limit on speed ( $3.2 \times 10^8$  cm sec<sup>-1</sup>) of CMEs as recorded by SOHO/LASCO in the years 1996-2003, we find that kinetic energy of the largest CME is  $5 \times 10^{32}$  erg. Furthermore, Emslie et al. [2012] report that only 21 CMEs were observed during 1997-2003, which had kinetic energies  $\geq 10^{32}$  erg. Gopalswamy [2006] reports a total of 4133 CMEs during the same period and that their average kinetic energy is  $5 \times 10^{29}$  erg. This suggests that  $\sim 0.5\%$  of CMEs have kinetic energies  $\geq 10^{32}$  erg. Emslie et al. [2012] report that the CME energy exceeds the flare bolometric energy by about half an order of magnitude. It is interesting that the maximum kinetic energy of CMEs coincides with the largest amount of radiated energy emitted by a solar flare. It has been suggested [Mullan and Mathioudakis, 2000] that the Sun's magnetic properties are such that the Sun has the capacity to store energy in magnetic form only up to a certain critical value ( $E_c \approx 5 \times 10^{32}$  ergs). Perhaps the upper limit is associated with a property of the dynamo which is generating the magnetic fields.

Aulanier et al. [2013] also estimated an upper limit to the solar flare energy to be  $\sim 6 \times 10^{33}$  erg by using the value of strongest magnetic field (i.e. 3.5 kG) ever measured in a sunspot. The existence of an upper limit on the capacity of a star to store

energy might be true in the case of other flare stars also. Study of statistical distribution of flares by analyzing as many light curves of M dwarfs as are available should help us to figure out the maximum flare energy that can be generated by each spectral type. This value may be related to the nature of the magnetic dynamo which operates in those stars. Therefore, information about dynamos in flare stars may be obtained if we can identify a possible cause for the upper limits on flare energy.

There is an increasing trend of magnetic activity with decreasing stellar mass (e.g., [Hawley et al. 1996](#)), and flares occur on a high fraction of magnetically active late-M dwarfs [[Kowalski et al., 2013](#)]. It is important to note that flares can be found in at least some dwarfs at all spectral types from M0 to L1 (e.g., [Hilton 2011](#); [Gizis et al. 2013](#); [Hawley et al. 2014](#)). In regard to this, the flare rates could also be used as a proxy for stellar activity, which can be constrained by analyzing statistical properties of flare rates of many M and L dwarfs using data obtained by missions such as *K2* and Transiting Exoplanet Survey Satellite (*TESS*). In turn, the flare rates can be useful parameters that may help us to understand the nature and evolution of magnetic dynamo in M and L dwarfs. In particular, it has been reported by [Houdebine et al. \[2017\]](#) that the rotation-activity-correlation has a different slope in dKe/dMe stars than in dK/dM stars. It would be interesting to see if this difference in dynamo properties also exists in flare data.

## 1.9 Importance of studying flares

### 1.9.1 Nature of the magnetic dynamo

Flares depend for their existence on magnetic fields, and the fields in stars with extensive convection zones themselves depend on the operation of a dynamo. The essence of a dynamo is that the motions of ionized gas in a star (such as those due to convection) lead to electric currents, each of which generates its own localized magnetic field. If the star has a way to organize the individual currents in a suitable manner, the overall result can be a global field [[Parker, 1955](#)]. One way to do the organizing

is to notice that in a turbulent medium, the combination of fluctuating velocities and fluctuating fields can lead to a net electromotive force (emf) which is proportional to the mean field [Charbonneau, 2014]:  $\text{emf} = \alpha B$ . This property of turbulence is referred to as the  $\alpha$ -effect. Coriolis forces in a rotating star create nonzero values of  $\alpha$ , but can also lead to large-scale rotational shear (RS): this shear can be especially severe if the stars convection zone has an interface with a radiative (stable) region deep inside the star.

Different dynamo models emerge depending on how large the  $\alpha$ -effect is relative to the RS effects. In a star where RS dominates in generating toroidal field, while the  $\alpha$ -effect generates poloidal fields, we refer to an  $\alpha\Omega$ -dynamo. If RS in a star is weak, then the  $\alpha$ -effect dominates in generating both toroidal and poloidal fields: this leads to an  $\alpha^2$ -dynamo. And if, in a star, it turns out that RS and  $\alpha$ -effect are comparable in magnitude, we have an  $\alpha^2\Omega$ -dynamo.

In the Sun, where an interface between convection and radiative core exists at a depth of about  $0.3R_{\odot}$  below the surface, RS is so large at the interface that the Sun's dynamo is classified as an  $\alpha\Omega$ -dynamo. In M stars later than M3-M4, theory [Limber, 1958] suggests that the interface disappears: in such stars, the star is expected to rely on an  $\alpha^2$ -dynamo (if the star is a slow rotator), or on an  $\alpha^2\Omega$ -dynamo (if the star is a fast rotator).

### 1.9.2 Rotation-activity relations

Magnetic fields in solar-type stars are believed to be generated mainly by an  $\alpha\Omega$  dynamo. Such stars display a pronounced correlation between rotation and activity in the following sense: as the rotation speed increases, indicators of the strength of magnetic activity (e.g. coronal X-ray flux, chromospheric emission in the  $H\alpha$  and CaII H and K lines) increase steeply. The correlation is referred to as the rotation-activity correlation (RAC), and the slope of the correlation is a measure of how sensitive the stellar

activity is to rotation. The value of the RAC slope may therefore contain information as to the nature of the dynamo which is at work in a sample of stars. Empirically, the RAC does not extend to arbitrarily fast rotations: there is a limit beyond which no further increase in activity level occurs, no matter how fast the rotation. This limit indicates that the dynamo has reached a saturated state. For the most rapid rotators (solar-type stars and early M dwarfs), one important magnetic activity indicator: the X-ray emission, is found to saturate at values  $L_X/L_{\text{bol}} \sim 10^{-3}$  [Vilhu, 1984; Micela et al., 1985; Pizzolato et al., 2003; Wright et al., 2011], and another important indicator: the H $\alpha$  emission, is also found to saturate at values  $L_{\text{H}\alpha}/L_{\text{bol}} \sim 10^{-3.8}$  [Douglas et al., 2014; Newton et al., 2017]. Here  $L_X$ ,  $L_{\text{H}\alpha}$  and  $L_{\text{bol}}$  are the X-ray, H $\alpha$  and bolometric luminosity respectively. The saturation in both activity indicators is independent of spectral type. There is a decline in both X-ray luminosity and H $\alpha$  luminosity between M0 and M6 spectral types. However, this decline is roughly proportional to the decline in the bolometric luminosity, at levels of saturated values mentioned above [Reiners and Basri, 2010].

The numerical value of the saturation level of  $L_X/L_{\text{bol}}$  may be determined by the upper limit on mechanical energy in the convective flows [Mullan, 1984]. Saturation is observed to set in at rotation periods of 1-10 d for solar-type stars, corresponding to Rossby numbers ( $\text{Ro} = P_{\text{rot}}/\tau$ , where  $\tau$  is the convective turnover time; Noyes et al. 1984) of order  $R_o \sim 0.13$  [Wright et al., 2011]. The early M dwarfs are observed to follow RAC similar to solar-type stars [Delfosse et al., 1998; Mohanty and Basri, 2003]. In summary, the rotation rate plays a significant role in shaping the magnetic dynamo of solar type and early-M dwarfs. When they are young, their rapid rotation rates empower strong magnetic dynamos. As they evolve, magnetic braking slows the rotation, which in turn decreases the magnetic activity [Donati and Landstreet, 2009; Gershberg, 2005; Telleschi et al., 2005].

It is important to note that Houdebine et al. [2017] have found that the empirical

RAC is steep in active stars with spectral types K4e-M2e: this is consistent with theoretical expectations that K4e-M2e dwarfs (where masses exceed  $0.3\text{-}0.35M_{\odot}$ ) do possess a radiative core. In such stars, an  $\alpha\Omega$  dynamo may indeed be operative, thereby causing the RAC slope to be steep. However, [Houdebine et al. \[2017\]](#) also find that for stars of spectral type M3e and M4e, the slope of the empirical RAC is distinctly shallower (at the  $3\sigma$  level). Thus, in M3e and M4e stars, rotation does not play as strong a role in determining the activity level: the diminished effects of rotation suggest that the  $\alpha^2$  (or  $\alpha^2\Omega$ ) dynamo is more effective in M3e-M4e stars. These stars have masses on the main sequence which overlap with the theoretical boundary (around masses of  $0.3\text{-}0.35 M_{\odot}$ ) where stars become completely convective. In such stars, which have no tachocline, there is no reason to expect that the  $\alpha\Omega$  dynamo should dominate.

### 1.9.3 Motivation for studying flares on UCDs

The UCDs are objects of special interest for studying magnetic activity. In addition to having masses which coincide with the hydrogen burning limit, they also show a transition from the familiar solar/stellar magnetic activity relations. They do not follow the same age-rotation-activity relations observed on solar-type and early M dwarfs. Some of them have very strong magnetic fields [[Shulyak et al., 2017](#); [Berdyugina et al., 2017a](#)] and are capable of producing superflares. Despite being rapid rotators with periods  $<10$  hours, they have reduced levels of X-ray and  $H\alpha$  activity. The value of  $L_X/L_{\text{bol}}$  drops from a saturated level of  $10^{-3}$  (M0-M6 spectral types) to  $10^{-4}$  for M7-M9 dwarfs and  $\lesssim 10^{-5}$  for L dwarfs. Likewise, the value of  $L_{H\alpha}/L_{\text{bol}}$  decreases from a saturated level of  $10^{-3.8}$  (for M0-M6 spectral types) by at least two orders of magnitude between M6 and L3 spectral types. [[Gizis et al., 2000](#); [West et al., 2004](#); [Stelzer et al., 2006](#); [Berger et al., 2010](#); [Schmidt et al., 2015](#)]. Furthermore, X-ray and  $H\alpha$  activity levels decrease by 1-2 orders of magnitude in the UCDs which rotate with maximum velocities: this is often called a ‘supersaturation’-like effect [[James et al., 2000](#); [Berger et al., 2008b](#); [Reiners and Basri, 2010](#)]. The UCDs do not show any trend of saturation in X-ray and  $H\alpha$  activity levels like in the case of solar-type stars when

there is increase in the rotation periods [Basri and Marcy, 1995; Mohanty and Basri, 2003; Berger et al., 2010]. This indicates that the magnetic dynamo that exists inside UCDs depends on their rotation rates differently from that of the solar-type stars. This could be due to a number of factors, including cool atmospheres which have reduced amounts of ionized gas and may therefore experience decoupling between the magnetic fields and the gas [Mohanty et al., 2002], or atmospheres which are undergoing centrifugal coronal stripping [James et al., 2000; Jardine and Unruh, 1999; Berger et al., 2008a].

Radio emission is another significant magnetic activity indicator. Radio activity (the ratio of radio to bolometric luminosity;  $L_{\nu,R}/L_{\text{bol}}$ ) follows a different trend than the other two indicators:  $L_X/L_{\text{bol}}$  and  $L_{\text{H}\alpha}/L_{\text{bol}}$ . While the values of  $L_X/L_{\text{bol}}$  and  $L_{\text{H}\alpha}/L_{\text{bol}}$  decline in UCDs, the values of  $L_{\nu,R}/L_{\text{bol}}$  increase from  $10^{-9}$  for early-M dwarfs to  $10^{-8}$  for mid-M dwarfs and to about  $10^{-6.5}$  for UCDs [Reiners and Basri, 2010]. In addition, UCD radio emission increases with rotation and does not show saturation even in the case of rapidly rotating objects [McLean et al., 2012]. Most active F-M stars and solar flares follow Güdel-Benz relation (GBR) according to which X-ray luminosity is related to radio luminosity as  $L_{\nu,R}/L_X \approx 10^{-15.5}$  [Guedel and Benz, 1993; Gudel et al., 1993; Benz and Guedel, 1994]. Berger et al. [2010] found that this proportionality between  $L_X$  and  $L_{\nu,R}$  does not hold for UCDs. They estimated that  $L_{\nu,R}/L_X \approx 10^{-14}$  for M7-M8 and becomes  $\gtrsim 10^{-12}$  for spectral types later than M9. More discussion regarding the diverging behaviour of UCDs from GBR can be found in Williams et al. [2014] in which the authors also mention the possibility of two categories of UCDs: i) radio-bright and X-ray-faint objects and ii) radio-faint and X-ray-bright objects; which have different magnetic field topologies. The presence of strong radio emission suggests that large scale magnetic fields exist in UCDs [Route and Wolszczan, 2012; Williams and Berger, 2015; Route and Wolszczan, 2016]. One interpretation of these data is that turbulent dynamos may be producing both large and small scale magnetic fields in the UCDs [Reiners and Christensen, 2010; Yadav et al., 2015]. Alternatively, X-rays and  $\text{H}\alpha$  emission may be powered by fast magnetic reconnection, whereas radio emission may be

generated by electrons which emerge from slow magnetic reconnection [Mullan, 2010].

The nature of magnetic dynamos in M/L dwarfs can be studied by taking different approaches. For example, by the study of i) the relation between the flare rates and rotation periods, ii) the distribution of peak flare energies, iii) the study of the values of the coefficient  $A$  in the FFD power laws, iv) the study of the variation of flare rates with spectral type, v) the study of the variation of flare rates with age. Some of these approaches are discussed below and some of them are discussed in Chapter 2.

**i) Rotation periods:** Cool starspots on the surface of M dwarfs give rise to rotational modulations from which rotation periods can be determined using the primary *Kepler*, *K2* and *TESS* light curves. For example, using the *Kepler* data, McQuillan et al. [2013] detected rotation periods in 1570 (63.2%) of 2483 M dwarfs, with periods in the range (0.37 - 69.7) days. *K2* can measure rotation periods in the range from a few hours to  $\sim 80$  days. The nature of the stellar dynamo might be better understood if we could examine the correlation between the rotation rates and the flare rates for a more homogenous and larger sample of M dwarfs. For example, Mondrik et al. [2019] analyzed the flare rates of a sample consisting of 34 mid-to-late M dwarfs using the MEarth photometric survey data. They found that the flare rates are small among the slowest rotators with periods  $>70$  d, but also are small among the fastest rotators with periods  $<10$  d. Maximum flare rates are found among intermediate period rotators with periods of (10 - 70 d). The fact that intermediate rotators have more flares than slow rotators is an indication that rotation is involved in the dynamo among such stars: such a result indicates that an  $\alpha\Omega$ -dynamo or an  $\alpha^2\Omega$ -dynamo may be at work. However, the fact that fewer flares occur at the fastest rotation suggests that the dynamo might have little or no sensitivity to rotation: this suggests that an  $\alpha^2$ -dynamo might be at work. The results of Mondrik et al. [2019] pose an interesting challenge to dynamo theorists, and suggest that analysis of a larger sample of flare stars would be worthwhile.

**ii) Peak flare energies:** An advantage of having access to a large number of M dwarf light curves obtained by *K2* is that we will have access to information about the strongest flare energies for a large homogenous and unbiased sample. This could help to put constraints on the strongest magnetic fields of M dwarfs of various masses and ages. This is possible if we can get a relation between the flare energies and the volumes associated with the corresponding flares by some means. For example, [Notsu et al. \[2019\]](#) studied the relation between the spot group area and the flare energy of the superflares observed on solar-type stars and the Sun. This can be seen in Figure 6 of their paper. Assuming that the spots cover different fractions of the star’s surface and using simple scaling relation between the flare energy, magnetic field strength and the area of spots such as that mentioned in Equation 5 of [Notsu et al. \[2019\]](#) paper, we can use such plot to get an upper limit to the magnetic fields for various stars.

Alternately following [Notsu et al. \[2019\]](#), we might attempt to derive a flare volume based on the area of spots/active regions determined from rotational modulation in the light curves of the flaring stars. [Notsu et al. \[2019\]](#) suggest that the flare volume ( $V$ ) should scale as  $V \propto \text{Area}^{3/2}$ . In fact, the least square fitting of [Notsu et al. \[2019\]](#) suggest that  $V \propto \text{Area}^{0.60 \pm 0.34}$  is a better fit to the data than  $V \propto \text{Area}^{3/2}$ . This result is based on 27 superflare energies and the corresponding spot group areas in Figure 6 (b) of [Notsu et al. \[2019\]](#) and which correspond to solar-type stars with  $T_{\text{eff}}$  in the range (5300-6300) K. In this regard, we note that [Mullan and Paudel \[2018\]](#) have suggested that  $V \propto \text{Area}$  would be more appropriate for the largest flares. An idea of the flare volumes then will be helpful to place upper limit to the magnetic fields associated with the flares.

**iii) Coefficient  $A$  of the power law:** There is valuable information stored in the coefficient  $A$  in the power law:  $dN/dE = AE^{-\alpha}$ . In principle, the energy released

in a flare originates when the magnetic field within a finite volume of an active region evolves to a state where the field must undergo a transition to a lower energy state, perhaps force-free, perhaps potential. In such cases, some or all of the original magnetic free energy provides energy for the various aspects of the flare process (bulk motion, heating, particle acceleration). Therefore, the coefficient  $A$  is expected to be determined (in any particular star) by two principal physical parameters: the change  $\Delta B$  in the magnetic field strength in the vicinity of the flare site, and the length scale  $L$  associated with the volume of the flare energy release. In flares where  $\Delta B$  remains constant throughout the volume of flare energy release, the particular combination of  $B$  and  $L$  which determines the flare energy is roughly  $(\Delta B^2/8\pi)$  times  $L^3$ .

The physics question is: Is there a way to disentangle the contributions of  $L^3$  and  $\Delta B^2$  from empirical estimates of the flare properties, such as the coefficient  $A$ ? For this purpose, we might think of analyzing the values of  $A$  for different spectral types from a different perspective. It is possible that two flaring stars can have the same values of parameter  $\beta$  (the slope of FFD) but different flare rates for the same range of flare energies i.e. the case when the fitted lines of FFDs are parallel. In this case, we may ask: *What is causing two stars to release the same flare energy (e.g.  $\log E = 32$  erg) at different rates?* A statistical analysis of the relation between difference in flare rates (i.e. values of coefficient  $A$ ) and difference in properties of flaring stars (e.g. rotation rates, effective temperatures, radii) might point to an improved understanding of the nature of magnetic dynamo activity in flare stars.

### 1.10 M dwarf flares in the context of planet habitability

Using the full four-year *Kepler* data, Dressing and Charbonneau [2015] estimated an occurrence rate of  $0.24_{-0.08}^{+0.18}$  Earth-size planets and  $0.21_{-0.06}^{+0.11}$  super-Earths per M dwarf habitable zone (HZ). These results and the discovery of the TRAPPIST-1 planetary system [Gillon et al., 2016, 2017; Luger et al., 2017] demonstrate that there is a significant chance of finding habitable planets around M dwarfs. The *Transiting*

*Exoplanet Survey Satellite (TESS; Ricker 2014)* will find many more HZ planets orbiting M dwarfs [Barclay et al., 2018]. With the discovery of many such planets, an essential next step in exoplanet research is to identify those with maximum probability of being habitable, especially those bright enough to be characterized by upcoming missions such as NASA's *James Webb Space Telescope (JWST)*.

The main question is: How suitable are the conditions for habitability on planets located in the HZ of M dwarfs? Since M dwarfs have smaller luminosity  $L$  than the sun, in order to replicate a mean global temperature of 288 K on the planet (so that water is liquid, as on Earth), the HZ must have radii  $R$  ( $\sim L^{0.5}$ ) which are a lot closer to the parent star. E.g. Trappist-1, with  $L = 5 \times 10^{-4} L_{\odot}$  [Van Grootel et al., 2018] has an HZ at 0.022 AU, i.e. closer to the parent star by a factor of 40-50 than the Earth is to the sun.

The closeness of the HZ to the parent star in an M dwarf planetary system implies that any planets located in the HZ of M dwarfs might be exposed to enhanced X-rays, UV radiation, high energy particles and coronal mass ejections (CMEs) associated with flares on the parent star. One of the best examples to mention here is M5.5 dwarf Proxima Centauri which is the closest red dwarf to the Sun, at a distance of 1.3 pc. It has a terrestrial planet in its habitable zone [Anglada-Escudé et al., 2016]. A superflare with total bolometric energy of  $10^{33.5}$  erg and 23 other flares with bolometric energies in range  $\log E$  (erg)  $\sim$  (30.6-32.4) were observed on Proxima Centauri in 2016 by the Evryscope. It has been predicted that at least five superflares occur each year on this star [Howard et al., 2018]. Flares were also observed using XMM-Newton and ALMA data [Güdel et al., 2004; MacGregor et al., 2018]. The most recent studies show that Proxima Centauri b receives  $30\times$  more EUV flux than Earth, and  $10\times$  more FUV flux and  $250\times$  more X-rays [Ribas et al., 2016].

High energy radiation may have adverse effects on the thermochemical equilibrium of

the planets' atmospheres. For example, the X-rays ( $<100 \text{ \AA}$ ) and extreme UV (EUV,  $100 - 912 \text{ \AA}$ ) can ionize gas and heat the atmosphere at altitudes which are situated above roughly the nano-bar level, and far UV (FUV,  $912 - 1700 \text{ \AA}$ ) photons can cause the photodissociation of  $\text{H}_2\text{O}$  molecules which can escape the X-ray/EUV heated atmosphere causing mass loss from the planet [Lammer et al., 2003; Bolmont et al., 2017].

Segura et al. [2010] and Tilley et al. [2017] have reported on modeling the effects of flares on planetary atmospheres. Segura et al. [2010] studied the possible impacts of the 1985 April 12 flare from the dM3 star AD Leo [Hawley and Pettersen, 1991], on an Earth-like planet in the HZ of this mid-M dwarf. Likewise, Tilley et al. [2017] studied the effects of high flare rate and high flare energies ( $10^{30.5} - 10^{34} \text{ erg}$ ) of the dM4 flare star GJ1243 on an Earth-like planet. In general, both studies find that if the flare output consists only of photons, then no significant ozone layer destruction occurs. In order to destroy the ozone, the main contributors must be energetic particles analogous to solar energetic particles (SEP) which are generated along with coronal mass ejections (CMEs) in large solar flares. The SEPs cause the dissociation of  $\text{N}_2$  molecules producing active N-atoms. They react with  $\text{O}_2$  to produce NO which in turn reacts with  $\text{O}_3$  to produce  $\text{NO}_2$ , thus destroying the ozone column. Assuming that particle fluxes can be generated by scaling from solar flares, Tilley et al. [2017] calculate that, in the case of a stellar flare with energy  $10^{34} \text{ ergs}$ , the CME/SEP effects could cause extensive ozone destruction on time-scales of years to decades. Even smaller repeated events can lead to extensive ozone destruction on century-long timescales [Youngblood et al., 2017]. However, studies of Type II radio bursts in flare stars [Crosley and Osten, 2018] indicate that a simple scaling from solar CME rates to CMEs in stellar flares is not consistent with their data: they conclude that this “casts serious doubt on the assumption that a high flaring rate corresponds to a high rate of CMEs”. As a result, impact of flares on ozone layer depletion remains under investigation.

Hence, in order to determine if the M dwarf planets are habitable, it is very important

to quantify the flaring rate of the parent star and how this rate changes as a function of its age and mass. This will enable us to calculate the total energy budget that is being produced and received by the planet during the flaring stage of the host star and during the different phases of planet formation.

Assuming all the flares result from the same physical process (e.g., magnetic reconnection), the correlations between different radiations emitted during flares will be helpful to estimate the total energy budget received by the planet. An idea about how the M dwarf flares evolve over time will be helpful to calculate the total energy received by the HZ planets in different stages of formation. The results may help to constrain when the flare rate is maximum for a given star's evolution. The effective temperatures of M dwarfs are in the range  $\sim 3800$  K (M0) -  $\sim 2500$  K (M9). Since the late-M dwarfs are cooler, their HZs are also closer to the parent star than for the early-M dwarfs. But if they have higher flare rates, the atmospheres of their HZ planets are likely to be more impacted by the intense radiations and energetic particles coming from the flares, thus reducing the probability of habitability.

### 1.11 The *Kepler* mission

The *Kepler* mission [Borucki et al., 2010; Koch et al., 2010], named after the 17th century scientist Johannes Kepler who formulated the laws of planetary motion, was launched by NASA in 2009. It consisted of a 0.95 m aperture Schmidt telescope and was placed in heliocentric orbit. Its main objective was to study the occurrence rate of Earth-like and larger planets around solar-type stars by monitoring more than 150,000 stars continuously for four years using the 'transit method'. This method is used to discover a new planet by studying the dimming of a star's light: tiny dips in the brightness, when the planet moves across the disk of the star.

*Kepler's* field of view (FOV) was a region in the Cygnus and Lyra constellations of the Milky Way galaxy and covered 105 square degrees in the sky. This is about 0.25

percent of the whole sky. The FOV was chosen in such a way that it had the maximum number of stars which could be monitored continuously without any blocking of the line of sight. *Kepler* had a photometric precision of 20 parts per million (ppm) for a 12th mag G-type star in a 6.5-hr integration [Borucki, 2017]. The *Kepler* mission was the first of its kind to provide long-baseline, high-precision, continuous light curves of tens of thousands of stars for planet and astrophysics research. It was highly successful in achieving its goals. Figure 1.2 shows an artist's conception of the *Kepler* mission. Since the solar-type stars are mostly bright in visible wavelengths, the *Kepler* mission was designed to operate in the wavelength range  $\sim 400\text{-}900$  nm with a peak around 600 nm which is close to the effective temperature of the Sun. The response function of the *Kepler* detector is shown in Figure 1.3.

In general, the term exoplanet is used to refer to all the planets beyond our Solar System. The total number of confirmed exoplanets discovered by *Kepler* as of 21 March, 2019 is 2338 which is mentioned in NASA Exoplanet Archive: <https://exoplanetarchive.ipac.caltech.edu>. Likewise, the total number of exoplanet candidates yet to be confirmed is 2423.

There were four reaction wheels on the *Kepler* telescope. They were used to keep the telescope pointed towards the FOV in Lyra/Cygnus. The wheels ensured high pointing accuracy. The *Kepler* lost two of its reaction wheels: #2 on 16 July 2012 and #4 on 14 May, 2013. Due to this, the primary *Kepler* mission officially ended on 15 August, 2013 as it was unable to continue pointing at the stars in the original FOV with high precision.

### 1.12 The *K2* mission

As the primary *Kepler* mission was not able to point accurately by using only two reaction wheels, a study suggested that the system should continue with a new mission plan named *K2* [Howell et al., 2014]. The main idea was to point the telescope

in the direction of the spacecraft orbit and adjust the roll angle in such a way as to minimize the imbalance created by the solar torque on the solar panels. This could be achieved by pointing the telescope near the ecliptic and changing the FOV as it orbits around the Sun. The *K2* mission started observing in June, 2014. Its FOVs were distributed around the ecliptic plane with a maximum observation time of  $\sim 80$  days for each FOV. The observing period of each FOV was called a “Campaign”. Starting from June, 2014, observations were obtained for Campaign 0 through Campaign 19. However some of the campaigns could not be observed for  $\sim 80$  days due to problems in the instrument. Figure 1.4 shows the different FOVs selected for the *K2* mission in various campaigns. The number of targets observed in each campaign was  $\sim 10,000$ , very few as compared to the primary *Kepler* mission. The photometric precision of *K2* mission was  $\sim 80$  ppm for 6-hr integrations of a 12th magnitude quiet star [Howell et al., 2014].

Unlike the *Kepler* mission, the *K2* targets were chosen on the basis of proposals submitted by the community through the Guest Observer program. This encouraged the community to propose for observing of the targets for a broad range of research topics including planet formation; stellar structure, rotation and activity; supernovae; asteroseismology; AGN activity; occurrence rate of planets around low mass stars: the M dwarfs; solar system objects and many more. Figure 1.5 summarizes the diversity of research fields which can be studied by using *Kepler* and *K2* and Figure 1.6 is a cartoon which shows the various objects of interest which were proposed to study during Campaign 18.

Up to now, the total number of confirmed exoplanets discovered by the *K2* mission is 359 and the number of those yet to be confirmed is 536. This information is obtained from NASA Exoplanet Archive as of 21 March, 2019. The *K2* mission officially ended on October 30, 2018 because the spacecraft was out of fuel. Figure 1.7 is the ‘last light’ image taken by the *K2* mission on 25 September, 2019 just before it ran out of fuel.

### 1.12.1 *Kepler* and *K2* data

The principal measurements done by *Kepler* and *K2* were time series photometry of the observed targets i.e. the main data products are the light curves. The *Kepler* and *K2* light curves are available for two different observation modes: short cadence mode [Gilliland et al., 2010] and long cadence mode [Jenkins et al., 2010]. The short cadence light curves are provided for intervals of 58.85 s. For this series of 9 frames with a 6.02 s exposure time are coadded. Likewise, the long cadence data are provided for intervals of 29.4 minutes. For this series of 270 frames with a 6.02 s exposure time are coadded.

In summary, the *Kepler* telescope spent nine years in space providing us very high quality data and helped to discover many interesting aspects of our galaxy, most importantly the occurrence of exoplanets. The main finding of *Kepler* and *K2* mission is that almost every star has a planet and there are more planets than stars in the Milky Way Galaxy (see for e.g., Dressing and Charbonneau 2015)

### 1.13 Dissertation Outline

Here is outline of the rest of this dissertation. In Chapter 2, I will present results regarding the flare rates of M/L dwarfs which were studied by using *K2* short cadence data. In Chapter 3, I will present the results regarding the flares which were observed on M6-M9 dwarfs in *K2* short cadence mode. Likewise, I will discuss about the largest flares which were observed on various L dwarfs in *K2* long cadence mode in Chapter 4. In Chapters 5 and 6, I will discuss about the largest flares observed on a young brown dwarf (CFHT-BD-Tau 4) and three other late-M dwarfs, and the impacts of such flares on planet formation as well as the planets which are in HZs of such M dwarfs. I will discuss about identification of a very short period M6 dwarf binary system in Chapter 7, and I will present the results of *Chandra* monitoring of a flaring L1 dwarf in Chapter 8. Finally, I will present a brief summary of the results of my projects in Chapter 9.

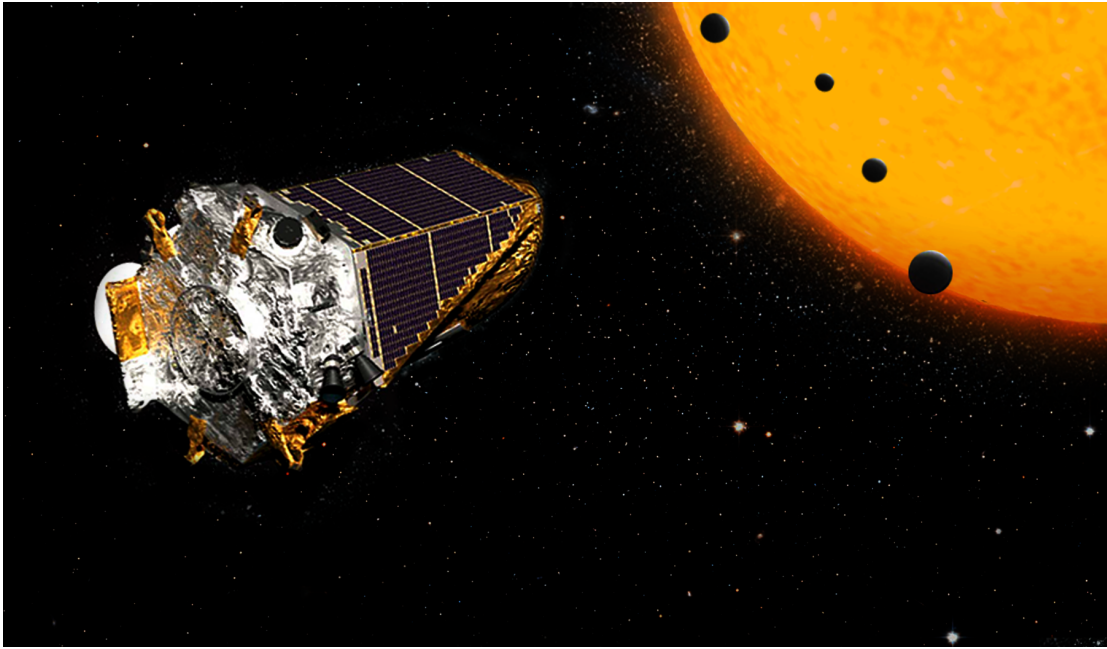


Figure 1.2: Artist's conception of the *Kepler* mission. Credit: NASA

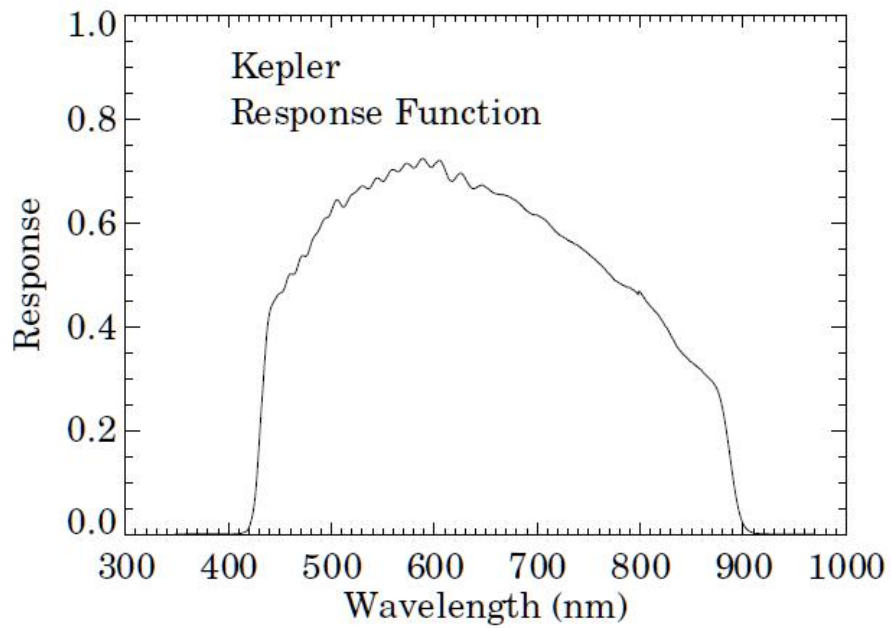
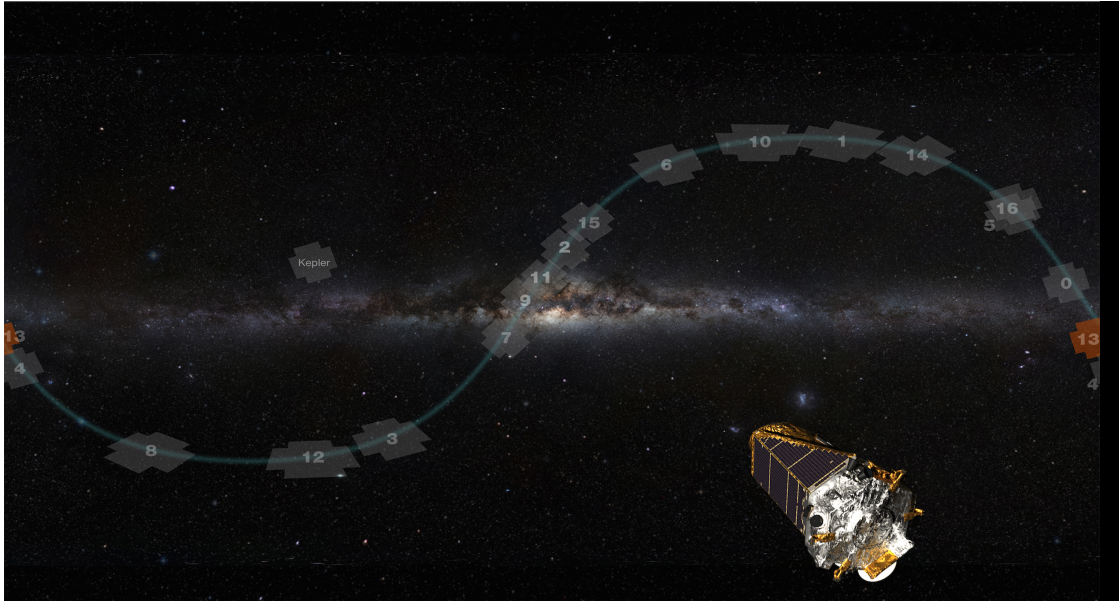
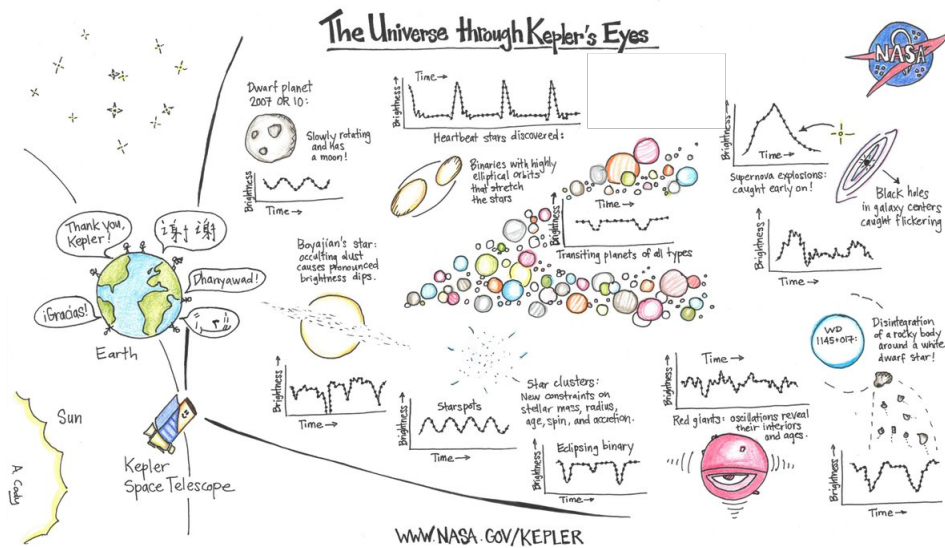


Figure 1.3: The shape of the *Kepler* bandpass which covers most of the optical spectrum. Credit: NASA



**Figure 1.4:** This image shows the *K2* mission's different FOVs as it orbited around the Sun. The FOV of the primary *Kepler* mission is also shown. Credit: NASA



**Figure 1.5:** This cartoon summarizes the various research areas of astronomy and astrophysics, which can be studied by using the *Kepler* and *K2* data. Reproduced with permission from Ann Marie Cody/NASA Ames.

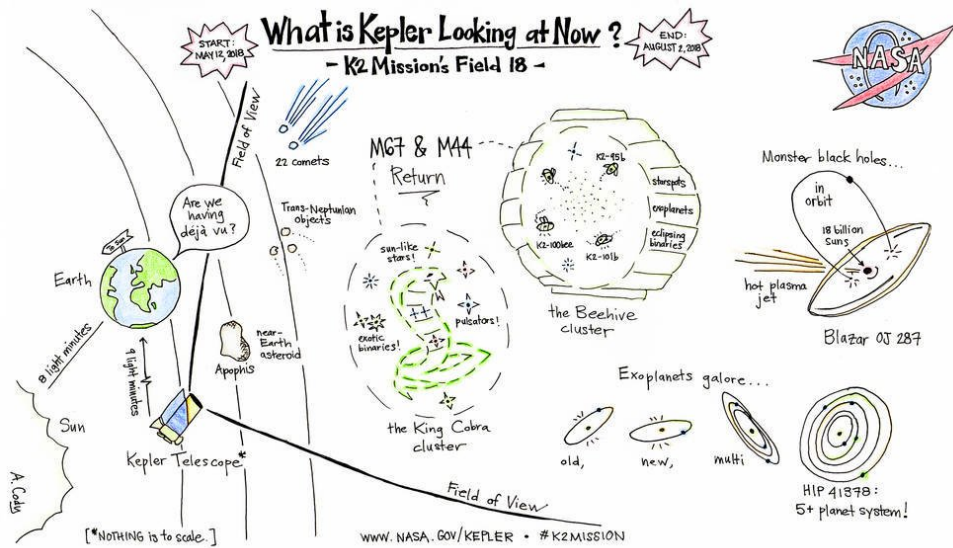


**Figure 1.6:** A cartoon showing the field of view in *K2* Campaign 18 which started on 12 May, 2018 and ended on 2 August, 2018. Reproduced with permission from Ann Marie Cody/NASA Ames.

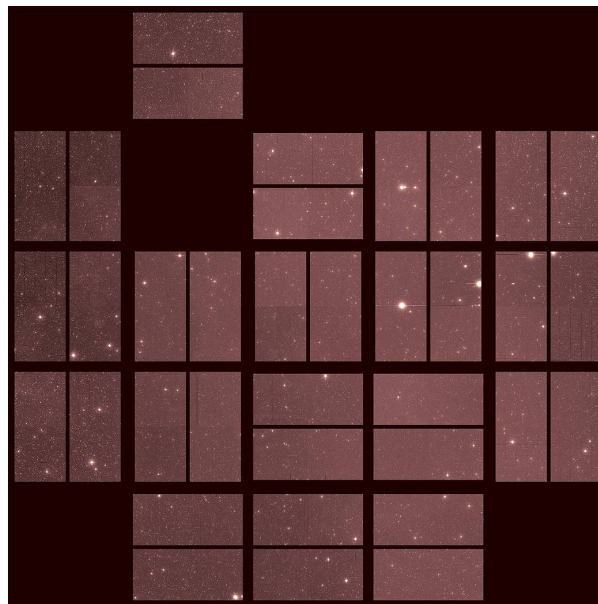


**Figure 1.7:** The 'last light' image taken by *K2* mission on 9/25/2018. It represents the end of *Kepler*'s 9+ year journey of data collection. Credit: NASA *Kepler*

## Chapter 2

### WHITE LIGHT FLARE RATES OF M/L DWARFS USING *K2* SHORT CADENCE DATA

#### 2.1 White light flares

A brief introduction on flares is given in the Section 1.7 in Chapter 1. White light flares (hereafter WLFs) are assumed to be produced when nonthermal electrons accelerated after reconnection hit a cold thick target in the lower chromosphere or upper photosphere. The precipitated electrons can cause the formation of hot “chromospheric condensations” which emit white light continuum: the continuum has a wavelength dependence in visible photons which approximates that of a blackbody with a temperature of order  $10^4$  K (Kowalski et al. [2015] and references therein). During a WLF, a faint star can become significantly brighter in optical light, by as much as several magnitudes. Some WLFs with exceptionally large amplitudes (relative to the photospheric level) on UCDs will be discussed later in this chapter and other chapters. Estimates of surface areas of flares show that the WLFs in UCDs cover larger fractional areas of the surface than do flares on bright stars such as the Sun [Kowalski et al., 2010; Walkowicz et al., 2011].

As mentioned in Chapter 1, in addition to the search of exoplanets, the *Kepler* and *K2* mission is also very useful for studying stellar properties, including WLF rates, asteroseismology, etc. WLF rates of several early-M and mid-M dwarfs were estimated using *Kepler* data [Ramsay et al., 2013; Martín et al., 2013; Hawley et al., 2014; Davenport, 2016]. The occurrence of WLFs on L dwarfs and young brown dwarfs [Gizis et al., 2013; Schmidt et al., 2016; Gizis et al., 2017b,a] suggests that WLFs are common in some UCDs. In this chapter, I analyze the WLFs of various M/L dwarfs which were observed

by the *K2* mission in short cadence mode in various campaigns in between Campaign 3 and Campaign 18. Most of the targets are UCDS. The results of work presented here suggest that in future, similar studies will contribute to understanding different flare properties (e.g. flare energy, duration, rate, etc) in those targets and how these properties depend on spectral type, age, mass, etc. In cases where rotation periods and ages of targets are known, such study may shed light on the rotation-age-activity relationships in UCDS. I also include in this chapter my own analysis of TRAPPIST-1 flares which were previously discussed by [Vida et al. \[2017\]](#) and [Davenport \[2017\]](#).

In Figure 2.1, I show the WLFs observed by *K2* on a flaring star GJ 3631 during Campaign 14. It can be seen from this figure, a flare can either have a single peak or multiple peaks. The flare with a single peak is called a classical flare and the one with multi-peaks is called a complex flare. Like most of the flares observed in other wavelengths, the WLFs are also characterized by an initial impulsive rise phase and then a gradual decay phase.

In this chapter, I discuss flare properties in the context of the flare frequency distribution (FFD). The main goal is to study the how the slope of FFD i.e.,  $\beta$  changes as a function of various spectral types of M/L dwarfs and its possible relation with the ages of objects. The other goals include the study of possible relation between the  $H\alpha$  emission and the flare rates of flaring objects, variation of maximum flare energies as a function of spectral type, etc. Such studies regarding various flare properties on the cool objects i.e. UCDS have been done very rarely. So the results of flare analysis presented in the chapter will be very crucial in understanding the various unexplored properties of flares on the cool objects and hence the nature of magnetic dynamo operating inside them.

Many studies have been done to compute the FFD in the Sun and in early-M and mid-M dwarfs. [Kurochka \[1987\]](#) reported the value of spectral index  $\beta$  to be  $\sim 0.80$  for

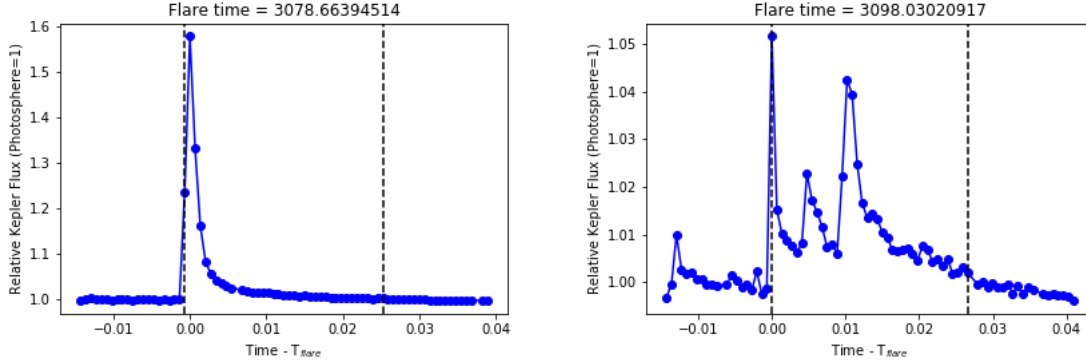


**Figure 2.1:** Examples of WLFs observed by *K2* on a flaring star GJ 3631 during Campaign 14. The flare on the left is also called a classical flare and the one on right is a complex flare. The two dashed vertical lines in each plot mark the start and end times of the flare. The time mentioned on the top of each time is the *Kepler* mission time at which the peak of the flare was observed. The time along *X*-axis is centered around the peak flare time and the flux along *Y*-axis is normalized by the median counts of the continuum.

the energy distribution of 15000 solar flares observed in  $H\alpha$  during 1978-79. In X-rays [Kasinsky and Sotnicova \[2003\]](#) fitted the FFD to 56,000 solar flares observed by *GOES* in the years 1972 - 2001 (almost 3 solar cycles): they found  $\beta = 0.666 \pm 0.005$ . [Hilton \[2011\]](#) calculated  $\beta = 0.73 \pm 0.1$  in the *U*-band energy range  $10^{27.94} \leq E_U \leq 10^{30.60}$  erg for four M6-M8 dwarfs. Likewise, using a simple linear fit [\[Gizis et al., 2017a\]](#) reported  $\beta = 0.59 \pm 0.09$  in energy range  $10^{31}$  erg to  $2 \times 10^{32}$  erg for a field L1 dwarf WISEP J190648.47+401106.8 (hereafter W1906+40) and  $\beta = 0.66 \pm 0.04$  in energy range  $4 \times 10^{31}$  erg to  $1.1 \times 10^{33}$  for a 24 Myr brown dwarf 2MASS J03350208+2342356 (hereafter 2M0335+2342). [Gizis et al. \[2017a\]](#) used a maximum likelihood estimation (MLE) to obtain  $\alpha = 1.6 \pm 0.2$  and  $1.8 \pm 0.2$  for W1906+40 and 2M0335+2342 respectively.

In this chapter, I report in Section 2.3 on *K2* photometry of targets in our sample, and I use the photometric data to estimate the energies of each flare. In Section 2.4, I discuss artificial flare injection and recovery. In Section 2.5, I present estimates of flare rates. In Section 2.6, I concentrate on the detailed properties of two superflares in our

sample. Discussion of results is presented in Section 2.7.

## 2.2 Sample

There are 42 targets in our sample; including W1906+40, 2M03350+2342 and 20355+1133 which were studied independently by Gizis et al. [2013] and Gizis et al. [2017a]. They have spectral types (hereafter STs) in the range M5 – L5, among which 2 have ST of M5 and the remaining have STs of  $\gtrsim$ M6. Most of the targets are old low mass stars and some may be brown dwarfs. Furthermore, there are also some famous and widely studied targets in our sample. Examples of such targets are: the nearby high proper motion, flaring star Wolf 359 (CN Leo); the star with seven planets: TRAPPIST-1; and the flaring star GJ 3631. The bar chart showing the distribution of targets in each ST is shown in Figure 2.2. Likewise, the color magnitude diagram (CMD) of all the targets is shown in Figure 2.4. I used Pan-STARRS1 (PS1) survey measurements, whenever available, to calculate the color-differences  $i - z$  and absolute magnitudes  $M_i$ . After initial inspection of whether flares were observed on a given target, I divided the sample into sub-samples of targets which were observed to flare in *K2* data and targets in which *K2* detected no flares. The total number of flaring targets in our sample is 22. In Figure 2.3, I compare the number of flaring targets with the total number of targets in each ST. The fraction of flaring targets is higher in M5-M8 STs. Among the flaring targets, 2 have STs of M5, 4 have STs of M6, 6 have STs of M7 and 5 have STs of M8. Likewise, there is only one flaring target with ST of M9 and 4 flaring targets with STs of L0/L1. *K2* also observed some nearby targets, in short cadence mode, with STs later than L1 but no flares were observed on them.

In Table 2.1 I list, for each flaring target the full name, the *Kepler* ID (EPIC) and the *K2* campaign number in which it was observed. From here onward, short name of each target will be used. Since the target W1906+40 was observed by primary *Kepler* mission, it does not have an assigned EPIC ID and a campaign number. The flare rates of some targets are already published in the literature, and these are mentioned in the

‘Note’ given in the bottom of Table 2.1. I did not measure the photometry of those targets again but updated the energies and flare rates using the recently published *Gaia* DR2 parallaxes whenever available. In Table 2.2, I list the physical properties: masses, radii, effective temperatures and parallaxes of the flaring targets, most of which are compiled from the literature. The parallaxes of most of the targets were measured by the *Gaia* mission [Gaia Collaboration et al., 2018b]. In Table 2.3, I list the STs and the apparent magnitudes:  $J$ ,  $K$ ,  $i$ ,  $z$ , and the absolute magnitudes  $M_i$  of each flaring target.  $J$  and  $K$  were measured by the 2MASS survey [Cutri et al., 2003] and  $i$  and  $z$  were measured, for most of the targets, by the PS1 survey [Chambers et al., 2016]. In Table 2.4, I list the kinematic properties of the flaring targets. The  $U$ ,  $V$  and  $W$  components of space motion are from the literature and are listed whenever available. The columns ‘pmRA’ and ‘pmDE’ correspond to the proper motion of the targets in right ascension (RA) and declination (DE) respectively, and most of them are measurements from the *Gaia* mission. The column ‘ $V_{\text{tan}}$ ’ corresponds to the tangential velocities of the targets. To calculate the tangential velocity for each target, I used the relation  $V_{\text{tan}} = 4.74d\mu$ , where  $d$  (in parsecs) is the distance of each target estimated using the parallax listed in Table 2.2 and  $\mu$  is the total proper motion (in arcsec per year).

Likewise, in Table 2.5, I list the activity indicators of the flaring targets, which are compiled from the literature. However, such information is not available for all the flaring targets. The columns ‘ $P_{\text{rot}}$ ’, ‘ $v\sin i$ ’, ‘EW  $H\alpha$ ’ and ‘ $\log L/L_{\odot}$ ’ correspond to the rotation periods, projected rotational velocities, equivalent width of the  $H\alpha$  emission line and logarithm of the bolometric luminosities of targets (in units of solar luminosity) respectively. The bolometric luminosities of two targets: GJ 3631 and LHS 2090 were estimated using the parameters listed in Table 2.2. Some of the rotation periods will be updated later in this chapter by using the measurements of *K2* light curves. It can be seen that most of the flaring targets have some level of  $H\alpha$  emission indicating that they are active stars. In addition, most of them are fast rotators with periods of less than 1 day. The exceptions are two targets: Wolf 359 and TRAPPIST-1

which have periods greater than 3 days. I also list the values of two important activity indicators: H $\alpha$  activity ( $\log L_{\text{H}\alpha}/L_{\text{bol}}$ ) and X-ray activity ( $\log L_{\text{X}}/L_{\text{bol}}$ ) of some flaring targets in Table 2.6. The values of radio-luminosity of many flaring objects have not been measured. Even if some radio measurements do exist, many are listed only as upper limits. So the values of activity in radio emission are not listed in Table 2.6.

In Table 2.7, I list the EPIC IDs, Names, STs and *K2* campaign numbers of the non-flaring targets. Among them, 10 are late-M dwarfs and 10 are L dwarfs with STs as late as L5. I also list the EWs of the H $\alpha$  emission line for some targets which are available in the literature. It can be seen that they have mostly low levels of H $\alpha$  emission. In Table 2.8, I list the measurements of PS1 and *Gaia* surveys for all non-flaring targets. The columns ‘ $M_i$ ’ and ‘ $V_{\text{tan}}$ ’ correspond to their absolute magnitudes and tangential velocities.

In Figure 2.5, I show the distribution of tangential velocities ( $V_{\text{tan}}$ ) of all the targets in the sample. This figure shows only the spread in the values of  $V_{\text{tan}}$  along the vertical axis. Since no any physical quantity is plotted along the horizontal axis, the spread of the values of  $V_{\text{tan}}$  along this axis has no meaning at all. The values of  $V_{\text{tan}}$  vary in the range (4 - 87) km s $^{-1}$ . To make it easier for the reader to compare, the flaring targets are represented by red dots and the non-flaring targets are represented by blue dots. It can be seen that both flaring and non-flaring targets have comparable tangential velocities. The objects with lower tangential velocities are considered to be young and those with higher tangential velocities are considered to be old. Hence the tangential velocity distribution of the targets in the sample indicates that we have a heterogenous population of targets in terms of kinematic ages if we use tangential velocities as proxies of ages. In such case, the youngest target in the sample is M7.5 dwarf 2M1332-0441 with  $V_{\text{tan}} = 4$  km s $^{-1}$  and the oldest target is L1 dwarf 2M0843+1024 with  $V_{\text{tan}} = 87$  km s $^{-1}$ . However, it should be noted that the ages inferred through tangential velocity are not accurate in some cases.

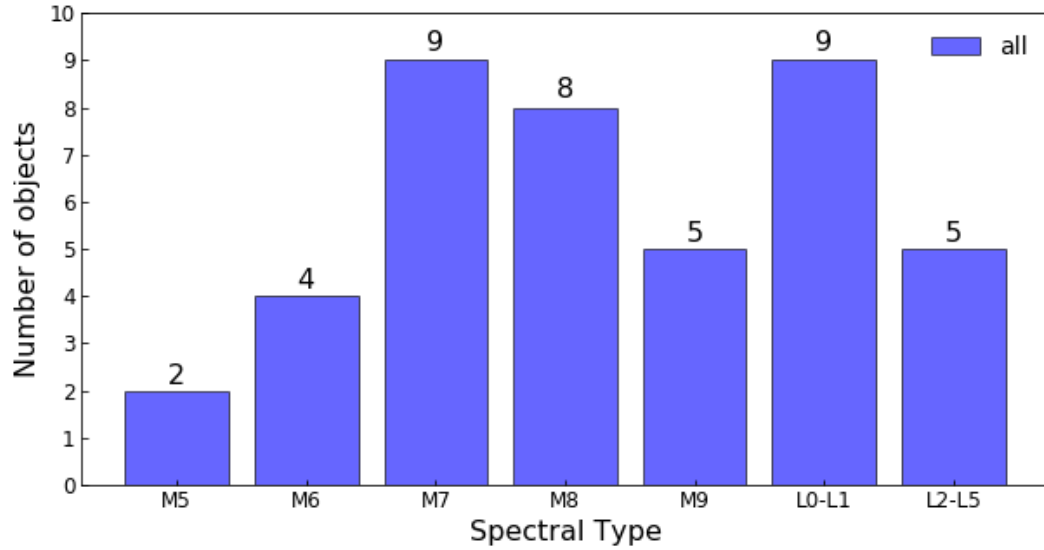


**Figure 2.2:** Bar chart showing the total number of targets in each spectral type. The total number of targets in the sample is 42.

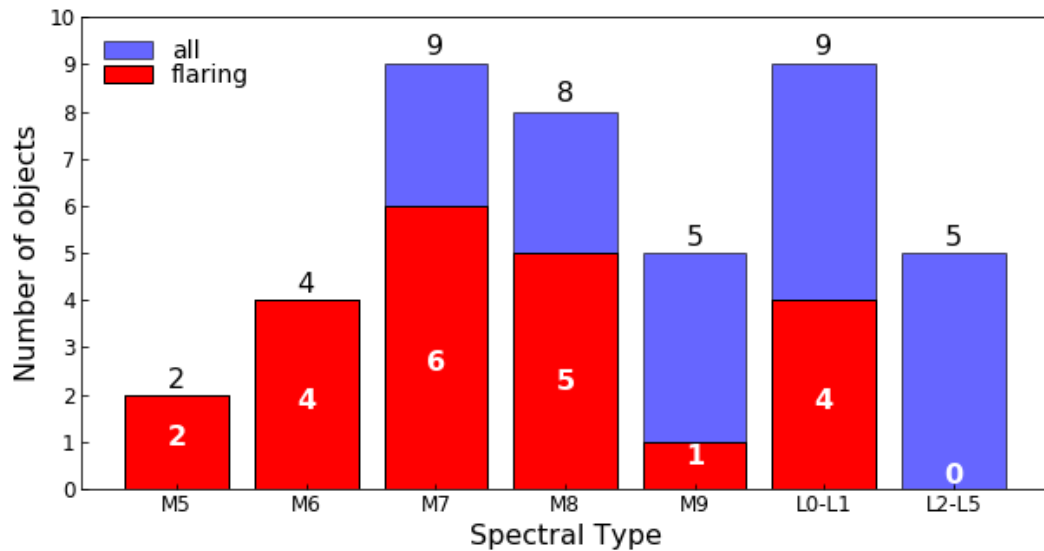


**Figure 2.3:** Bar chart comparing the number of flaring targets with those of all targets in each spectral type. The blue bars correspond to the total number of targets in each spectral type and the red bars correspond to the flaring targets. The numbers of all targets and of those which were observed to flare is indicated for each spectral type.

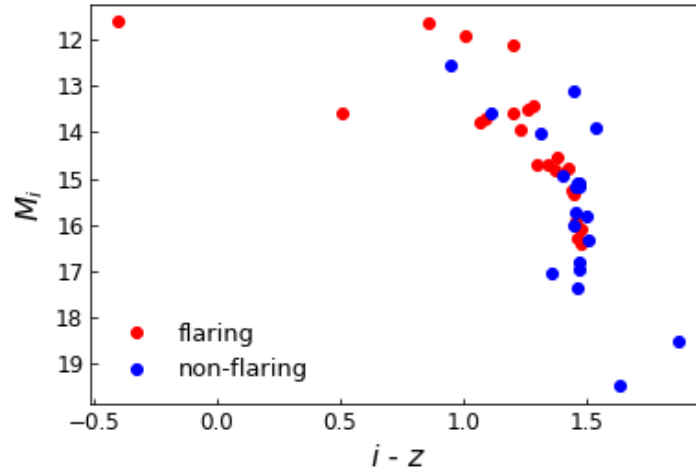


**Figure 2.4:** Color magnitude diagram of all targets in the sample. The  $X$ -axis corresponds to the color-difference of  $i$  and  $z$  magnitudes measured by PS1 survey (whenever available) and the  $Y$ -axis corresponds to absolute magnitudes  $M_i$ . The red dots correspond to flaring targets and the blue dots correspond to the non-flaring targets.

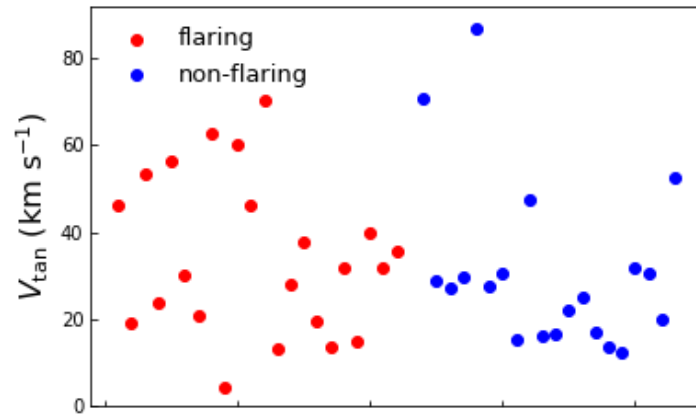


**Figure 2.5:** Tangential velocity distribution of all targets in the sample. The red dots represent the flaring targets and the blue dots represent the non-flaring targets. It should be noted here that I have not plotted  $V_{\text{tan}}$  as a function of any other physical quantity since the main idea is to show only the distribution of velocities.

**Table 2.1: Name and EPIC ID of flaring targets**

Name	EPIC	Cam. #
GJ 3631 (LHS 2320)	248601792	14
(2MASS J10521423+0555098)		
GJ 3636	248856413	14
(2MASS J11005043+1204108)		
Wolf 359 (CN Leo)	201885041	14
(2MASS J10562886+0700527)		
LHS 2090	212090371	16
(2MASS J09002359+2150054)		
2MASS J22285440-1325178*	206050032	3
(LHS 523, GJ 4281, LP 760-3)		
2MASS J22021125-1109461*	206135809	3
2MASS J08352366+1029318*	211332457	5
2MASS J22145070-1319590*	206053352	3
2MASS J13322442-0441126*	212826600	6
2MASS J23062928-0502285*	200164267	12
(TRAPPIST-1)		
2MASS J12215066-0843197*	228754562	10
2MASS J03264453+1919309*	210764183	4
2MASS J12212770+0257198*	201658777	10
2MASS J12321827-0951502*	228730045	10
WISEP J190648.47+401106.8*	N/A	
2MASS J03350208+2342356*	211046195	4
2MASS J15072779-2000431	249639465	15
2MASS J08252223+2021567	212006725	18
(CZ Cnc)		
2MASS J13300232-0453202	212820594	6,17
2MASS J23535946-0833311	246036729	12
2MASS J10554733+0808427	248691809	14
2MASS J10484281+0111580	248442470	14

**Note:** \*The flare rate of this object is already published.

W1906+40 was observed by primary *Kepler* mission, so it has no EPIC ID.

Table 2.2: Physical properties of flaring targets

Name	Mass	Radius	ref.	Temperature	ref.	parallax	ref.
	( $M_{\odot}$ )	( $R_{\odot}$ )		(K)		(mas)	
GJ 3631	0.130	0.154	1	3077±64	3	71.7830±0.0903	4
GJ 3636	0.149	0.172	1	3014±64	3	46.3490 ±0.1734	4
Wolf 359	0.102	0.128	1	2792±82	3	419.10	5
LHS 2090	0.095	0.121	1	2799±63	3	156.7584±0.1329	4
LHS 523	0.089	0.116		2766±82	3	91.8949±0.0948	4
2M2202-1109				2800±200	8	36.0631±0.2705	4
2M0835+1029				2498±19	9	36.8942±0.1959	4
2M2214-1319						25.3325±0.2004	4
2M1332-0441						52.91	10
TRAPPIST 1	0.089 ± 0.006	0.121 ± 0.003	2	2516 ± 41	2	82.4 ±0.8	2
2M1221-0843						19.4756±0.3240	4
2M0326+1919						34.1157±0.4179	4
2M1221+0257				2300±200	8	53.9501±0.2528	4
2MJ1232-0951						37.71±6.26	11
W1906+40						59.5710±0.1363	4
2M0335+2342	0.058±0.004	0.241	8, 12	2700	12	19.5277±0.1543	4
2M1507-2000						41.7961±0.2207	4
2M0825+2021	0.16		13			5.5257±0.3598	4
2M1330-0453						29.9934±0.3217	4
2M2353-0833						45.8744±0.2745	4
2M1055+0808	0.086	0.113	1			53.3382±0.1536	4
2M1048+0111				2100±300	8	66.4589±0.2143	4

**References:** 1) [Newton et al. \[2017\]](#); 2) [Van Grootel et al. \[2018\]](#); 3) [Muirhead et al. \[2018\]](#); 4) [Gaia Collaboration et al. \[2018b\]](#); 5) [Dupuy and Liu \[2012\]](#); 6) [Rajpurohit et al. \[2018\]](#); 7) [Jenkins et al. \[2009\]](#); 8) [Gagné et al. \[2015\]](#); 9) [Theissen et al. \[2017\]](#); 10) [Reiners and Basri \[2009\]](#); 11) [Best et al. \[2018\]](#); 12) [Gizis et al. \[2017a\]](#); 13) [Douglas et al. \[2014\]](#)

Table 2.3: Photometric properties of flaring targets

Name	Sp. Type	$J$	$K$	ref.	$i$	$z$	ref.	$M_i$
		(mag)	(mag)		(mag)	(mag)		(mag)
GJ 3631	M5	9.834±0.024	8.941±0.023	1	12.3371±0.0358	12.7351±0.0012	2	11.7
GJ 3636	M5	10.676±0.024	9.782±0.021	1	13.2980±0.0018	12.4438±0.0006	2	11.7
Wolf 359	M6V	7.085±0.024	6.084±0.017	1	10.320±0.03		3	13.6
LHS 2090	M6.5	9.436±0.020	8.437±0.021	1	12.8001±0.0010	11.7320±0.0010	2	13.8
LHS 523	M6.5	10.768±0.023	9.843±0.021	1	12.8		4	13.7
2M2202-1109	M6.5	12.361±0.024	11.374±0.026	1	15.810±0.002	14.6071±0.0022	2	13.6
2M0835+1029	M7	13.137±0.023	12.045±0.021	1	17.0025±0.0027	15.6262±0.0028	2	14.8
2M2214-1319	M7.5	13.459±0.026	12.321±0.026	1	16.9408±0.0041	15.7102±0.0042	2	14.0
2M1332-0441	M7.5	12.369±0.027	11.283±0.019	1	16.080±0.002	14.783±0.003	2	14.7
TRAPPIST-1	M8	11.354±0.022	10.296±0.023	1	15.1122±0.0017	13.7651±0.0126	2	14.7
2M1221-0843	M8	13.522±0.026	12.504±0.023	1	17.0717±0.0054	15.8108±0.0041	2	13.5
2M0326+1919	M8.5	13.115±0.024	11.930±0.021	1	17.132±0.003	15.7071±0.0003	2	14.8
2M1221+0257	L0	13.169±0.023	11.953±0.026	1	17.4369±0.0061	15.9640±0.0044	2	16.1
2M1232-0951	L0	13.727±0.027	12.554±0.030	1	18.0424±0.0015	16.5871±0.0035	2	16.0
W1906+40	L1	13.078±0.024	11.771±0.018	1	17.4139 ±0.005	15.9464±0.0067	2	16.3
2M0335+2342	M7	12.250±0.021	11.261±0.017	1	15.6818±0.0029	14.4760±0.0047	2	12.1
2M1507-2000	M7.5	11.713±0.023	10.661±0.021	1	15.3181±0.0039	14.0358±0.0025	2	13.4
2M0825+2021	M7	15.249±0.048	14.328±0.055	1	18.1940±0.0043	17.1918±0.0063	2	12.0
2M1330-0453	M8	13.339±0.029	12.243±0.026	1	17.1647±0.0056	15.7918±0.0033	2	14.6
2M2353-0833	M8.5	13.033±0.026	11.932±0.027	1	17.0368±0.0013	15.5887±0.0014	2	15.3
2M1055+0808	M9	12.550±0.026	11.368±0.023	1	16.6191±0.0046	15.1797±0.0038	2	15.3
2M1048+0111	L1	12.924±0.023	11.623±0.024	1	17.2764±0.0258	15.8037±0.0049	2	16.4

References: 1) [Cutri et al. \[2003\]](#); 2) [Chambers et al. \[2016\]](#); 3) [Zacharias et al. \[2012\]](#), 4) [Epchtein et al. \[1997\]](#)

**Table 2.4: Kinematic properties of flaring targets**

Name	$U$	$V$	$W$	ref.	pmRA	pmDE	ref.	$V_{tan}$
	(km s <sup>-1</sup> )	(km s <sup>-1</sup> )	(km s <sup>-1</sup> )		(mas yr <sup>-1</sup> )	(mas yr <sup>-1</sup> )		(km s <sup>-1</sup> )
GJ 3631	-31.5	-13.9	-18.4	1	-695.408±0.153	-60.602±0.131	2	46
GJ 3636	16.3	-2.6	-7.9	1	135.834±0.308	-126.307±0.212	2	19
Wolf 359	-27.8	-47.6	-13.4	1	-3871	-2725	1	54
LHS 2090					-515.662±0.203	-592.061±0.136	2	24
LHS 523					-328.102±0.166	-1044.811±0.151	2	57
2M2202-1109					131.699±0.612	-188.637±0.551	2	30
2M0835+1029					-18.817±0.336	-161.366±0.214	2	21
2M2214-1319					228.688±0.292	-245.920±0.269	2	63
2M1332-0441	-4	13	-13	3	47.074±3.891	8.025±3.453	2	4
TRAPPIST-1					930.879±0.247	-479.403±0.174	2	60
2M1221-0843					-188.585±0.480	12.834±0.329	2	46
2M0326+1919					263.729±0.655	-431.959±0.504	2	70
2M1221+0257	0.44±3.08	3.87±3.09	-6.27±3.87	4	-145.350±0.538	-43.503±0.283	2	13
2M1232-0951					-186.2±11.5	-122.2±8.9	5	28
W1906+40	-5.5	-11.6	-41.3	6	438.346±0.250	-179.978±0.285	2	37
2M0335+2342					50.337 ±0.317	-62.940±0.209	2	20
2M1507-2000	6	3	-12	3	96.686±0.360	-73.321±0.294	2	14
2M0825+2021					-33.939±0.644	-15.415±0.405	2	32
2M1330-0453					-93.666±0.561	-9.019±0.322	2	15
2M2353-0833	20	-13	-40	3	-50.202±0.388	-383.190±0.269	2	40
2M1055+0808					-329.775±0.250	-138.182±0.198	2	32
2M1048+0111					-440.006±0.368	-231.468±0.291	2	36

**References:** 1) [Newton et al. \[2016\]](#); 2) [Gaia Collaboration et al. \[2018b\]](#); 3) [Reiners and Basri \[2009\]](#); 4) [Schmidt et al. \[2010\]](#) 5) [Gagné et al. \[2015\]](#); 6) [Gizis et al. \[2013\]](#)

Table 2.5: Activity indicators (I) of flaring targets

Name	$P_{rot}$	ref.	$v \sin i$	ref.	EW H $\alpha$	ref.	$\log L/L_{\odot}$	ref.
	(days)		(km s $^{-1}$ )		( $\text{\AA}$ )			
GJ 3631	0.6920	1	19.1 $\pm$ 0.2	2	6.837 $\pm$ 1.160	3	-2.47	2
GJ 3636	0.2980	1	26.50 $\pm$ 0.80	4	3.640	24	-2.59	
Wolf 359	3.40*	5	<2.0	5	7.877 $\pm$ 2.135	3	-3.27 $\pm$ 0.12	5
LHS 2090	0.4390	1	14.3	5	5.645 $\pm$ 0.074	6	-3.05	
LHS 523			7.0 $\pm$ 2	7	4.4	17	-3.13	8
2M2202-1109					10.2	9		
2M1332-0441			9.0 $\pm$ 2.0	10	6.7	10	-3.18	11
TRAPPIST-1	3.30 $\pm$ 0.14				4.9	9	-3.28 $\pm$ 0.01	12
2M1221+0257			25.0 $\pm$ 3.0	13	6.05	14	-3.59	11
W1906+40	0.3702	15	11.2 $\pm$ 2.2	15	4.0	15	-3.67	15
2M0335+2342	0.2185	16	30	16	6.5	9	-2.55	16
2M1507-2000			64.0	11	2.15	18	-3.61	11
2M0825+2021	0.2029	19			10.4 $\pm$ 1.2	20		
2M1330-0453	0.5307	21						
2M2353-0833			4.5	22			-3.41	22
2M1055+0808					1.664 $\pm$ 0.268	23		
2M1048+0111	0.20	13	17	22	4.28	14	-3.69	22

**Note:** \*Period determined by using  $v \sin i$

**References:** 1) Newton et al. [2016]; 2) Houdebine et al. [2017]; 3) Gizis et al. [2002]; 4) Deshpande et al. [2013]; 5) Reiners et al. [2018]; 6) Newton et al. [2015]; 7) Cook et al. [2014]; 8) Williams et al. [2014]; 9) Gizis et al. [2000]; 10) Reiners and Basri [2010]; 11) McLean et al. [2012]; 12) Van Grootel et al. [2018]; 13) Crossfield [2014]; 14) Schmidt et al. [2015]; 15) Gizis et al. [2013]; 16) Gizis et al. [2017a]; 17) Mohanty and Basri [2003]; 18) Schmidt et al. [2007]; 19) Rebull et al. [2017]; 20) Douglas et al. [2014]; 21) Crossfield et al. [2018]; 22) Antonova et al. [2013]; 23) West et al. [2011]; 24) Reid et al. [1995]

**Table 2.6: Activity indicators (II) of flaring targets**

Name	$\log L_{H\alpha}/L_{bol}$	ref.	$\log L_X/L_{bol}$	ref.	
GJ 3631	-3.72	1	-2.787	2	
GJ 3636	-4.00 <sup>a</sup>				
Wolf 359	-3.97	3	-3.34	4	
LHS 2090	-4.12	1			
LHS 523	-4.15	5	-4.8	6	
2M1332-0441	-4.37	7			
TRAPPIST-1	-(4.60 - 4.40)	7, 8	-(3.70 - 3.40)	9	<b>Note:</b> This was
2M1221+0257	-4.88	10			
W1906+40	-5.0	11			
2M0335+2342	-5.5	12			
2M1507-2000	-4.47	13			
2M0825+2021	-3.9	14			
2M2353-0833	-4.42	15			
2M1048+0111	-5.07	10			

computed by using the results of [West and Hawley \[2008\]](#)

**References:**

- 1) [Newton et al. \[2017\]](#); 2) [Houdebine et al. \[2017\]](#); 3) [Reiners et al. \[2018\]](#); 4) [Schmitt and Liefke \[2004\]](#); 5) [Mohanty and Basri \[2003\]](#); 6) [Williams et al. \[2014\]](#); 7) [Reiners and Basri \[2010\]](#); 8) [Gizis et al. \[2000\]](#); 9) [Wheatley et al. \[2017\]](#); 10) [Schmidt et al. \[2015\]](#); 11) [Gizis et al. \[2013\]](#); 12) [Gizis et al. \[2017a\]](#); 13) [McLean et al. \[2012\]](#); 14) [Douglas et al. \[2014\]](#); 15) [Antonova et al. \[2013\]](#)

Table 2.7: List of targets with non-detection of flares by *K2*

EPIC	Name	Sp. Type	Cam. #	H $\alpha$ EW ( $\text{\AA}$ )	ref
206169988	2MASS J22522850-1019106	M7	3	0.03 $\pm$ 0.20	1
210327027*	2MASS J03552337+1133437	L5 $\gamma$	4		
210457230	2MASS J03552014+1439297	M8	4		
211073549	2MASS J03455065+2409037	M7.5	4		
211328277	2MASS J08433323+1024470	L1	5, 18		
211329075	2MASS J08315598+1025417	M9	5	1.69 $\pm$ 0.54	1
211628806	2MASS J08290664+1456225	L2	5		
211962038	2MASS J08264262+1939224	L0	5	0.50 $\pm$ 0.98	1
211963497	2MASS J09094822+1940428	L1	5		
212178513	2MASS J08313594+2341508	M7	5	1.10 $\pm$ 0.25	1
217976219	2MASS J19090821-1937479	L1	7		
201103788	2MASS J12022564-0629026	M9	10		
228803953	2MASS J12271545-0636458	M9	10		
246711015	2MASS J05021345+1442367	L0	13		
248018652	2MASS J04305718+2556394	M8.25	13		
248044306	2MASS J04300724+2608207	M8.5	13		
249914869	2MASS J1507476-162738	L5	15		
249903099	2MASS J15485834-1636018	L2	15		
251357067	2MASS J09161504+2139512	M9	16		
251555071	2MASS J13334540-0215599	L3	17		

Note: \*published in [Gizis et al. \[2017a\]](#)

References: 1) [West et al. \[2011\]](#)

Table 2.8: PS1 and *Gaia* measurements of non-flaring objects

EPIC	$i$	$z$	parallax	$M_i$	$V_{tan}$
	(mag)	(mag)	(mas)	(mag)	(km s <sup>-1</sup> )
206169988	17.4618±0.0034	16.5154±0.0027	10.5136±0.2209	12.6	71
210327027	19.2638±0.0023	17.6274±0.0099	109.6451±0.7368	19.5	29
210457230	17.7790±0.0084	16.3772±0.0050	27.1726±0.2452	15.0	27
211073549	19.5007±0.0159	18.1866±0.0100	8.0203±0.9029	14.0	30
211328277	19.3905±0.0141	17.9219±0.0062	32.5038±0.5645	17.0	87
211329075	17.6929±0.0061	16.2350±0.0035	31.5629±0.2960	15.2	28
211628806	19.1411±0.0111	17.7857±0.0061	38.1745±0.5740	17.1	31
211962038	18.8444±0.0085	17.3865±0.0051	23.7316±0.3967	15.7	16
211963497	19.1188±0.0098	17.6121±0.0089	27.8070±0.6728	16.3	48
212178513	16.9223±0.0019	15.8124±0.0044	21.5480±0.2147	13.6	16
217976219	19.0717±0.0053	17.6062±0.0059	45.2410±0.5166	17.4	17
201103788	17.9256±0.0042	16.4527±0.0042	27.3679±0.2431	15.1	22
228803953	18.2087±0.0041	16.7397±0.0072	24.8179±0.4849	15.2	25
246711015	18.4251±0.0048	16.9608±0.0082	21.5958±0.4645	15.1	17
248018652	18.5528±0.0053	17.1038±0.0047	8.1419±0.4600	13.1	14
248044306	19.2436±0.0140	17.7049±0.0054	8.6163±0.5330	13.9	12
249914869	17.8727±0.0060	15.9970±0.0044	135.2332±0.3274	18.5	32
249903099	18.1294±0.0067	16.6778±0.0049	37.4329±0.3189	16.0	30
251357067	17.3667±0.0045	15.8652±0.0033	48.8137±0.2322	15.8	20
251555071	19.6671±0.0180	18.1937±0.0083	26.9179±1.1259	16.8	52

Note: \*published in [Gizis et al. \[2017a\]](#)

## 2.3 Data Reduction and Computations

### 2.3.1 *K2* photometry

All the 42 targets listed in Table 2.1 and 2.7 were observed by *K2* mission in various campaigns (see the campaign number in Table 2.1 and 2.7) in both long cadence mode ( $\sim 30$  minute, Jenkins et al. [2010]) and short cadence mode ( $\sim 1$  minute, Gilliland et al. [2010]). The exception is L1 dwarf W1906+40 which was observed by the primary *Kepler* mission. I used short cadence data to study WLFs on all 42 targets. I used a method similar to that described in Gizis et al. [2017b,a] to perform photometry on targets. In order to estimate a *Kepler* magnitude which represents the brightness of our targets better than the original *Kepler* magnitude  $K_p$  provided in the *Kepler* Input Catalog (KIC), I used the relation  $\tilde{K}_p \equiv 25.3 - 2.5\log(\text{flux})$  [Lund et al., 2015]. Here, flux is the count rate measured through a 3-pixel radius aperture.  $\tilde{K}_p \approx K_p$  for most brighter (e.g., AFGK-type) stars [Gizis et al., 2017b]. The values of  $\tilde{K}_p$  for 21 flaring targets is given in Table 2.9.

Our experience in previous works [Gizis et al., 2017b,a] show that the standard light curves based on default apertures do not give the best results for the ultracool targets. One of the main reasons for this is that the *K2* mission was not as stable at pointing towards the targets as the primary *Kepler* mission. Due to this, the centroid of the targets kept on moving towards various nearby pixels. So I used the target pixel files (TPFs) of each target available in the Mikulski Archive for Space Telescopes (MAST) archive instead of using the standard light curves. Examples of pixel level data are shown in Figure 2.6 in which the left figure corresponds to M5 dwarf GJ 3636 and the right corresponds to L0 dwarf 2M1232-0951. Figure 2.6 shows that the flux of brighter targets is spread over more pixels than that of a faint target. I began by estimating the best position of each target in each image frame. I inspected some frames by eye to estimate a threshold value of counts for the target pixels in each frame, and used the astropy-affiliated package “photutils.daofind” to estimate the centroid position in each frame. I used the median of centroids obtained for all the frames as the best

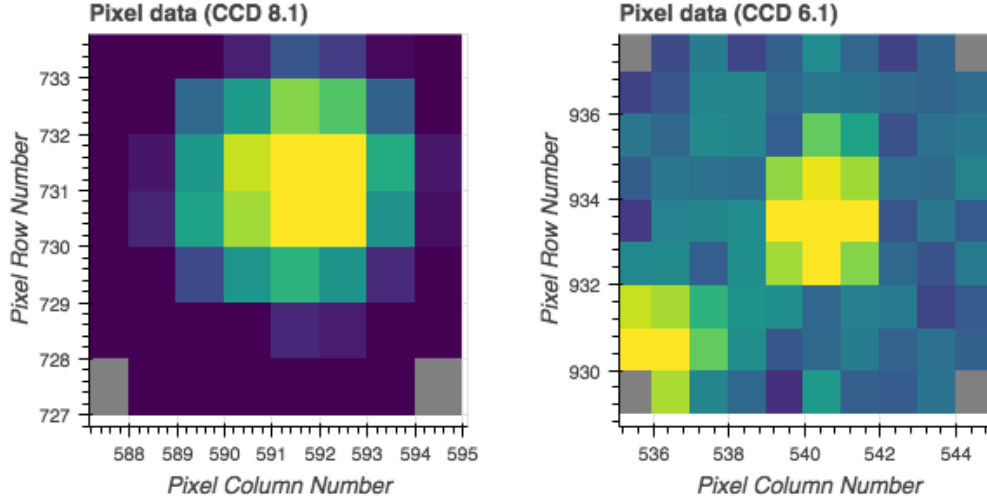


**Figure 2.6:** **Left:** Target pixel level data of M5 dwarf GJ 3636 in a randomly chosen cadence. **Right:** Target pixel level data of L0 dwarf 2M1232-0951 in a randomly chosen cadence.

position of our targets in their TPFs. I corrected the offset of centroid position in each frame due to spacecraft motion by using the information recorded as POS\_CORR1 and POS\_CORR2 in each TPF. After this, I used another astropy-affiliated photometry package “photutils.aperture\_photometry” to measure the photometry of all faint targets using a 2-pixel radius aperture. The same number of pixels was used by [Gizis et al. \[2017b,a\]](#) to measure photometry of UCDs. Since a significant amount of flux of the four brightest objects (GJ 3631, GJ 3636, Wolf 359 and LHS 2090) is spread over many pixels in comparison to the remaining faint targets, I measured their photometry using a 3-pixel radius aperture. I used only good quality (Quality=0) data points. The median count rate through both the 2-pixel radius aperture (CR2) and the 3-pixel radius aperture (CR3) for each target is given in [Table 2.9](#). Because the flux distribution of faint targets is limited to few pixels as seen in [Figure 2.6](#), CR2 is used for flare analysis of all targets in this chapter and CR3 is only used for estimation of  $\tilde{K}_p$ . The exception is for the four brightest ones for which CR3 is also used for flare analysis. An example of the *K2* light curve extracted from target pixel file by using a 3-pixel radius aperture for the M5 dwarf GJ 3631 is shown in [Figure 2.7](#).

**Table 2.9:** Median fluxes and *Kepler* magnitudes of flaring targets

Name	Median flux (cnts/s)		$\tilde{K}_p$ (mag)
	r = 2	r = 3	
GJ 3631	72538	75178	13.1
GJ 3636	24343	27768	14.2
Wolf 359	395565	411782	11.3
LHS 2090	45557	49274	13.6
2M2228-1325	16463	18063	14.7
2M2202-1109	2561	2695	16.7
2M0835+1029	891	1254	17.6
2M2214-1319	966	1058	17.7
2M1332-0441	1956	2220	16.9
TRAPPIST-1	5515	5717	15.9
2M1221-0843	809	884	17.9
2M0326+1919	761	771	18.1
2M1221+0257	508	577	18.4
2M1232-0951	358	381	18.9
2M0335+2342	2539	2732	16.7
2M1507-2000	3963	4467	16.2
2M0825+2021	243	250	19.3
2M1330-0453	784	832	18.0
2M2353-0833	729	774	18.1
2M1055+0808	1567	1674	17.2
2M1048+0111	675	728	18.2

**Note:** The median counts and  $\tilde{K}_p$  for W1906+40 are not mentioned here because its photometry was performed differently by the authors in [Gizis et al. \[2013\]](#).

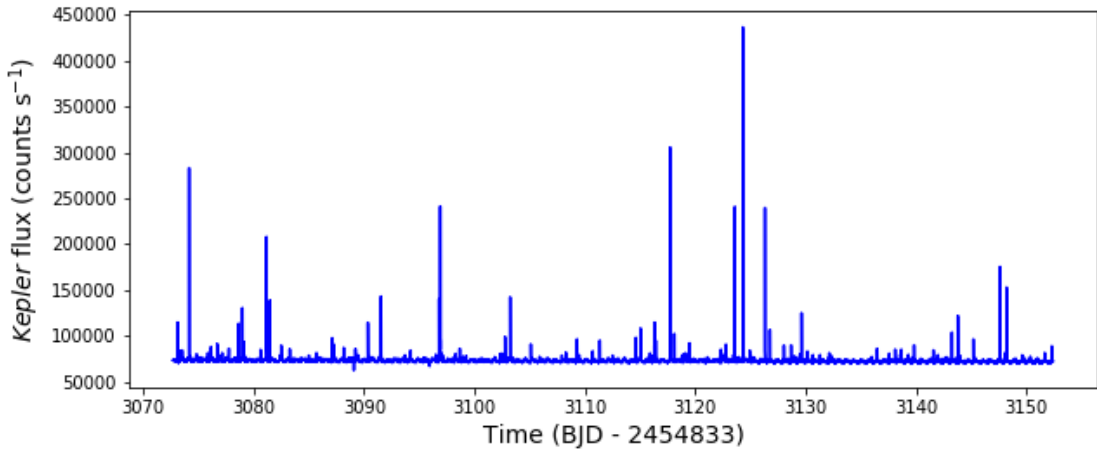


**Figure 2.7:** The *K2* light curve of the M5 dwarf GJ 3631 obtained by using a 3-pixel radius aperture from its TPF. The time along the *X*-axis is measured relative to the time when the *Kepler* mission began observation in 2009. The flux along the *Y*-axis is given in units of counts  $s^{-1}$  which were registered on the pixels considered.

### 2.3.2 Flare detection

Flare detection in the light curve of a target was a multi-step process. The initial step was to remove any periodic features in the light curve, which might be due to systematic or astrophysical non-flaring variability. These features add complexity to the light curve, and alter the morphology and duration of flares. I began by smoothing the original light curve of each target by using the Python package “pandas.rolling\_median” [McKinney, 2010] to remove the long term trends mainly caused by systematic errors in the light curve [Davenport, 2016]. I used a window of  $w = 3$ -day data points [Handberg and Lund, 2014]. I fitted this smoothed light curve with a third-order polynomial (as suggested by Davenport [2016]) and subtracted the result from the original light curve. I then followed a method similar to that described in Osten et al. [2012] to identify the flares in the smoothed light curve. I calculated relative flux  $F_{rel,i}$  for each data point

in the smoothed light curve, defined as:

$$F_{rel,i} = \frac{F_i - F_{mean}}{F_{mean}} \quad (2.1)$$

where  $F_i$  is the flux in  $i$ th epoch and  $F_{mean}$  is the mean flux of the entire light curve of each target. This relative flux was used to identify the flare candidates. I used the Lomb-Scargle periodogram to examine any other periodic features which we expect to be mainly due to astrophysical variability, e.g., due to the presence of starspots. If any periodic feature was detected, I fitted the smoothed light curve with a sinusoidal function using the dominant period, and subtracted from the smoothed light curve. In this way, I prepared the detrended light curves for our targets. I then calculated a statistic  $\phi_{ij}$  for each consecutive observation epoch  $(i,j)$  as:

$$\phi_{ij} = \left( \frac{F_{rel,i}}{\sigma_i} \right) \times \left( \frac{F_{rel,j}}{\sigma_j} \right), j = i + 1 \quad (2.2)$$

Here  $\sigma_i$  is the error in the flux which is associated with the  $i$ th epoch. This statistic defined in [Welch and Stetson \[1993\]](#) and [Stetson \[1996\]](#) was used to study variable stars using automated searches. It was later used by [Kowalski et al. \[2009\]](#) and [Osten et al. \[2012\]](#) for flare search in different stars. In order to identify the possible flare candidates in the light curve, I used the false discovery rate (FDR) analysis described in [Miller et al. \[2001\]](#). This method uses a critical threshold value of the  $\phi_{ij}$  statistic which is different for each target. To calculate this critical value of  $\phi_{ij}$ , I first discarded all those epoch pairs for which  $\phi_{ij} > 0$  but  $F_{rel,i,j} < 0$ . I then divided the remaining  $\phi_{ij}$  distribution in two distributions: the null distribution for which  $\phi_{ij} < 0$  and a possible flare candidate distribution for which  $\phi_{ij} > 0$ . The absolute value of the null distribution was fitted by a Gaussian function. The parameters of this Gaussian function was then used to calculate the  $p$ -values of each  $\phi_{ij}$  in the flare candidate distribution. I then followed each step described in Appendix B of [Miller et al. \[2001\]](#) to calculate the critical  $p$ -value and hence the critical  $\phi_{ij}$ . Epochs with  $\phi_{ij}$  greater than this value of the critical  $\phi_{ij}$  were considered to be better flare candidates in the light curve. The

value of the variable  $\alpha$  which is used in the [Miller et al. \[2001\]](#) FDR analysis is chosen to be 0.05 for *Kepler* data (based on private communication from R. Osten). This value of  $\alpha$  signifies that no more than 5% of the epochs with  $\phi_{ij}$  greater than the critical  $\phi_{ij}$  are false positives (mostly due to noise in the data). I also used an additional criterion, namely, that the detrended flux should exceed the photospheric level by  $2.5\sigma$ . This decreased the number of flare candidates in our data set to a few hundred. The final flares were chosen by inspecting the data by eye. In this way, even for the weakest flares, I ensured that there is at least a pair of epochs for which  $F_{rel,i,j} > 0$ : by this means, I was able to exclude any flares which had only a single measurement of flux brightening. For strong flares, there are multiple consecutive epoch with  $F_{rel,i} > 0$ . A more detailed explanation regarding this method of flare detection can be found in [Osten et al. \[2012\]](#).

The light curves of some flares observed on the M5 dwarf GJ 3631 are illustrated in [Figures 2.8 and 2.9](#). The flares shown in [2.8](#) are some of the largest flares observed on that target. Likewise, the flares shown in [2.9](#) are examples of small and complex flares observed on the same target. In all plots, the black vertical dashed lines represent the start and end times of flares, and the red horizontal dashed line represents the continuum (photospheric level). All the fluxes above the horizontal dashed line and in between two dashed vertical lines are considered to be flare fluxes. It can be seen that the larger flares have longer duration and some large flares (such as the one on the right side of [2.8](#)) are preceded by small flares.

### 2.3.3 Calibration of equivalent duration and calculation of flare energy

To calculate the flare energies, I first estimate the equivalent duration (hereafter ED) of each flare. It depends on the filter used but is independent of the distance to the flaring object and so it is widely used for determining flare energies. The ED of a flare is expressed as:

$$ED = \int [(F_f - F_c)/F_c] dt \quad (2.3)$$

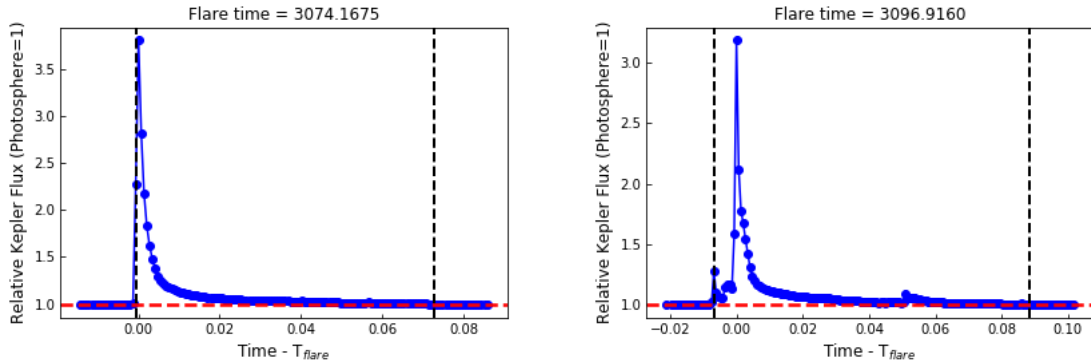


**Figure 2.8:** Examples of two large flares observed on the M5 dwarf GJ 3631. The black vertical dashed lines in both plots represent the start and end times of the flares. The red horizontal dashed line represents the continuum (photospheric) level. All fluxes above the continuum level in between the start and the end times are considered to be flare fluxes. The time mentioned above each plot is the peak flux time and is given in terms of *Kepler* mission time. The time along the *X*-axis is centered around the peak flux time. The flux along the *Y*-axis is normalized by the continuum level.

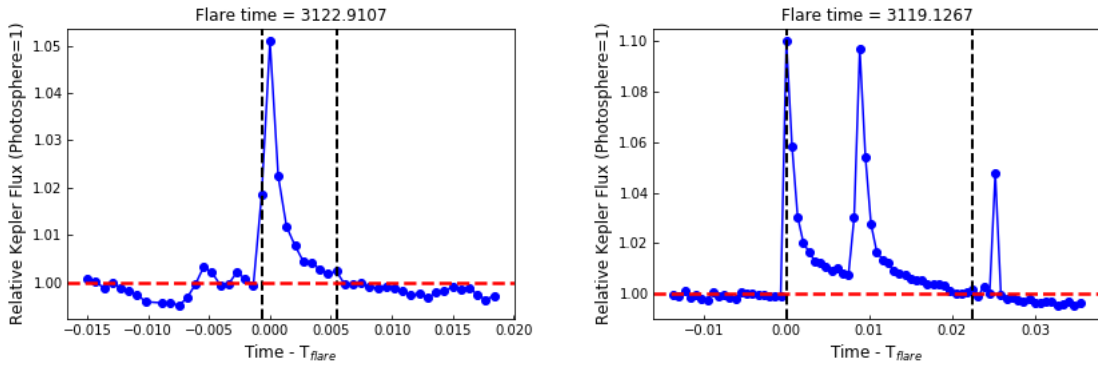


**Figure 2.9:** Examples of two small flares observed on the M5 dwarf GJ 3631. Though both have comparable amplitudes, the flare in the right side, being a complex flare, has greater energy.

where  $F_f$  is the flare flux and  $F_c$  is the continuum flux (i.e when the star is in its quiescent state). Numerically, the ED of a flare is obtained by taking the sum of products of ratios of flare fluxes to the continuum level and the duration of the cadence in which each flux data point was measured. For short cadence data, this duration is 58.85 s. ED has units of time and gives the area under the flare light curve. It is the equivalent time during which the star (in its quiescent state) would have emitted the same amount of energy as the flare actually emitted [Gershberg, 1972].

I followed the method described in Gizis et al. [2017a,b] to calibrate ED in terms of energy. *Kepler* measures photometry in the wavelength range 430nm to 900nm. In case of targets which have lower effective temperatures, a significant part of the flux is contributed by the longer wavelength part of this range but the WLF radiation contributes flux throughout the whole range of wavelengths in the *Kepler* band. This means that a given number of WLF counts measured in the *Kepler* band will have higher mean energy than the same number of photospheric counts from the target [Gizis et al., 2013]. For each target, I estimated the photospheric spectrum by using the matching late-M or L dwarf template spectrum [Bochanski et al., 2007; Schmidt et al., 2014] normalized to match the Pan-STARRS *i*-band photometry whenever available [Tonry et al., 2012; Chambers et al., 2016; Magnier et al., 2016]. The *Gaia* parallaxes were very important for this purpose.<sup>1</sup> As a white light flare can be best described by using a blackbody model with temperature = 10,000 K (see for e.g., Hawley and Pettersen 1991; Gizis et al. 2013)<sup>2</sup>, I modeled each flare as a 10,000 K blackbody normalized to have the same count rate through the *Kepler* response curve as the photosphere of the corresponding target on which it was observed. Using an 8,000 K blackbody gives values only 2% lower: this reduction is much less than other sources of uncertainty

---

<sup>1</sup> For LHS 523, which is too bright for Pan-STARRS, we normalize to the DENIS *I*-band photometry [Epchtein et al., 1997]

<sup>2</sup> It is also possible that flares on some UCDs might have cool temperatures (<4000 K, based on private communication from S. Littlefair)

Gizis et al. [2013]. I then estimated the energy emitted by the flare on a given target corresponding to an ED of 1 s. To estimate this energy, I did not only use the wavelengths in the *K2* band but also extrapolated to ultra-violet (UV) and infra-red (IR) wavelengths that are not detected by *K2*. So the flare energies reported in this chapter and others are those emitted by a 10,000 K blackbody continuum in UV/visible/IR wavelengths. They also include the atomic emission features between 430 nm and 900 nm which can be detected by *K2* but not the emission features in UV. It should be noted that the blackbody continuum dominates the flare energy budget in UV/visible wavelengths [Hawley and Pettersen, 1991; Osten and Wolk, 2015]. The final flare energies are computed by multiplying the ED of each flare by the energy emitted by a 10,000 K blackbody during an ED of 1 s.

Figure 2.10 shows the optical and near-infrared spectral energy distribution of TRAPPIST-1 and a 10,000 K flare with the same count rate through the *Kepler* filter<sup>3</sup>. Computation of total flare energies integrated over the UV/visible/IR is useful to compare the results with those obtained by using other surveys. For the 10,000 K blackbody flare model we adopt, this energy which includes UV/visible/IR wavelengths is 3.1 times the energy which includes only the wavelengths detected by *K2*, i.e.  $E_{\text{Kp}}$ . Likewise, for an 8,000 K blackbody the factor is 2.5. Gizis et al. [2013] argued this range is similar to that seen in an M dwarf flare by Hawley and Pettersen [1991]. Also, using the conversion relations between energies in various bands such as the *U*-band, *Kepler* band and bolometric flare energy ( $E_{\text{U}} = 0.65 E_{\text{Kp}}$ ,  $E_{\text{U}} = 0.11 E_{\text{bol}}$ ,  $E_{\text{Kp}} = 0.16 E_{\text{bol}}$ ) in Hawley et al. [2014] and Osten and Wolk [2015], the total bolometric flare energy is  $\sim 2$  times the energy in UV/visible/IR wavelengths reported in this work. In Appendix A, I list the time at which peak flare emission occurred, the equivalent duration, and the total (UV/visible/IR) energy for all of the flares which I identified in the flaring targets.

---

<sup>3</sup> For TRAPPIST-1 we used an average distance of 12.3 pc which is the average of distances mentioned in Gillon et al. [2016] and Weinberger et al. [2016]

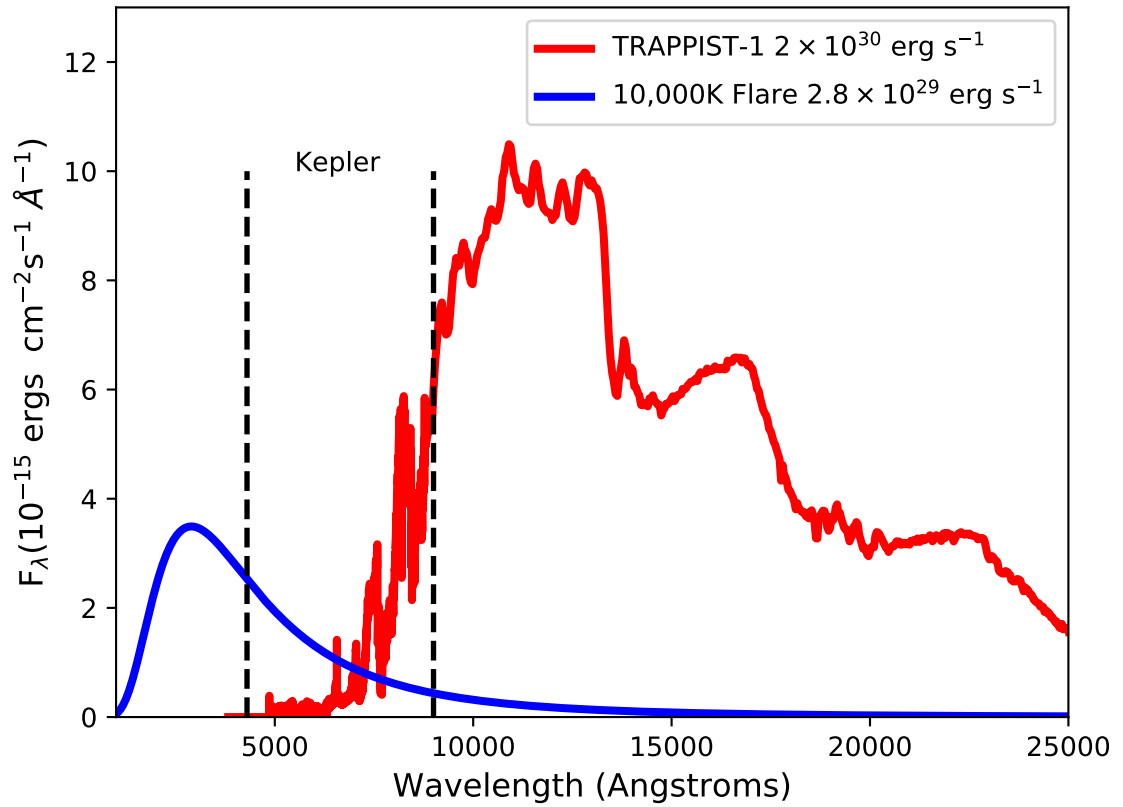


**Figure 2.10:** The optical and near-infrared spectral energy distribution of TRAPPIST-1 (red) and a hypothetical 10,000 K blackbody (blue). The wavelength range in between vertical dashed lines is the *Kepler* band. Using the distance of 12.3 pc, the bolometric luminosity of TRAPPIST-1 is  $2.0 \times 10^{30} \text{ erg s}^{-1}$  and that of 10,000 K flare is  $2.8 \times 10^{29} \text{ erg s}^{-1}$ .

## 2.4 Artificial flare injection and estimation of lowest detectable flare energy

In order to get an estimate of the minimum flare energy which could be detected by our algorithm, I generated artificial flares of randomly chosen amplitude and duration using the Davenport model [Davenport et al., 2014]. This was done by a slight modification of a similar module used in the software package known as “appaloosa” [Davenport et al., 2016]. I injected the artificial flares at random times to the detrended light curve with  $1-\sigma$  noise. To prepare this detrended light curve, I followed similar detrending process described in Section 2.3 and masked all other fluxes greater than  $1-\sigma$  level from the median flux. For simplicity, all injected artificial flares were single-peak “classic flares”. Care was taken to avoid any overlapping of the injected flares. I injected 10 artificial flares at once and used our algorithm to detect them. I kept track of times at which the artificial flares were injected and their equivalent durations. I repeated this process 1,000 times, so a total of 10,000 artificial flares were generated: however, due to restriction to non-overlapping events, some fraction of the 10,000 couldn’t be injected. I then calculated the flare energies of the injected artificial flares and compared these values with the energies I recovered by means of our algorithm. I found that weak flares having energies less than a certain energy were not detected by our algorithm. The light curves of different targets have different noise levels, so the minimum detectable energy of weak flares as found by our algorithm is different for each target. To estimate this minimum energy, I repeated the above process separately for each target. A list of minimum energies of artificial flares injected and later detected by our algorithm is given in Table 2.10, except for the two targets: W1906+40 and 2M0335+2342. For flare analysis, I discarded all the flares (if any) having energies less than the minimum energy of the artificial flares detected by our algorithm.

**Table 2.10: Minimum energies of injected and detected artificial flares**

Name	$E_{\min}$ ( $10^{30}$ erg)	$E_{\min}$ ( $10^{30}$ erg)
	injected	detected
GJ 3631	0.063	9.6
GJ 3636	0.26	2.5
Wolf 359	0.001	0.64
LHS 2090	0.005	0.45
2M2228-1325	0.043	0.56
2M2202-1109	0.025	2.0
2M0835+1029	0.019	2.0
2M2214-1319	0.012	4.0
2M1332-0441	0.028	1.8
TRAPPIST-1	0.012	0.53
2M1221-0843	0.006	4.0
2M0326+1919	0.065	1.9
2M1221+0257	0.019	1.2
2M1232-0951	0.012	2.6
2M1507-2000	0.031	2.1
2M0825+2021	0.10	75
2M1330-0453	0.011	2.9
2M2353-0833	0.009	1.9
2M1055+0808	0.009	0.55
2M1048+0111	0.004	1.1

**Note:** This table does not include W1906+40 and 2M0335+2342, as the flares on them were already analyzed by [Gizis et al. \[2013\]](#) and [Gizis et al. \[2017a\]](#) respectively.

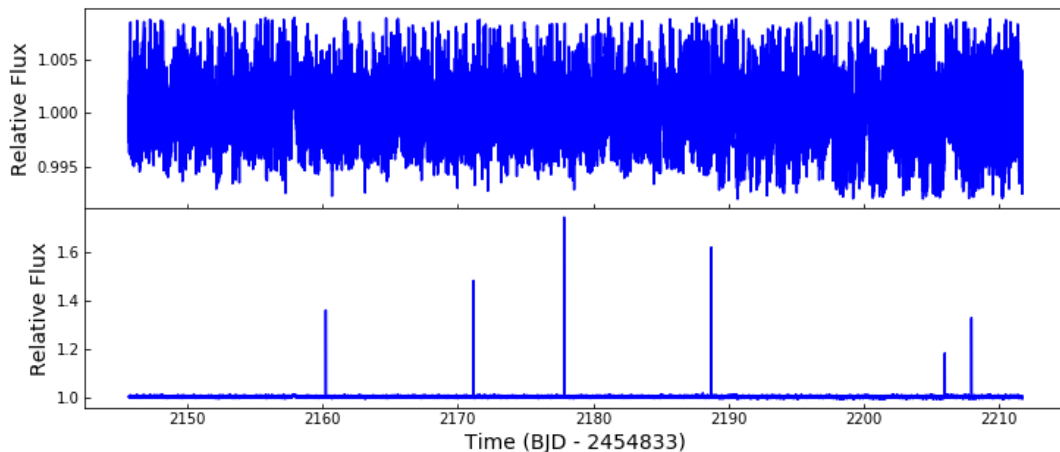


**Figure 2.11:** An example of artificial flare injection in 2M2228-1325 light curve. The upper plot is a detrended light curve with  $1\text{-}\sigma$  noise and the lower plot is the light curve with artificial flares injected at random times.

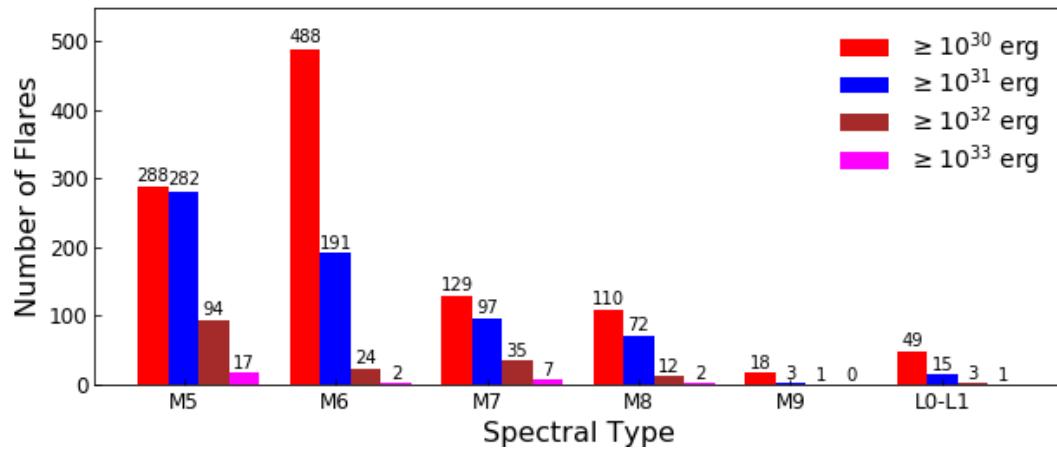
## 2.5 Flare statistics and Flare energy spectrum of target UCDs

Table 2.11 lists various properties of flares on flaring targets in the sample. In this table, the second column ‘BB energy for  $ED = 1\text{ s}$ ’ is the energy emitted by 10,000 K blackbody which has the same number of counts as the target in *Kepler* bandpass for an ED of 1s. The column ‘Rot. Period’ gives information if any periodic feature is seen in the light curve of each target after removing the long term trends using a rolling median method. If any periodicity is seen, the dominant period is listed. The periodicity might be due to the presence of starspots, and most probably gives an indication of the rotation period of the target. All the periods mentioned in this table are the dominant periods identified by using the Lomb-Scargle periodogram.  $N$  is the number of flares identified on a given target during the entire interval  $T$  of *K2* observations of that target (for  $T$  values, see Table 2.12). Likewise,  $E_{\min}$  is the minimum energy of all the identified flares on a given target and  $E_{\max}$  is the maximum energy of all the identified flares on a given target. Both  $E_{\min}$  and  $E_{\max}$  are given in units of  $10^{30}$  erg.

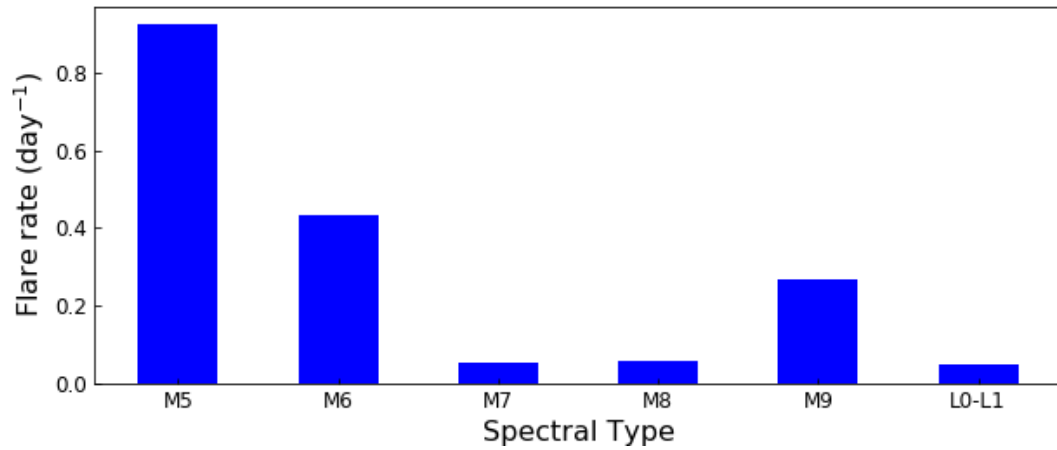
A total of 1105 flares were observed on 22 targets in the sample. The largest number

of flares (200) were observed on M6 dwarf LHS 2090, and a minimum number of flares (10) were observed on two targets: 2M2353-0833 (M8.5) and 2M1048+0111 (L1). The largest flare was observed on the M5 dwarf GJ 3631 and had an estimated total energy of  $1.8 \times 10^{34}$  erg. In Figure 2.12, I show the flare energy distribution for all spectral types. The energies are classified into four groups:  $\geq 10^{30}$ ,  $\geq 10^{31}$ ,  $\geq 10^{32}$  and  $\geq 10^{33}$  erg. Likewise, in Figure 2.13, I show the average number of flares observed every day in each spectral type and includes 22 flaring targets only. The flare rate along  $Y$ -axis was estimated by dividing the total number of flares by the number of flaring targets and the total time of observation of those targets for a given spectral type. The high average flare rate in the case of M9 ST is because there is only one flaring target with this ST. Since this plot does not contain any information regarding the flare energies, it is of limited importance. Figure 2.14 shows the total observation time of the flaring targets for each ST.

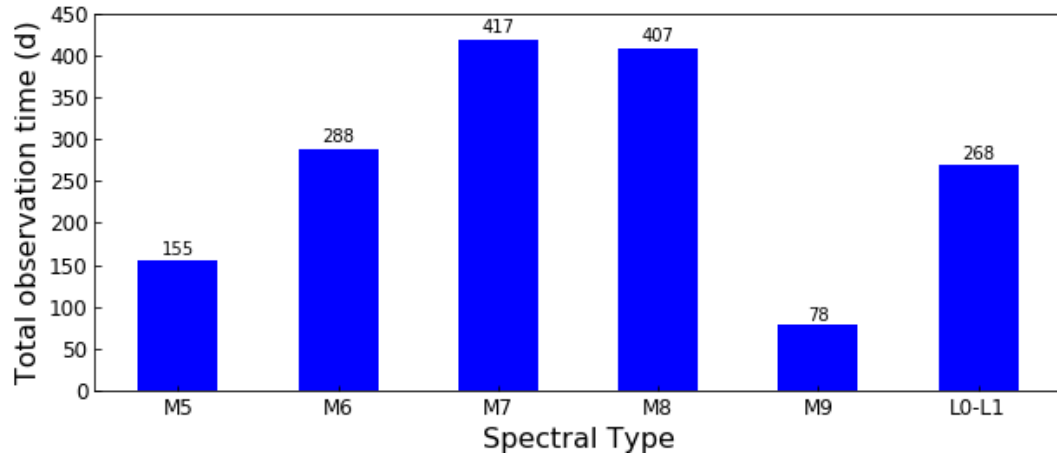
In Figure 2.15, I show the average number of flares observed every day in each spectral type by including all flaring and non-flaring targets. The flare rate along  $Y$ -axis was estimated by dividing the total number of flares by the number of targets observed in short cadence mode and the total time of observation of those targets for a given spectral type. Likewise, in Figure 2.16, I show the total observation time of all the targets, for each ST, which were observed in short cadence mode. Figures 2.15 and 2.16 do not include L2-L9 dwarfs as no flares were observed on the targets with these STs in short cadence mode.



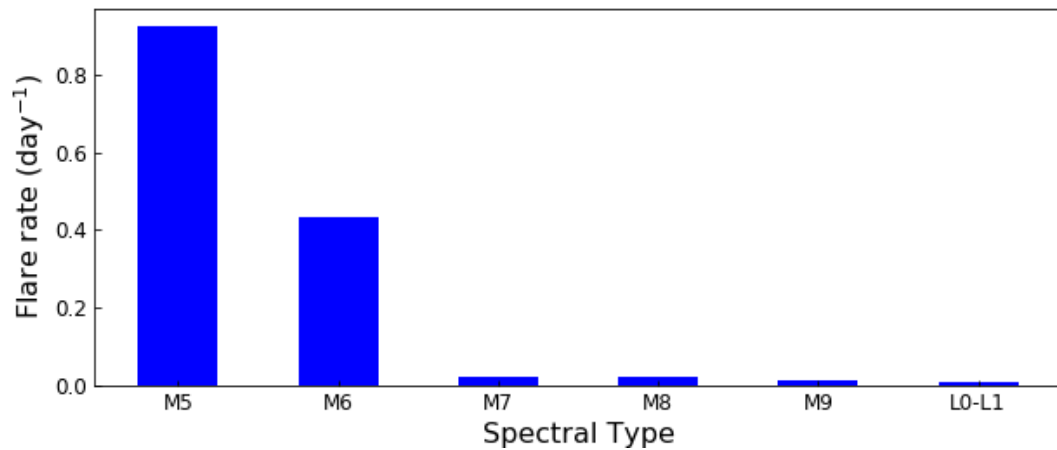
**Figure 2.12:** Bar chart showing the distribution of flare energies in each spectral types. Different colors refer to the flares with certain range of energies.



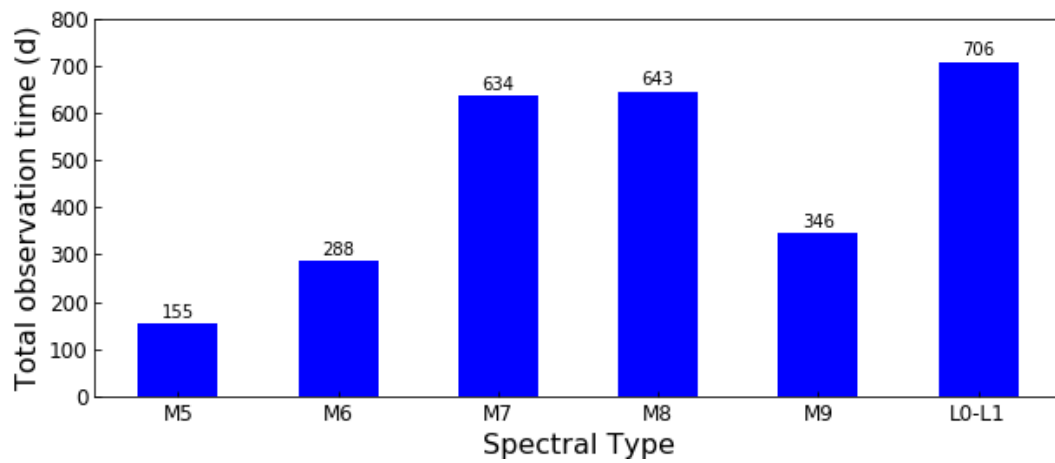
**Figure 2.13:** Average number of flares observed per day per target in each spectral type, except L2-L9. This plot includes only the flaring targets.



**Figure 2.14:** Bar chart showing the total time of observation (in units of days) of the flaring targets in each spectral type, except L2-L9.



**Figure 2.15:** Average number of flares observed per day per target in each spectral type, except L2-L9. This plot includes all flaring and non-flaring targets observed in short cadence mode.



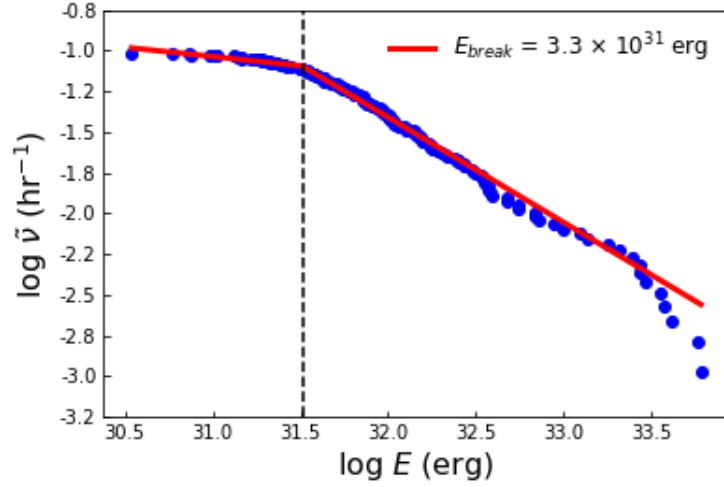
**Figure 2.16:** Bar chart showing the total time of observation (in units of days) of all targets in each spectral type, except L2-L9, which were observed in short cadence mode.

Table 2.11: Flare statistics

Target	BB energy for ED=1 s	Rot. Period	$N$	$E_{\min}$	$E_{\max}$
	erg	d		( $10^{30}$ erg)	( $10^{30}$ erg)
GJ 3631	$4.5 \times 10^{30}$	0.35	175	9.6	18000
GJ 3636	$4.4 \times 10^{30}$	0.25	113	3.1	1400
Wolf 359	$8.1 \times 10^{29}$	2.70	198	0.93	300
LHS 2090	$6.0 \times 10^{29}$	0.44	200	0.60	1500
2M2228-1325	$1.7 \times 10^{30}$		50	1.0	410
2M2202-1109	$7.0 \times 10^{29}$	0.42	50	3.0	1400
2M0835+1029	$2.2 \times 10^{29}$		11	2.3	6100
2M2214-1319	$4.9 \times 10^{29}$		26	9.0	1400
2M1332-0441	$2.5 \times 10^{29}$		31	1.8	220
TRAPPIST-1	$2.8 \times 10^{29}$	3.3	39	0.63	690
2M1221-0843	$7.7 \times 10^{29}$	0.27	36	11	1200
2M0326+1919	$2.4 \times 10^{29}$	0.97	18	2.8	230
2M1221+0257	$7.4 \times 10^{28}$	0.18	11	1.3	69
2M1232-0951	$8.7 \times 10^{28}$		11	2.6	3600
W1906+40	$6.4 \times 10^{28}$	0.37	21	0.6	170
2M0335+2342	$2.7 \times 10^{30}$	0.22	22	28	1500
2M1507-2000	$8.1 \times 10^{29}$		28	2.1	2600
2M0825+2021	$3.3 \times 10^{30}$	0.20	11	330	2300
2M1330-0453	$3.0 \times 10^{29}$	0.13	13	6.9	120
2M2353-0833	$1.4 \times 10^{29}$	0.87	10	3.3	30
2M1055+0808	$1.6 \times 10^{29}$		21	0.73	120
2M1048+0111	$5.8 \times 10^{28}$	0.24	10	1.2	15

Table 2.12 lists the values of the parameters I have fitted to the FFD of each of the targets. In this table  $T$  is the total observation time for a given target,  $\beta$  and  $\alpha_o$  are the fitted values of parameters in Eq. 1.1,  $\sigma_\beta$  and  $\sigma_{\alpha_o}$  are the statistical errors in  $\beta$  and  $\alpha_o$ . Likewise,  $E_{\min}$  and  $E_{\max}$  are the minimum and maximum *Kepler* energies used for fitting. The total observation time, in seconds, is computed by counting the total number of good (Quality = 0) data points and multiplying by 58.85 s which is the correct exposure time equivalent to short cadence. It is given in units of days in Table 2.12 in the column ‘ $T$ ’. I used the maximum-likelihood method described in Hogg et al. [2010] and implemented in the routine known as “emcee” [Foreman-Mackey et al., 2013] to fit a straight line to data (in a log-log plot) and hence obtain the optimal values of parameters  $\beta$  and  $\alpha_o$ . The routine “emcee” uses the standard Metropolis-Hastings Markov-Chain Monte Carlo (MCMC) procedure for marginalization and uncertainty estimation. The errors  $\sigma_\beta$  and  $\sigma_{\alpha_o}$  are obtained by dividing the values of  $\beta$  and  $\alpha_o$  by the square root of the number of flares used for fitting. The same process is followed by Lacy et al. [1976] and Hilton [2011] to calculate those errors. Here I report the intercept  $\alpha_o$  corresponding to energy  $10^{30}$  erg, not the zero energy. It will be helpful in comparing the flare rates of our targets with previously reported flare rates of other targets observed by *Kepler* and *K2*, most of which have flare energies greater than  $10^{30}$  erg [Ramsay et al., 2013; Hawley et al., 2014; Davenport, 2016; Gizis et al., 2017a].

I neglected the highest observed energy for fitting the line to reduce any bias in the analysis. Since the targets GJ 3631, GJ 3636, Wolf 359 and LHS 2090 have a flattened distribution at low energy probably due to lack of *K2* ability to detect the flares with energy below some threshold value, I need to select a minimum value of energy to be considered for fitting. This minimum value was chosen on the basis of initial inspection by fitting a broken power law as shown in Figure 2.17. The presence of a flattened distribution also indicate that the FFDs might follow two power laws: a shallower slope in the case of lower flare energies and a steeper slope in the case of higher flare energies. Such possibility is explained in Mullan and Paudel [2018]. For targets which



**Figure 2.17:** An example showing how a lower limit on flare energy was chosen for fitting in the case of targets with flattened distribution at low energy. The dashed vertical line corresponds to the lowest energy which was considered for fitting.

do not have a flattened distribution at low energy, all flares, even those with the lowest energies, were considered for fitting.

I also used the analytic solution to get the estimate of the parameter  $\alpha$  which is derived in [Clauset et al. \[2009\]](#) and references therein. Here I denote this estimate as  $\hat{\alpha}$  which is the maximum likelihood estimator (MLE) of the true value of the parameter  $\alpha$  and is expressed as:

$$\hat{\alpha} = 1 + n \left[ \sum_{i=1}^n \ln \frac{E_i}{E_{\min}} \right]^{-1} \quad (2.4)$$

with error

$$\sigma = \frac{\sqrt{n+1}(\hat{\alpha} - 1)}{n} \quad (2.5)$$

. Here  $n$  is the number of flares and  $E_i$ ,  $i = 1 \dots n$  are the observed values of energies  $E$  such that  $E_i \geq E_{\min}$ . The MLE solution  $\hat{\alpha}$  is an unbiased estimator of  $\alpha$  in the asymptotic limit of large sample size,  $n \rightarrow \infty$ . In addition, a more reliable estimate for the parameter  $\alpha$  can be obtained for sample sizes  $n \gtrsim 50$  [[Clauset et al., 2009](#)].

For small sample sizes  $n$ , Arnold [2015] suggests the value of  $\hat{\alpha}$  obtained by using Eq. 2.4 can be multiplied by a factor of  $(n - 2)/n$  in order to make the result unbiased. The unbiased value of  $\hat{\alpha}$  for each target is listed in Table 2.12. The same energy range used for fitting the power law FFD is used for estimating  $\hat{\alpha}$ . The number of flares on most of the targets is unfortunately too small to obtain a more accurate estimation of parameter  $\alpha$  using the analytic solution. As a result, I will use the results obtained by using the “emcee” routine for discussion and comparison of results with previous works. Table 2.12 also lists the slopes of FFDs for 2M0335+2342 and W1906+40, obtained by using the methods described above. It should be noted that they are slightly different from the values reported in previous papers because somewhat different energy intervals were chosen for fitting.

Table 2.12: Power law fits to FFDs of targets

Name	$T$	n	$\beta$	$\sigma_\beta$	$\alpha=\beta+1$	$\hat{\alpha}$	$\alpha_o$	$\sigma_{\alpha_o}$	$E_{\min}$	$E_{\max}$
	(days)			$(\beta/\sqrt{n})$			(hr <sup>-1</sup> )	$(\alpha_o/\sqrt{n})$	(10 <sup>30</sup> erg)	(10 <sup>30</sup> erg)
GJ 3631	77.8	140	0.70	0.06	1.70	1.65±0.06	-0.01	0.00	34	6000
GJ 3636	77.9	66	0.96	0.12	1.96	1.98±0.12	-0.06	0.01	28	1100
Wolf 359	77.3	144	0.87	0.07	1.87	1.76±0.06	-0.57	0.05	3.5	290
LHS 2090	77.1	109	0.95	0.10	1.95	1.83±0.08	-0.63	0.06	3.5	220
2M2228-1325	66.8	27	1.00	0.20	2.00	1.84±0.16	-0.50	0.10	16	180
2M2202-1109	67.5	49	0.64	0.10	1.64	1.47±0.07	-1.08	0.15	3.0	490
2M0835+1029	73.3	10	0.65	0.21	1.65	1.43±0.14	-1.90	0.60	2.3	33
2M2214-1319	66.9	25	0.70	0.14	1.70	1.54±0.11	-1.02	0.20	9.0	640
2M1332-0441	76.4	30	0.57	0.10	1.57	1.50±0.10	-1.58	0.29	1.8	97
TRAPPIST-1	70.6	38	0.63	0.10	1.63	1.47±0.08	-1.65	0.27	0.63	53
2M1221-0843	53.4	35	0.71	0.12	1.71	1.62±0.11	-0.75	0.13	11	1200
2M0326+1919	69.2	17	0.45	0.11	1.45	1.32±0.08	-1.70	0.41	2.8	190
2M1221+0257	53.5	10	1.04	0.33	2.04	1.85±0.28	-1.88	0.60	1.3	6.3
2M1232-0951	53.5	10	0.34	0.11	1.34	1.37±0.12	-2.00	0.63	2.6	390
W1906+40	83.0	15	0.54	0.14	1.54	1.40±0.10	-1.87	0.50	1.9	51
2M0335+2342	69.0	19	0.72	0.17	1.72	1.69±0.16	-0.64	0.15	69	1400
2M1507-2000	82.8	27	0.52	0.10	1.52	1.37±0.07	-1.56	0.30	2.1	580
2M0825+2021	49.21	9	1.04	0.35	2.04	2.65±0.60	0.67	0.22	330	870
2M1330-0453	141.7	12	0.87	0.25	1.87	1.68±0.21	-1.62	0.47	6.9	44
2M2353-0833	72.4	8	0.86	0.30	1.86	1.37±0.14	-1.65	0.60	5.7	24
2M1055+0808	78.1	20	0.66	0.15	1.66	1.63±0.15	-2.0	0.45	0.73	42
2M1048+0111	78.2	9	0.72	0.24	1.72	1.60±0.20	-2.17	0.72	1.2	10

**Note:** The intercept  $\alpha_o$  reported in this table gives the flare rate for flare energy 10<sup>30</sup> erg, not the zero energy. See the text for more description.

In Figures 2.18, 2.19 and 2.20, I plot the FFD of each target in the sample. In order to make it easy for the readers to compare the FFDs of different targets, I divided the targets into three groups: i) targets with STs of M5-M6, ii) targets with STs of M7 and iii) targets with STs of M8-L0/1. The FFDs of these three groups of targets are plotted in three figures separately. In each figure, the FFD for each target is presented separately in a different panel, and the panels are arranged in order of increasingly late spectral type in the case where there are targets of different spectral types in a given group. The FFDs of other targets in a given group are also plotted in the background of each panel to enable the reader to compare the FFD of a given target with others in that group. In each plot in Figures 2.18, 2.19 and 2.20, the blue dots represent the observed energies and the solid red line represents the fitted line.

Since the plots in Figures 2.18, 2.19 and 2.20 also contain the observed energies and the FFDs of other targets are plotted in the background, it is somewhat difficult when we want to compare the FFDs of a given target with others. To make it easier, I compare the FFDs of various targets using the fitted FFDs only in Figures 2.21, 2.22 and 2.23. In Figure 2.21, I compare the fitted FFDs of M5-M6 dwarfs. In Figure 2.22, I compare the fitted FFDs of M7-M8 dwarfs and in Figure 2.23, I compare the fitted FFDs of M8-L1 dwarfs. In each of the Figures 2.21, 2.22 and 2.23, I also plot the FFDs using the EDs of the flares to see how the flare rates might be affected by the luminosity of a 10,000 K blackbody, which was used to compute the flare energies. This is discussed in more detail later in this chapter.

It should be noted that the fitted line of some targets cover a very small range of energy which is less than one order in magnitude. Such FFDs are less helpful for comparison with the FFDs of other targets. In Figure 2.24, I compare the FFD of a young brown dwarf 2M0335+2342 with that of an L0 dwarf 2M1232-0951.

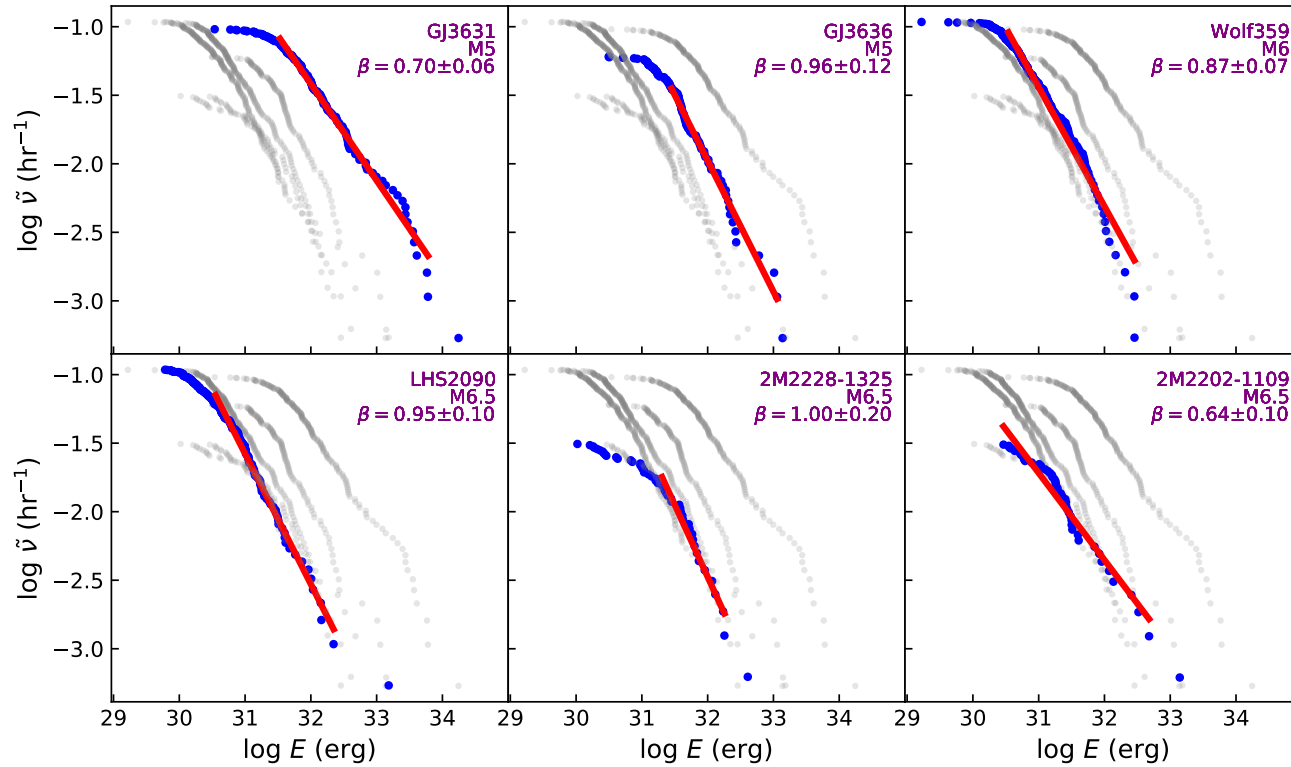


**Figure 2.18:** Individual FFD of M5 and M6 dwarfs in the sample. In each panel, the blue dots represent the observed data and the red solid line represents the fitted model. The FFDs of other targets with spectral types M5 and M6 are also plotted in the background for comparison.

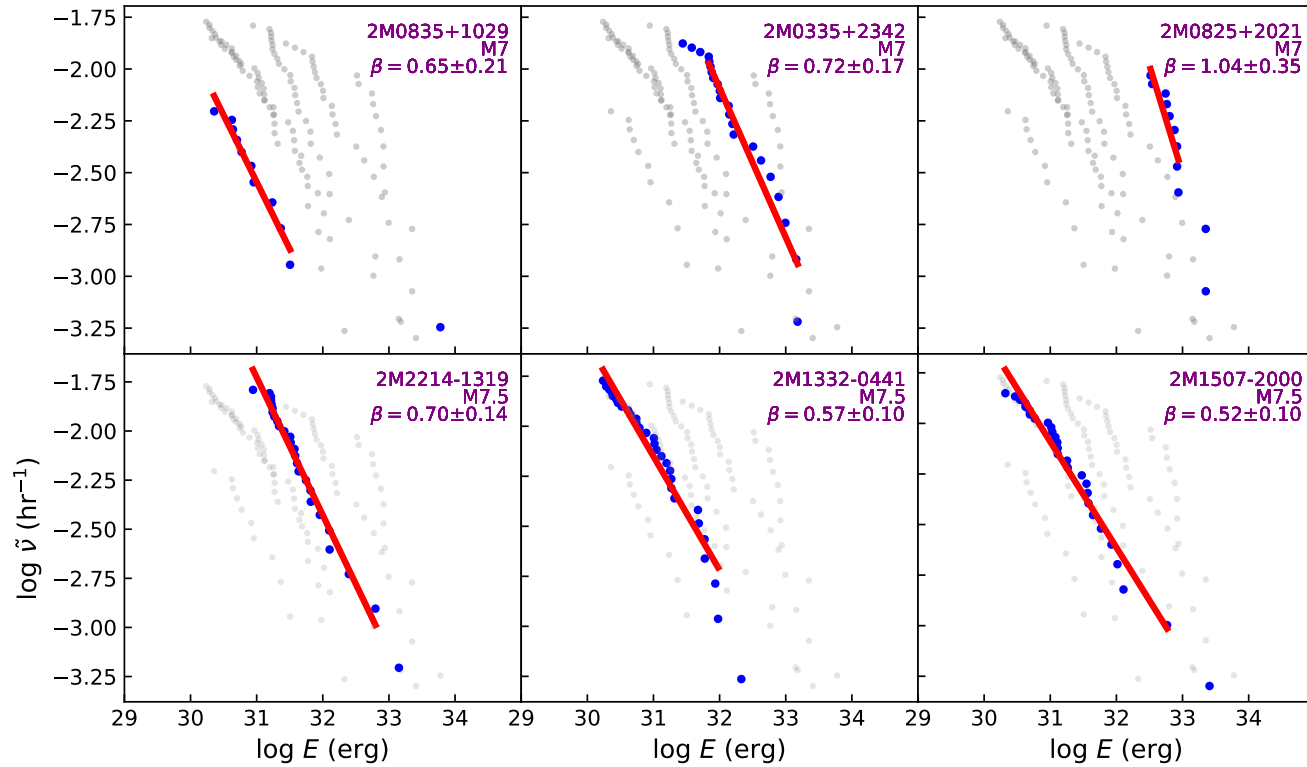


**Figure 2.19:** Individual FFD of M7 dwarfs in the sample. In each panel, the blue dots represent the observed data and the red solid line represents the fitted model. The FFDs of other targets with spectral type M7 are also plotted in the background for comparison.

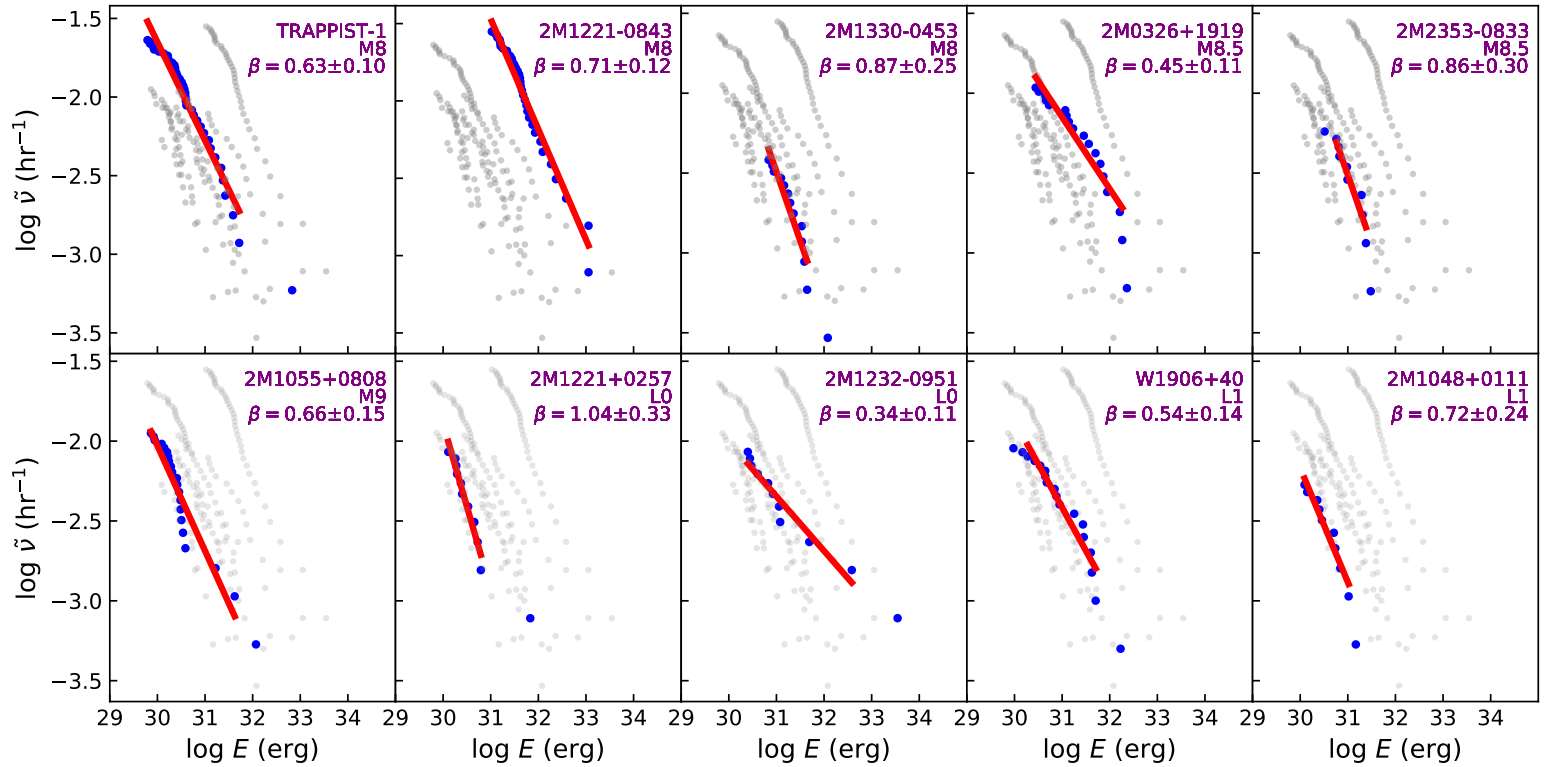


**Figure 2.20:** Individual FFD of M8, M9 and L dwarfs in the sample. In each panel, the blue dots represent the observed data and the red solid line represents the fitted model. The FFDs of other targets with spectral type M8, M9 and L are also plotted in the background for comparison.

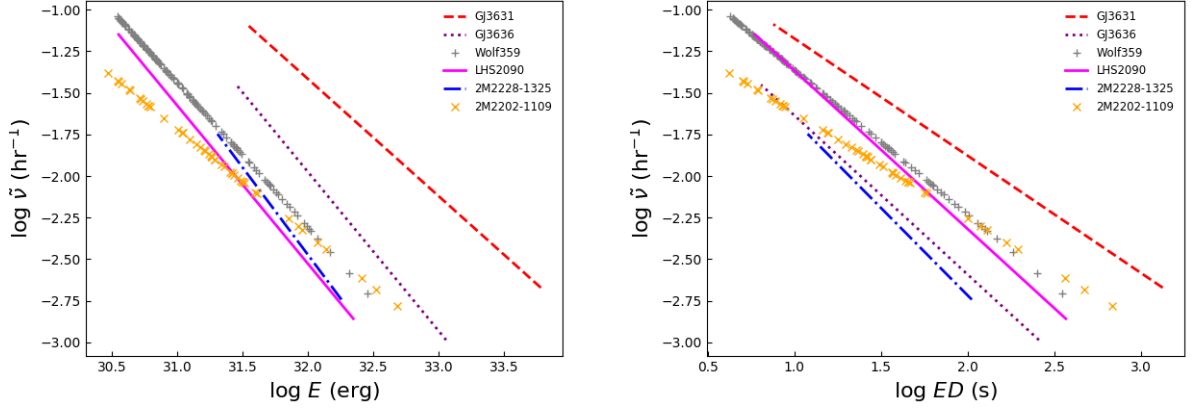


**Figure 2.21:** **Left:** Fitted FFDs of M5-M6 dwarfs in the sample. **Right:** This plot is similar to that in the left except that the flare energies are replaced by the corresponding EDs of the flares.

### 2.5.1 Possibility of a broken power-law or a power-law with exponential cutoff in the FFD of some UCDs

The presence of long tails at high energies in the FFDs suggests that a single power-law might not be the optimal fit to the FFD of all UCDs. In the case of 2 targets (2M2228-1325 with ST M6.5 and 2M0326+1919 with ST M8.5), I tried to fit two different models: (i) a broken power-law, and (ii) a power-law combined with an exponential cutoff. Results are shown in Figure 2.25. The broken power-law model can be expressed as:

$$f(E) = \begin{cases} A(E/E_{break})^{-\alpha_1} & : E < E_{break} \\ A(E/E_{break})^{-\alpha_2} & : E > E_{break} \end{cases} \quad (2.6)$$

while the power-law with exponential cutoff can be expressed as:

$$f(E) = A(E/E_0)^{-\alpha} \exp(-E/E_{cutoff}) \quad (2.7)$$

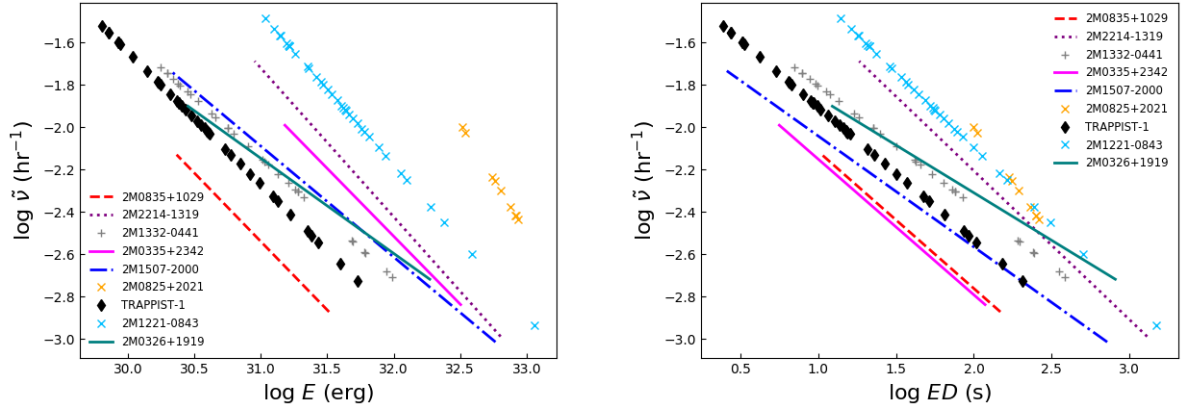


**Figure 2.22:** **Left:** Fitted FFDs of M7-M8 dwarfs in the sample. **Right:** This plot is similar to that in the left except that the flare energies are replaced by the corresponding EDs of the flares.

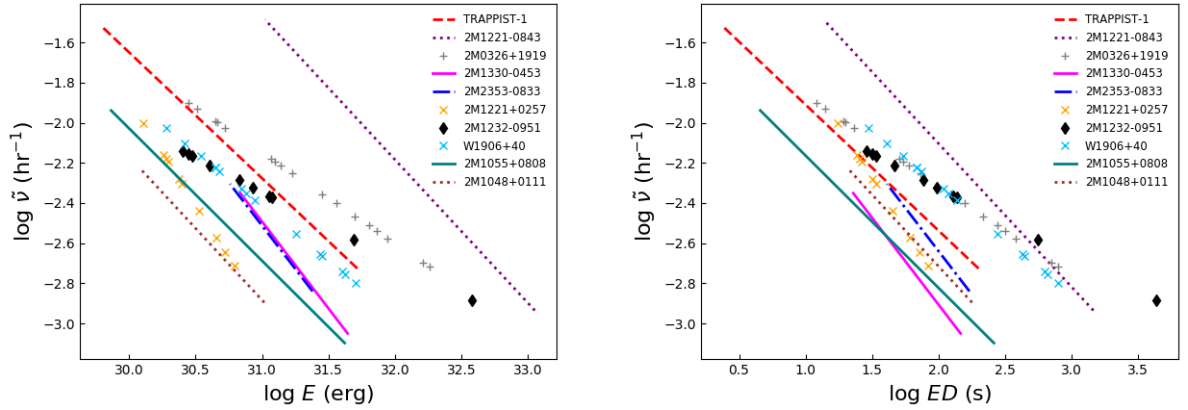


**Figure 2.23:** **Left:** Fitted FFDs of M8, M9 and L0 dwarfs in the sample. **Right:** This plot is similar to that in the left except that the flare energies are replaced by the corresponding EDs of the flares.

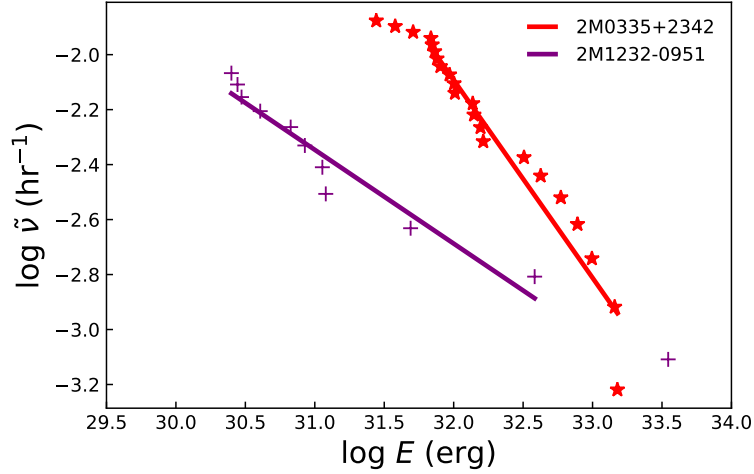


**Figure 2.24:** Comparison of the FFD of a young brown dwarf 2M0335+2342 (red) with that of an L0 dwarf 2M1232-0951 (purple). The dots represent observed data and solid lines represent the fitted power law model. This plot suggests that the L0 dwarf has a flare rate that is comparable to that of a 24 Myr old brown dwarf as regards high energy flares, despite the L0 dwarf having a cooler atmosphere.

I used the astropy-affiliated packages “`modeling.power-laws.BrokenPowerLaw1D`” and “`modeling.powerlaws.ExponentialCutoffPowerLaw1D`” to estimate the model parameters. And I used the astropy-affiliated package “`modeling.fitting.LevMarLSQFitter`” to fit the data. The later package uses the Levenberg-Marquardt algorithm and least squares statistic for fitting. I used a likelihood ratio test to decide which model better fits the observed data, by considering the broken power-law model as alternate, and the power-law with exponential cutoff as the null model. In the case of 2M2228-1325, I found that the broken power-law provides a better fit to the data with  $\alpha_1 = 0.2$ ,  $\alpha_2 = 0.8$ ,  $E_{\text{break}} = 1.5 \times 10^{31}$  erg and  $A = 30.7$ . The  $p$ -value of the likelihood-ratio test statistic is 0.005 (i.e. I reject the null model for a significance level of 0.05). I used the energies greater than  $E_{\text{break}}$  for determining the slope of the FFD. But, in the case of 2M0326+1919, I found that the power-law with exponential cutoff provides a better fit to the data. In this case, the fitted parameters are  $A = 14.7$ ,  $E_{\text{cutoff}} = 1.6 \times 10^{32}$  erg,  $E_0 = 6.0 \times 10^{30}$  erg and  $\alpha = 0.2$ . The  $p$ -value of the test statistic is 0.60 (i.e. I accept the

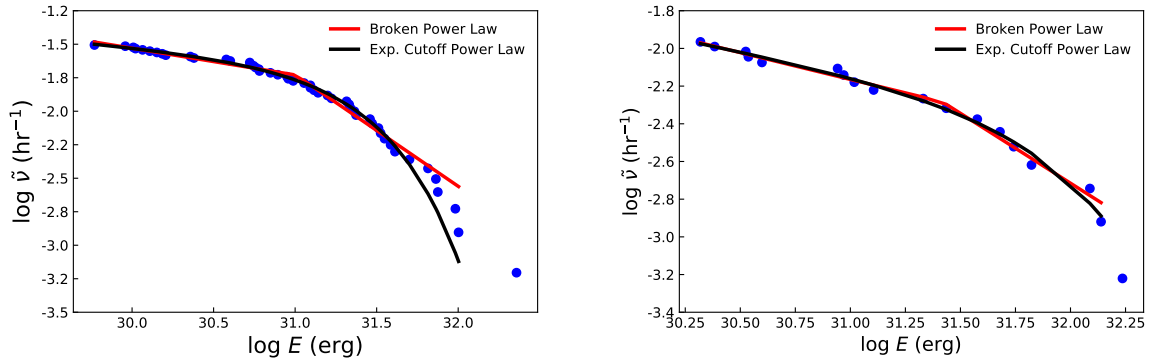


**Figure 2.25:** **Left:** Comparison between broken power law and power law with cutoff in case of 2M2228-1325. **Right:** Comparison between broken power law and power law with cutoff in case of 2M0326+1919.

null model for a significance level of 0.05). The possible break in the power-law could be due to a number of factors, including the sensitivity of the instrument in observing weak flares, or saturation, or an upper limit on the energy which any flare on a given target is able to release [Gershberg, 2005]. As far as I have been able to determine, the FFDs which follow broken power-law are seldom discussed in the literature. So are the FFDs which follow power-law with exponential cutoff. However, the possibility that some FFDs might follow different power laws in the high energy regime and low energy regime is explained in Mullan and Paudel [2018].

## 2.6 Superflares observed on two UCDS

One of the advantages of short cadence *K2* data is that it helps to study the time scales associated with rapid rise, rapid decay and gradual decay phase of superflares (flares with energies  $\geq 10^{33}$  erg). There are multiple superflares observed on the targets in the sample. However, two of them have very large amplitudes and long EDs compared to the rest of the superflares. Here I present the photometry of two such superflares.

### 2.6.1 Photometry of superflare observed on L0 dwarf 2MASS J12321827-0951502

A superflare was observed on the L0 dwarf 2M1232-0951 at *Kepler* time 2811.7662319, when the flare flux rose to 51529 cnts/s ( $\tilde{K}_p = 13.44$ ,  $\Delta\tilde{K}_p = -5.41$ ): this count rate is  $\sim 144$  times larger than the photospheric level (358 cnts/s). To determine the relevant time-scales of the flare, I used the [Davenport et al. \[2014\]](#) (hereafter D14) model to fit the flare light curve. This yields values for the time scale  $t_{1/2}$  associated with the rise of flux from and return to half maximum flux. The model also yields values for two decay time scales, one rapid (close to flare maximum), and the other gradual (later in the flare). The D14 model uses a flare template that was based on the flare properties of the M4 dwarf GJ 1243 using *Kepler* short cadence data. In this model, the rapid rise phase is best fitted by using a fourth order polynomial, and the decay phase is best fitted by using the sum of two exponentials which can be expressed as:

$$\Delta F = A(\alpha_i e^{-\gamma_i \Delta t / t_{1/2}} + \alpha_g e^{-\gamma_g \Delta t / t_{1/2}}) \quad (2.8)$$

where  $\Delta F$  is flare only flux,  $A$  is flare amplitude and  $\Delta t = t - t_f$  ( $t_f$  is the peak flare time). In D14 template, the values of the different parameters of Eq.(2.8) are  $\alpha_i = 0.6890(\pm 0.0008)$ ,  $\alpha_g = 0.3030(\pm 0.0009)$ ,  $\gamma_i = 1.600(\pm 0.003)$  and  $\gamma_g = 0.2783(\pm 0.0007)$ . [Schmidt et al. \[2016\]](#) used this model to estimate the value of  $t_{1/2}$  to be in the range 3 (best fit) to 6.2 (minimal fit) minutes for a superflare observed on the L0 dwarf ASASSN-16ae. Likewise, [Gizis et al. \[2017b\]](#) estimated  $t_{1/2} = 6.9$  minutes for the L1 dwarf W1906+40 using same model. Slightly different value of parameters were used by [Gizis et al. \[2017b\]](#) to fit a superflare on the L1 dwarf SDSSp J005406.55-003101.8 to estimate  $t_{1/2} = 7.8$  minutes. Here, the estimation of  $t_{1/2}$  for 2M1232-0951 is done using *K2* short cadence data, so it is more accurate than those reported for ASASSN-16ae and SDSSp J005406.55-003101.8. To fit the flare of interest here (i.e. the superflare on 2M1232-0951), I started by examining if the D14 model could fit the observed data. However, I found that it did not provide an especially good fit for the late decay phase.

To get an initial estimation of decay phase time scale, I fitted the late decay phase separately by a single exponential curve and used the parameters obtained in this way to fit the entire curve. Figure 2.26 shows the observed flux and fitted model<sup>4</sup>. At first glance in Figure 2.26(a), there seems to be a good agreement between observed data and fitted model. But, the discrepancy can be clearly seen in log-log version of same plot as shown in Figure 2.26(b). The values of fitted parameters for this flare are:  $\alpha_i = 0.9691$ ,  $\alpha_g = 0.0310$ ,  $\gamma_i = 0.4551$  and  $\gamma_g = 0.01543$ . Likewise other fitted parameters are  $A = 51005.76$ ,  $t_{1/2} = 1.054$  minute and time of flare = 2811.7661 days. The observation shows that the flux decreases from its maximum value (51529 counts  $\text{s}^{-1}$ ) to about one-half of its maximum value (27370 counts  $\text{s}^{-1}$ ) in an interval of about 1 minute. Since the best cadence time for gathering *K2* data is also about 1 minute, I estimate that a more accurate value of  $t_{1/2}$  could be around 2 minutes for this superflare. The ED of this flare is 11.4 hours and its total (UV/visible/IR) energy is  $3.6 \times 10^{33}$  erg. The total flare duration is 4.2 hours.

Using the above fitted parameters and solving for the value of  $\Delta t = t - t_f$  at which impulsive decay switches to gradual decay, we get  $\Delta t = 7.83t_{1/2}$  after the peak flare which occurs at  $\Delta t = 0$ . Now using this time reference, I found that the rise phase contains 22.15%, the impulsive decay phase 38.70% and the gradual decay phase 39.15% of the total energy.

## 2.6.2 Photometry of a superflare observed on M7 dwarf 2MASS J08352366+1029318

Next superflare was observed on the M7 dwarf 2M0835+1029 at *Kepler* time 2379.88288303, when the flare flux is 53213 counts  $\text{s}^{-1}$  ( $\tilde{K}_p = 13.26$ ,  $\Delta\tilde{K}_p = -4.29$ ): this peak flux is  $\sim 60$  times larger than the photospheric level (891 counts  $\text{s}^{-1}$ ). For this flare

---

<sup>4</sup> This curve is based on medians of parameters of at least 1.5 million samples generated by using Markov Chain Monte Carlo sampling of the posterior function using emcee (Foreman-Mackey et al. [2013] with uniform priors). All the flare fits presented in this paper are fitted using this method. For better results, I ensured that the mean acceptance fraction of the sample ensemble to be between 0.25 and 0.5 as mentioned in emcee documentation.

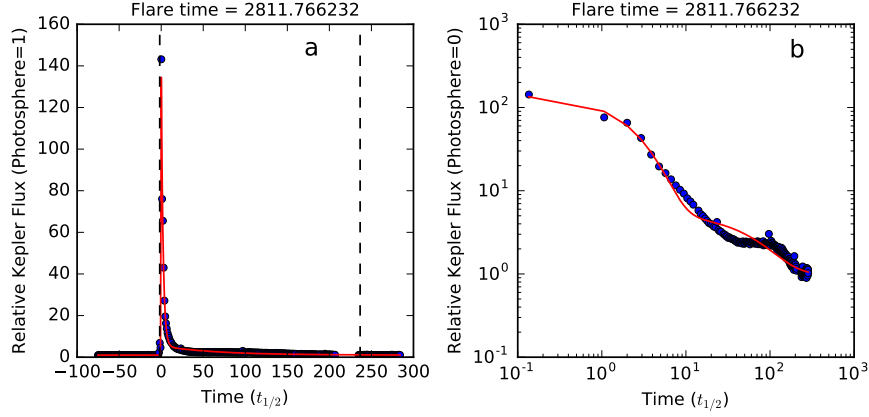


**Figure 2.26:** (a) Superflare observed on 2M1232-0951. The blue dots represent the observed flux and the red curve represents the fitted flux using slightly different parameters in the D14 model. The time is zero centered at peak flare time and scaled by  $t_{1/2}$ . The vertical dashed lines represent the flare start and end times. (b) This plot is a log-log version of plot shown in (a).

also, I found the original parameters of the D14 model do not fit the data particularly well. I consider that I need to make slight changes to the D14 values. I used a fitting procedure similar to that used for the 2M1232-0951 superflare discussed in Section 2.6.1. I found the following values for the fitted parameters of the M7 superflare:  $\alpha_i = 0.8182$ ,  $\alpha_g = 0.1818$ ,  $\gamma_i = 0.6204$  and  $\gamma_g = 0.08467$ . Likewise, I found the other fitted parameters are  $A = 58480$ ,  $t_{1/2} = 1.73$  minutes and time of flare = 2379.8825 days. Both the observed flux and the fitted model for this superflare are shown in Figure 2.27(a). This figure and its corresponding log-log version Figure 2.27(b) show that there is better agreement between the observed flare curve and the fitted model than in the previous case of the superflare observed on the L0 dwarf 2M1232-0951. The ED of this flare is 7.7 hours and its total energy (UV/optical/infrared) is  $6.1 \times 10^{33}$  erg. The total flare duration is 4.5 hours.

In this superflare, I found that the value of  $\Delta t = t - t_f$  at which transition between impulsive decay and gradual decay takes place is  $\Delta t = 2.81t_{1/2}$  after the peak flare ( $\Delta t$

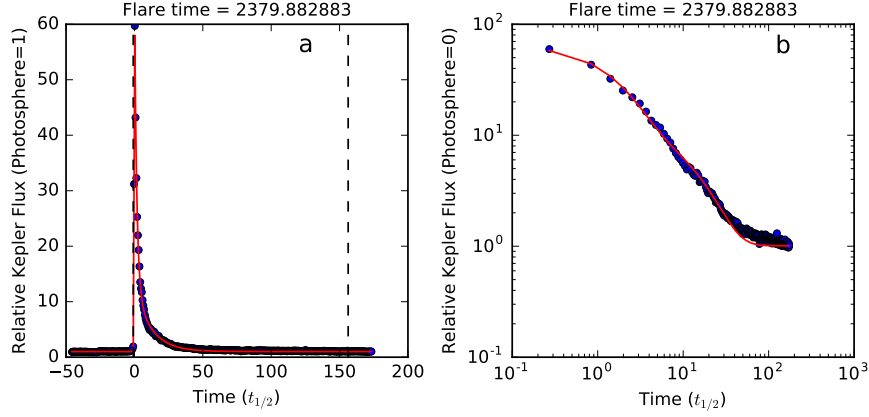


**Figure 2.27:** (a) Superflare observed on 2M0835+1029. The blue dots represent the observed flux and the red curve represents the fitted flux using slightly different parameters in D14 model. The vertical dashed lines represent the start and stop times of flare. The time is zero centered at peak flare time and scaled by  $t_{1/2}$ . (b) This plot is log-log version of plot shown in (a).

= 0). Now using this time reference, we found that the rise phase contains 19.57%, the impulsive decay phase contains 25.86% and the gradual decay phase 54.58% of the total flare energy.

## 2.7 Discussion and conclusions

I analyzed the WL flare rates of 42 mid to late-M dwarfs and L dwarfs. Among the 42 targets, 3 were independently studied by [Gizis et al. \[2013\]](#) and [Gizis et al. \[2017a\]](#): these are W1906+40, 2M03350+2342 and 20355+1133. Since they are also important targets for flare analysis, I have included them in my sample. Except for W1906+40 which was observed by the primary *Kepler* mission, all the remaining targets were observed during various *K2* campaigns in short cadence mode. Among the 42 targets, flares were detected on 22 only, meaning  $\sim 50\%$  of the targets produced flares which were detected by *K2*.

A total of 1105 flares were identified on all flaring 22 targets. The flares have total estimated energies in a range of  $\log E$  (erg)  $\sim$ (29.5 - 34). The presence of noise in the data makes it difficult to detect the weakest flares in UCDs. Due to this, the minimum detectable flare energy is  $>10^{29}$  erg on the targets. This minimum is related to the sensitivity of the *K2* instrument in detecting small flares which have very small amplitudes: these become buried within the noise level of the light curves. The flare energies are estimated for UV/optical/IR wavelengths. The highest energy flare was observed on the M5 dwarf GJ 3631 and had an estimated total energy of  $\log E$  (erg) = 34.3. More flares were observed on mid-M dwarfs than on late-M and L dwarfs. Likewise, most of the high energy flares were also observed in mid-M dwarfs which can be seen in Figure 2.12. For example, 2 M5 dwarfs have 94 flares with energies  $\log E$  (erg)  $>$  32 and 4 M6 dwarfs have 24 flares with energies  $\log E$  (erg)  $>$  32 during a total observation time of 155 and 288 days respectively. Furthermore, the average number of flares observed per hour is higher in the case of M5 and M6 dwarfs in comparison to the late-M dwarfs. Since there is only one flaring M9 dwarf in the sample, the higher average number of flares for spectral type M9 as seen in Figure 2.13 should not be over-interpreted.

The flare frequencies follow power law distributions in energy with slopes  $-\alpha$  lying in the range from -1.3 to -2.0. The values of these slopes were determined by using a maximum-likelihood method of fitting a straight line, as implemented in “emcee” software. I also estimated the values of slopes using an analytical method. The late-M dwarfs in the sample have FFD which are comparable to those in active mid and late-M dwarfs studied by Hilton [2011]. Compared to Hilton [2011], the flares observed by *Kepler* have higher energy and are less frequent. Yet, we find similar slopes ( $-\alpha$ ).

I also analyzed flares on TRAPPIST-1 using the official *K2* pipeline reduced data. I identified 39 good flares on it with total (UV/optical/IR) flare energies in the range from  $6.3 \times 10^{29}$  to  $7.0 \times 10^{32}$  erg. I find that its FFD has a slope of  $-\alpha = -1.6$ .

Previously, [Vida et al. \[2017\]](#) published the FFD of TRAPPIST-1 using raw data and estimated a similar value of the slope but in a slightly different energy range  $1.3 \times 10^{30}$  -  $1.2 \times 10^{33}$  erg. In comparison to other M8 dwarfs in the sample, TRAPPIST-1 has a steeper slope than that of the M8.5 dwarf: 2M0326+1919 ( $-\alpha = -1.5$ ). But it has a shallower slope than the remaining M8 dwarfs in the sample. However, two M8 dwarfs 2M1330-0453 and 2M2353-0833 have flares with energies in a very narrow range,  $\sim 1$  order of magnitude, and the energies used for fitting have ranges less than an order of magnitude. So it is meaningful to compare the slope of TRAPPIST-1 with the remaining M8 dwarf 2M1221-0843 only, which has a steeper slope ( $-\alpha = -1.7$ ) in a slightly different energy range.

The slopes of mid and late-M dwarfs lie in between -1.5 & -2.0. We should note that the slopes also depend on the range of energy chosen for fitting. It can be seen from [Table 2.12](#) that the flare energies of all M dwarfs, used for fitting, do not span same range. Some M dwarfs have fitted flare energies that span  $<1$  order of magnitude and one of them viz. GJ 3631 has fitted flare energies that span  $\sim 3$  orders of magnitude. Likewise, the slopes of L dwarfs lie in between -1.3 & -2.0. Only two L dwarfs (2M1232-0951 and W1906+40) have fitted flare energies which span a range of  $>1$  order of magnitude.

### 2.7.1 Variation of the power-law slope $\beta$ according to spectral type

Since the range of flare energies used for fitting varies from  $<1$  to  $\sim 3$  orders of magnitude for different targets, it will be less meaningful to compare the slopes of FFDs of all the targets in the sample when we study the variation of slopes  $\beta$  ( $= \alpha - 1$ ) in each spectral type. So in the present discussion, I consider only those targets whose fitted flare energies span a range  $>1$  order of magnitude. There are 17 such targets in the sample. The five targets which cannot be considered are: 2M0825+2021 (M7), 2M1330-0453 (M8), 2M2353-0833 (M8.5), 2M1221+0257 (L0) and 2M1048+0111 (L1).

**Table 2.13: Average values of  $\beta$  and  $\alpha_o$** 

<b>Spectral Type</b>	$\beta$	$\alpha_o$
M4	1.0	0.68
M5	0.83	-0.04
M6	0.88	-0.66
M7	0.63	-1.3
M8	0.60	-1.4
L0+L1	0.44	-1.9

Furthermore, in order to study how the values of  $\beta$  and hence flare rates change in each spectral type, it would be more meaningful if we knew the ages of targets and could classify them according to their ages and spectral types. But we do not have age information for the targets. So I computed the average values of  $\beta$  and  $\alpha_o$  for each spectral type simply by taking the mean of  $\beta$  and  $\alpha_o$  values of all the targets for a given spectral type. In this way, the average flare rates are computed by mixing both active and less active targets of similar spectral types. The average values of  $\beta$  and  $\alpha_o$  are tabulated in Table 2.13. Since the number of targets in each spectral type is very small, the corresponding errors in average values of  $\beta$  and  $\alpha_o$  are not computed. While computing the mean values of  $\beta$  and  $\alpha_o$ , the total observation time of the flaring objects having same spectral type is considered.

Using the average values of  $\beta$  and  $\alpha_o$  in Table 2.13, I compare the average flare rates of targets with spectral types varying from M4 to L0+L1 in Figure 2.28. For the L0+L1 category, I used the average flare rate of 2M1232-0951 (L0) and W1906+40 (L1). For comparison with previous works, I compare the flare rates of the M4 dwarf GJ 1243 taken from Hawley et al. [2014] who also report the slope of FFD using energies of flares observed by the *Kepler* mission. We can see that the flare rates of GJ 1243 are higher than those of late-M dwarfs and early L dwarfs by about two (or more)

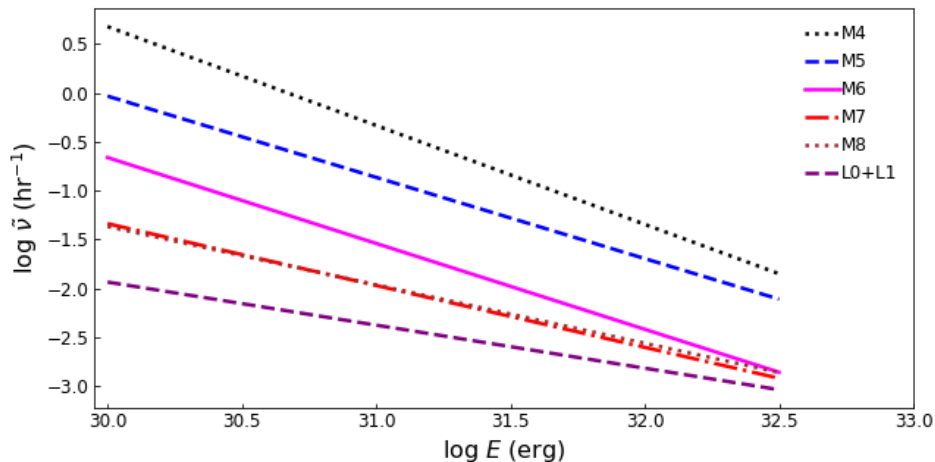


**Figure 2.28:** Comparison of average flare rates of each spectral type in our sample. The flare rates of GJ 1243 (M4) are taken from [Hawley et al. \[2014\]](#). There is only one flaring M9 dwarf, so the flare rate of this spectral type is not plotted in this figure.

orders of magnitude for flares with energy  $10^{30}$  erg. As the energy of a flare is determined by the product of the energy density ( $\Delta B^2/8\pi$ ) and the volume associated with the flare, the reasons for these systematic differences must be related to a combination of flare volumes, flare field strengths and the rate of field line stressing.

### 2.7.2 Effect of $H\alpha$ luminosity on flare rates

Here I analyze the effect of  $H\alpha$  luminosity on the flare rates of flaring targets, as  $H\alpha$  emission is one of the important indicators of magnetic activity in the chromosphere. We do not have information about  $H\alpha$  luminosity of all the targets in the sample. Furthermore, the number of flares observed on them is unequal. To minimize the bias, I chose a sample of targets on which  $\geq 20$  flares are observed and for which we have information about their bolometric as well as  $H\alpha$  luminosity. There are 10 such targets. In [Figure 2.29](#), I compare the fitted FFDs of those targets. From this plot we can see that the flare rates of the most active flaring object (GJ 3631; M5 dwarf) are  $\sim 1.5$  orders of magnitude greater than that of the object with the smallest flare

rate (W1906+40; L1 dwarf) for flares with energies of  $\log E$  (erg) = 31.5. At first glance, we might think that this is related to the higher effective temperatures in M5 dwarfs than L1 dwarfs (by  $\sim 1000$  K). This might indicate that the stars with higher bolometric luminosities might have higher flare rates. To examine this, I normalized the flare energies by the corresponding bolometric luminosities of the objects and compared the flare rates of same 10 targets in Figure 2.30. In this figure, we can see that the flare rates of objects with the highest and the lowest flare rates differ by  $\sim 1$  order of magnitude. The patterns of the FFDs in Figures 2.29 and 2.30 are not significantly different apart from some “tightening up” of the separation between individual FFDs. As in Figure 2.28, the faintest stars have the smallest flare rates.

In Figure 2.31, I compare the flare rates of the 10 objects by normalizing the flare energies by the corresponding  $H\alpha$  luminosities of the objects. Now we can see a significant change in the flare rates. In this case the flare rates of the highest and least flaring object differ by  $\sim 0.5$  order of magnitude. There is one outlier in the plot. It is M7 dwarf 2M0335+2342 which is a young,  $\sim 24$  Myr old object and is a member of  $\beta$  Pic moving group. It is overluminous with bolometric luminosity ( $\log L_{\text{bol}}/L_{\odot} = -2.55$ , Gizis et al. 2017a).

The flare rates could be even closer if we were to take into account the errors associated with the flare energies, which might be greater in the case of faint targets whose light curves have a low signal to noise ratio. If we consider only the brightest flaring targets in the sample whose median (photospheric) count rates are greater than 15,000 counts  $\text{s}^{-1}$  and compare the flare rates by normalizing the flare energies by the corresponding  $H\alpha$  luminosities, we find that the flare rates are almost similar. This can be seen in Figure 2.32. Now we see a significant “tightening up” of the FFDs: it seems that the  $H\alpha$  emission from the star brings order to the flare energies and rates. It should be noted that the  $H\alpha$  luminosity of the flaring targets were measured in different times than when those targets were observed by the *K2* mission. Since  $H\alpha$

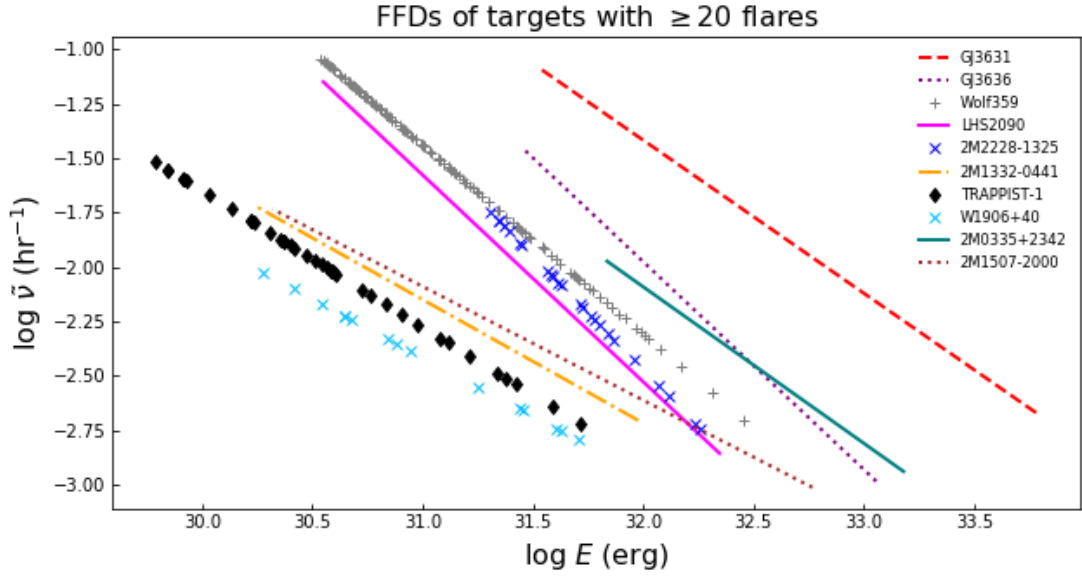


**Figure 2.29:** The FFDs of 10 targets on which  $\geq 20$  flares were observed and for which we have information of both  $H\alpha$  and bolometric luminosity.

emission level may change with time, the effect of  $H\alpha$  luminosity on the flare rates can be studied more accurately if we can take the contemporaneous measurement of  $H\alpha$  emission when the flares are observed.

### 2.7.3 Comparison of flare rates of L dwarfs with earlier spectral types

Figure 2.28 shows that the FFDs in cool stars tend to have shallower slopes than the warmer M dwarfs. This suggests that they have lower flare rates for small energy flares but this is not the case when we examine the rates of high energy flares. For example, the FFD of L0 dwarf 2M1232-0951 has a very shallow slope ( $-\alpha = -1.3$ ) compared to other objects in the sample. The fitted line covers three orders in magnitude. A shallower slope signifies that the occurrence rate of bigger flares is relatively higher in this target than in other targets in our sample. The FFD of another L dwarf W1906+40 as obtained by Gizis et al. [2013] also suggests that L dwarfs have shallower slopes. Figure 2.24 compares the FFD of 2M1232-0951 with that of the young

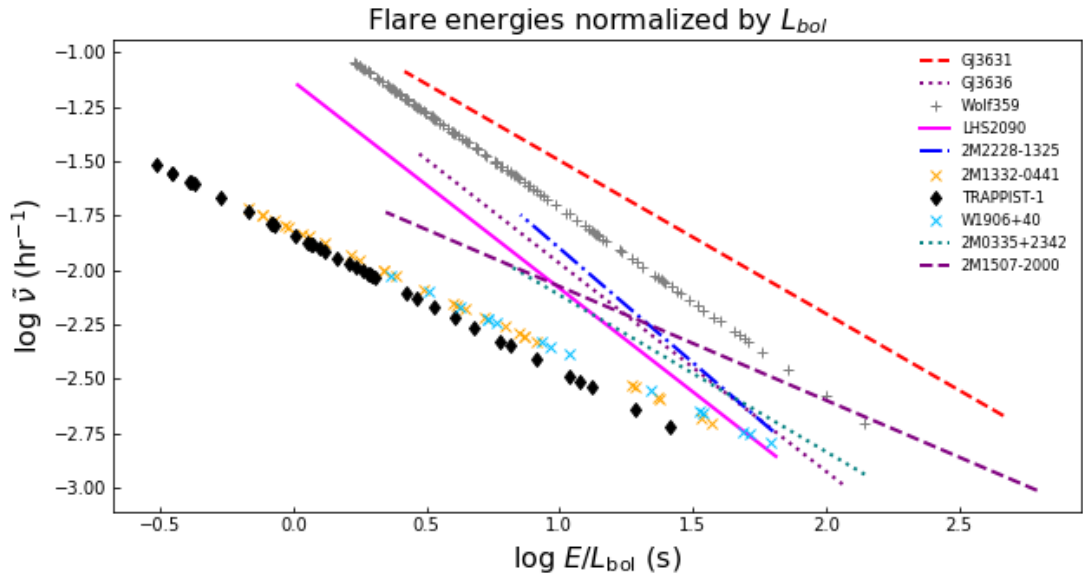


**Figure 2.30:** The flare rates of same targets used in Figure 2.29, with the flare energies normalized by the corresponding bolometric luminosities of the targets.

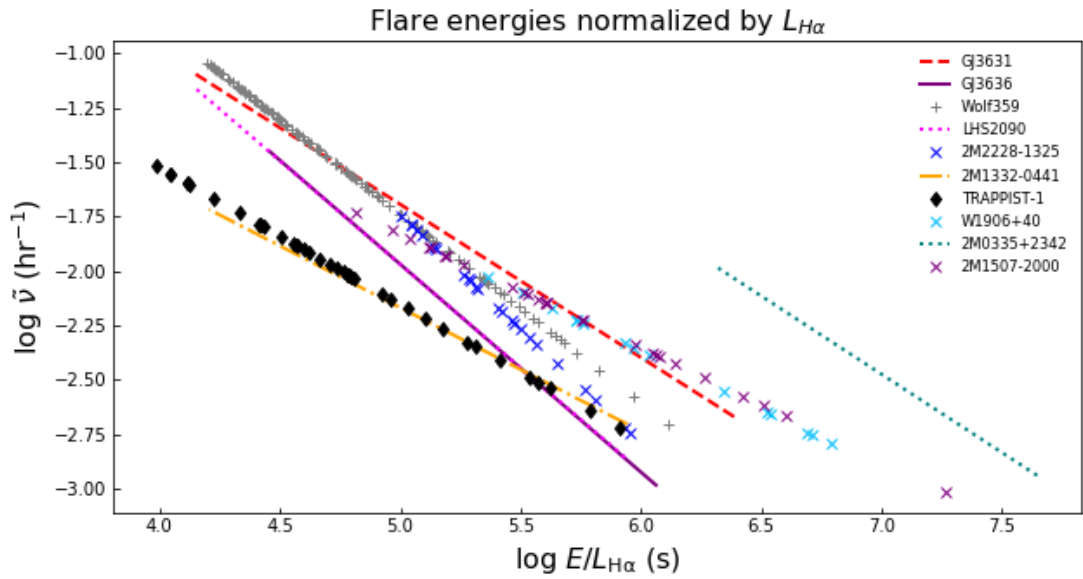


**Figure 2.31:** The flare rates of same targets used in Figure 2.29, with the flare energies normalized by the corresponding H $\alpha$  luminosities of the targets.

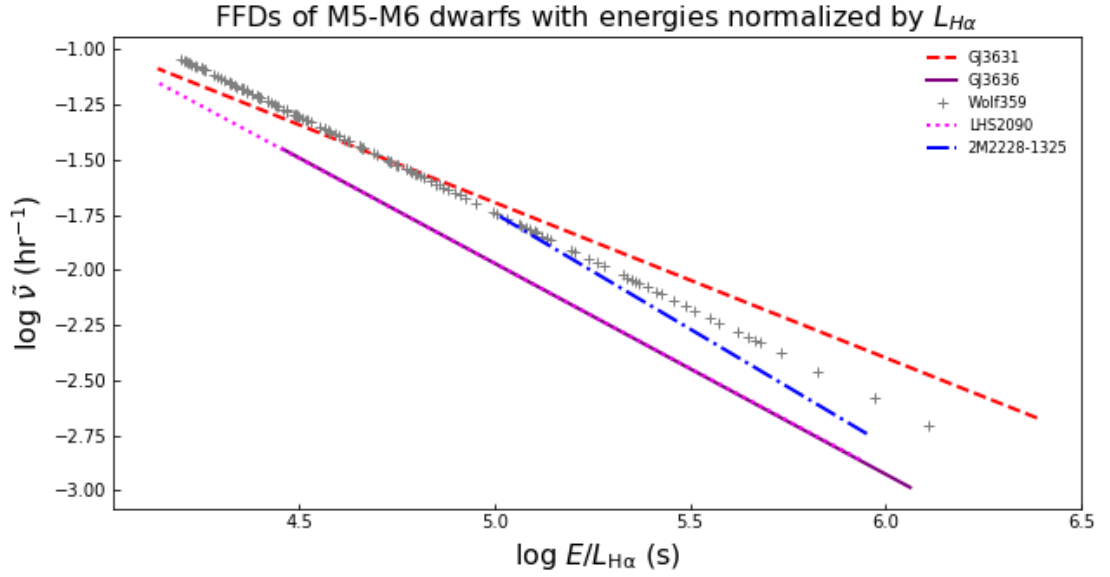


**Figure 2.32:** The flare rates of targets with ST of M5 and M6, with the flare energies normalized by the corresponding  $H\alpha$  luminosities of the targets.

BD 2M0335+2342 (M7). The convergence of two fitted lines at observed high flare energies suggests that both targets have comparable flare rate for such energies. But for low flare energy such as  $\log E \sim 30.5$  erg, the L0 dwarf has a lower flare rate. The convergence of lines is also clearly seen in Figure 2.28 in case of spectral types  $\geq M6$ , which again indicates comparable flare rates for observed higher flare energies. An even more interesting fact about 2M1232-0951 is that its largest flare has an energy comparable to the highest flare energy observed in M5, M6 and M7 dwarfs. This raises a question: do stars with later spectral types have better efficiency in converting magnetic energy to higher energy flares than those with low energies? We have to understand the relationship between the magnetic field, volume and rate at which the magnetic field lines are stretched to store energy. The stretching of magnetic field lines probably depends on the speed of convective flows.

The steeper slopes:  $-\alpha = -2.0$  and  $-\alpha = -1.7$ , which we have obtained in the case

of other two L dwarfs: 2M1221+0257 and 2M1048+0111 are valid for a very narrow energy ranges:  $\log E$  (erg)  $\sim 30.1 - 30.8$  and  $\log E$  (erg)  $\sim 30.1 - 31.0$ . There is one high energy flare on 2M1221+0257 but its energy was not included for fitting purpose. It will be inappropriate to compare the flare rates of these two L dwarfs with the remaining two based on the slopes obtained here as the energy ranges considered for obtaining the slopes are very different.

The fraction of L0 and L1 dwarfs having chromospheric H $\alpha$  emission is  $\sim 90\%$  and  $\sim 67\%$ , respectively, with a decline in H $\alpha$  activity in comparison to earlier spectral types [Schmidt et al., 2015]. One suggestion to explain this behaviour is that the lower effective temperatures and hence less ionization reduce the effectiveness of the interaction between the magnetic field and gas in the photosphere [Mohanty et al., 2002]. In addition, the L0-L1 dwarfs do not have clearly developed rotation-activity connections despite being rapid rotators [Reiners and Basri, 2008]. We do not have proper information about the rotation periods, or ages, or activity levels for the two L dwarfs 2M1232-0951 and 2M1221+0257. But what we know is that 2M1232-0951 has a longer time-scale variability [Koen, 2013], and 2M1221+0257 has a variable H $\alpha$  emission with equivalent width 25.65 Å and  $\log L_{\text{H}\alpha}/L_{\text{bol}} = -4.18$  [Reiners and Basri, 2008]. This limited information is not enough to interpret the observed results of L dwarfs.

#### 2.7.4 Energies and timescales associated with two superflares of largest amplitudes observed on two UCDs

We observed superflares on two targets: 2M1232-0951 and 2M0835+1029, with large amplitudes and long EDs. Those flares have total (UV/optical/IR) energies  $3.6 \times 10^{33}$  erg and  $6.1 \times 10^{33}$  erg. They have very short FWHM time scales of  $\sim 2$  minutes. In the case of 2M1232-0951, the superflare brightened by a factor of  $\sim 144$  relative to the quiescent photospheric level. Likewise, the superflare observed on 2M0835+1029 brightened by a factor of  $\sim 60$  relative to the quiescent photospheric level.

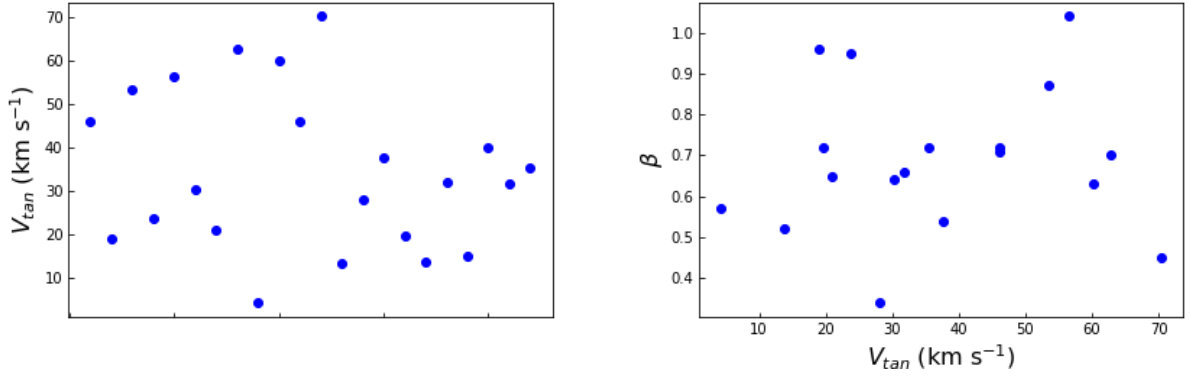


**Figure 2.33:** **Left:** Tangential velocity distribution of flaring targets. Since no physical quantity is plotted along the  $X$ -axis, spread of the velocities in horizontal direction has no meaning at all. **Right:** Plot showing the relation between tangential velocities and slopes of FFDs ( $\beta$ ) of the flaring targets whose fitted flare energies span a range  $>1$  order of magnitude.

### 2.7.5 Variation of power-law index $\beta$ as a function of kinematic age

**Table 2.14:** Average slopes of FFDs of targets classified by kinematic age

Target type	Average $V_{\text{tan}}$ ( $\text{km s}^{-1}$ )	Average $\beta$
old	57	$0.73 \pm 0.17$
young	29	$0.63 \pm 0.18$
very young	14	$0.69 \pm 0.17$

The left plot of Figure 2.33 shows the tangential velocity distribution of flaring targets. The tangential velocities of flaring targets are in the range: (4 - 70)  $\text{km s}^{-1}$ . This implies that if we make use of the tangential velocity estimates as age indicators, our flaring targets have different kinematic ages. Based on the values of tangential velocities of the flaring targets, I classify the flaring targets in three different categories: very young ( $V_{\text{tan}} = 0\text{-}20 \text{ km s}^{-1}$ ), young ( $V_{\text{tan}} = 21\text{-}40 \text{ km s}^{-1}$ ) and old ( $V_{\text{tan}} > 40 \text{ km s}^{-1}$ ) targets. TRAPPIST-1, 2M0326+1919 and 2M2214-1319 seem to be the oldest targets and 2M1332-0441 seems to be the youngest one. In support of our claim of

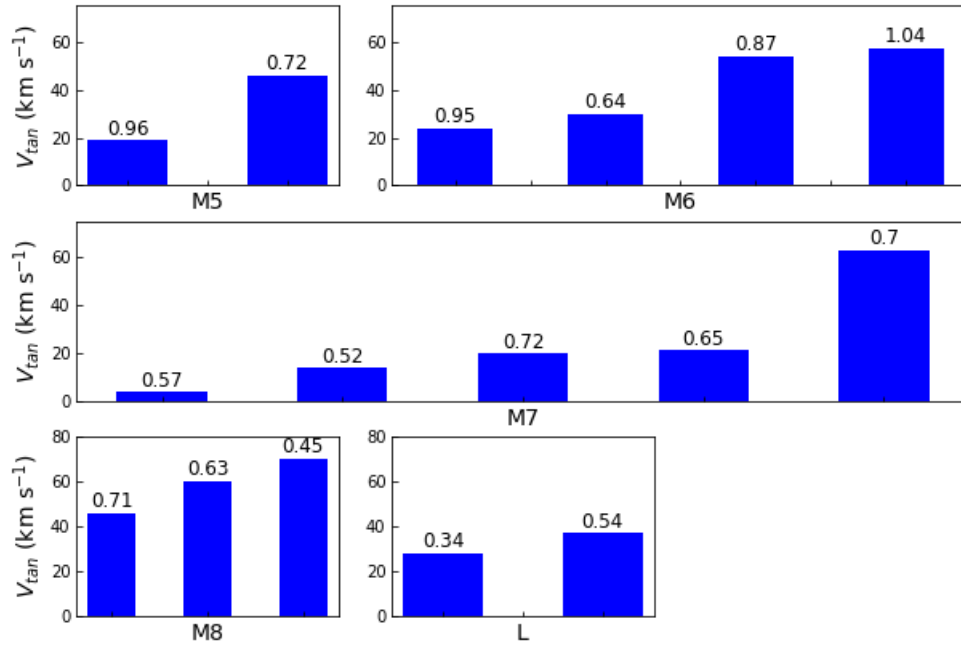


**Figure 2.34:** Plot showing the variation of slopes of FFDS ( $\beta$ ) and the tangential velocity for each flaring target. In each panel, the tangential velocity is plotted along Y-axis and the values of  $\beta$  are indicated above each blue bar. To make it easy for comparison, the  $\beta$  values of objects are given in the increasing order of tangential velocities.

a great age for TRAPPIST-1, we may cite [Burgasser and Mamajek \[2017\]](#) who have reported an age of  $7.6 \pm 2.2$  Gyr. The right plot in [Figure 2.33](#) shows the variation of slopes of FFD ( $\beta$ ) as a function of tangential velocities of flaring targets. We can see that there is no systematic relation between the values of  $\beta$  and the tangential velocities.

In [Figure 2.34](#), I compare the slopes of FFDs of targets with the same spectral types but of various kinematic ages. I again consider only 17 targets mentioned above for the analysis in this part. The target with ST of M9 is not included in [Figure 2.34](#). In the case of spectral type M5, the FFD of the older target (GJ 3631) has a shallower slope. In the case of spectral type M6, the FFDs of the youngest target (LHS 2090) and oldest target (LHS 523) have comparable slopes. If we consider the errors in  $\beta$  values, the slopes are not significantly different from each other for all 4 objects. In the case of ST of M7, the FFD of 2M1332-0441 has a shallower slope than other targets of similar spectral type, has the lowest tangential velocity, and is therefore presumably the youngest. Another young target (2M1507-2000) has also a shallower slope in comparison to the older targets with ST of M7. But the slopes are comparable ( $\sim 0.60$ ) within an error bar of  $1\sigma$  if we take into account the associated errors.

In the case of M8 dwarfs, despite having comparable ages, the FFD of TRAPPIST-1 has a slightly steeper slope than 2M0326+1919 : moreover, TRAPPIST-1 has a higher occurrence rate of low energy flares than the same M8.5 dwarf. The FFD of the youngest target 2M1221-0843 has the steepest slope in comparison to the older targets of the same spectral type. Likewise, the L1 dwarf W1906+40 has a steeper slope than 2M1232-0951 despite having comparable kinematic ages and spectral type. Like in the analysis above, we should note that the values of  $\beta$  do not differ significantly if we consider the associated errors in the case of both M8 and L0/L1 spectral types.

In [Table 2.14](#), I list the average values of  $\beta$  computed for three categories of targets:

very young, young and old targets. The targets were classified only on the basis of kinematic ages, regardless of their spectral types. We see no significant differences in the average values of  $\beta$  for targets of various kinematic ages if we consider the associated errors. The average value of  $\beta$  for targets of all ages in Table 2.14 is  $0.69 \pm 0.18$ . We regard this is an interesting result because this value also agrees with the predictions of one particular model of flares [Mullan and Paudel, 2018]. Furthermore, this value is also close to the results of Kasinsky and Sotnicova [2003] who analyzed  $\sim 57,000$  solar flares using X-ray data obtained by the Geostationary Operational Environmental Satellite (*GOES*) satellite from 1972 to 2001. This observation time included three solar cycles. Kasinsky and Sotnicova [2003] found that the mean value of  $\beta$  was  $0.666 \pm 0.005$  and that the value of  $\beta$  varied between 0.50 (near solar minimum in 1974) and 0.80 (near solar maximum in 2000). Davenport et al. [2019] used *Kepler* light curves to study a sample of 347 flaring stars with known rotation periods and found that the value of  $\beta$  remains almost constant with age of stars. The ages were inferred by using gyrochronology. Hence the conclusion of age-independence of the FFD slopes in the sample of (sub)stellar objects in this work extends the conclusions obtained by Davenport et al. [2019] to sub-stellar masses. The results of Kasinsky and Sotnicova [2003]; Davenport et al. [2019] and this project strongly suggest a universal value of  $\beta$  and hence the universal nature of the physical phenomenon that produces flares in (sub)stellar objects of various masses and ages.

### 2.7.6 Do FFDs always follow a single power law distribution?

The FFDs of two of the targets seem to show deviations from a single power law dependence. Using the likelihood ratio test, we found that the FFD of one target (2M2228-1325) seems to follow a broken power law distribution while the FFD of another target (2M0326+1919) seems to follow a power law distribution with an exponential cutoff. Unfortunately, since the number of flares observed on both targets is small, we cannot conclude if such deviations of FFDs from regular power laws are due to instrumental sensitivity or due to saturation at large energies. Gershberg [2005] (p.

227) mentions that the curvatures seen in FFD of some targets were absent when they were observed again, and the number of observed flares was increased. Curved FFDs can be seen in case of EQ Peg, UV Cet and AD Leo in Figure 38 (p. 224) of [Gershberg \[2005\]](#). Other examples of departures of FFD from single power-laws are provided by GJ 1243 and GJ 1245 AB [[Hawley et al., 2014](#)], and by KIC 11551430 [[Davenport, 2016](#)].

## Chapter 3

### WHITE LIGHT FLARES OBSERVED ON M6-M9 DWARFS USING *K2* LONG CADENCE DATA

In this chapter, I present the results of white light flares on objects with spectral type: M6, M7, M8 and M9, which were observed by *K2* in various campaigns in long cadence ( $\sim 30$  min) mode. I analyzed light curves of 314 objects, among which 40 objects are M6 dwarfs, 188 are M7 dwarfs, 60 are M8 dwarfs and 26 are M9 dwarfs. The information of all the targets is given in Appendix B in four different tables, one for each spectral types: M6, M7, M8 and M9. Each table contains information regarding the EPIC ID, 2MASS names, Pan-STARRS (PS1) photometry, absolute magnitude ( $M_i$ ) and *Gaia* parallax of almost all the objects with a given spectral type. If PS1 and/or *Gaia* measurements are not available for a given object, the corresponding photometry and parallax is taken from literature and is mentioned in the bottom of each table. Some of the targets studied in this chapter were also studied in Chapter 2. As it was not possible to obtain the short cadence data of many targets, we had few targets in our sample in Chapter 2. However, we have a bigger sample of targets with long cadence data, whose flare properties will be studied in this chapter.

#### 3.1 Data reduction

Because of the similar reason explained in Section 6.3 of Chapter 2, I used the target pixel files (TPFs) of the objects to extract the light curves. The TPFs were obtained from MAST archive. Instead of using aperture photometry, I performed Point Source Function (PSF) photometry to extract the light curves of targets. The PSF photometry is also known as Point Response Function (PRF). Under this method, a parameterized model developed by using the response of the pixels to stars of different

brightness is fitted to the data. Using apertrue photometry (AP) method, we sum all the fluxes within certain pixels to extract the light curves. The AP method performs better for isolated stars and when there is limited telescope motion and very less time-varying background signals. The PSF method is preferred for extracting the light curves of objects which lie in the crowded region of the sky. Furthermore, it is also helpful in overcoming the other limitations of AP method mentioned above [Vinícius et al., 2018]. I used the PSF fitting model incorporated in the Python package ‘Lightkurve’ [Vinícius et al., 2018]. The light curves were then detrended against any systematics like the instrumental noise by using the *K2* Systematics Correction (‘K2SC’, Aigrain et al. 2016).

### 3.2 Flare search and estimation of energies

Using the light curves detrended by using ‘K2SC’, I used the method described in Section 2.3 in Chapter 2 to identify the flares in the light curves of the objects.

The flare energies were estimated by using the method described in Section 2.3.3 in Chapter 2. The energy of a 10,000 K blackbody corresponding to each target for an ED of 1s is given in Tables 3.3, 3.4, 3.5 and 3.6 in the column ‘energy’ for objects with spectral types M6, M7, M8 and M9 respectively. In all such tables, ‘EPIC’ refers to EPIC ID of each object, ‘Cam. #’ refers to the campaign number in which the object was observed and  $T$  is the total observation time of the object in a given campaign.

### 3.3 Results

I identified a total of 245 flares on 314 objects. The total observation time of all the objects is 67.8 years. The information regarding the time in which the flares were observed, the EDs and energies of each flares observed on the objects is given in four separate tables in Appendix C for spectral types of M6, M7, M8 and M9. In the Tables B.1, B.2, B.3 and B.4 of Appendix C, ‘EPIC’ refers to the EPIC ID of the object,  $T_{\text{peak}}$  refers to the *Kepler* time in which the peak of the flare was observed, ‘ED’ refers to

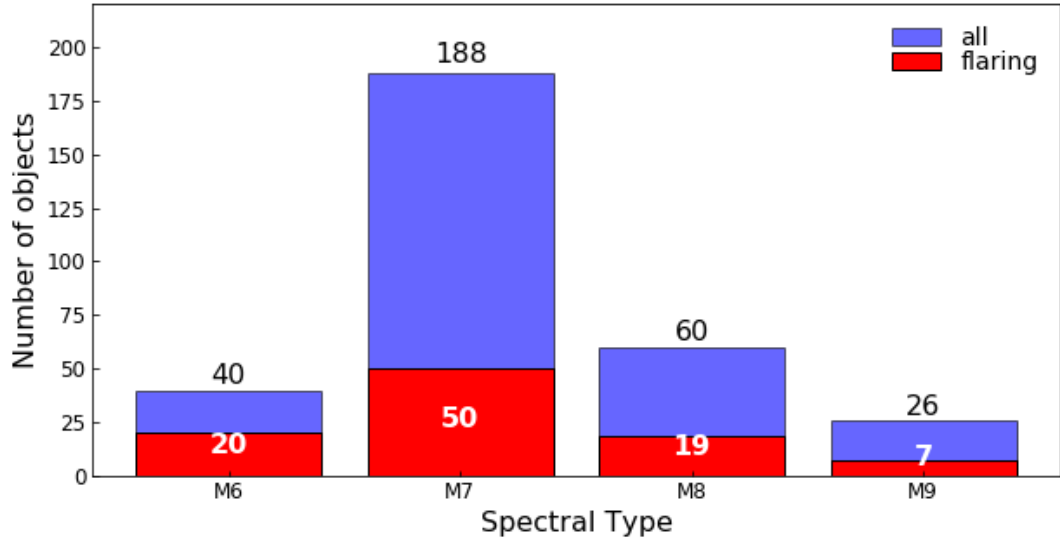


**Figure 3.1:** Bar chart comparing the number of flaring targets with the total number of targets for spectral types: M6 - M9, observed by *K2* in long cadence mode.

equivalent duration of flare and ‘log  $E$ ’ refers to the energy of the flare in log scale.

The overall results are summarized in Table 3.1 and 3.2. In Table 3.1,  $N$  is the total number of objects for a given spectral type. Likewise,  $N_f$  is the total number of objects on which at least one flare was observed, ‘No. of flares’ refers to the total number of flares observed on the objects and  $T$  is the total observation time of all the objects with a given spectral type.

In Table 3.2, I summarize the results of flare energies observed on the objects. For simplicity, I divided the energies in five separate intervals:  $\log E$  (erg) = (31 - 32), (32 - 33), (33 - 34), (34 - 35) and (35 - 36) respectively. The number of flares with energies in a given interval for objects with a given spectral type is presented.

Figure 3.1 is a bar chart showing the total number of objects and the number of flaring objects in each spectral type.

**Table 3.1: Flare statistics of M6 - M9 dwarfs. I.**

Sp. Type	$N$	$N_f$	No. of flares	$T$ (yrs)
M6	40	20	58	9.3
M7	188	50	121	39.3
M8	60	19	49	12.6
M9	26	7	17	6.6
Total	314	96	245	67.8

**Table 3.2: Flare statistics of M6 - M9 dwarfs. II.**

$\log E$ (erg)	Spectral Type			
	M6	M7	M8	M9
31 - 32	0	6	4	1
32 - 33	29	25	17	1
33 - 34	23	59	19	11
34 - 35	6	30	8	4
35 - 36	0	1	1	0
Total	58	121	49	17

**Table 3.3: Obs. time and ED1 of flaring M6 dwarfs**

EPIC	Cam. #	$T$	energy (erg)
206050032	3	70.5	$1.7 \times 10^{30}$
206135809	3	70.5	$7.0 \times 10^{29}$
206296292	3	70.5	$4.0 \times 10^{30}$
206494490	3	70.5	$2.6 \times 10^{30}$
212402103	6,17	147.6	$1.0 \times 10^{30}$
220195996	8	80.3	$3.6 \times 10^{30}$
245995471	12	80.4	$6.6 \times 10^{29}$
246322698	12	80.4	$1.3 \times 10^{30}$
246403896	12	80.4	$3.0 \times 10^{30}$
246404848	12	80.4	$1.7 \times 10^{30}$
247051861	13	82.2	$6.5 \times 10^{31}$
201744267	14	81.3	$1.8 \times 10^{30}$
248456554	14	81.3	$1.6 \times 10^{30}$
248525204	14	81.3	$3.0 \times 10^{30}$
248609711	14	81.3	$6.6 \times 10^{30}$
248624299	14	81.3	$2.9 \times 10^{30}$
248631849	14	81.3	$3.1 \times 10^{30}$
248744078	14	81.25	$1.2 \times 10^{30}$
248750733	14	81.3	$1.6 \times 10^{30}$
248751905	14	81.3	$3.0 \times 10^{30}$

Table 3.4: **Obs. time and ED1 of flaring M7 dwarfs**

EPIC	Cam. #	$T$ (day)	energy (erg)
206053352	3	70.5	$4.9 \times 10^{29}$
206181579	3	70.5	$9.9 \times 10^{29}$
206213997	3	70.5	$3.40 \times 10^{29}$
212826600	6,17	147.6	$3.0 \times 10^{29}$
201425001	10	56.2	$1.0 \times 10^{30}$
246015548	12	80.4	$4.1 \times 10^{30}$
246034587	12	80.4	$2.6 \times 10^{30}$
246393886	12	80.4	$4.37 \times 10^{30}$
246395512	12	80.4	$3.0 \times 10^{30}$
246401499	12	80.4	$6.5 \times 10^{29}$
246468225	12	80.4	$9.8 \times 10^{29}$
248029954	13	82.2	$4.9 \times 10^{30}$
201581268	14	81.3	$9.6 \times 10^{30}$
248452093	14	81.3	$7.2 \times 10^{29}$
248565564	14	81.3	$1.9 \times 10^{30}$
248580531	14	81.3	$7.5 \times 10^{29}$
248659481	14	81.3	$2.9 \times 10^{30}$
248682489	14	81.3	$5.2 \times 10^{29}$
248718280	14	81.3	$7.1 \times 10^{29}$
248755514	14	81.3	$1.7 \times 10^{30}$
249639465	16	81.1	$8.1 \times 10^{29}$
211411366	16	81.1	$5.8 \times 10^{30}$
211478560	16	81.1	$2.7 \times 10^{30}$
211742071	16	81.1	$3.2 \times 10^{30}$
211758584	16	81.1	$1.4 \times 10^{30}$
211770368	16	81.1	$4.7 \times 10^{30}$
211892842	16	81.1	$4.0 \times 10^{30}$
211917847	16	81.1	$3.2 \times 10^{30}$
211947924	16	81.1	$3.0 \times 10^{30}$
211964067	16	81.1	$1.7 \times 10^{30}$
212019105	16,18	132.0	$2.2 \times 10^{30}$
212075399	16	81.1	$1.2 \times 10^{30}$
212156288	16,18	132.0	$2.8 \times 10^{30}$
251314012	16	81.1	$1.8 \times 10^{30}$
251317744	16	81.1	$4.4 \times 10^{30}$
251358654	16	81.1	$7.3 \times 10^{30}$
251365679	16	81.1	$1.1 \times 10^{30}$
251394863	16	81.1	$8.4 \times 10^{30}$

Continued on next page

**Table 3.4 – continued from previous page**

EPIC	Cam. #	$T$ (day)	energy (erg)
251558388	17	67.1	$1.3 \times 10^{30}$
211910449	18	50.8	$1.8 \times 10^{30}$
212006725	18	50.8	$3.3 \times 10^{30}$
212027121	18	50.8	$2.6 \times 10^{30}$
212071306	18	50.8	$3.6 \times 10^{30}$
212080305	18	50.8	$2.8 \times 10^{30}$
212091105	18	50.8	$1.5 \times 10^{30}$
212106472	18	50.8	$2.5 \times 10^{30}$
212108940	18	50.8	$1.6 \times 10^{30}$
212123277	18	50.8	$2.6 \times 10^{30}$
212170953	18	50.8	$2.7 \times 10^{30}$
212176032	18	50.8	$1.6 \times 10^{30}$

**Table 3.5: Obs. time and ED1 of flaring M8 dwarfs**

EPIC	Cam. #	$T$ (day)	energy (erg)
210764183	4	72.3	$2.4 \times 10^{29}$
211046195	4	72.3	$2.8 \times 10^{30}$
220170497	8	80.3	$4.9 \times 10^{29}$
228754562	10	56.2	$7.7 \times 10^{29}$
246013537	12	80.4	$7.5 \times 10^{29}$
248044306	13	82.2	$5.3 \times 10^{29}$
201580841	14	81.3	$7.1 \times 10^{29}$
201800829	14	81.3	$6.0 \times 10^{29}$
248413181	14	81.3	$5.0 \times 10^{29}$
248445614	14	81.3	$4.2 \times 10^{29}$
248567554	14	81.3	$2.0 \times 10^{29}$
248592301	14	81.3	$5.9 \times 10^{29}$
249472713	16	81.1	$2.2 \times 10^{29}$
211616100	16	81.1	$1.1 \times 10^{30}$
212184948	16	81.1	$4.5 \times 10^{29}$
212820594	17	67.1	$3.0 \times 10^{29}$
211301854	18	50.8	$1.1 \times 10^{30}$
211981759	18	50.8	$3.1 \times 10^{30}$
212035340	5,18	125.6	$2.1 \times 10^{30}$

**Table 3.6: Obs. time and ED1 of flaring M9 dwarfs**

EPIC	Cam #	$T$	energy (erg)
201453319	14	81.3	$4.3 \times 10^{29}$
203912136	2	78.8	$9.8 \times 10^{29}$
210457230	4	72.3	$2.1 \times 10^{29}$
212022056	5,16,18	206.8	$7.3 \times 10^{29}$
212136544	5,18	125.7	$3.4 \times 10^{29}$
246404954	12	80.4	$4.7 \times 10^{29}$
248600681	14	81.3	$3.6 \times 10^{29}$
248691809	14	81.3	$1.6 \times 10^{29}$

## Chapter 4

### A STUDY OF FLARES ON L/T DWARFS USING *K2 LONG* CADENCE DATA

#### 4.1 Introduction

As stated in Chapter 1, L dwarfs are the UCDs with effective temperatures  $\lesssim 2300$  K. Since the lowest mass hydrogen burning stars have spectral types as late as  $\sim L4$ , the early L dwarfs can be either young brown dwarfs or old hydrogen burning low mass stars. The objects with spectral types later than L4 are all brown dwarfs. Because of lower effective temperatures, the L dwarfs have weak chromospheric emission lines, but some have strong radio-emissions. Furthermore, the coronae are usually not detected in these cool objects. The L dwarfs are rapidly rotating objects with periods  $< 10$  hours and they do not follow the solar/stellar magnetic activity relations [Reiners and Basri, 2008; Berger et al., 2010; Williams et al., 2014; Cook et al., 2014]. In this chapter, I report on the studies of L/T dwarfs taking advantage of *K2 long* cadence data.

##### 4.1.1 Previous studies: $H\alpha$ emission

$H\alpha$  emission is one of the important indicators of magnetic activity. It signifies the presence of strong magnetic fields and hence the possibility of flare production. Despite having cool and hence almost neutral atmospheres, the L dwarfs are known to have some level of  $H\alpha$  emission. An extensive study of  $H\alpha$  emission from L dwarfs was done by Schmidt et al. [2015] and Pineda et al. [2016]. Schmidt et al. [2015] studied 551 L dwarfs using the data obtained by SDSS, 2MASS and WISE survey. Among the 551 L dwarfs, 181 had reported  $H\alpha$  emission and upper limits. The authors classified active L dwarfs as those with  $H\alpha$  equivalent width (EW)  $> 0.75 \text{ \AA}$ , and inactive L

dwarfs as those with upper limits (non-detections) of  $H\alpha$  EW  $\leq 0.75 \text{ \AA}$ . They found that  $\sim 90\%$  of L0 dwarfs are active and this fraction decreases to  $\sim 60\%$  in the case of L3 dwarfs. Likewise, the activity fractions for the L4 and L5 dwarfs are 33% and 50% respectively. The L6-L8 dwarfs have either very weak or no activity. Likewise, there is a decline in the chromospheric activity (as measured by  $\log L_{H\alpha}/L_{\text{bol}}$ ) from a value of  $\sim -3.8$  in M0-M4 dwarfs to a value of  $-5.7$  in the case of L3 dwarfs.

[Pineda et al. \[2016\]](#) studied  $H\alpha$  emission from late-L and T dwarfs using optical (6300-9700  $\text{\AA}$ ) spectra obtained by the *Keck* telescopes. They reported a detection rate of  $9.2 \pm_{2.1}^{3.5}\%$  for a sample of 109 L4-T8 dwarfs. In particular, they detected  $H\alpha$  emission in  $9.3 \pm_{2.4}^{4.5}\%$  mid-to-late L dwarfs (L4-L8) in a sample of 75 objects. Likewise, they reported an  $H\alpha$  emission detection rate of  $7.1 \pm_{2.2}^{6.2}\%$  for a sample of 42 T dwarfs. The sample of L and T dwarfs studied by [Pineda et al. \[2016\]](#) might also include binary systems. So the overall detection rate in single stars might be lower than they have reported.

#### 4.1.2 Previous studies: X-ray and radio emission

As mentioned in Chapter 1, the L dwarfs do not follow the activity-rotation relations which occur in stars with spectral types earlier than M6.5 despite being rapid rotators. If they were to follow the same activity-rotation relations, the L dwarfs would have saturated X-ray emission  $L_X/L_{\text{bol}} \approx 10^{-3}$  [[Cook et al., 2014](#)]. However, they show a significant lower level of X-ray emission.

Up to now, there has been no detection of X-rays from L dwarfs except Kelu-1AB which is a binary system of two L dwarfs: Kelu-1A (L2 $\pm$ 1) and Kelu-1B (L3.5 $\pm$ 1) [[Liu and Leggett, 2005](#)]. [Audard et al. \[2007\]](#) reported the detection of X-rays from Kelu-1AB with luminosity of  $2.9_{-1.3}^{+1.8} \times 10^{25} \text{ erg s}^{-1}$ . [Cook et al. \[2014\]](#) compiled the largest catalog of L dwarfs with X-ray measurements: the catalog contains 10 L dwarfs with spectral types in the range L0-L8, with upper limits of X-ray luminosity in the

range  $\log L_X/L_{\text{bol}} < -(5.0 - 3.0)$ . In addition to those L dwarfs, we also studied X-ray emission from a flaring L1 dwarf: WISEP J190648.47+401106.8 using *Chandra* data. No X-ray photons were detected from this L dwarf during an observation period of  $\sim 50$  ks. The upper limit to X-ray luminosity is estimated to be equal to  $1.1 \times 10^{25}$  erg  $\text{s}^{-1}$  at 0.95 confidence level. More details can be found in Chapter 8.

The L dwarfs show a deviation from the Güdel-Benz relation (GBR), i.e.  $L_X$  proportional to  $L_{\nu, \text{R}}$ . Though there is a decline in X-ray emission as we go to later L dwarfs, radio emission does not follow this decline. They are found to be radio-overluminous compared to the GBR prediction. According to the GBR, the ratio of radio luminosity to X-ray luminosity ( $\log L_{\nu, \text{R}}/L_X$ ) is  $\sim -15.5$ . However, the radio observations of some L dwarfs reveal that this ratio is found to be larger than the above value even when they are in quiescent state. This can easily be seen in Figure 6 of [Williams et al. \[2014\]](#). The radio emission also signifies the presence of strong magnetic fields. However, the deviation from Güdel-Benz relation suggests that both X-ray and radio emission might not be linked to same physical process and hence same population of electrons as in the case of F–mid-M stars. The radio emission is assumed to be produced by a different mechanism known as electron cyclotron maser (ECM) in the cooler objects like L and T dwarfs [[Hallinan et al., 2008](#)].

A compilation of the L and T dwarfs with radio emission can be found in [Williams \[2018\]](#). The number of L dwarfs with known radio emission is currently 9, among which 4 are confirmed to have radio emission that varies with periods of  $\lesssim 1$  hr time scales. Likewise, 4 T dwarfs are known to have radio emission; all of them being variable with periods of  $\lesssim 1$  hr time scales. Radio emission has been observed on objects with spectral type as late as T6.5 [[Kao et al., 2016](#)].

### 4.1.3 Flares on L and T dwarfs

L dwarfs have lower flare rates than M dwarfs. As a result it is very difficult to study the WLF rates using ground-based telescopes with limited observation times. For e.g., [Koen \[2013\]](#) and [Ramsay et al. \[2015\]](#) did not detect any flares on the L dwarfs which they monitored using ground-based telescopes. The precise photometry and continuous monitoring of the *K2* mission makes it relatively easy to study the WLF rates of L dwarfs. Using this opportunity, [Gizis et al. \[2013\]](#) were able to detect 21 white light flares on the L1 dwarf WISEP J190648.47+401106.8 (hereafter W1906+40) by monitoring this object for three months in short cadence mode. The flares had (UV/visible/infrared) energies in the range  $\sim(10^{29} - 10^{32})$  erg. W1906+40 is the first L dwarf on which white light flares were observed. Up to now, WLFs have been observed on 6 L dwarfs: W1906+40, SDSS J053341.43 +001434.1 (hereafter S0533+00; L0), SDSSp J005406.55- 003101.8 (L1), 2M1221+0257 (L0), 2M1232-0951 (L0) and ULAS J224940.13-011236.9 (hereafter U22-011; L2.5) [[Gizis et al., 2013](#); [Schmidt et al., 2016](#); [Gizis et al., 2017b](#); [Paudel et al., 2018a](#); [Jackman et al., 2019](#)]. All of these L dwarfs, except S0533+00 and U22-011, were monitored by the *Kepler/K2* mission. Among all the WLFs observed on L dwarfs, the most powerful is the one observed on S0533+00 by the ground-based All Sky Automated Survey for SuperNovae (ASASSN). This flare had a total estimated bolometric energy of  $>6.2 \times 10^{34}$  erg [[Schmidt et al., 2016](#)]. Furthermore, U22-011 is the coolest flaring object detected so far: it has  $T_{\text{eff}} < 2000$  K. It was observed by using the Next Generation Transit Survey (NGTS) and the flare had a total estimated energy of  $3.4 \times 10^{33}$  erg [[Jackman et al., 2019](#)]. No flares have so far been reported on T dwarfs.

The noise level in the *K2* long cadence data is  $>10\%$  for the fainter targets. As a result, flares with small amplitudes ( $\lesssim 1.5$  times the photospheric level) cannot be reliably detected. However, the flares with larger amplitudes ( $\gtrsim 1.5$  times the photospheric level) can be easily detected even if the object is very faint and has very low photospheric emission. One such large flare with total (UV/visible/infrared) energy  $\sim 10^{33}$

erg was observed on the L1 dwarf SDSSp J005406.55-003101.8 by [Gizis et al. \[2017b\]](#) using long cadence data.

In Chapter 2, I analyzed the WLF rates of 4 flaring L dwarfs observed in *short* cadence mode, and I compared them with the rates of mid and late-M dwarfs. In this chapter, I will analyze the WLF rates of L and T dwarfs which were observed in *K2 long* cadence mode. In addition, I report for the first time, the detection of flares on an L5 dwarf. One of the flares observed on the L5 dwarf has the largest amplitude and energy among all the L dwarfs monitored by the *Kepler/K2* mission.

#### 4.1.4 Sample of L/T dwarfs observed by *K2*

I analyzed the light curves of 47 L/T dwarfs which had good light curves. This is the biggest sample of L/T dwarfs for which the flare rates have been studied. In Table 4.1, I list the total observation times of L/T dwarfs in each *K2* campaign. The total observation time of all L dwarfs in the sample is 4402.0 days and this is equal to 12.1 years. The main reason for observing those L/T dwarfs is that they were in the field of view of *K2* mission and that we wanted to observe more cool objects as far as possible to know their flare rates.

In Table 4.2, I list the L and T dwarfs which were observed in various *K2* campaigns with good photometry. The first column is the EPIC ID of each object and the second column is the 2MASS name of each object except for EPIC 236324763. Likewise, the third and fourth column give the information regarding the *K2* campaign in which each object was observed and its optical spectral type respectively. Some objects do not have an optical spectral type, so their near-infrared (NIR) spectral types are listed instead. The fifth column is the reference for the spectral type and the sixth column indicates whether the object was observed in short cadence mode or not. The total number of L dwarfs observed in short cadence mode is eleven. Figure 4.1 shows the distribution of L/T dwarfs in each spectral type. Since there are only two T dwarfs in

**Table 4.1: Total observation time by campaign**

<b>Campaign #</b>	<b># of L dwarfs</b>	<b>Time of Obs. (d)</b>
2	1	77.2
3	0	0
4	2	144.5
5	16	1196.8
6	2	160.9
7	1	81.4
8	1	80.3
9	0	0
10	5	281.0
11	1	71.0
12	2	161
13	0	0
14	6	487.5
15	2	179.5
16	7	567.7
17	3	201.3
18	14	711.6
<b>Total</b>		<b>4402.0</b>

the sample, their distribution is shown in only one bin.

Table 4.2: List of L and T dwarfs observed by *K2*

EPIC	2MASS/other name	Cam. #	Sp. Type	ref	Short Cadence
204341806	J16073799-2242468	2	L0	1	
210522262	J04070752+1546457	4	L3.5	2	
210879793	J04090950+2104393	4	L3	3	
211962038	J08264262+1939224	5, 18	L0	8	Yes
211970944	J08175266+1947279	5, 18	L0	2	
212102189	J08302724+2203456	5, 16, 18	L0	2	
211328277	J08433323+1024470	5, 18	L1	2	Yes
211357895	J08503593+1057156	5, 18	L6	4	
211628806	J0829066+145622	5, 18	L2	3	Yes
211680042	J08312221+1538511	5, 18	L1	2	
211727819	J08373282+1617380	5,18	L0	2	
211891128	J08365239+1835455	5, 18	L0	2	
211963497	J09094822+1940428	5	L1	2	Yes
211978512	J09053102+1954334	5	L0	2	
212111554	J08580549+2214582	5, 16, 18	L1	2	
212128548	J08564793+2235182	5,18	L3	5	
229227169	J13530778-0857119	6	L0	1	
217976219	J19090821-1937479	7	L1	1	Yes
220186653	J00540655-0031018	8	L1	6	
201181297	12130336-0432437	10	L5	6	
201299167	J12025263-0227483	10	L1	2	
201482905	J12035812+0015500	10	L3	7	
201658777	J12212770+0257198	10	L0	6	Yes
228730045	J12321827-0951502	10	L0	8	Yes
230214048	J17074571-1744523	11	T5 (NIR)	13	
236324763	VVV BD001	11	L5 p	12	

Continued on next page

Table 4.2 – continued from previous page

EPIC	2MASS/other name	K2 Campaign #	Sp. Type	ref	Short Cadence
246080803	J2344062-073328	12	L4.5	9	
246303486	J23255604-0259508	12	L3	10	
201528766	J10501247+0058032	14	L0	2	
248442470	J10484281+0111580	14	L1	6	Yes
248523311	J10340564+0350164	14	L0	2	
248653486	J10431944+0712326	14	L0	2	
248862470	J10433508+1213149	14	L8 (NIR)	10	
248891072	J10345117+1258407	14	L0	2	
249343675	J15230657-2347526	15	L0	14	Yes
249914869	J1507476-162738	15	L5	3	Yes
211467731	J08560211+1240150	16	L0	2	
211854467	J08585891+1804463	16	L2	2	
212119590	J08354537+2224310	16	L0	2	
212127137	J08535917+2233363	5,16, 18	L2	2	
251355936	J0918382+213406	16	L2.5	4	
211646606	J08381155+1511155	16	T3 (NIR)	11	
229227143	J13530778-0857119	6, 17	L0	1	
251551345	J13433872-0220446	17	L1	2	
251555071	J13334540-0215599	17	L3	2	Yes
211981633	J08375977+1957279	5, 18	L0	2	
211602578	J08403612+1434247	5, 18	L1	2	

**References:** 1) [Best et al. \[2018\]](#); 2) [Schmidt et al. \[2010\]](#); 3) [Kirkpatrick et al. \[2000\]](#) 4) [Kirkpatrick et al. \[1999\]](#); 5) [Cruz et al. \[2003\]](#); 6) [Schmidt et al. \[2015\]](#); 7) [Schmidt et al. \[2007\]](#); 8) [Bardalez Gagliuffi et al. \[2014\]](#); 9) [Kirkpatrick et al. \[2008\]](#); 10) [Burgasser et al. \[2010\]](#); 11) [Mace \[2014\]](#); 12) [Beamín et al. \[2013\]](#); 13) [Griffith et al. \[2012\]](#); 14) [Koen et al. \[2017\]](#)

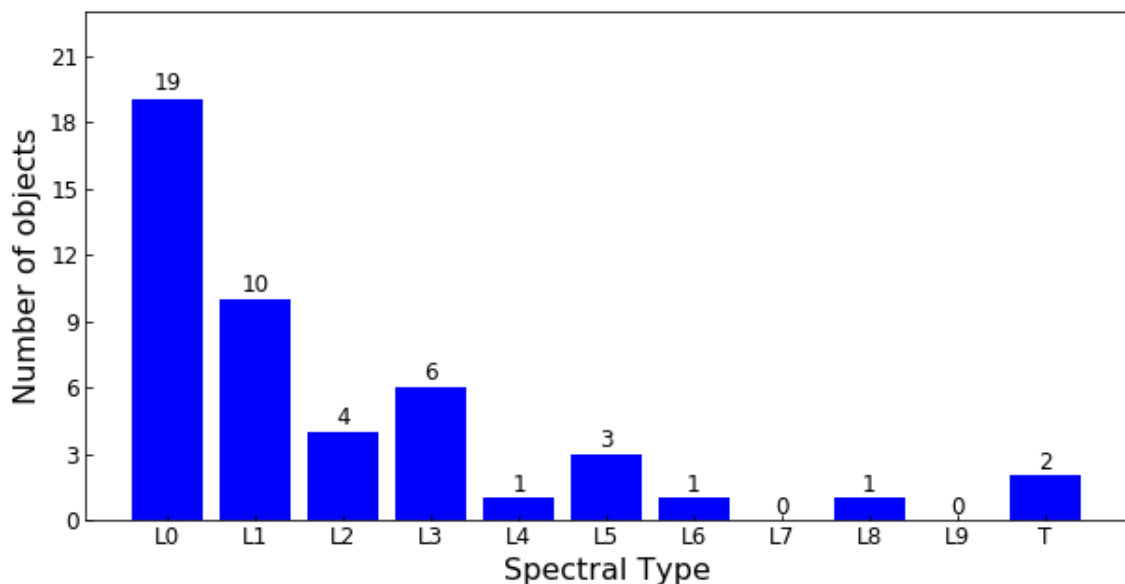


**Figure 4.1:** The distribution of L/T dwarfs by spectral type. There are only two T dwarfs in our sample, so their distribution is shown in only one bin.

## 4.2 Data reduction, flare search and flare energy estimation

I used the method described in Section 3.1 of Chapter 3 to determine the light curves of the targets. Likewise, I used the method described in Section 2.3 of Chapter 2 to identify the flares and estimate the corresponding flare energies. I examined by eye every brightening in the pixel level data to make sure all the flares were identified. Among the sample of 47 L/T dwarfs, 9 were observed to flare. The total estimated energy of a 10,000 K blackbody corresponding to each flaring L dwarf is given in Table 4.3. Details of three of the flares, one on an L2 dwarf and other two on an L5 dwarf are discussed in the next two sub-sections.

### 4.2.1 Flare on 2MASS J08585891+1804463

2MASS J08585891+1804463 (hereafter 2M0858+1804) is an L2 dwarf [Schmidt et al., 2010] and was observed by the *K2* in Campaign 16 for 70.7 d in long cadence mode only. It has a photospheric (continuum) level of 71 counts  $\text{s}^{-1}$  in the *K2* light curve. A flare was observed on 2M0858+1804 on *Kepler* time 3286.7039 during which

**Table 4.3: Values of ED1 for each flaring L dwarf**

EPIC	energy (erg)
211891128	$4.6 \times 10^{28}$
220186653	$5.3 \times 10^{28}$
201658777	$7.4 \times 10^{28}$
228730045	$8.6 \times 10^{28}$
211854467	$5.8 \times 10^{28}$
236324763	$6.5 \times 10^{28}$
201528766	$2.9 \times 10^{28}$
249343675	$9.8 \times 10^{28}$
212102189	$8.7 \times 10^{28}$

the star brightened by a factor of  $\sim 3$  relative to the local photospheric level measured 10 hours before the flare. <sup>1</sup> The flare has an ED of 2.0 hr and lasted for 0.20 d. It has a total estimated energy of  $4.2 \times 10^{32}$  erg. It is shown in Figure 4.2. 2M0858+1804 is the second L2 dwarf known to produce a white light flare.

#### 4.2.2 Flares on an L5 dwarf VVV BD001

VVV BD001 (VVV J172640.2-273803, hereafter V01) is an L5 brown dwarf discovered by [Beamín et al. \[2013\]](#) using the Vista Variables in the Vía Láctea (VVV) survey [[Minniti et al., 2010](#); [Saito et al., 2012](#)]. It is an unusual blue dwarf that is located at a distance of  $18.5 \pm 0.14$  pc, towards the Galactic bulge, and is a high proper motion object with  $\mu_\alpha = -544.5 \pm 0.6$  mas yr<sup>-1</sup> and  $\mu_\delta = -326.4 \pm 0.4$  mas yr<sup>-1</sup>. This corresponds to a tangential velocity of 56 km s<sup>-1</sup>. V01 is the first brown dwarf to be discovered in the very crowded region of sky where it is located. The left plot in Figure 4.3 shows the position of V01 as displayed by VizieR Photometry Viewer with the center at  $\alpha = 17^h 26' 40''.20$   $\delta = -27^\circ 38' 3''.00$ . It can be seen from this figure

<sup>1</sup> There was a ‘thruster firing’ of the instrument right before the peak flare time, but the centroid of the target remained in the same pixel with no significant change in the brightness level during that cadence.

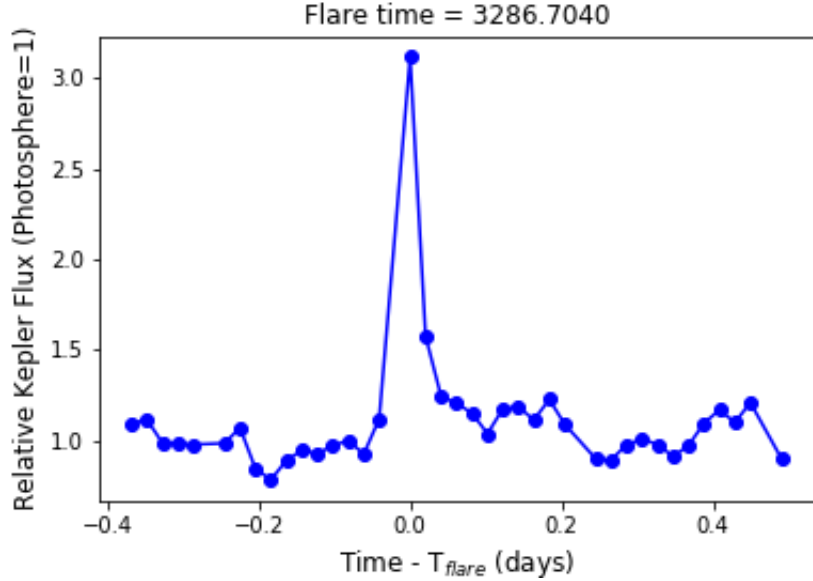


**Figure 4.2:** The flare observed on L2 dwarf 2MASS J08585891+1804463.

that V01 lies very close within a fraction of an arcsec to two other stars.

V01 was observed in long cadence mode by the *K2* mission during Campaign 11 for  $\sim 71$  days. The right plot in Figure 4.3 shows pixel data of V01 obtained by the *K2* mission. The centroid of V01 lies in the pixel inside the circle. I performed point source function (psf) photometry to measure the light curve of V01 from the available target pixel file. The median count rate of V01 in the *K2* light curve is  $122 \text{ counts s}^{-1}$ .

Two strong flares were detected on V01. Following the detection of flares on the L2.5 dwarf U22-011 (in 2019), V01 is now the coolest object known to undergo flares. The largest flare occurred on *Kepler* mission time 2845.4432 during which V01 brightened by more than 300 times above its photospheric level. The count rate at the peak of this flare is  $41874 \text{ counts s}^{-1}$ . This flare had an ED of 198 hr and lasted for 0.55 d. I estimate that a 10,000 K flare with an ED of 1s has an energy of  $6.5 \times 10^{28} \text{ erg}$ . Using this estimation, the total estimated energy emitted during the largest flare is  $4.6 \times 10^{34} \text{ erg}$ .

Table 4.4: Properties of VVV BD001

	Value	Units	Ref.
<b>PHOTOMETRIC PROPERTIES</b>			
Sp. Type	L5±1		1
<i>J</i>	13.27±0.02	mag	1
<i>H</i>	12.67±0.02	mag	1
<i>K<sub>s</sub></i>	12.20±0.02	mag	1
<i>i</i>	17.90±0.02	mag	2
<i>G</i>	18.23±0.00	mag	3
<i>K<sub>p</sub></i>	14.73	mag	4
<b>PHYSICAL PARAMETERS</b>			
$\alpha$	261.7 <sup>a</sup> (±0.3 mas)	deg	3
$\delta$	-27.6 <sup>a</sup> (±0.2 mas)	deg	3
parallax	54.0 ± 0.4	mas	3
$\mu_\alpha$	-544.5 ± 0.6	mas yr <sup>-1</sup>	3
$\mu_\delta$	-326.4 ± 0.4	mas yr <sup>-1</sup>	3

<sup>a</sup>epoch J2015.5

**References:**

- (1) [Beamín et al. \[2013\]](#); (2) [Chambers et al. \[2016\]](#);  
(3) [Gaia Collaboration et al. \[2018b\]](#); (4) [Huber et al. \[2017\]](#)

A second flare on V01 occurred at *Kepler* mission time 2827.7696 during which V01 brightened by a factor of 15 times the photospheric level. The count rate at the peak of this flare is 1832 counts s<sup>-1</sup>. It has an ED of 8.0 hr and lasted for 0.06 d. The total estimated energy of this flare is  $2.0 \times 10^{33}$  erg.

### 4.3 Results

I identified a total of 11 flares on 47 L/T dwarfs observed in *K2* long cadence mode. All of them were on L dwarfs, with most on the early L dwarfs. Those flares have energies in the range  $(0.9 - 460) \times 10^{32}$  erg and have EDs in the range (1.3 - 198) hr. More information regarding the ED, peak flare time, flare energy and flare duration of each flare is given in Table 4.5. In Table 4.6, I list the 2MASS, PS1, *Gaia* properties

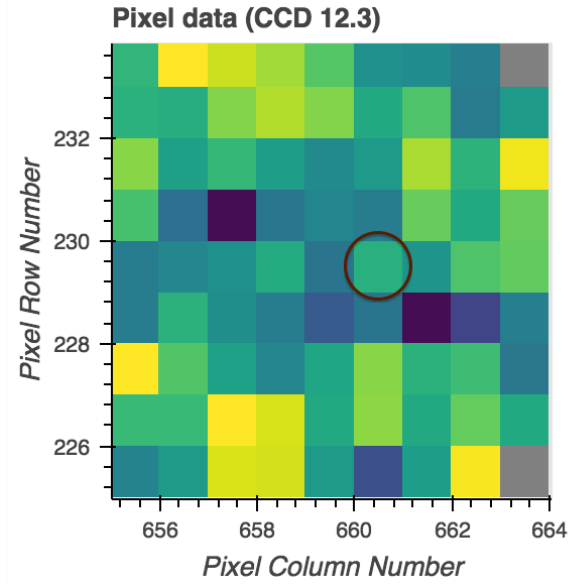
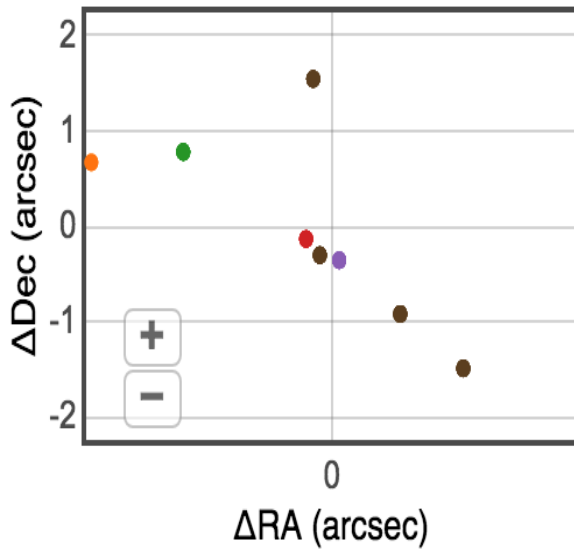


**Figure 4.3:** **Left:** Position of V01 as shown by VizieR Photometry Viewer with center at  $\alpha = 17^h 26' 40''.20$   $\delta = -27^\circ 38' 3''.00$ . **Right:** Pixel data of V01. The centroid is located at (660,229) inside the circled pixel.

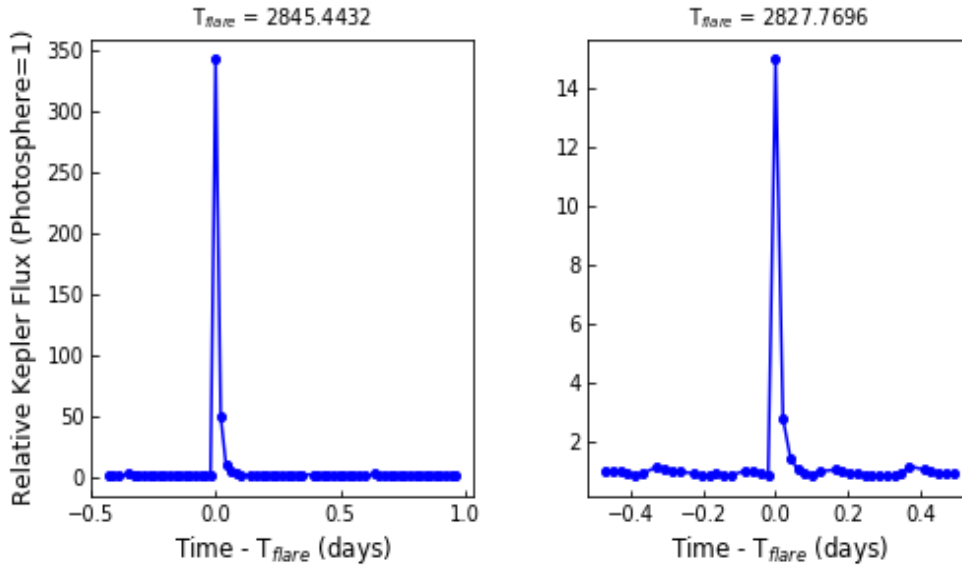


**Figure 4.4:** Flares observed on V01. The time along the X-axis is centered at peak flare time mentioned above each plot. The flux along the Y-axis is normalized by the median flux which corresponds to photospheric level.

**Table 4.5: Properties of flares on L dwarfs**

<b>EPIC</b>	<b>Sp. Type</b>	$T_{\text{peak}}$ (BJD - 2454833)	<b>ED</b> (hr)	<b>Energy</b> (erg)	<b>duration</b> (d)
211891128	L0	2377.0389	11.4	$2.0 \times 10^{33}$	0.02
220186653	L1	2595.7841	15.4	$3.0 \times 10^{33}$	0.2
201658777	L0	2799.9338	0.30	$8.8 \times 10^{31}$	0.02
228730045	L0	2811.7645	11.4	$3.6 \times 10^{33}$	0.18
228730045	L0	2755.0599	1.3	$3.9 \times 10^{32}$	0.04
211854467	L2	3286.7039	2.4	$4.2 \times 10^{32}$	0.06
236324763	L5	2845.4432	198	$4.6 \times 10^{34}$	0.55
236324763	L5	2827.7696	8.0	$2.0 \times 10^{33}$	0.06
201528766	L0	3138.0292	19.7	$2.0 \times 10^{33}$	0.27
249343675	L0	3238.3152	1.8	$6.4 \times 10^{32}$	0.18
212102189	L0	3427.1071	3.5	$1.1 \times 10^{33}$	0.72

of the flaring L dwarfs. The EW of H $\alpha$  emission is also listed whenever available. In view of our detection of a flare on an L2 dwarf, the number of flaring objects with this spectral type is now doubled. White light flares are now observed on objects with spectral type as late as L5. The amplitude of the flare (relative to the quiescent level of the star) observed on the L5 dwarf V01 is the largest among all the flares observed on the targets I studied using the *K2* data.

#### 4.3.1 FFD of L dwarfs using long cadence data

In Figure 4.5, I plot the FFD of L dwarfs using *K2* long cadence data. The total time of observation (12.1 yrs) of all L dwarfs is taken into account while estimating the FFD. The slope ( $\beta$ ) of the fitted line is  $0.42 \pm 0.13$  and the cumulative frequency intercept at  $10^{30}$  erg is  $-1.63 \pm 0.52$  ( $\text{day}^{-1}$ ). Using these results, it is estimated that a superflare of energy  $10^{33}$  erg occurs every 2.1 years and a superflare of energy  $10^{34}$  occurs every 5.6 years on the L dwarfs.

**Table 4.6: Properties of flaring L dwarfs**

EPIC	$J$ (mag)	$K_s$ (mag)	$i$ (mag)	distance (pc)	H $\alpha$ EW (Å)
211891128	16.51±0.12	15.18±0.10	20.8±0.1	67.3±13.0 <sup>a</sup>	
220186653	15.73±0.05	14.38±0.07	20.07±0.04	51.9±3.3 <sup>b</sup>	5.0 <sup>e</sup>
201658777	13.17±0.02	11.95±0.03	17.44±0.01	18.5 <sup>c</sup>	6.1 <sup>f</sup>
228730045	13.73±0.03	12.55±0.03	18.04±0.00	26.4±4.9 <sup>d</sup>	
211854467	16.35±0.10	15.14±0.12	20.80±0.03	76.4±14.7 <sup>a</sup>	
236324763	13.27±0.02	12.20±0.02	17.90±0.02	18.5±0.1 <sup>b</sup>	
201528766	16.58±0.14	15.78	20.39±0.02	54.0±10.4 <sup>a</sup>	
249343675	14.20±0.03	12.90±0.03	18.40±0.01	33.1±0.4 <sup>b</sup>	
212102189	15.66±0.06	14.46±0.09	19.81±0.01	59.6±3.4 <sup>b</sup>	

**Notes:**

- i)  $J$  and  $K_s$  magnitudes are from 2MASS survey [Cutri et al., 2003].
- ii)  $i$  magnitudes are from Pan-STARRS survey [Chambers et al., 2016].

**References:**

- <sup>a</sup>Schmidt et al. [2010]; <sup>b</sup>Gaia Collaboration et al. [2018a]; <sup>c</sup>Bailer-Jones et al. [2018];
- <sup>d</sup>Paudel et al. [2018a]; <sup>e</sup>Gizis et al. [2017b]; <sup>f</sup>Schmidt et al. [2015]

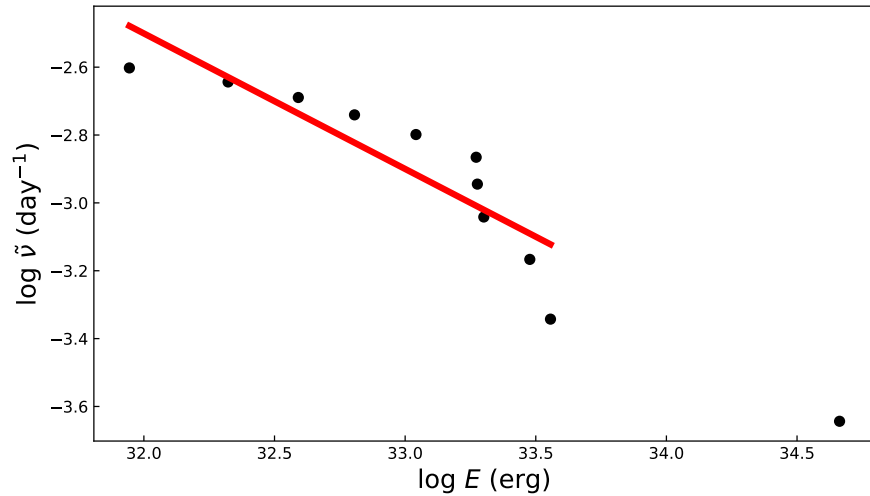


**Figure 4.5:** The FFD estimated by using the energies of all flares identified on L dwarfs observed by *K2* long cadence mode.

## Chapter 5

### MONSTER FLARES OBSERVED ON THE YOUNG BROWN DWARF CFHT-BD-TAU 4

#### 5.1 INTRODUCTION

Rapidly rotating young ( $\sim 2$  Myr) solar mass stars in the Orion Nebula Cluster are capable of producing X-ray flares with energies in the range  $10^{34}$ - $10^{36}$  erg [Wolk et al., 2005]. Similarly, low mass stars and young brown dwarfs (hereafter BDs) in Orion Nebula region and Taurus molecular cloud also have high X-ray emission. There is no significant difference in X-ray activity levels of the low mass stars and the young BDs with similar spectral types implying that X-ray activity levels are determined by effective temperatures rather than masses and surface gravities of (sub)stellar objects [Preibisch et al., 2005; Güdel et al., 2007; Grosso et al., 2007; Getman et al., 2008a,b]. Hence, young BDs can be magnetically active as the low mass stars, and produce huge flares. The young stars and BDs may have accreting or non-accreting disks which limit the X-ray flare loop sizes ( $<$  Keplerian corotation radii, Getman et al. 2008b). In addition to the magnetic reconnection events which occur in diskless stars, the interaction of disks of young stars with their magnetospheres can also trigger large scale magnetic reconnection events which manifest as flares [Zhu et al., 2009]. Stelzer et al. [2000] report the presence of an accretion disk makes no difference on X-ray flares on stars in clusters with ages 1-3 Myr.

The results of Gizis et al. [2017a] show that young brown dwarfs like 2MASS J03350208+2342356 (24 Myr old brown dwarf, hereafter 2M0335+2342) and CFHT-PL-17 (a brown dwarf member of Pleiades) are capable of producing strong white light superflares with energies  $> 10^{33}$  erg. Superflares are thus ubiquitous in *Kepler* G, K, M and L stars

[Maehara et al., 2012; Shibayama et al., 2013; Notsu et al., 2013; Candelaresi et al., 2014; Gizis et al., 2017a,b]. The young brown dwarfs are in the process of contraction and have radii  $>0.5R_{\odot}$  if they are few million years old. They are fully convective and have high luminosities. The energy flux scaling law predicts that strong magnetic fields are produced in young BDs and exoplanets [Reiners and Christensen, 2010; Christensen et al., 2009]. This is supported by detection of 5 kG magnetic field on a 22 Myr, M8.5 brown dwarf LSR J1835+3259 [Berdyugina et al., 2017b]. Reiners et al. [2009b] however reported weak magnetic fields with strengths of few hundred gauss in four young ( $\lesssim 10$  Myr) accreting BDs with  $v \sin i > 5 \text{ km s}^{-1}$ . The weaker fields may be due to presence of disk around such objects or that they do not follow scaling law [Reiners and Christensen, 2010].

In this chapter, I present the photometric measurements of two superflares observed on a very young brown dwarf CFHT-BD-Tau 4 (hereafter CT4). Discovered by Martín et al. [2001], the presence of disk around CT4 makes it more valuable for studies regarding planet formation around low mass stars and BDs [Ricci et al., 2014]. I present the photometric and physical properties of CT4 in Section 5.2. In Section 5.3, I present the data reduction, flare photometry and flare energy computation, and discuss the results in Section 2.7.

## 5.2 TARGET CHARACTERISTICS

CT4 (2MASS J04394748+2601407) is a young M7 brown dwarf in the Taurus star-forming region, with an estimated age  $\sim 1$  Myr old [Luhman et al., 2017] and at a distance of  $147.1 \pm 5.2$  pc [Gaia Collaboration et al., 2016, 2018b]. It has an effective temperature ( $T_{eff}$ ) equal to 2900 K and bolometric luminosity ( $L_{bol}$ ) equal to  $0.03 L_{\odot}$  [Reiners et al., 2009a]. It is a well studied BD in wavelengths ranging from X-rays to millimeters [Martín et al., 2001; Liu et al., 2003; Pascucci et al., 2003; Klein et al., 2003; Apai et al., 2004; Grosso et al., 2007]. Using the Submillimeter Common-User Bolometer Array (SCUBA) on James Clerk Maxwell Telescope (JCMT) and the Max-Planck

Millimeter Bolometer (MAMBO) array on the IRAM 30 m telescope, [Klein et al. \[2003\]](#) reported the presence of circumstellar cold dust around this young object. The spectral energy distribution (SED) of this circumstellar dust fits a flat disk model better than spherical dust distribution model and resembles to that of T Tauri disk with a mass estimation of  $(0.3-1.5)M_J$  [[Pascucci et al., 2003](#)]. The mid-infrared observations done by using GEMINI/T-ReCS suggest the presence of  $2\mu\text{m}$  silicon like grains is prominent in the disk [[Apai et al., 2004](#)]. In addition, Atacama Large Millimeter/submillimeter Array (ALMA) observations at 0.89 mm and 3.2 mm show that large grains of at least  $\sim 1$  mm are also present in the outer disk region and the outer radius of disk is  $>80$  AU [[Ricci et al., 2014](#)].

[Martín et al. \[2001\]](#) detected a strong  $\text{H}\alpha$  emission with an equivalent width  $340 \text{ \AA}$ , and  $\text{Br}\gamma$  emission from CT4. Likewise, [Grosso et al. \[2007\]](#) detected quiescent X-rays with luminosity equal to  $24.3 \times 10^{28} \text{ erg s}^{-1}$  and X-ray activity,  $\log(L_X/L_{\text{bol}}) = -3$  which is also the saturated X-ray emission level of early M dwarfs. Hence the two magnetic activity indicators  $\text{H}\alpha$  emission and X-ray emission signify the presence of active chromosphere and corona in this substellar object. [Jayawardhana et al. \[2003\]](#) classify CT4 as a non-accretor using the shape and width of  $\text{H}\alpha$  emission profile but [Reiners et al. \[2009b\]](#) mention that it may have magnetospheric accretion. Different authors have reported different values of visual extinction parameter  $A_V$  for CT4. [Martín et al. \[2001\]](#) reported its value equal to 3.0 mag in their discovery paper, using the  $I$ - $J$  colors of field M dwarfs and the interstellar extinction law of [Rieke and Lebofsky \[1985\]](#). Likewise, [Monin et al. \[2010\]](#); [Luhman et al. \[2017\]](#); [Alves de Oliveira et al. \[2012\]](#); [Andrews et al. \[2013\]](#) report its value equal to 2.6 mag, 5.0 mag, 5.4 mag and  $5.67 \pm 0.89$  mag respectively. [Monin et al. \[2010\]](#) do not specify clearly how they estimated  $A_V$  particularly for CT4. [Alves de Oliveira et al. \[2012\]](#) estimated  $A_V$  from the  $J$ - $H$  vs.  $H$ - $K_s$  diagram. [Luhman et al. \[2017\]](#) used SpeX spectrum of CT4 and estimated the value of  $A_V$  by comparing the spectral slopes at  $1\mu\text{m}$ , of various young M dwarfs. Likewise, [Andrews et al. \[2013\]](#) estimated  $A_V$  by fitting the stellar photosphere models to the

optical and near-infrared spectral energy distribution (SED) of the object. In addition to all the above values of  $A_V$ , Zhang et al. [2018] estimated it to be  $6.37 \pm 0.85$  mag. Their estimation is based on the intrinsic optical–near-infrared color as a function of spectral type. They used spectral type of  $M7.2 \pm 0.9$  for CT4, which was estimated by using their own reddening-free spectral classification system. As this value of  $A_V$  is based on more precise photometry measured by Pan-STARRS1  $3\pi$  survey, we use it for estimation of flare energies in this paper<sup>1</sup>. The photometric and physical properties of CT4 are summarized in Table 5.1.

## 5.3 DATA REDUCTION AND COMPUTATIONS

### 5.3.1 *K2* photometry

I followed the method described in Section 2.3.1 of Chapter 2 to measure the photometry of flares observed on CT4. It was observed as EPIC 248029954 by *Kepler K2* mission during Campaign 13 (08 March, 2017 - 27 May, 2017) in long cadence ( $\sim 30$  minute) mode [Jenkins et al., 2010]. The total observation time is 80.52 day, and there are 3651 good ( $Q = 0$ ) data points. Average flux measured during 29.4 minute interval is obtained for each data point. In case of CT4, the median counts through 3-pixel radius aperture is less than through 2-pixel radius aperture due to the negative counts in the outer pixels surrounding the target pixel. The median count rate through 2-pixel radius aperture is  $478 \text{ count s}^{-1}$  which corresponds to photospheric continuum level. This gives  $\tilde{K}_p = 18.6$  which is estimated using Lund et al. [2015] relation:  $\tilde{K}_p \equiv 25.3 - 2.5 \log(\text{count rate})$ . There is no significant difference in  $\tilde{K}_p$  calculated using either 2-pixel or 3-pixel radius aperture in case of UCDS. I used 2-pixel radius aperture to measure the photometry of flares discussed in this paper. The *K2* light curve of CT4 is shown in Figure 5.1 in which we can see periodic nature of the curve. Using Lomb-Scargle periodogram, I find that the period of this periodic feature is 2.98 days,

---

<sup>1</sup> Zhang et al. [2018] also estimated the value of  $A_V$  based on color-color diagrams using  $\text{H}_2\text{O}$  indices but suggest that the value of  $A_V$  based on intrinsic optical–near-infrared color sequences is more precise whenever the reddening-free spectral type of the object is well-defined, and  $\approx M5\text{-L}2$ .

**Table 5.1: Properties of CFHT-BD-Tau 4**

Parameter	Value	Unit	Ref.
PHOTOMETRIC PARAMETERS			
Sp. Type	M7		1
$V$	$21.56 \pm 0.01$	mag	2
$J$	$12.17 \pm 0.02$	mag	3
$H$	$11.01 \pm 0.02$	mag	3
$K_s$	$10.33 \pm 0.02$	mag	3
$r$	$20.20 \pm 0.04$	mag	4
$i$	$17.54 \pm 0.02$	mag	4
$z$	$15.79 \pm 0.01$	mag	4
$G$	$17.78 \pm 0.01$	mag	5
PHYSICAL PARAMETERS			
$T_{\text{eff}}$	2900	K	6
$M$	$0.064^2$	$M_{\odot}$	6
$R$	0.65	$R_{\odot}$	6
$\log L/L_{\odot}$	-1.57		6
$v \sin i$	$6_{-4}^{+2}$	km s <sup>-1</sup>	6
Age	$\sim 1$	Myr	7
parallax	$6.80 \pm 0.24$	mas	5
$\alpha$	$069.94787355129^b (\pm 0.2 \text{ mas})$	deg	5
$\delta$	$+26.02787631047^b (\pm 0.1 \text{ mas})$	deg	5

<sup>b</sup>epoch J2015.5, ICRS

**References:**

- (1) Martín et al. [2001]; (2) Kraus et al. [2006];  
(3) Skrutskie et al. [2006]; (4) Chambers et al. [2016];  
(5) Gaia Collaboration et al. [2018b]; (6) Reiners et al. [2009b];  
(7) Luhman et al. [2017]

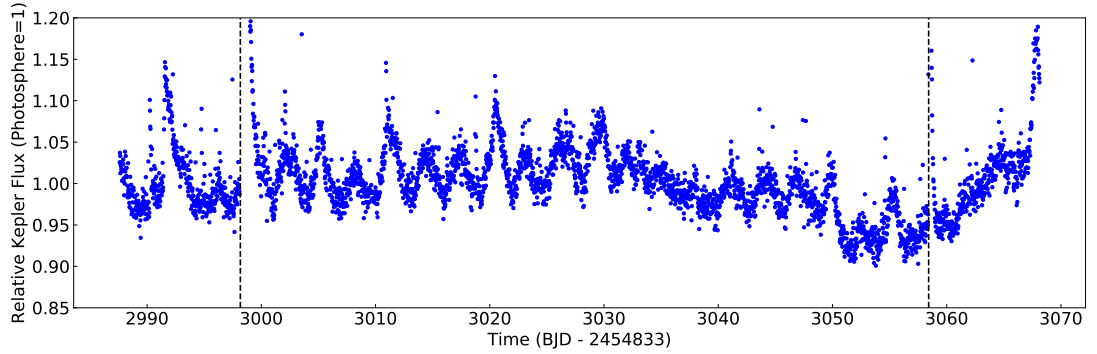


**Figure 5.1:** The *K2* light curve of CT4. The two superflares are not shown in full scale to focus the periodic nature of the curve. Using Lomb-Scargle periodogram, the dominant period of the light curve is 2.98 day. The two dashed vertical lines mark the peak flux times of the superflares.

and is comparable to rotation period of  $2.93 \pm_{2.4}^{0.9}$  day reported by [Scholz et al. \[2018\]](#) for CT4. I compared the light curve obtained by using aperture photometry with that obtained by using psf photometry and EVEREST detrending code [[Luger et al., 2016](#)]. There is no significant differences between the light curves.

### 5.3.2 Computation of Flare Energies

I followed the method described in Section 2.3.3 of Chapter 2 to estimate the energies of flares on CT4. I estimated the photospheric spectrum of CT4 by using an active M7 template spectrum [[Bochanski et al., 2007](#)] normalized to match the Pan-STARRS *i*-band photometry [[Tonry et al., 2012](#); [Chambers et al., 2016](#); [Magnier et al., 2016](#)]. As *Kepler* flux of CT4 is affected by extinction, I first reddened the blackbody spectrum using astropy application `specutil.extinction` for  $A_V = 6.37$ , and  $R_V = 3.1$ . Here, the value of  $R_V (= A_V / E(B - V))$  is the typical value used for Milky Way Galaxy. I used the mean extinction law as mentioned in [Cardelli et al. \[1989\]](#). Then, I computed the photospheric flux of the reddened 10,000 K blackbody, which is normalized to have the same count rate through the *Kepler* filter as the photosphere of CT4. The total (UV/optical/IR) energy of CT4 flare having equivalent duration of 1 s is  $4.9 \times 10^{30}$

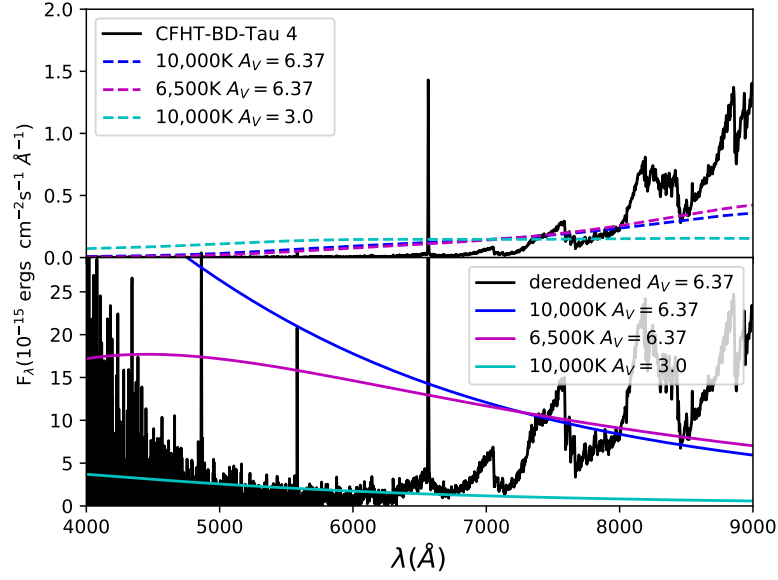


**Figure 5.2:** Optical spectral energy distribution (SED) of CT4 (black solid curve). The three dashed lines represent the SEDs of hypothetical blackbody flares of temperature 10,000 K, 6,500 K and 10,000 K which produce the same counts through *Kepler* filter, corresponding to  $A_V = 6.37$ , 6.37 and 3.0 respectively. The upper plot is the reddened version of SEDs, and the lower plot is the dereddened version of SEDs.

erg and  $5.4 \times 10^{32}$  erg corresponding to  $A_V = 0.0$  and 6.37 respectively. These energies were used to estimate the total (UV/optical/IR) flare energy by multiplying with ED of the flare. I adopted a distance of 147.1 pc to estimate the flare energies. Figure 5.2 shows optical spectral energy distribution (SED) of CT4. For comparison, we also plot SEDs of 10,000 K and 6,500 K blackbody flares that produce the same counts as CT4 through *Kepler* filter. The upper plot shows the reddened SEDs, and the lower plot shows the dereddened SEDs for two values of  $A_V$ : 6.37 and 3.0.

### 5.3.3 Flare photometry

The strongest superflare detected on CT4 is shown in Figure 5.3. At first, the flux increased to 1753 count  $s^{-1}$  and 20006 count  $s^{-1}$  at *Kepler* mission day 2998.1243 and 2998.1447 respectively. It increased to peak value of 22788 count  $s^{-1}$  ( $\tilde{K}_p = 14.4$ ,

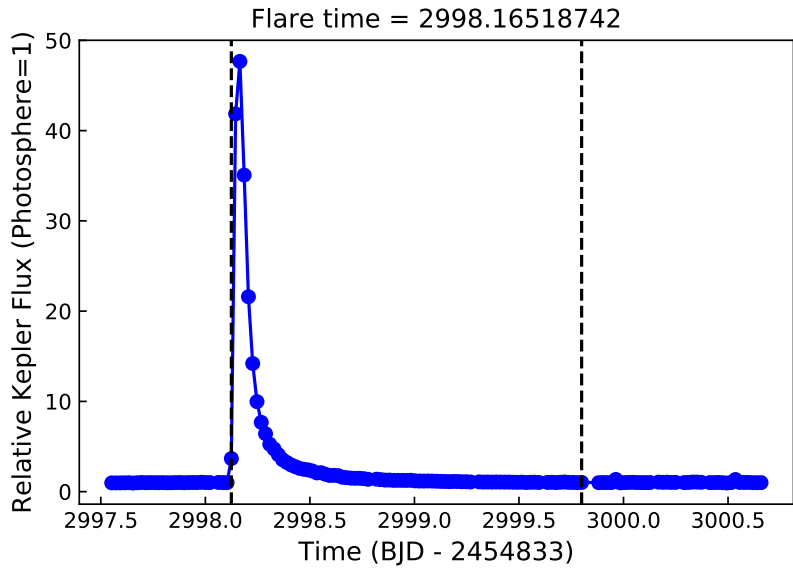


**Figure 5.3:** The strongest superflare observed on CT4. The blue dots represent the observed data. The dashed vertical lines represent the start and end times of flare.

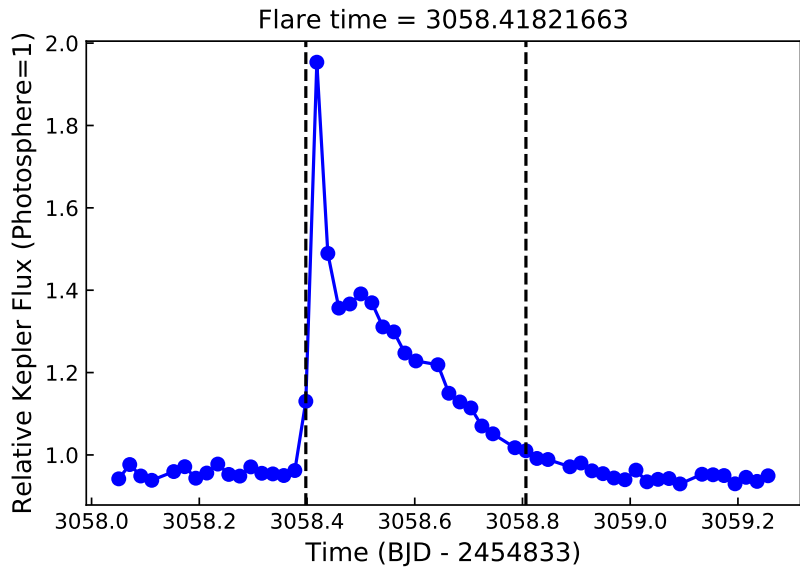


**Figure 5.4:** Next superflare observed on CT4. The blue dots represent the observed data. The dashed vertical lines represent the start and end times of flare.

**Table 5.2: Flare properties**

	ED (hour)	$A_V = 0.0$	$A_V = 6.37$	flare duration (day)
Flare 1	107	$1.9 \times 10^{36}$ erg	$2.1 \times 10^{38}$ erg	1.7
Flare 2	2.4	$4.2 \times 10^{34}$ erg	$4.7 \times 10^{36}$ erg	0.41

$\Delta\tilde{K}_p = -4.20$ ) on *Kepler* mission day 2998.1651, during which the target brightened by  $\sim 48$  times the quiescent photospheric level. Then, the flare continued to decay for over the next several hours as seen in Figure 5.3. This flare has an equivalent duration of  $\sim 107$  hour, and an estimated total (UV/optical/IR) energy equal to  $2.1 \times 10^{38}$  erg, for  $A_V = 6.37$ . The total flare duration is 1.7 day. The rise time of the flare is longer than that of superflares observed on some ultracool dwarfs. Further discussion is given in Section 2.7.

The next superflare identified on CT4 is shown in Figure 5.4. It is a complex flare with two peaks. The first peak is at *Kepler* mission day 3058.4182, and the second peak is at *Kepler* mission day 3058.4999. The flux counts at those times are 934 count  $s^{-1}$  and 665 count  $s^{-1}$  respectively. This flare has an ED of  $\sim 2.4$  hour, and flare duration of 0.41 day. The estimated total (UV/optical/IR) energy of this flare is  $4.7 \times 10^{36}$  erg, for  $A_V = 6.37$ . The properties of both flares are summarized in Table 5.2. For comparison, I also list the flare energies for zero extinction i.e.  $A_V = 0.0$ .

## 5.4 Discussion

Two superflares were observed on CT4 using *Kepler K2* Campaign 13 long cadence data. The total (UV/optical/IR) energies of those flares are estimated to be  $2.1 \times 10^{38}$  erg and  $4.7 \times 10^{36}$  erg, for  $A_V = 6.37$ . The stronger of the two superflares has ED of  $\sim 107$  hour and the weaker has ED of  $\sim 2.4$  hour. The energies of these flares are larger than the strongest flares reported on other young brown dwarfs 2M0335+2342 and CFHT-PL-17 in Gizis et al. [2017b].

While the energy partition may not be same even for the flares that occur on same star [Osten et al., 2016], we may get an approximate estimation of soft X-ray (0.01-10 keV) energy ( $E_X$ ) radiated during the stronger superflare by using the conversion factors:  $E_X/E_{\text{bol}} = 0.3$ , and  $E_{\text{Kp}}/E_{\text{bol}} = 0.16$  (assuming 9,000 K blackbody temperature) for active stars, listed in Table 2 of Osten and Wolk [2015]. Here,  $E_{\text{bol}}$  is the total bolometric flare radiated energy, and is related to the coronal radiated flare energy  $E_{\text{cor}}$  and the optical flare energy  $E_{\text{opt}}$ , by  $E_{\text{bol}} = E_{\text{cor}} + E_{\text{opt}}$ . Likewise,  $E_{\text{Kp}}$  is the *Kepler* flare energy. Our estimation of  $E_{\text{Kp}}$  for the stronger superflare is  $6.8 \times 10^{37}$  erg (assuming 10,000 K blackbody temperature). Using this value of  $E_{\text{Kp}}$  and the conversion factors mentioned above, we get  $E_X \approx 1.3 \times 10^{38}$  erg. The occurrence of those two superflares during the observed time of 78.31 days implies that CT4 is highly active which is also supported by its high  $\text{H}\alpha$  and X-ray emission and it is very young. We observed only two flares on CT4 because it was observed in long cadence mode. It might also be true that this flare rate is related with the intrinsic flare rate of CT4. This can be confirmed by observing it in short cadence ( $\sim 1$  minute) mode.

If we had short cadence ( $\sim 1$  min, Gilliland et al. 2010) data for CT4, it would be possible to detect more weaker flares. Using the results of flare frequency distribution of 24 Myr brown dwarf 2M0335+2342 over the range  $10^{31}$  to  $10^{33}$  erg as reported by Gizis et al. [2017a], the expected rate of flare with energy equal to that of stronger superflare observed on CT4 is 0.004 per year, much less than the observed results. It is interesting to note that the energies of superflares observed on CT4 are comparable to energy of the most powerful flare reported by Gahm [1990]. He studied the energies of 13 flares on seven T Tauri stars which were observed by using Strömgren filters and reported an upper limit of flare energy  $\sim 7.0 \times 10^{36}$  erg in optical spectral region. His results are based on ground based observations over several nights with as few as 3 observations per night.

I emphasize that the flare energies reported in this chapter have huge uncertainties for several reasons. The flare energies strongly depend on the value of  $A_V$ , as can be seen in Table 5.2. The flares contribute more flux in the shorter wavelengths in *Kepler* band pass, and the shorter wavelengths are more affected by extinction in interstellar medium. Consequently, fewer photons are recorded giving rise to shorter ED and less flare energy. Furthermore, we have not taken into account the contribution of atomic emission lines to total energy budget. The atomic emission lines and blackbody components contribute in different proportions during the impulsive and gradual phase of the flares [Hawley and Pettersen, 1991].

Gahm [1990] pointed out that the light curves of strong flares on T Tauri stars are characterized by a slow rise and then a slow decline in brightness. This is different than that is observed in flares of ordinary flare stars, most of which are characterized by a rapid rise followed by a gradual decline. While it would be more clear if we had short cadence data of CT4, the long cadence data somehow suggests similar characteristics as pointed by Gahm [1990]. It took one hour for the strongest flare to reach the peak flux level. The full width half maximum (FWHM) time scale of the flare is between 1.5 and 2.0 hours. This time scale is very different than that observed on typical superflares on older, diskless targets. The FWHM time scale of strongest flares on some UCDs is of the order of few minutes. For example, the two superflares observed on the L0 dwarf 2MASS J12321827-0951502 and the M7 dwarf 2MASS J08352366+1029318 had very short FWHM time scales of order  $\sim 2$  minutes [Paudel et al., 2018a]. It should be noted that 2MASS J12321827-0951502 and 2MASS J08352366+1029318 were observed in short cadence ( $\sim 1$  min, Gilliland et al. 2010) mode. It is not clear whether the presence of disk changes the nature of flare light curves of young objects like CT4.

Assuming a similarity between the solar flares and the flares on BDs, we may get a rough estimation of maximum magnetic field strength  $B_z^{max}$  associated with the stronger superflare observed on CT4 using the scaling relation in Aulanier et al. [2013]:

$$E = 0.5 \times 10^{32} \left( \frac{B_z^{max}}{1000G} \right)^2 \left( \frac{L^{bipole}}{50Mm} \right)^3 \text{ erg.} \quad (5.1)$$

where  $E$  is the bolometric flare energy, and  $L^{bipole}$  is linear separation between bipoles. If we take  $L^{bipole}$  to be equal to  $\pi R_*$  ( $R_*$  = radius of star) as the maximum distance between a pair of magnetic poles on the surface of CT4, a strong magnetic field of 13.5 kG is required to produce the stronger superflare with energy  $2.1 \times 10^{38}$  erg. In general, it is possible for fully convective M dwarfs to have strong average magnetic fields with the highest observed value to be 7.0 kG in the case of WX Ursae Majoris (Gliese 412 B) [Shulyak et al., 2017]. Likewise, a  $\sim 22$  Myr old M8.5 brown dwarf LSR J1835+3259 is reported to have a strong magnetic field of strength 5 kG [Berdyugina et al., 2017b]. However, the above value of magnetic field strength estimated in case of CT4 using solar flare model is higher compared to results of Reiners et al. [2009b] who reported weak magnetic fields (few hundred gauss) with an upper limit  $\sim 1$  kG on four accreting brown dwarfs including CT4. Using magnetospheric accretion model to young accreting brown dwarfs in combination with observed data, Scholz and Jayawardhana [2006] and Stelzer et al. [2007] also predicted weak magnetic fields of strength  $\sim$ kilogauss on the surface of those young objects. The longer FWHM time scale of the superflare observed on CT4 might be possible due to the reason that it occurred as a result of reconnection between the magnetic loops on CT4 and its disk. In such case, even the weak magnetic fields might be capable of producing superflares with huge energies because of the larger volumes associated with longer magnetic loops.

It is possible that an outburst from magnetospheric accretion could mimic a flare. Using magnetospheric model to a star-disk system, the rate of energy released  $L_{acc}$  due to accretion of gas onto the star can be calculated by using

$$L_{acc} = \frac{GM_*\dot{M}}{R_*} \left( 1 - \frac{R_*}{R_{in}} \right) \quad (5.2)$$

where  $M_*$  and  $R_*$  are mass and radius of the star;  $\dot{M}$  is the accretion rate, and  $R_{in}$  is the inner radius of accretion disk [Gullbring et al., 1998]. We do not have accurate estimation of inner disk radius and accretion rate of CT4. Liu et al. [2003] suggest  $R_{in} \sim (2-3)R_*$  for young brown dwarfs. Their results are based on 38 cool objects in IC348 and Taurus which have spectral types M6-M9 and ages  $\leq 5$  Myr. Using  $R_{in} = 2.5R_*$ , an accretion rate  $\log \dot{M} = -6.70 M_{\odot} \text{yr}^{-1}$  is required for the stronger superflare to emit the energy of  $2.1 \times 10^{38}$  erg in the observed flare duration. This accretion rate is higher than those reported for young accreting BDs GY11 and 2MASS J053825.4-024241. Rigliaco et al. [2011] reported an accretion rate of  $\log \dot{M} \sim -9.86 \pm 0.45 M_{\odot} \text{yr}^{-1}$  for 2MASS J053825.4-024241, with comparable mass, age and spectral type as CT4. Likewise, Comerón et al. [2010] reported  $\log \dot{M} \sim -9.02 M_{\odot} \text{yr}^{-1}$  for another deuterium burning brown dwarf GY 11. The higher value of requisite rate of accretion suggests that it is unlikely for the stronger superflare to occur due to magnetospheric accretion process.

The TRAPPIST-1 planetary system [Gillon et al., 2016, 2017; Luger et al., 2017] demonstrates the existence of planets around low-mass stars and BDs, increasing the importance of the study of planet formation around low-mass stars and BDs. The superflares observed on CT4 will be very helpful to understand how such flares impact the dynamical and chemical evolution of disk around it. Such flares result to enhanced UV and X-ray emission which can create innerhole in the disk through photoevaporation [Owen et al., 2011]. The high energy X-rays also increase the ionization of the disk, which might trigger magnetorotational instability (MRI) that is supposed to drive magneto-hydrodynamical turbulence in the protoplanetary disk. This has several consequences on planet formation and depends on the energy of X-rays [Feigelson, 2010; Cleeves et al., 2015]. In addition, the study of superflares on young objects like CT4 might be helpful in explaining the mysteries regarding the formation of the chondrules and the calcium-aluminium-rich inclusions (CAIs), which need transient heat sources

to melt the precursor material. It is impossible to explain the formation of these materials in the context of thermodynamic equilibrium between the PMS stars and the disks around them. Some possible proposed transient heat sources are nebular lightning, protoplanetary induced shocks, activity associated with the young star having disk, and nearby Gamma Ray Burst (GRB) [McBreen and Hanlon, 1999; Desch and Cuzzi, 2000; Duggan et al., 2001; Feigelson et al., 2002]. If strong flares acted as heating sources for formation of chondrules/CAIs, it is unclear how they were transported to the Asteroid belt [Feigelson, 2005].

## Chapter 6

### HIGH SUPERFLARE RATES ON RAPIDLY ROTATING LATE-M DWARFS

#### 6.1 Introduction

As mentioned in Chapter 1, it is important to constrain the flare rates of M dwarfs as a function of their masses and ages to assess the habitability of M dwarf planets. We can see from Chapter 3 that some M dwarfs have multiple superflares within a single campaign of *K2* observation. However, it might be more useful to analyze the largest superflares with huge energies, since they are more capable of posing serious problems on the exoplanets in the habitable zones around the M dwarfs. In this chapter, I analyze some largest superflares observed on three late-M dwarfs: 2MASS J08315742+2042213 (hereafter 2M0831+2042), 2MASS J08371832+2050349 (hereafter 2M0837+2050) and 2MASS J08312608+2244586 (hereafter 2M0831+2244). Those superflares were also mentioned in Chapter 3 and they will be analyzed more thoroughly in this chapter. In Section 6.2, I discuss the physical and photometric characteristics of the targets. In Section 6.3, I present the data reduction, flare photometry and flare energy computation. I discuss the results in Section 6.4.

#### 6.2 Target Characteristics

The properties of three targets are listed in Table 6.1. The corresponding properties of TRAPPIST-1 are also listed in the same table to enable readers to compare its properties with other stars studied in this paper. In addition, the new estimates of radial velocities (RVs) and *UVW* components of space motion of the targets are listed. The RVs were measured via cross correlation of SDSS spectra to the [Bochanski et al. \[2007\]](#) template spectra, and the *UVW* were calculated from photometric distances

and proper motions from SDSS-2MASS-WISE coordinates, described in Schmidt et al. (2019, in prep.).

The stars 2M0831+2042 and 2M0837+2050 have spectral types of M7 and M8 respectively [West et al., 2011]. Both objects are members of the open cluster Praesepe [Boudreault et al., 2012], which is also known as the Beehive Cluster, M44 or NGC 2632. Gaia Collaboration et al. [2018a] estimate the distance of this cluster to be 186.2 pc (distance modulus = 6.350) and its age to be  $\sim 700$  Myr. The M7 and M8 stars mentioned above have H $\alpha$  emission with equivalent width (hereafter EW)  $9.3 \pm 0.3$  and  $20.3 \pm 0.6$  Å respectively [Schmidt et al., 2015].

2M0831+2244 is an M9 dwarf [West et al., 2011] located at a distance of 74.0 pc [Gaia Collaboration, Brown, Vallenari, Prusti, de Bruijne, Babusiaux, and Bailer-Jones, 2018b]. It has an H $\alpha$  emission with EW  $7.3 \pm 0.5$  Å [Schmidt et al., 2015]. It has a tangential velocity of  $\sim 21$  km s $^{-1}$  suggesting that it is younger than another late-M dwarf TRAPPIST-1 which has a tangential velocity of  $\sim 60$  km s $^{-1}$ . Youth is also supported by its rotation period of  $\sim 7$  hrs measured by *K2*. The BANYAN  $\Sigma$  tool [Gagné et al., 2018] suggests that it is not a member of any known nearby moving groups or stellar associations within 150 pc, by using astrometry measured by *Gaia* and the RV listed in Table 6.1. So 2M0831+2244 is probably a field star.

Table 6.1: Properties of targets

PHOTOMETRIC PROPERTIES							
Target name	sp. type	$K_p$ (mag)	$J$ (mag)	$K$ (mag)	$i$ (mag)	$H\alpha$ EW Å	
2M0831+2042	M7	19.6	15.56±0.06	14.70±0.09	18.51±0.01	9.3±0.3 <sup>a</sup>	
2M0837+2050	M8	20.0	15.90±0.07	14.88±0.09	18.80±0.01	20.3±0.6 <sup>a</sup>	
2M0831+2244	M9	19.8	14.91±0.04	13.84±0.04	18.77±0.01	7.3±0.5 <sup>a</sup>	
TRAPPIST-1	M8	15.9	11.35±0.02	10.30±0.02	15.11±0.00	4.9 <sup>b</sup>	
KINEMATIC PROPERTIES							
	$\mu_\alpha$ (mas yr <sup>-1</sup> )	$\mu_\delta$ (mas yr <sup>-1</sup> )	$V_{\tan}$ (km s <sup>-1</sup> )	RV (km s <sup>-1</sup> )	$U$ (km s <sup>-1</sup> )	$V$ (km s <sup>-1</sup> )	$W$ (km s <sup>-1</sup> )
2M0831+2042	-35.8±0.9	-13.5±0.5	34	38 ±11	41±12	10 ±12	1 ±12
2M0837+2050	-39.2±1.2	-13.3±0.6	37	30±12	23±10	2±16	8.3±8.3
2M0831+2244	59.7±0.9	-2.41±0.59	21	4±25	-16 ±19	12±8.4	21 ±13
TRAPPIST-1	924±4 <sup>c</sup>	-467±3 <sup>c</sup>	60	-53 <sup>d</sup>	-44 <sup>e</sup>	-67 <sup>e</sup>	16 <sup>e</sup>
EPIC IDS AND OTHER PROPERTIES							
	EPIC ID	Member	Age	parallax	period		
2M0831+2042	212027121	Praesepe	~700 Myr	5.36±0.05 mas	0.556±0.002 d		
2M0837+2050	212035340	Praesepe	~700 Myr	5.36±0.05 mas	0.193±0.000 d		
2M0831+2244	212136544			13.5±0.6 mas	0.292±0.001 d		
TRAPPIST-1	200164267		7.6±2.2 Gyr <sup>f</sup>	82.4±0.8 <sup>g</sup> mas	3.29 ±0.07 d		

**Note:**

- i) Spectral types are from West et al. [2011] and Liebert and Gizis [2006].
- ii)  $J$  and  $K$  magnitudes are from 2MASS Survey [Cutri et al., 2003].
- iii)  $i$  magnitudes are from Pan-STARRS Survey [Chambers et al., 2016].
- v) The distances and proper motions are from *Gaia* DR2 except for TRAPPIST-1.

**References:**

<sup>a</sup>Schmidt et al. [2015]; <sup>b</sup>Gizis et al. [2000]; <sup>c</sup>Theissen [2018]; <sup>d</sup>Reiners et al. [2018]; <sup>e</sup>Reiners and Basri [2009]; <sup>f</sup>Burgasser and Mamajek [2017]; <sup>g</sup>Van Grootel et al. [2018]

## 6.3 Data reduction and computations

### 6.3.1 *K2* photometry

All three objects were observed by the *K2* mission twice: once in Campaign 5 (27 April, 2015 - 10 July, 2015), and once in Campaign 18 (12 May, 2018 - 02 July, 2018). Both observations were obtained in long cadence ( $\sim 30$  minute) mode [Jenkins et al., 2010]. Additionally, 2M0831+2042 was observed in Campaign 16 (07 December, 2017 - 25 February, 2018). I performed point source function (psf) photometry to extract the lightcurves of the targets from their Target Pixel Files (TPFs). For this I also used the Python package ‘Lightkurve’ [Vinícius, Barentsen, Hedges, Gully-Santiago, and Cody, 2018]. The lightcurves were then detrended using the *K2* Systematics Correction (‘K2SC’, Aigrain et al. [2016]). The median count rates of 2M0831+2042, 2M0837+2050 and 2M0831+2244 are 192, 132 and 163 counts  $s^{-1}$  respectively. The *Kepler* magnitude ( $\tilde{K}_p$ ) of each object is listed in Table 6.1.  $\tilde{K}_p$  was estimated using the Lund et al. [2015] relation  $\tilde{K}_p \equiv 25.3 - 2.5\log(\text{count rate})$ . I used only good quality ( $Q = 0$ ) data points for flare photometry presented in this paper.

Using the Lomb-Scargle periodogram (hereafter LSP), periodic features with periods of  $0.556 \pm 0.002$ ,  $0.193 \pm 0.000$  and  $0.292 \pm 0.001$  d were detected in the lightcurves of 2M0831+2042, 2M0837+2050 and 2M0831+2244 respectively. The uncertainties in the periods are based on half width at half maximum (HWHM) of the periodogram peaks [Mighell and Plavchan, 2013]. These periods might be due to spot modulations of the objects: if so, the features most likely represent their rotation periods. If this is correct, the fastest rotator among our targets (2M0837+2050) rotates in a period which is shorter than 97% of the M dwarfs which are classified as “Class A rotators” by Newton et al. [2016]. Interestingly, this target turns out to be the site of the largest flare we report in this paper. The phase folded light curves of three targets are shown in Figure 6.1, 6.2 and 6.3 respectively. The corresponding periodogram is also shown inside each figure.

### 6.3.2 Flare detection and estimation of flare energies

I used the method described in Section 2.3 of Chapter 2 to identify the flares on the targets. In the case of light curves measured in the long cadence mode, very small flares have relatively small amplitudes and last only for a few minutes (less than the duration of one long cadence at  $\sim 30$  minutes). They show up as single point brightening. Because of this, they do not qualify as flare candidates and hence are difficult to identify by using robust statistical techniques.

I identified one strong superflare on 2M0831+2042, one on 2M0837+2050, and five superflares on 2M0831+2244 in Campaign 18 light curves. I also identified four superflares on 2M0837+2050 in Campaign 5 data. The peak flare times, equivalent durations, changes in *Kepler* magnitude ( $\tilde{K}_p$ ) and flare durations of each superflares are listed in Table 6.2. I plot the strongest superflares on our targets in Figure 6.4, 6.5 and 6.6. Likewise, I plot the remaining superflares identified on 2M0831+2050 in Figure 6.7 and those on 2M0831+2244 in Figure 6.8 respectively. In each plot, the flare flux is normalized by the median flux in the corresponding light curve. The time on the top of each plot is the peak flare (*Kepler* mission) time of the corresponding flare inside the plot.

I used the method described in Section 2.3.3 of Chapter 2 to estimate the flare energies of superflares identified on the targets. I report here that a flare with ED of 1 s on 2M0831+2042 has an energy of  $2.6 \times 10^{30}$  erg. Likewise, a flare with ED of 1s on 2M0837+2050 has  $2.1 \times 10^{30}$  erg and a flare with ED of 1 s on 2M0831+2244 has  $3.4 \times 10^{29}$  erg. I estimated the flare energies by multiplying these energies with the EDs of flares observed on corresponding targets. All the flare energies are listed in Table 6.2 and they include the UV/visible/IR wavelengths.

It should be noted that the flare duration of some large flares are longer than the rotational periods of the stars. In such cases, the estimated flare energies would be

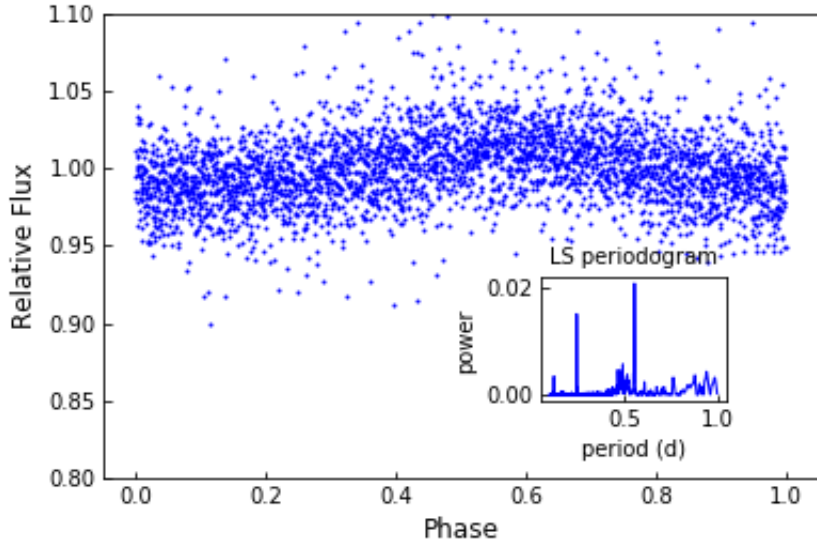


**Figure 6.1:** The phase folded *K2* Campaign 5 light curve of M7 dwarf 2M0831+2042 corresponding to period of 0.556 d. The LSP is also shown inside. The second peak in the LSP corresponds to instrumental noise of  $\sim 0.25$  d.

less than the real values if the flaring region is not located at polar region. The phase folded light curves shown in Figure 6.1, 6.2 and 6.3 however suggest that the rotational modulations lead to underestimation of the flare energies by very small fraction.

### 6.3.3 Comparison of flare rates with TRAPPIST-1

In Figure 6.9 (left plot), I compare the flare frequency distribution of TRAPPIST-1 with two of the targets: 2M0837+2050 and 2M0831+2244. This is a log-log plot of cumulative frequency( $\tilde{\nu}$ ) of flare energies. The cumulative frequency of flares with energy  $E$  is the number of flares with energies  $\geq E$ . The flare energies of TRAPPIST-1 are taken from Paudel et al. [2018a]. The total observation time of TRAPPIST-1 is 70.6 days and there are 39 flares with energies in the range  $(0.65 - 710) \times 10^{30}$  erg in the UV/visible/IR wavelengths. The total observation times of 2M0837+2050 and 2M0831+2244 are 115.58 and 112.78 days respectively, and include both Campaign 5 and 18.

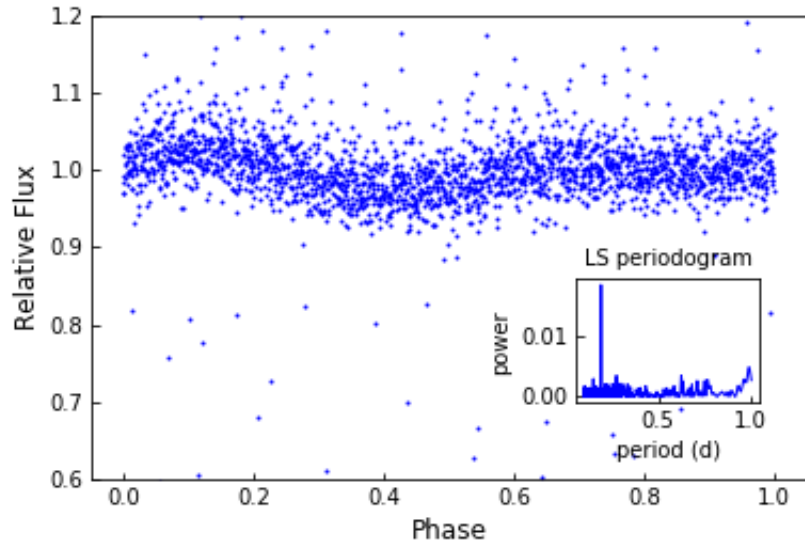


**Figure 6.2:** The phase folded *K2* Campaign 18 light curve of M8 dwarf 2M0837+2050 corresponding to period of 0.193 d. The LSP is also shown inside.

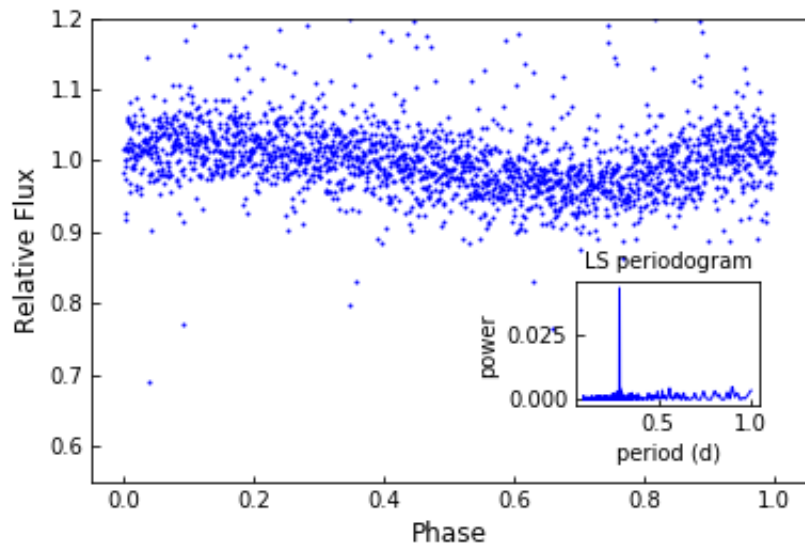


**Figure 6.3:** The phase folded *K2* Campaign 18 light curve of M9 dwarf 2M0831+2244 corresponding to period of 0.292 d. The LSP is also shown inside.

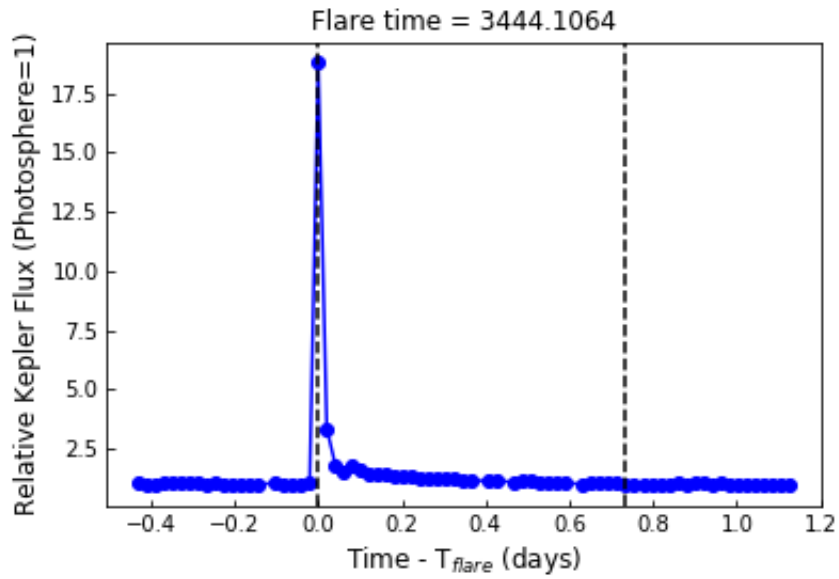


**Figure 6.4:** The superflare observed on M7 dwarf 2M0831+2042. The blue dots represent the observed data, and the vertical dashed lines represent the start and end times of the flare. The time along the  $X$ -axis is centered at the peak flare time.

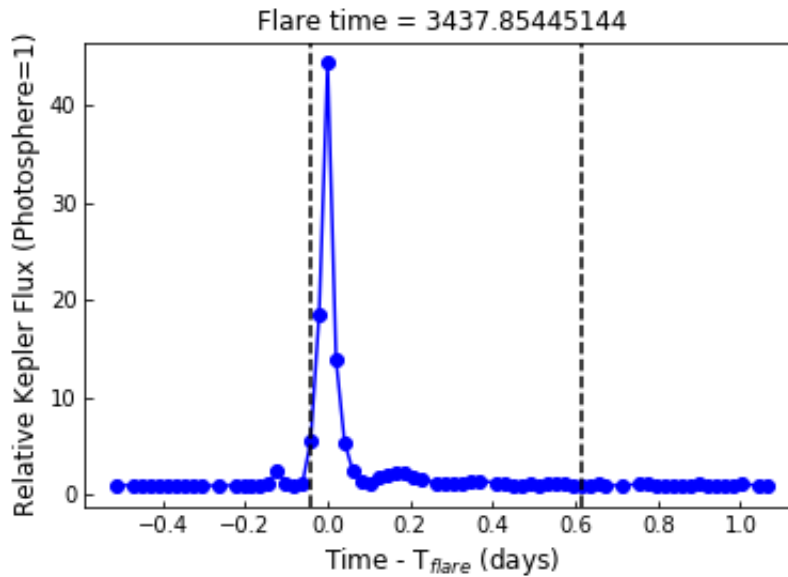


**Figure 6.5:** The largest superflare observed on M8 dwarf 2M0837+2050. The blue dots represent the observed data, and the vertical dashed lines represent the start and end times of the flare. The time along the  $X$ -axis is centered at the peak flare time.

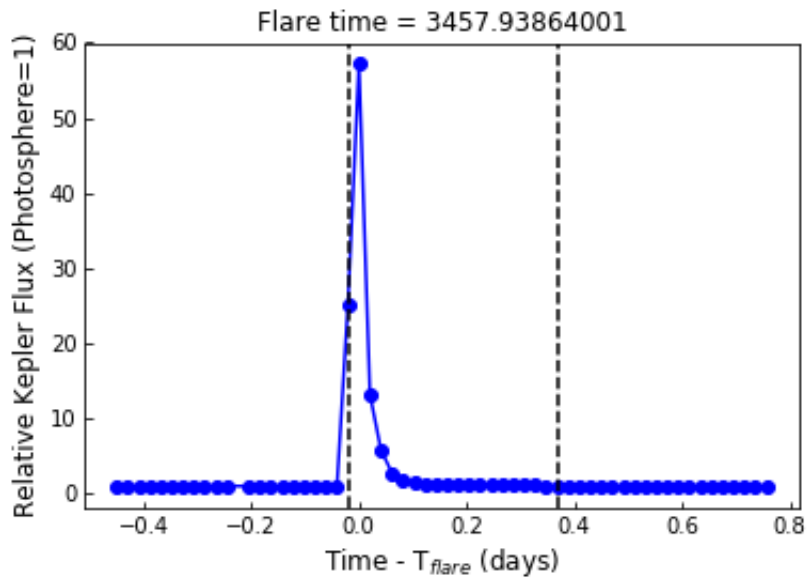


**Figure 6.6:** The largest superflare observed on M9 dwarf 2M0831+2244. The blue dots represent the observed data, and the vertical dashed lines represent the start and end times of the flare. The time along the  $X$ -axis is centered at the peak flare time.

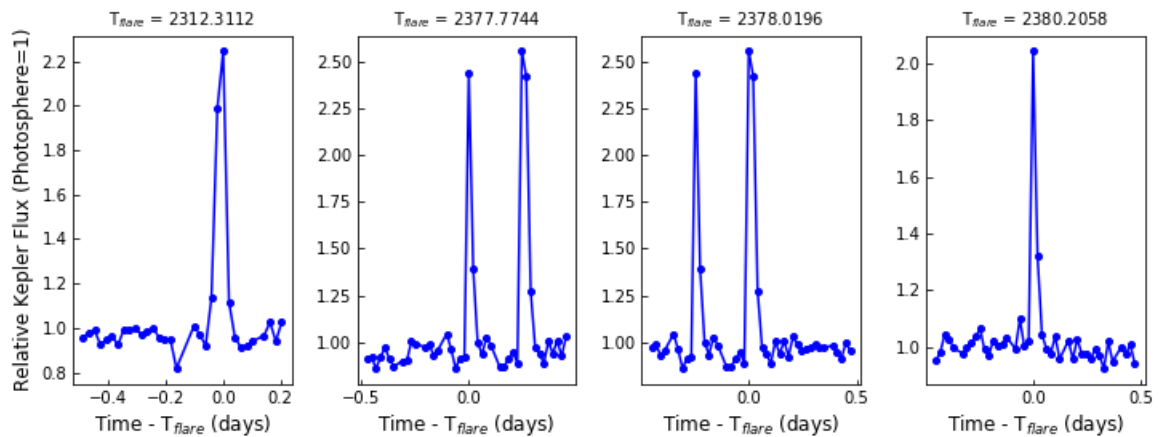


**Figure 6.7:** Other superflares observed on 2M0837+2050 in Campaign 5 data. The blue dots represent the observed data and the time is centered at peak flare time. Though the second and the third plots are similar, the only difference is the peak flare time mentioned on the top of them, corresponding to each flare.

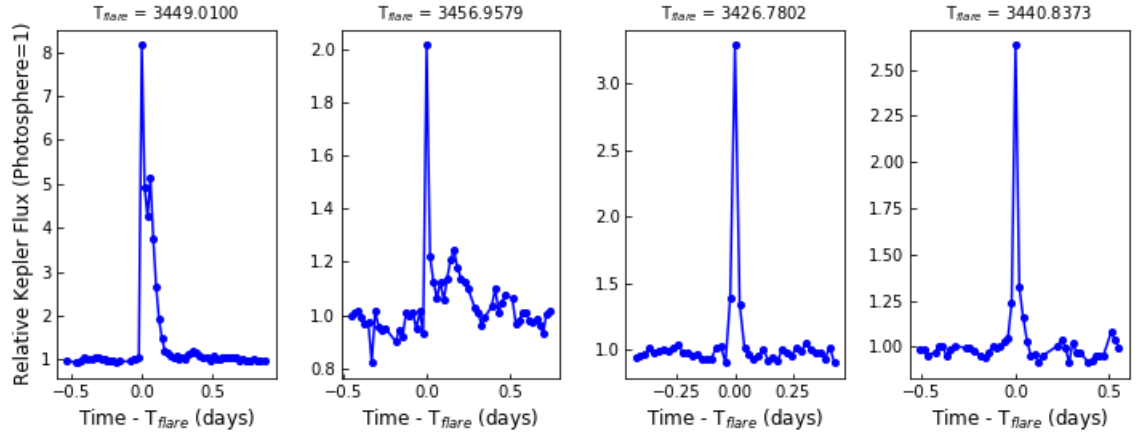


**Figure 6.8:** Other superflares observed on 2M0831+2244. The blue dots represent the observed data and the time is centered at peak flare time.

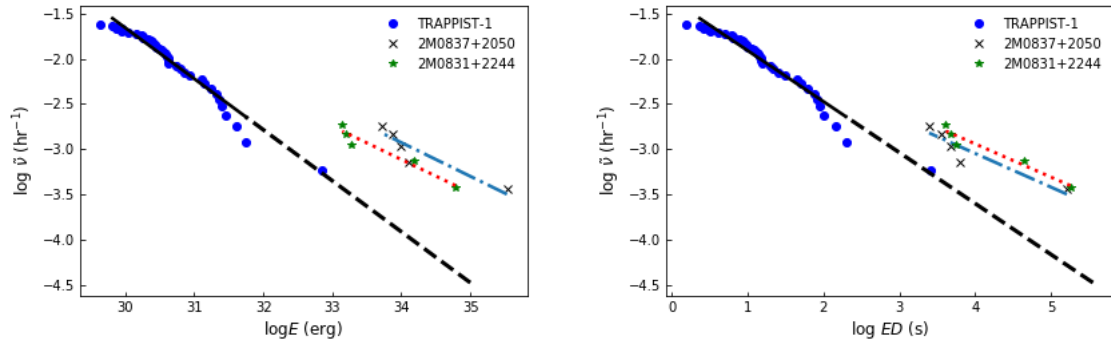


**Figure 6.9:** **Left:** Comparison of flare frequency distribution of TRAPPIST-1 with 2M0837+2050 and 2M0831+2244. The solid black line plotted over TRAPPIST-1 flare energies is fitted line using parameters from [Paudel et al., 2018a] and the dashed black line represents extrapolation to energy  $\log E$  (erg) = 35. **Right:** Same as the figure in left. The flare energies are replaced by corresponding EDs.

**Table 6.2: Properties of superflares**

Target	$T_{\text{peak}}$ (BJD - 2454833)	$\Delta\tilde{K}_p$	ED (hr)	Energy (erg)	flare duration (d)
2M0831+2042	3444.1064	-3.2	13.7	$1.3 \times 10^{35}$	0.74
2M0837+2050	3437.8544	-4.1	46.4	$3.5 \times 10^{35}$	0.65
2M0837+2050	2378.0196	-1.1	1.7	$1.3 \times 10^{34}$	0.06
2M0837+2050	2312.3112	-1.0	1.3	$1.0 \times 10^{34}$	0.06
2M0837+2050	2377.7744	-1.1	1.0	$7.4 \times 10^{33}$	0.04
2M0837+2050	2380.2058	-0.9	0.7	$5.2 \times 10^{33}$	0.04
2M0831+2244	3457.9386	-4.4	50.21	$6.1 \times 10^{34}$	0.40
2M0831+2244	3449.0100	-2.3	12.6	$1.5 \times 10^{34}$	0.50
2M0831+2244	3426.7801	-1.3	1.6	$1.9 \times 10^{33}$	0.06
2M0831+2244	3456.9579	-0.8	1.3	$1.6 \times 10^{33}$	0.31
2M0831+2244	3440.8373	-1.1	1.2	$1.4 \times 10^{33}$	0.08

The flare energy distribution of TRAPPIST-1 follows a power law of form

$$\log \tilde{\nu} = \alpha - \beta \log E \quad (6.1)$$

with  $\beta \sim 0.6$  [Vida et al., 2017; Paudel et al., 2018a]. In the case of TRAPPIST-1, the black solid line represents this distribution of observed flare energies while the dashed black line represents the extrapolation of the fitted line up to flare energy of  $10^{35}$  erg to make it easier to compare with the other two targets. The extrapolation may not necessarily represent the true distribution. Likewise, the dashed lines overplotted on flare energies of 2M0837+2050 and 2M0831+2244 also represent the fitted lines. However, the lack of sufficient data point means they may not be the best representation of the real flare energy distribution of the corresponding targets. We should note here that TRAPPIST-1 light curves were obtained in short cadence ( $\sim 1$  minute) mode while we do not have such light curves for 2M0837+2050 and 2M0831+2244. This is why flares of smaller energies were not detected on the targets studied here.

In Figure 6.9 (right plot), I compare the flare rates using the EDs of flares.

### 6.3.4 X-ray energy emitted during the largest flare on 2M0837+2050

To understand the relative impact of these superflares on exoplanets, these superflares are placed in the solar context using the *GOES* (Geostationary Operational Environmental Satellite) flare classification scheme. The *GOES* flare classification scheme (A, B, C, M, X) is based solely on the peak 1–8 Å soft X-ray solar flux as observed from Earth, and each letter represents an increased order of magnitude from  $10^{-8} \text{ W m}^{-2}$  to  $10^{-3} \text{ W m}^{-2}$  as observed at 1 AU. In the units of energy emitted per second, *GOES* A1 flare corresponds to  $2.8 \times 10^{22} \text{ erg s}^{-1}$  and *GOES* X1 flare corresponds to  $2.8 \times 10^{27} \text{ erg s}^{-1}$ . The results of Namekata et al. [2017] are used here to estimate the flare energy in the *GOES* bandpass. They compared the superflares of solar-type stars with the solar white-light flares and found a power-law relation between the white light (WL) flare energy ( $E_{WL}$ , which the authors mention as the total energy radiated by a 10,000 K blackbody), and *GOES* soft X-ray (SXR) flux ( $F_{GOES}$ ). Using Figure 5(b) in their paper, a  $10^{30} \text{ erg}$  WL flare corresponds to  $\sim 6 \times 10^{-5} \text{ W m}^{-2}$  in the *GOES* band. Using this relation, we estimate that  $E_{WL} = 1.67 \times 10^{34} F_{GOES}$ , where the units of  $F_{GOES}$  are  $\text{W m}^{-2}$ . The estimated total WL flare energy of the largest superflare on 2M0837+2050 is  $7.0 \times 10^{35} \text{ erg}^1$ . Using the relation in Namekata et al. [2017], it is estimated that  $F_{GOES} = 42 \text{ W m}^{-2}$  which is equivalent to  $1.2 \times 10^{32} \text{ erg s}^{-1}$ , corresponding roughly to an X43,000 class flare. The X-ray flux in the HZ at 0.02 AU (approximately the location of TRAPPIST-1 d) would be  $1.1 \times 10^5 \text{ W m}^{-2}$  ( $= 1.1 \times 10^8 \text{ erg s}^{-1} \text{ cm}^{-2}$ ). It should be noted that the scaling based on solar-flares may not be necessarily same in the case of late-M dwarfs.

## 6.4 Summary and Discussion

Strong superflares were detected on three late-M dwarfs: 2M0831+2042 (M7 V), 2M0837+2050 (M8 V) and 2M0831+2244 (M9 V), in *K2* long cadence light curves.

---

<sup>1</sup> We obtained this energy by first estimating the total energy in the *Kepler* band ( $E_{Kp}$ ; 400-900 nm) and then converting  $E_{Kp}$  to bolometric energy by using the conversion relations in Osten and Wolk [2015] and Hawley et al. [2014].

The strong superflare observed on 2M0831+2042 has an ED of 13.7 hr and has an estimated energy of  $1.3 \times 10^{35}$  erg. Five superflares were detected on 2M0837+2050 with EDs in the range (0.7 - 46.4) hr and estimated energies in the range  $(5.2 - 350) \times 10^{33}$  erg. Likewise, five superflares were detected on 2M0831+2244 with EDs in the range (1.2 - 50.21) hr and estimated energies in the range  $(1.4 - 61) \times 10^{33}$  erg.

2M0837+2050 and 2M0831+2244 now have the highest known superflare rates among late-M dwarfs. 2M0837+2050 is  $\sim 700$  Myr old and 2M0831+2244 also appears to be young as suggested by its tangential velocity estimate. In addition, they are rapidly rotating with periods of  $0.193 \pm 0.000$  and  $0.292 \pm 0.001$  d respectively, which we detected in their *K2* light curves using Lomb-Scargle periodogram. The high flare rates could be the result of strong magnetic dynamos enhanced by rapid rotation. Our results are in tension with those of [Mondrik et al. \[2018\]](#) who analyzed the flare rates of a sample of 34 mid-to-late M dwarfs. They found that the flare rates are small among the slowest rotators with periods  $>70$  d, but also are small among the fastest rotators with periods  $<10$  d. Maximum flare rates are found among intermediate period rotators with periods of (10 - 70) d.

The rapid rotation rates and hence high flare rates of 2M0837+2050 and 2M0831+2244 could also be the result of their presence in binary systems. [Douglas et al. \[2017\]](#) measured the rotation periods of 677 low-mass stars ( $1 \gtrsim M \gtrsim 0.1 M_{\odot}$ ) in the Praesepe cluster by using *K2* light curves and found that  $\sim 50\%$  of the rapidly rotating  $\gtrsim 0.3 M_{\odot}$  stars are in binary systems. The sample consisted of both confirmed and candidate binary systems but there is no information regarding binarity of the remaining  $\gtrsim 0.3 M_{\odot}$  fast rotators. Furthermore, [Douglas et al. \[2016\]](#) found that almost all  $\gtrsim 0.3 M_{\odot}$  fast rotating stars in the Hyades cluster, with age comparable to the Praesepe cluster, are in binary systems.

#### 6.4.1 Flare rates of $\sim 700$ Myr TRAPPIST-1 like objects

The flare rates of the M8 dwarf 2M0837+2050 are of particular importance for studies which are focused on the atmospheres of planets in the HZ of TRAPPIST-1. This is because both 2M0837+2050 and TRAPPIST-1 have a similar spectral type (M8) but different ages ( $\sim 700$  Myr, 7.6 Gyr respectively). I compare the flare frequency distributions of the two targets in Figure 6.9. The energy of the largest flare on 2M0837+2050 is larger by 2.7 orders of magnitude than the largest flare observed on TRAPPIST-1 and occurs at approximately the same occurrence rate. The results presented here may provide some guidance as to how large flares could have been on TRAPPIST-1 during its youth. While we do not have enough flares to reliably constrain the flare rates, the observed flares suggest that  $10^{34}$  erg flares occur on 2M0837+2050 at a 10 times higher rate than on TRAPPIST-1. To be sure, the two M8 stars are not exactly comparable because 2M0837-2050 rotates almost 20 times faster than TRAPPIST-1. In view of this faster rotation, it is hardly surprising that the flare energy on 2M0837+2050 is hundreds of times larger than the largest flare on TRAPPIST-1.

The higher superflare rate of M9 dwarf 2M0831+2244 also supports the result in the previous paragraph. Comparison of the tangential velocity of TRAPPIST-1 ( $\sim 60$  km  $s^{-1}$ ) with that of the 2M0831+2244 ( $\sim 21$  km  $s^{-1}$ ) suggests that the latter is a younger object, with an age less than 7.5 Gyr. 2M0837+2050 and 2M0831+2244 have almost identical flare frequency distributions as seen in Figure 6.9. The small differences between them might be due to differences in the rotation rates and/or the effective temperatures. The larger EW of H $\alpha$  emission of 2M0837+2050 is also consistent with a higher flare rate than 2M0831+2244.

In Figure 6.9 (right plot), I compare the rates using only the EDs of flares. It suggests that the rates are almost similar for 2M0837+2050 and 2M0831+2244. However, we have only one data point of TRAPPIST-1 for which the ED value overlaps with the

EDs of 2M0837+2050 and 2M0831+2244 flares. Though this single data point suggests that flares with comparable EDs occur more frequently on younger targets, we cannot perform any further statistical analysis and conclude anything at this point.

#### 6.4.2 Particle flux associated with the largest superflare on 2M0837+2050

In Section 6.3.4, it is estimated that the largest superflare from 2M0837+2050 is  $\sim$ X43,000 class in the *GOES* classification scheme of solar flares. For comparison, the Carrington event of 1859, probably the largest solar flare ever recorded, was  $\sim$ X45 class [Cliver and Dietrich, 2013]. Segura et al. [2010] estimate that the Great AD Leo flare [Hawley and Pettersen, 1991] was X2300 class, and the extreme flare from young M dwarf binary DG CVn that triggered the Swift Burst Alert Telescope was estimated to be X600,000 class [Osten et al., 2016]. Solar flares  $>$ X10 class have a  $\sim$ 100% probability of accompaniment by a CME [Yashiro et al., 2006], but events larger than the Carrington event have never been observed from the Sun and the relationship between CME properties and superflares is not yet known (e.g., Aarnio et al. 2011). To estimate the particle flux associated with the largest superflare on 2M0837+2050, we use the recently published results of Herbst et al. [2019] who combined the *GOES* data with the SphinX data and estimated a new power-law for the peak size distribution of solar proton flux. The scaling relations of solar proton flux and soft X-ray flux are also derived by Cliver et al. [2012] and Takahashi et al. [2016]. Herbst et al. [2019] found that the solar proton flux and  $F_{GOES}$  ( $\text{W m}^{-2}$ ) are related as:  $F(>10 \text{ MeV in pfu}) = (1.22 \times 10^5 F_{GOES} + 3.05 \exp(-0.001 F_{GOES}))^{1.72}$ . Extending this solar scaling relation out to observationally unconstrained superflare regime, we find that  $F_{GOES} = 42 \text{ W m}^{-2}$  obtained in Section 6.3.4 leads to  $F(>10 \text{ MeV}) = 3.5 \times 10^{11} \text{ pfu}$  at 1 AU. This corresponds to a value of  $8.7 \times 10^{14} \text{ pfu}$  at 0.02 AU. For comparison, the  $>10 \text{ MeV}$  proton flux that Segura et al. [2010] estimated would have impacted a hypothetical HZ planet at 0.16 AU for the Great AD Leo flare was  $6 \times 10^8 \text{ pfu}$ , and this proton flux was sufficient to destroy 94% of the  $\text{O}_3$  column density of a modeled Earth-like planet.

In the case of some highly energetic SEP events (470 MeV to 4 GeV), the acceleration site of protons is CME driven shock which is located at 5-15  $R_{\odot}$  [Kahler, 1994]. Such distance is equivalent to  $\sim(0.002 - 0.007)$  AU in the case of M8 dwarfs which have an average radii of  $\sim 0.1R_{\odot}$ , and is closer than the average orbital radii of HZ around them. This implies that it is possible for such protons to be injected out during the superflares on 2M0837+2050. However, this interpretation is solely based on the SEP events observed on the Sun. Furthermore, the average magnetic field strength of active M8 stars is much stronger than that of our Sun, and the magnetic field topology of active M dwarfs might be different from that of our Sun (e.g., Donati and Landstreet 2009) and hence the acceleration site of the protons.

#### 6.4.3 Estimation of CME masses associated with the superflares on 2M0837+2050

In studies of the Sun and active solar analog stars, a strong correlation has been observed between the radiative energy emitted by a flare and the mass ejected in the associated coronal mass ejection (CME). For example, Aarnio et al. [2011] showed that for the Sun, the flare energy emitted in X-rays correlates with CME mass in a power-law relationship. Aarnio et al. [2012] showed that the same solar relationship can be extended to extremely active, young solar-type stars, such that one relationship applies to X-ray flare energies spanning  $10^{28}$  to  $10^{38}$  erg, and the most energetic flares having associated CME masses of  $\sim 10^{22}$  g [Aarnio et al., 2012]. Osten and Wolk [2015] argued that this flare-CME relationship has a physical basis that is scalable and generally applicable to flaring stars from solar type down to mid-M type. Thus, it should be possible to apply empirically calibrated flare-CME relationships to the flares observed in our sample. The bolometric energies of superflares on 2M0837+2050 are in the range  $\sim 1.0 \times 10^{34}$  -  $\sim 7.0 \times 10^{35}$  (see footnote in Section 6.3.4 for the estimation of bolometric energies), whereas the empirical relationship of Aarnio et al. [2012] applies to the X-ray emitted energy. However, as discussed by Günther et al. [2019], the empirical conversions between X-ray flare energies to bolometric flare energies (see, e.g., Maehara et al. 2015) suggest that to good approximation one can adopt the

relationship  $E_{\text{bol}} \approx 10^2 E_{X\text{-ray}}$ . Therefore, as in [Günther et al. \[2019\]](#), the empirical relation of [Aarnio et al. \[2012\]](#) is modified as  $M_{\text{CME}} = (2.7 \pm 1.2) \times (0.01 E_{\text{flare}})^{0.63 \pm 0.04}$ , where  $E_{\text{flare}}$  is the bolometric flare energy and all units are cgs. We infer CME masses associated with our observed flares to be in the range of  $\sim 10^{20.6}$  g to  $\sim 10^{21.8}$  g.

#### 6.4.4 Comparison of superflare on 2M0837+2050 with that on M2 dwarf GSC 8056-0482 for possible UV flux estimates

It is also instructive to compare the flare we discovered on one of our targets with a flare on another M dwarf, although they differ in their global properties. The superflare which we have discovered on the M8 dwarf 2M0837+2050 is larger by  $\sim 100\times$  than the  $\sim 4 \times 10^{33}$  erg flare observed on GSC 8056-0482 by [Loyd et al. \[2018\]](#). The latter star (hereafter GSC) differs from our target star 2M0837+2050 in that it is warmer (sp. type = M2,  $T_{\text{eff}} \sim 3440$  K; [Pecaut and Mamajek 2013](#)) and younger ( $\sim 40$  Myr; [Kraus et al. 2014](#)). In view of these differences, we need to exercise caution in making comparisons. The FUV energy of the superflare on GSC was estimated to be  $10^{32.1}$  erg and is the largest energy flare ever observed in the FUV with the *Hubble Space Telescope (HST)*. Assuming the same ratio (18%: [Loyd et al. 2018](#)) of FUV energy to bolometric energy of the GSC flare, we estimate that the FUV energy of our superflare on 2M0837+2050 is  $> 6.3 \times 10^{34}$  erg. This suggests that the FUV energy emitted during the superflare on 2M0837+2050 is greater than that on GSC by more than 2.7 orders of magnitude.

[Loyd et al. \[2018\]](#) analyzed FUV flares on 12 M dwarfs in the  $\sim 40$  Myr Tuc-Hor young moving group, with spectral types M0.0-M2.3. They found that the flares on those M dwarfs were 100-1000 $\times$  more energetic than those on field age ( $\sim 1 - 9$  Gyr) M dwarfs. Combining their results with those we obtained in this paper, it is possible that strong flares with FUV energy in excess of  $10^{36}$  erg can occur on the young  $\sim 40$  Myr M8 dwarfs. If superflares with energies of  $10^{36}$  ergs occur frequently on young M8 dwarfs, the large amount of UV flux in the superflares may have serious consequences

on the atmospheres of planets in HZ including complete loss of O<sub>3</sub> column [Segura et al., 2010; Tilley et al., 2017; Youngblood et al., 2017; Howard et al., 2018]. Such results will be very important to study the environment around planet-hosting stars like TRAPPIST-1 when they were very young.

#### 6.4.5 Timescales of planet formation and life on Earth

The median lifetime of circumstellar disks, the planets forming regions, is  $\sim 3$  Myr and the dissipation rate is slower in case of low mass stars than that of high-mass stars [Williams and Cieza, 2011]. The disk lifetimes of M dwarfs are of the order of  $\sim 10$  Myr. This is inferred from the fact that the dust disk around young M dwarfs are similar to those around T-Tauri stars whose disk life timescales are  $\sim 10$  Myr [Boss, 2006; Pascucci et al., 2011]. On the other hand, the timescale of formation of rocky planets in our solar system is  $\sim 10$ -120 Myr and that of gas giants is  $< 5$  Myr. A longer disk lifetime of M dwarfs may indicate a different timescale of planet formation around them [Apai, 2013]. It is very likely the M dwarf planets might have already formed at ages of the Praesepe cluster ( $\sim 700$  Myr).

On the other hand, the emergence of life also requires a minimum amount of time: in the only system for which we have data, it appears that an interval of some 200 Myr elapsed between the time of Earth formation and the time when the oldest known life emerged [Dodd et al., 2017]. If this time-scale is relevant to emergence of life on exoplanets, then the level of flare activity on a star whose age is less than 200 Myr may not be relevant to astrobiology. The timescale for decay in superflare rate may also set timescale for life emergence. The latter also depends on planet properties such as the presence of magnetic fields.

#### 6.4.6 How can the superflares be beneficial to studies regarding CMEs associated with stellar flares?

The presence of strong superflares highlights the importance of studying the distribution of magnetic field strengths on late-M dwarfs. Information about field strengths is necessary if we are to determine whether they are strong enough to suppress the CMEs associated with the strong superflares. For example, [Alvarado-Gómez et al. \[2018\]](#) estimated that a large-scale dipolar field of strength 75 G is sufficient to suppress the escape of the largest solar-like CMEs with kinetic energies of  $\sim 3 \times 10^{32}$  erg. Assuming that the requisite field strength  $B$  to suppress a CME of a certain kinetic energy (KE) scales in such a way that  $B^2/8\pi \sim \text{KE}$ , [Mullan et al. \[2018\]](#) have argued that a global stellar field of 750 G could suffice to suppress CMEs in Trappist-1 with  $\text{KE} = 3 \times 10^{34}$  ergs. Using the same scaling, magnetic fields of order 7.5 kG may be required to suppress CMEs with  $\text{KE} = 3 \times 10^{36}$  ergs. Such suppression of energetic CMEs seems possible in some M dwarfs similar to WX UMa on which strong mean magnetic fields of strength 7.0 kG exist [[Shulyak et al., 2017](#)]. But we do not know the upper limit of the flare energy and the KE of CMEs that can be emitted by an M dwarf of given mass and age. Hence it is important to the study of evolution of M dwarf flares through time to know the maximum flare energies that can be produced by each spectral type at different ages. In addition, we need more simultaneous observations of M dwarf flares at multiple wavelengths to constrain the flare energy distribution, which together with the maximum flare energies will enable us to estimate the total energy budgets received by the planets from their parent stars. Such energies will be valuable inputs to exoplanet atmosphere and climate models. If information can be obtained as to the time  $T$  which must elapse before life emerges on an exoplanet, then the results of atmosphere and climate models at times  $> T$  could help put constraints on the habitability of planets in the HZ of M dwarfs.

#### 6.4.7 Possible benefits of superflares to the planets in the HZ of M dwarfs

The superflares could also be beneficial to the planets in the HZ of M dwarfs. In an Earth-like planet orbiting within the classical HZ of a solar-type star or M dwarf, an H/He envelope having mass-fraction (ratio of mass of envelope to mass of core,  $M_{env}/M_{core}$ ) of the order of 1% may lead to very high surface temperatures and pressures unsuitable for the existence of liquid water. However, liquid water can be retained if the H/He envelope mass-fraction can be reduced to  $\ll 10^{-3}$  via photoevaporation or other mechanisms (Owen and Mohanty 2016 and references therein). In this regard, the superflares may be helpful to strip off the thick H/He envelope if it is present. In addition, the superflares could help in producing haze forming monomers through photolysis of methane, in planets whose atmosphere is dominated by methane. The hazes might shield the planet's surface from UV radiation which in certain circumstances can be harmful to life [Tilley et al., 2017]. Moreover, enhancement of photon fluxes is not always harmful to life. Certain UV photons can be beneficial for the onset of life by contributing to generation of the bases which occur in nucleic acids [Airapetian et al., 2016; Ranjan et al., 2017]. And as another example of positive consequences of enhanced photon fluxes, we note that the optical photons which are enhanced during flares will increase the effectiveness of oxygenic photosynthesis in a planet lying in the HZ of a flare star [Mullan and Bais, 2018].

## Chapter 7

### 2MASS J10274572+0629104: THE VERY SHORT PERIOD YOUNG M6 DWARF BINARY SYSTEM IDENTIFIED IN *K2* DATA

#### 7.1 INTRODUCTION

It is known that  $\sim 25\%$  of M dwarfs are found to be in binary or higher order multiple systems [Duchêne and Kraus, 2013], and UCDs have a binary fraction of  $20\pm 4\%$  [Allen, 2007]. The existence of planets around M dwarfs [Dressing and Charbonneau, 2015; Gillon et al., 2016, 2017; Luger et al., 2017] imply that the study of various fundamental parameters such as rotational period, multiplicity, age, etc, is important for characterizing these planets. The rotational period, in particular, measures the angular momentum evolution of M dwarfs, and can be used for estimating their ages - when combined with other properties like activity and color. Rotation also plays a role in powering the magnetic dynamo of fully convective stars with masses  $M < 0.35M_{\odot}$  (Newton et al. 2016 and references therein).

There are different methods of identifying binary systems, including direct imaging, radial velocity (RV) variability, spectral blend inversion, astrometric variability and overluminosity on color magnitude diagrams (Bardalez Gagliuffi et al. 2014 and references therein). These methods are biased toward different types of binary systems based on separations, mass ratios and/or luminosity ratios. The high precision photometry of the *Kepler* and *K2* missions [Koch et al., 2010; Howell et al., 2014] have provided another binary detection method: beat patterns in the combined light curves of variable stars with different rotation periods. Such patterns were seen in *Kepler* light curves of rapidly rotating M dwarfs studied by Rappaport et al. [2014]. Here we report the discovery of a very low-mass binary by this method: 2MASS J10274572+0629104

(hereafter 2M1027+0629) which most likely consists of two mid-M dwarfs with very similar rotation periods.

2M1027+0629 (aka SDSS J102745.73+062910.1) was previously reported as a single M6 red dwarf by [West et al. \[2011\]](#). It has a high quality SDSS spectrum which shows H $\alpha$  emission with an equivalent width of  $9.6 \pm 1.4 \text{ \AA}$ . In Section 7.2, I describe *K2* photometry, *Gaia* DR2 astrometry and photometry, NIRSPEC spectroscopy of 2M1027+0629, and white light flares observed on it. In Section 7.3 I discuss the results of observations obtained by *K2*, *Gaia* and NIRSPEC.

## 7.2 OBSERVATIONS

### 7.2.1 *K2* photometry

2M1027+0629 was monitored continuously by *Kepler K2* mission [[Howell et al., 2014](#)] in long cadence ( $\sim 30$  minutes, [Jenkins et al. 2010](#)) mode in Campaign 14 (31 May, 2017 - 19 August, 2017). Its Ecliptic Plane Input Catalog (EPIC) ID number is 248624299. The total observation time is 79.64 days, and the total number of good quality ( $Q = 0$ ) data points is 3560. Each data point represents the average flux measured during a 29.4 minute interval. I followed the method described in Section 2.3.1 of Chapter 2 to measure the photometry of 2M1027+0629. The median count rate through 2-pixel radius aperture is  $889 \text{ counts s}^{-1}$ . A part of *K2* light curve is shown in Figure 7.1 in which we can see the beat patterns resulting from two closely separated periods. The phase-folded light curves in Figure 7.2 show that the two periods are very close to each other. This is further supported by the analysis below.

The Lomb-Scargle (LSP) periodogram of the *K2* light curve is shown in Figure 7.3 with the normalized values of power in *Y*-axis. I used ‘astroML.time\_series.lomb\_scargle’ to obtain this LSP and it is constructed by taking a sample of 10,000 periods in the range (0.1-0.32)day, after getting an initial estimation that the periods lie in this range. The two closely spaced peaks in this LSP correspond to  $0.2114 \pm 0.0002$  days and

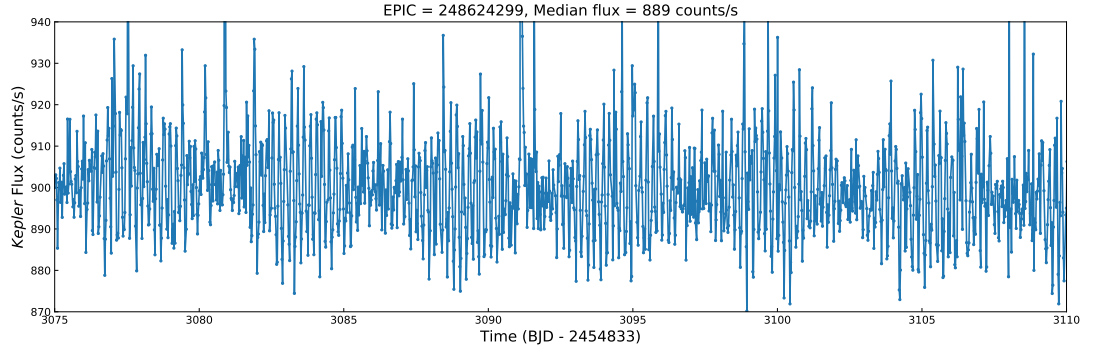


**Figure 7.1:** The *K2* light curve of 2M1027+0629, in Campaign 14. Only a portion of the light curve is shown to focus on the beat patterns which are produced as a result of two closely separated periods 0.2114 days and 0.2199 days.

0.2199 $\pm$ 0.0003 days. The uncertainties in the periods are based on half width at half maximum (HWHM) of the periodogram peaks as suggested by [Mighell and Plavchan \[2013\]](#). The two periods are likely due to various possibilities: i) spot modulations of two rapidly rotating stars in a binary system, ii) two starspots on a single star, rotating differentially because of their position in different latitudes, or iii) due to stellar pulsations. However, we can rule out the last two possibilities. More explanation is given in Section 7.3.

## 7.2.2 *Gaia* Astrometry and photometry

2M1027+0629 is one of the  $\sim 1.7$  billion sources, which has five-parameter astrometric solution measured by the *Gaia* mission [[Gaia Collaboration et al., 2016](#)]. The *Gaia* DR2 [[Gaia Collaboration et al., 2018b](#)] released on 25 April, 2018 lists its parallax to be  $10.1 \pm 0.3$  mas. This corresponds to a distance of  $99.0 \pm 2.9$  pc which is obtained by taking the inverse of *Gaia* parallax, and is farther than the previously reported photometric distance of 67.6 pc [[West et al., 2011](#)] assuming it to be a single star. In addition, the *Gaia* proper motions are  $\mu_{\alpha} = -1.2 \pm 0.5$  mas yr $^{-1}$  and  $\mu_{\delta} = -15.1 \pm 0.5$  mas yr $^{-1}$ .

Table 7.1: Properties of 2M1027+0629

	Value	Units	Ref.
<b>PHOTOMETRIC PROPERTIES</b>			
Sp. Type	M6		1
$J$	14.11±0.03	mag	1
$H$	13.51±0.04	mag	1
$K_s$	13.22±0.04	mag	1
$i$	17.034±0.004	mag	2
$G$	17.782±0.003	mag	3
$K_p$	18.17	mag	4
H $\alpha$ EW	9.6±1.4	Å	1
<b>PHYSICAL PARAMETERS</b>			
$\alpha$	156.940573 <sup>a</sup> (±0.2 mas)	deg	3
$\delta$	6.486120 <sup>a</sup> (±0.3 mas)	deg	3
parallax	10.1 ± 0.3	mas	3
$\mu_\alpha$	-1.2 ± 0.5	mas yr <sup>-1</sup>	3
$\mu_\delta$	-15.1 ± 0.5	mas yr <sup>-1</sup>	3
<b>SPECTRAL PROPERTIES</b>			
RV	-9.8±0.6	km s <sup>-1</sup>	
$v \sin i$	21.5±1.1	km s <sup>-1</sup>	
$T_{\text{eff}}$	3110±40	K	
log $g$	5.2±0.2	cgs	
<b>CALCULATED KINEMATICS</b>			
$X$	-34.1±1.1	pc	
$Y$	-53.5±1.8	pc	
$Z$	75.9±2.5	pc	
$U$	6.1±0.3	km s <sup>-1</sup>	
$V$	-0.57±0.43	km s <sup>-1</sup>	
$W$	-10.4±0.5	km s <sup>-1</sup>	

Note: RV is heliocentric.

<sup>a</sup>epoch J2015.5

References:

- (1) West et al. [2011]; (2) Chambers et al. [2016];  
(3) Gaia Collaboration et al. [2018b]; (4) Huber et al. [2017]

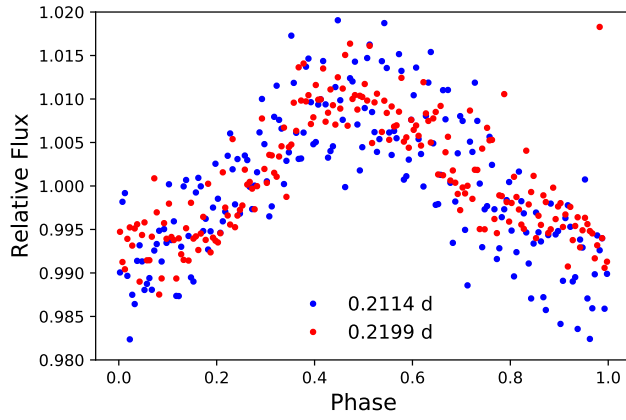


**Figure 7.2:** Phase folded lightcurves of 2MJ1027+0629. The blue lightcurve corresponds to period of 0.2114 day and the red lightcurve corresponds to period of 0.2199 day. Both lightcurves were binned using phase bin width = 0.005.

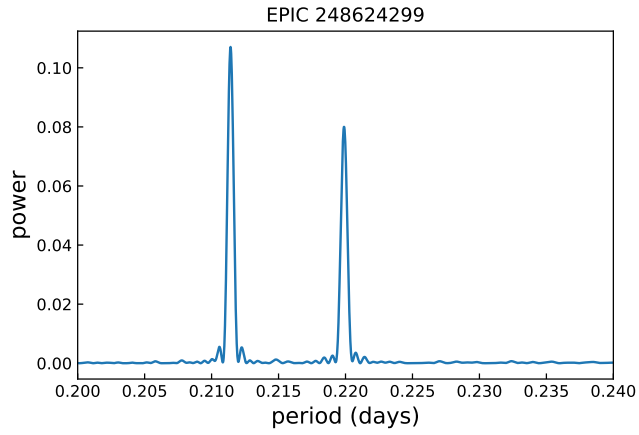


**Figure 7.3:** Lomb-Scargle periodogram of 2MJ1027+0629. The two peaks correspond to periods of 0.2114 and 0.2199 day.

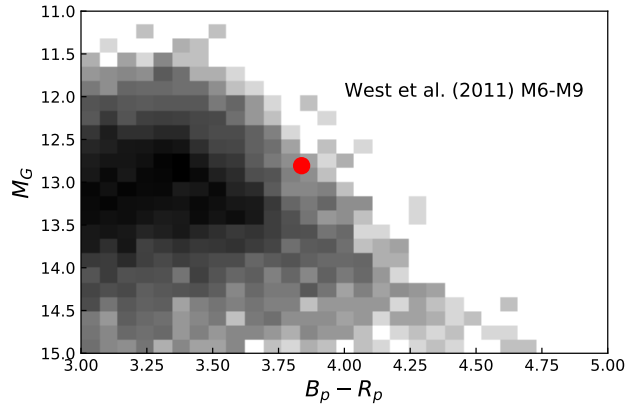


**Figure 7.4:** Color magnitude diagram of M6-M9 dwarfs using *Gaia* DR2. 2M1027+0629 is marked in red and lies at the upper edge of the main sequence.

Figure 7.4 is the color magnitude diagram of M dwarfs obtained by using *Gaia* distance and magnitudes. To make this plot, we matched a list of spectroscopic M6-M9 dwarfs from West et al. [2011] with *Gaia* DR2. 2M1027+0629 is marked in red. We can see that it lies at the upper edge of the main sequence. This is a clear indication that it is a binary system of stars.

### 7.2.3 Spectroscopy

High resolution near-infrared spectra of 2M1027+0629 were obtained with the Near InfraRed SPECTromter (NIRSPEC; McLean et al. 2000) on the Keck II Telescope on 2018 April 26 (UT) in partly cloudy conditions. The N7 order-sorting filter and 0432-wide slit were used to measure 2.00-2.39  $\mu\text{m}$  spectra over orders 32-38 with  $\lambda/\Delta\lambda \approx 20,000$  ( $\Delta v \approx 15 \text{ km s}^{-1}$ ) and dispersion of  $0.315 \text{ \AA pixel}^{-1}$ . Two exposures of 1500 s each were obtained at an airmass of 1.04, nodding  $7''$  along the slit for sky subtraction. This was followed by observations of the A0 V star 69 Leo ( $V = 5.404$ ) at similar airmass. Flat field and dark frames were obtained at the start of each night for detector calibration. Data were reduced and the raw extracted spectrum forward modeled following the methodology described in Burgasser et al. [2016], with BT-Settl

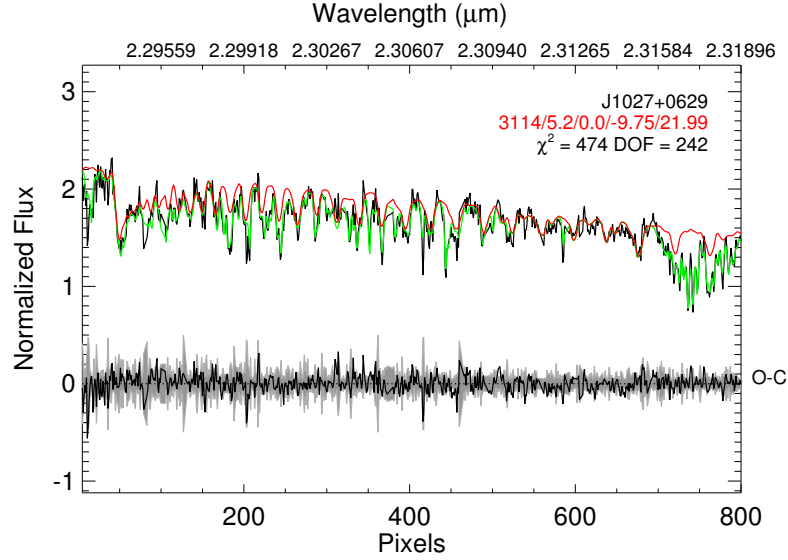


**Figure 7.5:** NIRSPEC spectrum of 2M1027+0629 obtained on UT 2018 April 26 (black line). The red line represents BT-Settl Solar-metallicity spectral model from [Allard et al., 2012]. The best fit parameters are  $T_{\text{eff}} = 3110 \pm 40$  K,  $\log g = 5.2 \pm 0.2$ ,  $RV = -9.8 \pm 0.6$  km s $^{-1}$  and  $v \sin i = 21.5 \pm 1.1$  km s $^{-1}$ . The difference between data and model (O-C) is shown in black at the bottom of the plot; the  $\pm 1\sigma$  uncertainty spectrum is indicated in gray.

Solar-metallicity spectral models drawn from Allard et al. [2012]. The best fit-model (shown in Figure 7.5) has  $T_{\text{eff}} = 3110 \pm 40$  K,  $\log g = 5.2 \pm 0.2$  (cgs),  $RV = -9.8 \pm 0.6$  km s $^{-1}$  and  $v \sin i = 21.5 \pm 1.1$  km s $^{-1}$ . Using radial velocity and *Gaia* astrometry ( $\alpha = 156.940573^\circ$  and  $\delta = 6.486120^\circ$ ),  $UVW$  components of space velocities of 2M1027+0629 are  $U = 6.1 \pm 0.3$  km s $^{-1}$ ,  $V = -0.57 \pm 0.43$  km s $^{-1}$ , and  $W = -10.4 \pm 0.5$  km s $^{-1}$ .

Using the *Gaia* astrometry and parallax, and the RV we estimated by using NIRSPEC, I used the BANYAN tool [Gagné et al., 2018] to examine if 2M1027+0629 is a member of any known moving group. The BANYAN tool includes 27 known and well-characterized stellar associations within 150 pc and uses Bayesian analysis to estimate the membership probability. It suggests that 2M1027+0629 does not belong to any

known stellar association. In Table 7.1, I list all the photometric and physical properties of 2M1027+0629, which are available in literature, measured by *Gaia* mission, and spectral properties from best-fit model to NIRSPEC spectrum.

#### 7.2.4 Flares

Three strong white light flares were detected in the *K2* light curve, as shown in Figure 7.6. The three flares (left to right) in Figure 7.6 have equivalent durations (time during which the flare emits the same amount of energy as the star does in its quiescent state Gershberg 1972) of 15.0 minutes, 29.1 minutes, and 20.3 minutes respectively. To estimate the flare energy, we need the bolometric energy of flare for an equivalent duration of 1 second. I followed the method described in Section 2.3.3 in Chapter 2 to estimate the energies of flares on 2M1027+0629. Assuming that both stars have equal luminosity, same spectral type of M6, and are at same distance of  $99.0 \pm 2.9$  pc measured by *Gaia*, the total (UV/optical/IR) energy of 10,000 K flare having equivalent duration of 1 second was estimated to be  $2.9 \times 10^{30}$  erg. This energy was multiplied with the equivalent duration to estimate the total (UV/optical/IR) energies of the flares to be  $2.6 \times 10^{33}$ ,  $5.0 \times 10^{33}$  and  $3.5 \times 10^{33}$  erg respectively.

### 7.3 Discussion and Conclusion

Using LS periodogram, we find two closely separated periods  $0.2114 \pm 0.0002$  days and  $0.2199 \pm 0.0003$  days, in the *K2* light curve of 2M1027+0629, and correspond to the rotation period of two stars in a binary system. They form beat patterns in the light curve. The *Gaia* parallax supports the evidence for 2M1207+0629 as a near-equal luminosity binary system. Previously, West et al. [2011] reported its photometric distance to be 67.6 pc, assuming it as a single star. The *Gaia* DR2 parallax of  $(10.1 \pm 0.3)$  mas corresponds to  $(99.0 \pm 2.9)$  pc, and hence this binary system appears to be twice as luminous as a single M6 star. The values of *UVW* components of space velocities are consistent with a young age, as are the rotation periods. Furthermore, the membership probabilities calculated by using the BANYAN  $\Sigma$  tool suggests that it

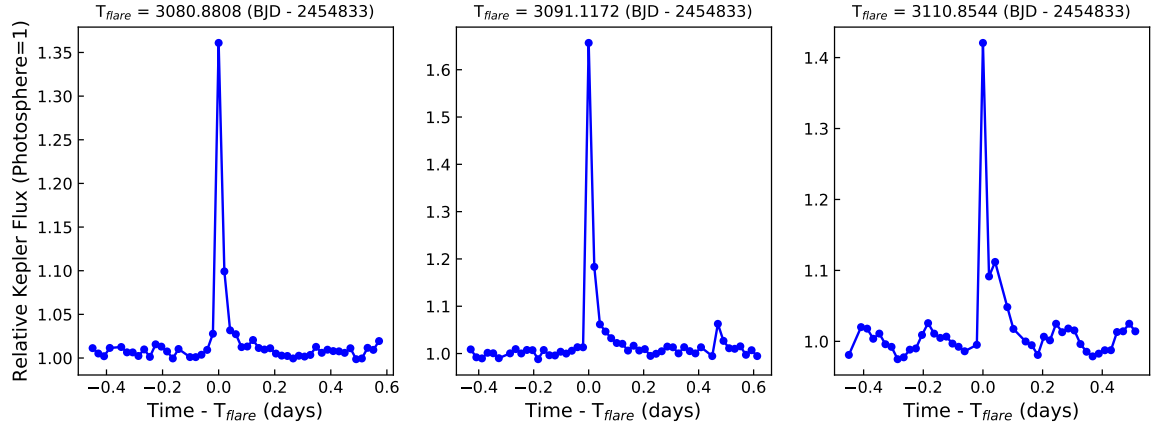


**Figure 7.6:** The three strong flares observed on 2M1027+0629. The blue dots represent the observed data. The time along the X-axis of each panel is centered at peak flare time mentioned above each panel.

does not belong to any known moving group.

In addition to the rotation periods mentioned above, three strong white light flares were detected in the *K2* light curve, which have equivalent durations of 15.0 minutes, 29.1 minutes and 20.3 minutes respectively. The total (UV/optical/IR) energies of those flares are estimated to be  $2.6 \times 10^{33}$  erg,  $5.0 \times 10^{33}$  erg, and  $3.5 \times 10^{33}$  erg respectively. If we consider the flares to occur on one of the stars, these flares have amplitudes  $\sim 2$  relative to the quiescent photospheric level. The energy of flares observed on binary system of 2M1027+0629 are comparable to those of largest flares observed on another binary system GJ 1245AB which consists of two nearly identical M5 dwarfs with rotation periods of 0.2632 and 0.709 d [Lund et al., 2015]. This may indicate that 2M1027+0629 might also be active as GJ 1245AB. But, since we do not have short cadence data for 2M1027+0629, we cannot do direct comparison of the flare rates with that of GJ 1245AB.

The beat patterns in the light curves of stars can also arise due to two more phenomena. One is the result of differential rotation of the star, such that spots in different latitudes would have close periods. The horizontal shear differential rotation parameter ( $\Delta\Omega$ ) of M dwarfs are however very small ( $<0.1$  rad day<sup>-1</sup>; Reinhold et al. 2013). For the two observed periods here,  $\Delta\Omega = 1.2$  rad day<sup>-1</sup>. The next is the result of stellar pulsations. There is not any observational evidence of pulsating M dwarfs and the theoretical calculations predict pulsations due to convectionally excited oscillations or due to  $\epsilon$  mechanism (which is related to the nuclear reaction rate in the core) in M dwarfs, have very short periods ranging from a few minutes to about half an hour. In addition, the convectionally excited oscillations in M dwarfs would have amplitudes no more than a few ppm [Rodríguez-López et al., 2012; Corsaro et al., 2013; Rappaport et al., 2014]. We can rule out both possibilities in the case of 2M1207+0629.

The two similar rapid rotation periods indicate that both stars are likely to have similar spectral types of M6 [Stauffer et al., 2016]. Additional follow-up observation of this system using high resolution AO imaging and spectroscopy is necessary to constrain the separation and the masses of the two stars, and orbital period of the system, which will be valuable to understand the various aspects like rotation-activity-age relationships, evolution of angular momentum in rapidly rotating stars in binary system, and gyrochronology.

## Chapter 8

### CHANDRA MONITORING OF A FLARING L1 DWARF WISEP J190648.47+401106.8

#### 8.1 WISEP J190648.47+401106.8

WISEP J190648.47+401106.8 (hereafter W1906+40) is a field L1 dwarf having old disk kinematics, normal surface gravity and solar-like metallicity. It has been studied by using various telescopes: *Kepler*, *Karl G. Jansky Very Large Array (JVLA)*, *Gemini North*, *Spitzer Space Telescope*, *MMT* and *Kitt Peak*. The results of such studies show that it is a magnetically active low mass star with quiescent radio and variable  $H\alpha$  emission. It is at a distance of  $16.35_{-0.34}^{+0.36}$  pc and has a bolometric luminosity of  $10^{-3.67\pm 0.03} L_{\odot}$ . Its effective temperature is estimated to be  $2300\pm 75$  K and  $v\sin i$  is equal to  $11.2\pm 2.2$  km s $^{-1}$ . Likewise, its radio luminosity is estimated to be  $\nu L_{\nu} = (4.5\pm 0.9) \times 10^{22}$  erg s $^{-1}$  at a mean observing frequency of 6.05 GHz. In addition, it has photometric variability with a period of 8.9 hr and an amplitude of 1.5% [Gizis et al., 2013, 2015]. Gizis et al. [2013] detected 21 WLFs on W1906+40 for the first time in any L dwarf, using *Kepler* and *Gemini* observations. The most powerful flare had an estimated total (UV/visible/IR) energy of  $\sim 10^{32}$  erg. W1906+40 is reported to have a WLF rate of  $10^{-3}$  to  $10^{-2.5}$  hr $^{-1}$ , or 1-2 per month for energy  $> 10^{31}$  erg, which is comparable to the rate in the Sun [Neidig and Cliver, 1983; Gershberg, 2005].

The radio emission,  $H\alpha$  emission and WLFs are the major factors indicating that it might be possible to detect X-ray photons from W1906+40. In addition it is nearer, warmer and more luminous than Kelu-1AB (a binary system of two L dwarfs) on which X-rays have already been detected [Audard et al., 2007]. The initial goal of the work presented in this chapter was to compare the radio, X-ray and  $H\alpha$  energy budget to

the white light flare energy budget for the first time in any L dwarf. This could be very helpful to understand the chromospheric and coronal structure of ultracool objects.

I describe details of *Chandra* observation and *CIAO* data reduction procedures in Section 8.2. In Section 8.3, I present the final result regarding the net counts and luminosity of X-ray photons from W1906+40 and compare it with that of another L1 dwarf.

## 8.2 OBSERVATIONS AND DATA REDUCTION

### 8.2.1 *Chandra Observations*

W1906+40 was observed by *Chandra X-ray Observatory* for 49 ks on 2015 August 14, 07:51:46-22:26:01 UTC. The ObsID for this target is 16666 and Sequence Number is 200987. The observation was made using the Advanced CCD Imaging Spectrometer-S3 (ACIS-S3) chip in VFAINT data mode and TIMED readmode. Chip S3 is a backside illuminated CCD and is better for observing faint sources because of its high sensitivity (larger effective area) at lower energies [Weisskopf et al., 2002]. More details about *Chandra* can be found in *Chandra* Proposers' Observatory Guide (POG)<sup>1</sup>.

### 8.2.2 *CIAO Data Reduction*

I processed and analyzed the *Chandra* data of W1906+40 using the standard data reduction pipeline in *Chandra* Interactive Analysis of Observations (*CIAO*) software version 4.8 [Fruscione et al., 2006] together with CALDB version 4.7.9. In the beginning, the level=1 event file was reprocessed using `chandra_repro` tool. While running this tool, very faint mode processing was enabled by keeping `check_vf_pha=yes`. This helps to clean potential background events. To remove pixel randomization, the default value of the `pix_adj` parameter was used. For ACIS data, this refers to using the subpixel EDSE (Energy Dependent Subpixel Event Repositioning) algorithm. In

---

<sup>1</sup> <http://exc.harvard.edu/proposer/POG/>

addition, the `chandra_repro` tool updates the latest charge transfer inefficiency (CTI) correction, applies the latest time-dependent gain adjustment, filters for bad grade events and applies Good Time Intervals (GTIs). After running this tool, all the available new calibration products were applied and a new level=2 event file was created.

With a level=2 event file in hand, *CIAO* tools `fluximage` and `mkpsfmap` were used to create exposure-corrected images, exposure maps and corresponding PSF maps for different energy bands. The parameters: `binsize` was chosen to be 1 (this creates images of size 3874×3988 pixels with pixel size of 0.492 arcseconds); `ecf` was chosen to be 0.9 and a characteristic energy for each band was chosen. Using the above images, next the *CIAO* tool `wavdetect` (Freeman et al. 2002) was used to detect X-ray sources using scales 1, 2, 4, 8, and 16, and a significance threshold of  $5 \times 10^{-7}$ . It yielded 33 sources in the entire image in the energy range 0.5-2.0 keV. Unfortunately, W1906+40 was not detected by this process. In Figure 8.1, we can see the nearby sources detected in the energy range 0.5-2.0 keV. The position of W1906+40 lies inside the green circle.

### 8.2.3 *Astrometry*

According to POG, Chandra’s pointing accuracy is better than 0.4 arcsec. To improve it further, the astrometric correction for our observations was done by cross-matching the list of X-ray sources detected by using `wavdetect` with Two Micron All Sky Survey (2MASS) catalog. Only sources with ‘AAA’ quality photometry and magnitudes lying in the range  $K_s = 8-14$  were used to minimise the effects due to very bright sources and faint background objects. After having two source lists, one obtained using `wavdetect` and one using 2MASS catalog, I used `wcs_match` to determine the transformation parameters to shift input sources to the reference source locations by using `method="trans"` which determines a simple translation only solution. Using those parameters, I updated aspect solution file and event file using `wcs_update`. In addition, I updated the headers to correct the optical axis and tangent plane location

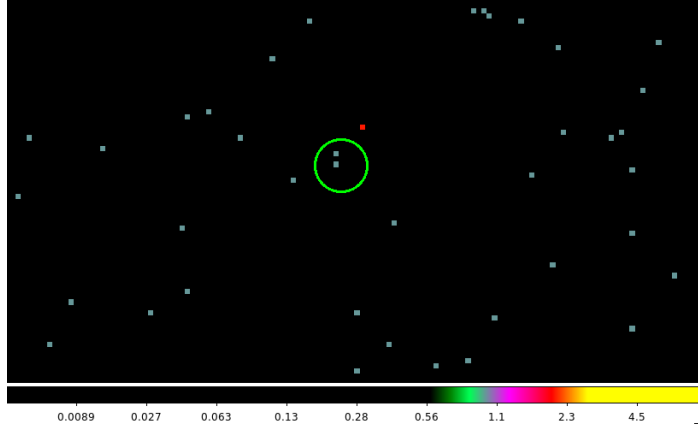


**Figure 8.1:** Circle of radius 2.5 arcsec, encircling the position of W1906+40 in its center at R.A= $19^h06^m48^s.63$  and Dec= $+40^\circ11'05''.90$ . We can see two dots inside the circle, representing X-ray sources but *Chandra* detected only 1 photon from each of them, meaning that they are equally probable to be background noise.

to make correct coordinate transformations from sky to detector coordinates.

### 8.3 RESULTS

I used the *CIAO* tool `srcflux` to compute the net counts and the net flux from our source. This exercise yielded a formal count of zero X-ray photons from W1906+40 during the observation time. For this reason, I was unable to calculate the energy flux of X-rays from W1906+40. However, *CIAO* also returns the upper limit of the flux based on a model-dependent estimate, using the `modelflux` script. The model dependent estimate of the upper limit of energy flux of X-ray photons from W1906+40 was found to be  $3.3 \times 10^{-16} \text{ erg cm}^{-2} \text{ s}^{-1}$  at the 95% confidence interval. Using this value of energy flux, I estimate the upper limit to X-ray luminosity of W1906+40 to be equal to  $1.1 \times 10^{25} \text{ erg s}^{-1}$  at the 95% confidence level. Likewise, the activity level has an upper limit of  $\log L_X/L_{\text{bol}} \approx -4.9$ .

The upper limit value of X-ray luminosity and corresponding activity level obtained for W1906+40 is comparable with that of another L1 dwarf 2MASS J06023045+3910592

[Cook et al., 2014].

## Chapter 9

### CONCLUSIONS AND FUTURE WORK

#### 9.1 FFDs of mid-to-late M and L dwarfs using *K2* short cadence data

I examined the WLFs on 42 mid-to-late M and L dwarfs using *K2 short* cadence data, among which 22 targets were found to experience at least one flare. Among the flaring targets, 2 have spectral type M5, 4 are M6, 6 are M7, 5 are M8, 1 is M9 and 4 are L0/L1. This sample of flaring targets included some targets whose flare rates are already published in the literature. A total of 1105 flares were identified on all the flaring targets, with the corresponding flare energies in the range  $\log E$  (erg)  $\sim(29.5-34)$ . The flare energies are estimated for UV/visible/IR wavelengths. The lower limit in the observed flare energy is mostly related to the lack of sensitivity of the *K2* mission in detecting small flares which become buried within the noise level of the light curves. It is found that the mid-M dwarfs produce a greater number of high energy flares in a higher rate than the late-M and L dwarfs. As in the case of solar flares, the flare frequency distributions at intermediate energies follow power law distributions in energy with slopes  $-\alpha$  lying in the range from -1.3 to -2.0. The individual FFD of each flaring M/L dwarf is shown in Figures 2.18, 2.19 and 2.20.

I computed the average values of the power-law index  $\beta$  ( $= \alpha - 1$ ) for each spectral type by considering only the targets whose fitted FFDs have flare energies that span  $> 1$  order of magnitude. I also compared the average flare rates in each spectral type with that of M4 dwarf GJ 1243. There are 17 such targets. The slopes are comparable in the case of M4, M5 and M6 dwarfs (see Figure 2.28). However, the late-M dwarfs and L dwarfs have shallower slopes. The L dwarfs have the shallowest slopes

with a mean value of 0.44. Likewise, the flare rates of GJ 1243 are higher than those of late-M dwarfs and early L dwarfs by about two (or more) orders of magnitude for flares with energy  $10^{30}$  erg (see Figure 2.28). It is expected on physical grounds that such systematic differences are related to a combination of flare volumes, flare field strengths and the rate of field line stressing.

The comparison of mean FFDs of L dwarfs (2M1232-0951 and W1906+40) with objects of earlier spectral types suggests that L dwarfs have lower rates for small energy flares but this is not the case for high energy flares. The FFDs converge towards high energies indicating that flare rates are comparable at high energies (see Figure 2.28). This also suggests that the cooler objects may have better efficiencies in converting magnetic energy to high energy flares than those with low energies. One possible physical process which might contribute to shallower FFD slopes in L dwarfs is discussed by Mullan and Paudel [2018]. The model is based on production of flares by instability in coronal magnetic loops in which the footpoints of magnetic flux ropes are subject to random walk due to convective (granular) flows. The existence of shallower slopes of the FFD in the coolest stars has been shown to arise in the presence of reduced electrical conductivity in the coolest stars.

## 9.2 Effect of $H\alpha$ luminosity in the flare rates

I studied the effect of  $H\alpha$  luminosity on the flare rates of some objects. For this, I chose a sample of targets on which  $\geq 20$  flares are observed and for which we have information about their bolometric as well as  $H\alpha$  luminosity. It can be seen that the spread in the FFDs is reduced if the flare energies are normalized by the corresponding  $H\alpha$  luminosities of the targets (See Figure 2.31). The difference in the normalized flare rates of the highest and least flaring object differ by  $\sim 0.5$  order of magnitude. The effect is more prominent if we compare the FFDs of warmer M dwarfs (here M5 and M6) for which FFDs “tighten up” significantly. Though the physical reason causing such tightening remains unclear, it suggests a possible role of  $H\alpha$  activity in causing

the flare rates of the (sub)stellar objects to differ from those in warmer M dwarfs. The effect of H $\alpha$  luminosity in the flare rates can be studied properly if we can take the contemporary H $\alpha$  measurements during the observation period of the flaring objects.

### 9.3 Variation of power-law index $\beta$ as a function of kinematic age

I used the tangential velocities of target stars as a proxy of age to study the variation of power-law index  $\beta$  as a function of kinematic age. Using a sample of targets whose fitted FFDs span flare energies  $>1$  order of magnitude, I found that the mean values of  $\beta$  in three categories of targets (very young, young and old) are comparable (see Table 2.14). The mean value of  $\beta$  for all targets is  $0.69 \pm 0.18$ . Interestingly, this value is close to a mean value of  $0.666 \pm 0.005$  obtained for  $\sim 57,000$  solar flares studied by Kasinsky and Sotnicova [2003] for three solar cycles. The mean value of  $\beta$  is also close to the value  $\beta = 0.667$  predicted by a model of granular induced field line stressing as the origin of flares [Mullan and Paudel, 2018]. This might suggest that the mean value of  $\beta$  could be the same for all stars throughout their ages.

There is diversity both in age and spectral type among the targets which I used in my study. The results suggest that the flare rate of a given target may depend on many factors other than just age and spectral type (effective temperature). Some of such factors may be rotation rate, magnetic field topology, the number of spots, etc. We need to study the FFDs for a larger sample of UCDS over a wide range of energies to see how those factors impact the flares. Changes in flare FFDs during the solar cycle have been reported by Kasinsky and Sotnicova [2003]: they found that the value of  $\beta$  varied between 0.50 (near solar minimum in 1974) and 0.80 (near solar maximum in 2000). The results of Lee et al. [2016] suggests that the occurrence rate ( $R$ ) of big solar flares and front-side halo coronal mass ejections are higher during the descending phase of solar cycle than other phases. They report a strong anti-correlation between  $R$  and annual average latitude of sunspot groups. Could this be due to some underlying physical phenomenon? We may also think of similar scenarios in the case of the

targets studied here. [Route \[2016\]](#) has reported some evidence of magnetic cycles in UCDs. The flare rate on UCDs might depend on the phase of their magnetic cycle. More information about rotational velocities of UCDs will be helpful to understand such correlations (if they exist).

In Chapter 3, I switched to a consideration of *long* cadence data. I used the *K2 long* cadence data and analyzed the WLFs on 314 M6-M9 dwarfs with a goal of identifying the maximum possible flare energies in various spectral types. I identified a total of 245 flares on 96 targets during an observation time of 67.8 years of all (314) the targets. An analysis of maximum flare energies in spectral types M5-L5 is discussed below (Section 9.4). In Chapter 4, I analyzed the WL flares of 47 L/T dwarfs also using the *K2 long* cadence data. Among them only 2 are T dwarfs on which no flares were observed. The total observation time of L dwarfs is 12.1 years. I identified 11 huge flares on early and mid-L dwarfs with flare energies in the range  $(0.9 - 460) \times 10^{32}$ . I identified flares on an L2 dwarf (2M0858+1804) and an L5 dwarf (V01). 2M0858+1804 is the second L2 dwarf on which WLFs are observed and V01 is the first L5 dwarf on which WLFs are observed. It is also the coolest object known to produce white light flares. More interestingly, two huge flares were identified on the L5 dwarf in a single *K2* campaign in an interval of  $\sim 18$  days. The largest flare had an amplitude of  $\sim 340$  relative to the photospheric level and an ED of 198 hr. This is the largest amplitude seen in any flares I analyzed in my project. The results of the huge flares observed on L dwarfs suggest that a superflare with energy  $10^{33}$  erg occurs every 2.1 years and a superflare with energy  $10^{34}$  erg occurs every 5.6 years on L dwarfs.

#### 9.4 Maximum flare energies observed in each spectral type

In Figure 9.1, I compare the maximum flare energies observed in targets of various spectral types. This plot contains the results of both short and long cadence data. In this figure, the maximum energies correspond to the targets: GJ 3631 (M5),

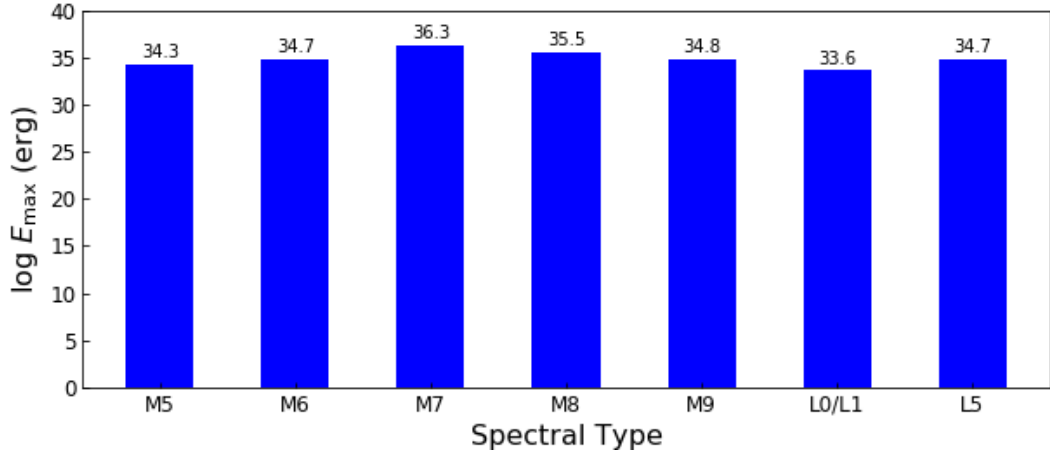


**Figure 9.1:** Maximum flare energies observed on targets of various spectral types using both *K2* short and long cadence data.

2M0432+1812 (M6), CFHT-BD-Tau 4 (M7)<sup>1</sup>, 2M0837+2050 (M8), 2M0831+2244 (M9), 2M1231-0951 (L0) and VVV BD001 (L5).

The results in Figure 9.1 suggest that there is no significant difference in the maximum energies of flares produced by targets of various spectral types. The effective temperature difference between ST of M5 and ST of L5 is  $>1000$  K. But an L5 dwarf is also capable of producing large flares with energies almost comparable to those of an M5 dwarf. Whatever the individual differences between spectral types, the results in Figure 9.1 suggest that the maximum value of flare energy,  $\propto B^2 \times \text{volume}$ , is within an order of magnitude, more or less the same in all stars in the spectral range M5 - L5. If we assume a similarity between the solar flares and the flares on (sub)stellar objects, and apply a solar-flare model as discussed in Section 5.4 of Chapter 5 to interpret the superflares observed on the targets, we find that very strong magnetic fields of the order of kilogauss are required to produce them.

---

<sup>1</sup> The energy of the largest flare on this target could be as large as  $\sim 10^{38}$  erg. See Chapter 5 for more details.

## 9.5 Timescales associated with the superflares on UCDs

In Chapter 2, I characterized superflares observed on two UCDs: 2M0835+1029 (M7) and 2M1232-0951 (L0). They had amplitudes of  $\sim 60$  and  $\sim 144$  relative to the quiescent photospheric level. Furthermore, they had very short FWHM timescales of the order of  $\sim 2$  minutes. Since they were observed in short cadence mode, such short timescales suggest that it would be worthwhile to observe the flares even in shorter cadences to understand the precise timescales associated with the impulsive and the decay phase of the flares and the physics behind such timescales.

## 9.6 Summary of additional works

In Chapter 5, I studied two huge superflares observed on a young BD: CFHT-BD-Tau 4. The stronger superflare had an estimated total (UV/visible/IR) energy up to  $2.1 \times 10^{38}$  erg. The energy of the flare depends on the value of the visual extinction parameter  $A_V$  used for correcting the extinction. This flare had an ED of  $\sim 107$  hr and an amplitude of  $\sim 48$  relative to the quiescent photospheric level. This is the largest flare observed on any brown dwarf. Since this BD has a disk, such a huge superflare might be helpful in studying the impact of superflares on the dynamical and chemical evolution of the disk around it and hence understand the planet formation around low-mass stars and BDs.

In Chapter 6, I studied some of the largest superflares observed on three late-M dwarfs: 2M0831+2042 (M7), 2M0837+2050 (M8) and 2M0831+2244 (M9). Multiple superflares were observed on 2M0837+2050 and 2M0831+2244 with flare energies as high as  $\sim 10^{35}$  erg. They have rotation periods of  $0.556 \pm 0.002$ ,  $0.193 \pm 0.000$  and  $0.292 \pm 0.001$  d respectively, which were measured by using the *K2* light curves. 2M0831+2042 and 2M0837+2050 are known to be members of the relatively young ( $\sim 700$  Myr) open cluster Praesepe. I compared the flares of such younger targets with those of TRAPPIST-1. The comparison of the FFDs based on the number of superflares on 2M0837+2050 and 2M0831+2244 suggest that superflares of energy  $10^{34}$  erg might occur at a 10 times

higher rate than on TRAPPIST-1 which has comparable spectral type but is much older (7.6 Gyr). The study of flares on such younger targets may provide some guidance as to how large flares could have been on TRAPPIST-1 during its youth. The particle flux corresponding to the largest superflare is estimated to be  $8.7 \times 10^{14}$  pfu at 0.02 AU, the location of the habitable zone around TRAPPIST-1. Such a proton flux could easily destroy the  $O_3$  column density of a modeled Earth-like planet. In addition, the CME masses associated with the superflares are estimated to be in the range  $\sim 10^{20.6}$  g to  $\sim 10^{21.8}$  g. However, both particle flux and the CME mass estimates are based on solar scaling relations and these scalings may not necessarily hold true in the case of low-mass stars and BDs (e.g., [Mullan and Paudel 2019](#)).

In Chapter 7, I studied a new binary system of an M6 dwarf 2M1027+0629. It was identified by using the *K2* light curve which is consisted with a beat pattern of two very close periodic signals. Using LS periodogram, the rotation periods of the two stars in this binary system are  $0.2114 \pm 0.0002$  and  $0.2199 \pm 0.0003$  d. The Near-infrared spectroscopy of this system yields  $T_{\text{eff}} = 3110 \pm 40$  K,  $\log g = 5.2 \pm 0.2$  (cgs),  $RV = -9.8 \pm 0.6$  km s $^{-1}$  and  $v \sin i = 21.5 \pm 1.1$  km s $^{-1}$ . The color-magnitude diagram and the distance based on *Gaia* measurements suggest that the binary system consists of two stars with similar spectral types of M6, and with nearly identical luminosity.

In Chapter 8, I studied the corona of a flaring L dwarf (W1906+40) on which 21 WL flares were observed by using the primary *Kepler* data. I analyzed 49 ks *Chandra* data to search for X-ray photons from this target. However, no X-ray photons were detected. The model dependent estimate of the upper limit of energy flux of X-ray photons from W1906+40 is  $3.3 \times 10^{-16}$  erg cm $^{-2}$  s $^{-1}$  at 95% confidence interval. The corresponding estimation of the upper limit to X-ray luminosity is equal to  $1.1 \times 10^{25}$  erg s $^{-1}$  at 95% confidence level. Likewise, the activity level has an upper limit of  $\log L_X/L_{\text{bol}} \approx -4.9$ .

The flare rates of M/L dwarfs reported in this dissertation should be helpful in predicting the number of flares on targets of similar types, which could be observed by future photometric surveys. They are also very important for gyrochronology and studying the planets in habitable zone of stars like TRAPPIST-1. The biggest flares might be capable of damaging atmospheric chemistry and other habitable conditions of the planets. More details regarding possible impacts and benefits of studying the large superflares can be found in Chapter 6. The study of large flares should also be useful in constraining the limits in the magnetic field strengths in low-mass stars and BDs.

## 9.7 FUTURE WORK

The *TESS* mission is expected to observe a large number of M dwarfs across the sky, including many which may eventually be identifiable as members of nearby moving groups and stellar associations. During two years of survey, it will observe 200,000 stars at 2-minute cadence, most of which have F5-M5 spectral types. It will also obtain full-frame images at a cadence of 30-minutes. In particular, of the 200,000 *TESS* targets with 2 minute cadence data, 40% are M dwarfs. As a result, there will be tens of thousands of M dwarf light curves at 2-minute cadence. For the long cadence data, it is expected that *TESS* will provide high quality light curves for a few million stars. So there will likely be thousands of 30-minute cadence M dwarf light curves to draw a sample from. *TESS* data can be used to do the following science:

### i) **Study of flare rates as a function of M dwarfs' mass and age:**

*TESS* data can be used to know how the flare rates change with the evolution of the star. This is possible by analyzing *TESS* light curves of thousands of M dwarfs that belong to various nearby moving groups and stellar associations, and have ages ranging from a few million years to giga years. It is also possible to estimate the flare frequency distribution (FFD) of M dwarfs over a wide range of flare energies,  $\log E$  (erg)  $\sim$ (29 - 36) with more accuracy. This will be the widest range of energy for which the FFDs will be estimated in stars other than the Sun. The short cadence data can be used to estimate the FFD of both the smallest and the largest flares for each individual star

in the sample. Likewise, the long cadence data can be used to estimate the FFD of the largest flares on M dwarfs. The rich *TESS* data set will allow us to constrain the flare rates of M dwarfs as a function of their masses and ages for a statistically large and more homogenous sample. Such a large and systematic study of the evolution of M dwarf flares would be the first of its kind.

ii) **Simultaneous multiwavelength study of flaring M dwarfs:**

In order to know how much energy the planets in the habitable zones of M dwarfs receive during their different phases of formation, it is very important to know the correlations between various radiations emitted by the parent stars, during both flaring and quiescent state. The simultaneous observations of *TESS* targets by using other facilities like Swift, VLA, HST and some ground-based facilities will be very helpful in this regard.

Information as to how the M dwarf flares evolve over time and the correlations between different wavelengths will be helpful to calculate the total energy received by the HZ planets in different stages of formation. The results should be able to constrain when the flare rate is maximum for a given star's evolution. The results of multi-wavelength studies and evolution of M dwarf flares will provide valuable inputs into exoplanet atmosphere and climate models, thus providing constraints on the habitability of planets in the HZ of M dwarfs.

*TESS* however will get high quality data mainly for the brightest nearby M dwarfs. The L dwarfs may be too faint for this mission to study in depth. In addition, the flare rates of L dwarfs are very low and the large flares have very short FWHM. So we need to observe them for longer times. This suggests that it would be helpful if another mission like *Kepler* with observing cadences shorter than 1 minute, will be launched again to study the flares on L dwarfs. As H $\alpha$  emission is observed in some T dwarfs, it would be worthwhile to observe more cool objects with spectral types as late as T by using such a mission. This will be helpful to determine if there exists a spectral type

at which flare emission ultimately cuts-off: such a cut-off could occur if the convective flows in a cool (sub)stellar object eventually become incapable (due to reduced flow speeds or reduced conductivity) of stressing the local magnetic fields.

## Bibliography

- A. N. Aarnio, K. G. Stassun, W. J. Hughes, and S. L. McGregor. Solar Flares and Coronal Mass Ejections: A Statistically Determined Flare Flux - CME Mass Correlation. *Sol. Phys.*, 268:195–212, January 2011. doi: 10.1007/s11207-010-9672-7.
- A. N. Aarnio, S. P. Matt, and K. G. Stassun. Mass Loss in Pre-main-sequence Stars via Coronal Mass Ejections and Implications for Angular Momentum Loss. *ApJ*, 760:9, November 2012. doi: 10.1088/0004-637X/760/1/9.
- S. Ahmed and S. J. Warren. A homogeneous sample of 34 000 M7-M9.5 dwarfs brighter than  $J = 17.5$  with accurate spectral types. *A&A*, 623:A127, Mar 2019. doi: 10.1051/0004-6361/201834591.
- Suzanne Aigrain, Hannu Parviainen, and Benjamin Pope. K2SC: Flexible systematics correction and detrending of K2 light curves using Gaussian Process regression. 2016. URL <http://arxiv.org/abs/1603.09167>.
- V. S. Airapetian, A. Gloer, G. Gronoff, E. Hébrard, and W. Danchi. Prebiotic chemistry and atmospheric warming of early Earth by an active young Sun. *Nature Geoscience*, 9:452–455, June 2016. doi: 10.1038/ngeo2719.
- F. Allard, D. Homeier, and B. Freytag. Models of very-low-mass stars, brown dwarfs and exoplanets. *Philosophical Transactions of the Royal Society of London Series A*, 370:2765–2777, June 2012. doi: 10.1098/rsta.2011.0269.
- P. R. Allen. Star Formation via the Little Guy: A Bayesian Study of Ultracool Dwarf Imaging Surveys for Companions. *ApJ*, 668:492–506, October 2007. doi: 10.1086/521207.
- J. D. Alvarado-Gómez, J. J. Drake, O. Cohen, S. P. Moschou, and C. Garraffo. Suppression of Coronal Mass Ejections in Active Stars by an Overlying Large-scale Magnetic Field: A Numerical Study. *ApJ*, 862:93, August 2018. doi: 10.3847/1538-4357/aacb7f.
- C. Alves de Oliveira, E. Moraux, J. Bouvier, and H. Bouy. Spectroscopy of new brown dwarf members of  $\rho$  Ophiuchi and an updated initial mass function. *A&A*, 539:A151, March 2012. doi: 10.1051/0004-6361/201118230.
- S. M. Andrews, K. A. Rosenfeld, A. L. Kraus, and D. J. Wilner. The Mass Dependence between Protoplanetary Disks and their Stellar Hosts. *ApJ*, 771:129, July 2013. doi: 10.1088/0004-637X/771/2/129.
- G. Anglada-Escudé, P. J. Amado, J. Barnes, Z. M. Berdiñas, R. P. Butler, G. A. L. Coleman, I. de La Cueva, S. Dreizler, M. Endl, B. Giesers, S. V. Jeffers, J. S. Jenkins, H. R. A. Jones, M. Kiraga, M. Kürster, M. J. López-González, C. J. Marvin, N. Morales, J. Morin, R. P. Nelson, J. L. Ortiz, A. Ofir, S.-J. Paardekooper, A. Reiners, E. Rodríguez, C. Rodríguez-López, L. F. Sarmiento, J. P. Strachan,

- Y. Tsapras, M. Tuomi, and M. Zechmeister. A terrestrial planet candidate in a temperate orbit around Proxima Centauri. *Nature*, 536:437–440, August 2016. doi: 10.1038/nature19106.
- A. Antonova, G. Hallinan, J. G. Doyle, S. Yu, A. Kuznetsov, Y. Metodieva, A. Golden, and K. L. Cruz. Volume-limited radio survey of ultracool dwarfs. *A&A*, 549:A131, Jan 2013. doi: 10.1051/0004-6361/201118583.
- D. Apai. Protoplanetary disks and planet formation around brown dwarfs and very low-mass stars. *Astronomische Nachrichten*, 334:57, February 2013. doi: 10.1002/asna.201211780.
- D. Apai, I. Pascucci, M. F. Sterzik, N. van der Bliek, J. Bouwman, C. P. Dullemond, and T. Henning. Grain growth and dust settling in a brown dwarf disk. Gemini/T-ReCS observations of CFHT-BD-Tau 4. *A&A*, 426:L53–L57, November 2004. doi: 10.1051/0004-6361:200400080.
- B. C. Arnold. *Pareto Distributions*. CRC Press, Boca Raton, FL, second edition, 2015.
- M. J. Aschwanden, M. J. Wills, H. S. Hudson, T. Kosugi, and R. A. Schwartz. Electron Time-of-Flight Distances and Flare Loop Geometries Compared from CGRO and YOHKO Observations. *ApJ*, 468:398, September 1996. doi: 10.1086/177700.
- M. Audard, R. A. Osten, A. Brown, K. R. Briggs, M. Güdel, E. Hodges-Kluck, and J. E. Gizis. A Chandra X-ray detection of the L dwarf binary Kelu-1. Simultaneous Chandra and Very Large Array observations. *A&A*, 471:L63–L66, September 2007. doi: 10.1051/0004-6361:20078093.
- G. Aulanier, P. Démoulin, C. J. Schrijver, M. Janvier, E. Pariat, and B. Schmieder. The standard flare model in three dimensions. II. Upper limit on solar flare energy. *A&A*, 549:A66, January 2013. doi: 10.1051/0004-6361/201220406.
- C. A. L. Bailer-Jones, J. Rybizki, M. Fouesneau, G. Mantelet, and R. Andrae. Estimating Distance from Parallaxes. IV. Distances to 1.33 Billion Stars in Gaia Data Release 2. *AJ*, 156:58, August 2018. doi: 10.3847/1538-3881/aacb21.
- I. Baraffe, G. Chabrier, F. Allard, and P. H. Hauschildt. New Evolutionary Tracks for Very Low Mass Stars. *ApJL*, 446:L35, June 1995. doi: 10.1086/187924.
- T. Barclay, J. Pepper, and E. V. Quintana. A Revised Exoplanet Yield from the Transiting Exoplanet Survey Satellite (TESS). *ApJS*, 239:2, November 2018. doi: 10.3847/1538-4365/aae3e9.
- D. C. Bardalez Gagliuffi, A. J. Burgasser, C. R. Gelino, D. L. Looper, C. P. Nicholls, S. J. Schmidt, K. Cruz, A. A. West, J. E. Gizis, and S. Metchev. SpeX Spectroscopy of Unresolved Very Low Mass Binaries. II. Identification of 14 Candidate Binaries with Late-M/Early-L and T Dwarf Components. *ApJ*, 794:143, October 2014. doi: 10.1088/0004-637X/794/2/143.
- G. Basri and G. W. Marcy. A surprise at the bottom of the main sequence: Rapid rotation and NO H-alpha emission. *AJ*, 109:762–773, February 1995. doi: 10.1086/117319.
- J. C. Beamín, D. Minniti, M. Gromadzki, R. Kurtev, V. D. Ivanov, Y. Beletsky, P. Lucas, R. K. Saito, and J. Borissova. One more neighbor: The first brown dwarf in the VVV survey. *A&A*, 557:L8, September 2013. doi: 10.1051/0004-6361/201322190.

- A. O. Benz and M. Güdel. Physical Processes in Magnetically Driven Flares on the Sun, Stars, and Young Stellar Objects. *ARA&A*, 48:241–287, September 2010. doi: 10.1146/annurev-astro-082708-101757.
- A. O. Benz and M. Guedel. X-ray/microwave ratio of flares and coronae. *A&A*, 285: 621–630, May 1994.
- S. V. Berdyugina, D. M. Harrington, O. Kuzmychov, J. R. Kuhn, G. Hallinan, A. F. Kowalski, and S. L. Hawley. First Detection of a Strong Magnetic Field on a Bursty Brown Dwarf: Puzzle Solved. *ApJ*, 847:61, September 2017a. doi: 10.3847/1538-4357/aa866b.
- S. V. Berdyugina, D. M. Harrington, O. Kuzmychov, J. R. Kuhn, G. Hallinan, A. F. Kowalski, and S. L. Hawley. First Detection of a Strong Magnetic Field on a Bursty Brown Dwarf: Puzzle Solved. *ArXiv e-prints*, September 2017b.
- E. Berger, G. Basri, J. E. Gizis, M. S. Giampapa, R. E. Rutledge, J. Liebert, E. Martín, T. A. Fleming, C. M. Johns-Krull, N. Phan-Bao, and W. H. Sherry. Simultaneous Multiwavelength Observations of Magnetic Activity in Ultracool Dwarfs. II. Mixed Trends in VB 10 and LSR 1835+32 and the Possible Role of Rotation. *ApJ*, 676: 1307–1318, April 2008a. doi: 10.1086/529131.
- E. Berger, J. E. Gizis, M. S. Giampapa, R. E. Rutledge, J. Liebert, E. Martín, G. Basri, T. A. Fleming, C. M. Johns-Krull, N. Phan-Bao, and W. H. Sherry. Simultaneous Multiwavelength Observations of Magnetic Activity in Ultracool Dwarfs. I. The Complex Behavior of the M8.5 Dwarf TVLM 513-46546. *ApJ*, 673:1080–1087, February 2008b. doi: 10.1086/524769.
- E. Berger, G. Basri, T. A. Fleming, M. S. Giampapa, J. E. Gizis, J. Liebert, E. Martín, N. Phan-Bao, and R. E. Rutledge. Simultaneous Multi-Wavelength Observations of Magnetic Activity in Ultracool Dwarfs. III. X-ray, Radio, and H $\alpha$  Activity Trends in M and L dwarfs. *ApJ*, 709:332–341, January 2010. doi: 10.1088/0004-637X/709/1/332.
- W. M. J. Best, E. A. Magnier, M. C. Liu, K. M. Aller, Z. Zhang, W. S. Burgett, K. C. Chambers, P. Draper, H. Flewelling, N. Kaiser, R.-P. Kudritzki, N. Metcalfe, J. L. Tonry, R. J. Wainscoat, and C. Waters. Photometry and Proper Motions of M, L, and T Dwarfs from the Pan-STARRS1  $3\pi$  Survey. *ApJS*, 234:1, January 2018. doi: 10.3847/1538-4365/aa9982.
- J. J. Bochanski, A. A. West, S. L. Hawley, and K. R. Covey. Low-Mass Dwarf Template Spectra from the Sloan Digital Sky Survey. *AJ*, 133:531–544, February 2007. doi: 10.1086/510240.
- E. Bolmont, F. Selsis, J. E. Owen, I. Ribas, S. N. Raymond, J. Leconte, and M. Gillon. Water loss from terrestrial planets orbiting ultracool dwarfs: implications for the planets of TRAPPIST-1. *MNRAS*, 464:3728–3741, January 2017. doi: 10.1093/mnras/stw2578.
- W. J. Borucki. Kepler: A Brief Discussion of the Mission and Exoplanet Results. *Proceedings of the American Philosophical Society*, 161:38–65, March 2017.
- W. J. Borucki, D. Koch, G. Basri, N. Batalha, T. Brown, D. Caldwell, J. Caldwell, J. Christensen-Dalsgaard, W. D. Cochran, E. DeVore, E. W. Dunham, A. K. Dupree,

- T. N. Gautier, J. C. Geary, R. Gilliland, A. Gould, S. B. Howell, J. M. Jenkins, Y. Kondo, D. W. Latham, G. W. Marcy, S. Meibom, H. Kjeldsen, J. J. Lissauer, D. G. Monet, D. Morrison, D. Sasselov, J. Tarter, A. Boss, D. Brownlee, T. Owen, D. Buzasi, D. Charbonneau, L. Doyle, J. Fortney, E. B. Ford, M. J. Holman, S. Seager, J. H. Steffen, W. F. Welsh, J. Rowe, H. Anderson, L. Buchhave, D. Ciardi, L. Walkowicz, W. Sherry, E. Horch, H. Isaacson, M. E. Everett, D. Fischer, G. Torres, J. A. Johnson, M. Endl, P. MacQueen, S. T. Bryson, J. Dotson, M. Haas, J. Kolodziejczak, J. Van Cleve, H. Chandrasekaran, J. D. Twicken, E. V. Quintana, B. D. Clarke, C. Allen, J. Li, H. Wu, P. Tenenbaum, E. Verner, F. Bruhweiler, J. Barnes, and A. Prsa. Kepler Planet-Detection Mission: Introduction and First Results. *Science*, 327:977, February 2010. doi: 10.1126/science.1185402.
- A. P. Boss. Rapid Formation of Gas Giant Planets around M Dwarf Stars. *ApJ*, 643: 501–508, May 2006. doi: 10.1086/501522.
- S. Boudreault, N. Lodieu, N. R. Deacon, and N. C. Hambly. Astrometric and photometric initial mass functions from the UKIDSS Galactic Clusters Survey - III. Praesepe. *MNRAS*, 426:3419–3434, November 2012. doi: 10.1111/j.1365-2966.2012.21854.x.
- A. J. Burgasser and E. E. Mamajek. On the Age of the TRAPPIST-1 System. *ApJ*, 845:110, August 2017. doi: 10.3847/1538-4357/aa7fea.
- A. J. Burgasser, K. L. Cruz, M. Cushing, C. R. Gelino, D. L. Looper, J. K. Faherty, J. D. Kirkpatrick, and I. N. Reid. SpeX Spectroscopy of Unresolved Very Low Mass Binaries. I. Identification of 17 Candidate Binaries Straddling the L Dwarf/T Dwarf Transition. *ApJ*, 710:1142–1169, February 2010. doi: 10.1088/0004-637X/710/2/1142.
- A. J. Burgasser, C. H. Blake, C. R. Gelino, J. Sahlmann, and D. Bardalez Gagliuffi. The Orbit of the L Dwarf + T Dwarf Spectral Binary SDSS J080531.84+481233.0. *ApJ*, 827:25, August 2016. doi: 10.3847/0004-637X/827/1/25.
- A. Burrows, W. B. Hubbard, J. I. Lunine, and J. Liebert. The theory of brown dwarfs and extrasolar giant planets. *Reviews of Modern Physics*, 73:719–765, July 2001. doi: 10.1103/RevModPhys.73.719.
- S. Candelaresi, A. Hillier, H. Maehara, A. Brandenburg, and K. Shibata. Superflare Occurrence and Energies on G-, K-, and M-type Dwarfs. *ApJ*, 792:67, September 2014. doi: 10.1088/0004-637X/792/1/67.
- J. A. Cardelli, G. C. Clayton, and J. S. Mathis. The relationship between infrared, optical, and ultraviolet extinction. *ApJ*, 345:245–256, October 1989. doi: 10.1086/167900.
- P. A. Cassak, D. J. Mullan, and M. A. Shay. From Solar and Stellar Flares to Coronal Heating: Theory and Observations of How Magnetic Reconnection Regulates Coronal Conditions. *ApJL*, 676:L69, March 2008. doi: 10.1086/587055.
- G. Chabrier and I. Baraffe. Structure and evolution of low-mass stars. *A&A*, 327: 1039–1053, November 1997.
- G. Chabrier, I. Baraffe, F. Allard, and P. Hauschildt. Evolutionary Models for Very Low-Mass Stars and Brown Dwarfs with Dusty Atmospheres. *ApJ*, 542:464–472, October 2000. doi: 10.1086/309513.

- K. C. Chambers, E. A. Magnier, N. Metcalfe, H. A. Flewelling, M. E. Huber, C. Z. Waters, L. Denneau, P. W. Draper, D. Farrow, D. P. Finkbeiner, C. Holmberg, J. Koppenhoefer, P. A. Price, R. P. Saglia, E. F. Schlafly, S. J. Smartt, W. Sweeney, R. J. Wainscoat, W. S. Burgett, T. Grav, J. N. Heasley, K. W. Hodapp, R. Jedicke, N. Kaiser, R.-P. Kudritzki, G. A. Luppino, R. H. Lupton, D. G. Monet, J. S. Morgan, P. M. Onaka, C. W. Stubbs, J. L. Tonry, E. Banados, E. F. Bell, R. Bender, E. J. Bernard, M. T. Botticella, S. Casertano, S. Chastel, W.-P. Chen, X. Chen, S. Cole, N. Deacon, C. Frenk, A. Fitzsimmons, S. Gezari, C. Goessl, T. Goggia, B. Goldman, E. K. Grebel, N. C. Hambly, G. Hasinger, A. F. Heavens, T. M. Heckman, R. Henderson, T. Henning, M. Holman, U. Hopp, W.-H. Ip, S. Isani, C. D. Keyes, A. Koekemoer, R. Kotak, K. S. Long, J. R. Lucey, M. Liu, N. F. Martin, B. McLean, E. Morganson, D. N. A. Murphy, M. A. Nieto-Santisteban, P. Norberg, J. A. Peacock, E. A. Pier, M. Postman, N. Primak, C. Rae, A. Rest, A. Riess, A. Riffeser, H. W. Rix, S. Roser, E. Schilbach, A. S. B. Schultz, D. Scolnic, A. Szalay, S. Seitz, B. Shiao, E. Small, K. W. Smith, D. Soderblom, A. N. Taylor, A. R. Thakar, J. Thiel, D. Thilker, Y. Urata, J. Valenti, F. Walter, S. P. Watters, S. Werner, R. White, W. M. Wood-Vasey, and R. Wyse. The Pan-STARRS1 Surveys. *ArXiv e-prints*, December 2016.
- P. Charbonneau. Solar Dynamo Theory. *ARA&A*, 52:251–290, August 2014. doi: 10.1146/annurev-astro-081913-040012.
- U. R. Christensen, V. Holzwarth, and A. Reiners. Energy flux determines magnetic field strength of planets and stars. *Nature*, 457:167–169, January 2009. doi: 10.1038/nature07626.
- A. Clauset, C. R. Shalizi, and M. E. J. Newman. Power-Law Distributions in Empirical Data. *ArXiv e-prints*, 2009.
- L. I. Cleves, E. A. Bergin, C. Qi, F. C. Adams, and K. I. Öberg. Constraining the X-Ray and Cosmic-Ray Ionization Chemistry of the TW Hya Protoplanetary Disk: Evidence for a Sub-interstellar Cosmic-Ray Rate. *ApJ*, 799:204, February 2015. doi: 10.1088/0004-637X/799/2/204.
- T. D. Clements, T. J. Henry, A. D. Hosey, W.-C. Jao, M. L. Silverstein, J. G. Winters, S. B. Dieterich, and A. R. Riedel. The Solar Neighborhood. XLI. A Study of the Wide Main Sequence for M Dwarfs Long-term Photometric Variability. *AJ*, 154:124, September 2017. doi: 10.3847/1538-3881/aa8464.
- E. W. Cliver and W. F. Dietrich. The 1859 space weather event revisited: limits of extreme activity. *Journal of Space Weather and Space Climate*, 3(27):A31, October 2013. doi: 10.1051/swsc/2013053.
- E. W. Cliver, A. G. Ling, A. Belov, and S. Yashiro. Size distributions of solar flares and solar energetic particle events. *ApJL*, 756:L29, September 2012. doi: 10.1088/2041-8205/756/2/L29.
- F. Comerón, L. Testi, and A. Natta. Strong accretion on a deuterium-burning brown dwarf. *A&A*, 522:A47, November 2010. doi: 10.1051/0004-6361/200913620.
- B. A. Cook, P. K. G. Williams, and E. Berger. Trends in Ultracool Dwarf Magnetism. II. The Inverse Correlation Between X-Ray Activity and Rotation as Evidence for a

- Bimodal Dynamo. *ApJ*, 785:10, April 2014. doi: 10.1088/0004-637X/785/1/10.
- E. Corsaro, H.-E. Fröhlich, A. Bonanno, D. Huber, T. R. Bedding, O. Benomar, J. De Ridder, and D. Stello. A Bayesian approach to scaling relations for amplitudes of solar-like oscillations in Kepler stars. *MNRAS*, 430:2313–2326, April 2013. doi: 10.1093/mnras/stt059.
- L. E. Cram and D. J. Mullan. Model chromospheres of flare stars. I - Balmer-line profiles. *ApJ*, 234:579–587, December 1979. doi: 10.1086/157532.
- M. K. Crosley and R. A. Osten. Low-frequency Radio Transients on the Active M-dwarf EQ Peg and the Search for Coronal Mass Ejections. *ApJ*, 862:113, August 2018. doi: 10.3847/1538-4357/aacf02.
- I. J. M. Crossfield. Doppler imaging of exoplanets and brown dwarfs. *A&A*, 566:A130, June 2014. doi: 10.1051/0004-6361/201423750.
- Ian J. M. Crossfield, Natalia Guerrero, Trevor David, Samuel N. Quinn, Adina D. Feinstein, Chelsea Huang, Liang Yu, Karen A. Collins, Benjamin J. Fulton, Björn Benneke, Merrin Peterson, Allyson Bieryla, Joshua E. Schlieder, Molly R. Kosiarek, Makennah Bristow, Elisabeth Newton, Megan Bedell, David W. Latham, Jessie L. Christiansen, Gilbert A. Esquerdo, Perry Berlind, Michael L. Calkins, Avi Shporer, Jennifer Burt, Sarah Ballard, Joseph E. Rodriguez, Nicholas Mehrle, Courtney D. Dressing, John H. Livingston, Erik A. Petigura, Sara Seager, Jason Dittmann, David Berardo, Lizhou Sha, Zahra Essack, Zhuchang Zhan, Martin Owens, Isabel Kain, Howard Isaacson, David R. Ciardi, Erica J. Gonzales, Andrew W. Howard, and José Vinícius de Miranda Cardoso. A TESS Dress Rehearsal: Planetary Candidates and Variables from K2 Campaign 17. *The Astrophysical Journal Supplement Series*, 239: 5, Nov 2018. doi: 10.3847/1538-4365/aae155.
- K. L. Cruz, I. N. Reid, J. Liebert, J. D. Kirkpatrick, and P. J. Lowrance. Meeting the Cool Neighbors. V. A 2MASS-Selected Sample of Ultracool Dwarfs. *AJ*, 126: 2421–2448, November 2003. doi: 10.1086/378607.
- R. M. Cutri, M. F. Skrutskie, S. van Dyk, C. A. Beichman, J. M. Carpenter, T. Chester, L. Cambresy, T. Evans, J. Fowler, J. Gizis, E. Howard, J. Huchra, T. Jarrett, E. L. Kopan, J. D. Kirkpatrick, R. M. Light, K. A. Marsh, H. McCallon, S. Schneider, R. Stiening, M. Sykes, M. Weinberg, W. A. Wheaton, S. Wheelock, and N. Zacarias. *2MASS All Sky Catalog of point sources*. June 2003.
- J. R. A. Davenport. The Kepler Catalog of Stellar Flares. *ApJ*, 829:23, September 2016. doi: 10.3847/0004-637X/829/1/23.
- J. R. A. Davenport. Infrared Flares from M Dwarfs: A Hinderance to Future Transiting Exoplanet Studies. *Research Notes of the American Astronomical Society*, 1:2, December 2017. doi: 10.3847/2515-5172/aa95c3.
- J. R. A. Davenport, S. L. Hawley, L. Hebb, J. P. Wisniewski, A. F. Kowalski, E. C. Johnson, M. Malatesta, J. Peraza, M. Keil, S. M. Silverberg, T. C. Jansen, M. S. Scheffler, J. R. Berdis, D. M. Larsen, and E. J. Hilton. Kepler Flares. II. The Temporal Morphology of White-light Flares on GJ 1243. *ApJ*, 797:122, December 2014. doi: 10.1088/0004-637X/797/2/122.
- J. R. A. Davenport, D. M. Kipping, D. Sasselov, J. M. Matthews, and C. Cameron.

- MOST Observations of Our Nearest Neighbor: Flares on Proxima Centauri. *ApJL*, 829:L31, October 2016. doi: 10.3847/2041-8205/829/2/L31.
- J. R. A. Davenport, K. R. Covey, R. W. Clarke, A. C. Boeck, J. Cornet, and S. L. Hawley. The Evolution of Flare Activity with Stellar Age. *ApJ*, 871:241, February 2019. doi: 10.3847/1538-4357/aafb76.
- X. Delfosse, T. Forveille, C. Perrier, and M. Mayor. Rotation and chromospheric activity in field M dwarfs. *A&A*, 331:581–595, March 1998.
- S. J. Desch and J. N. Cuzzi. The Generation of Lightning in the Solar Nebula. *Icarus*, 143:87–105, January 2000. doi: 10.1006/icar.1999.6245.
- R. Deshpande, C. H. Blake, C. F. Bender, S. Mahadevan, R. C. Terrien, J. K. Carlberg, G. Zasowski, J. Crepp, A. S. Rajpurohit, C. Reyl e, D. L. Nidever, D. P. Schneider, C. Allende Prieto, D. Bizyaev, G. Ebelke, S. W. Fleming, P. M. Frinchaboy, J. Ge, F. Hearty, J. Hern andez, E. Malanushenko, V. Malanushenko, S. R. Majewski, R. Marchwinski, D. Muna, D. Oravetz, K. Pan, R. P. Schiavon, M. Shetrone, A. Simmons, K. G. Stassun, J. C. Wilson, and J. P. Wisniewski. The SDSS-III APOGEE Radial Velocity Survey of M Dwarfs. I. Description of the Survey and Science Goals. *AJ*, 146:156, December 2013. doi: 10.1088/0004-6256/146/6/156.
- Matthew S. Dodd, Dominic Papineau, Tor Grenne, John F. Slack, Martin Rittner, Franco Pirajno, Jonathan O’Neil, and Crispin T. S. Little. Evidence for early life in earth’s oldest hydrothermal vent precipitates. *Nature*, 543:60 EP –, 03 2017. URL <https://doi.org/10.1038/nature21377>.
- J.-F. Donati and J. D. Landstreet. Magnetic Fields of Nondegenerate Stars. *ARA&A*, 47:333–370, September 2009. doi: 10.1146/annurev-astro-082708-101833.
- S. T. Douglas, M. A. Ag eros, K. R. Covey, E. C. Bowsher, J. J. Bochanski, P. A. Cargile, A. Kraus, N. M. Law, J. J. Lemonias, H. G. Arce, D. F. Fierroz, and A. Kundert. The Factory and the Beehive. II. Activity and Rotation in Praesepe and the Hyades. *ApJ*, 795:161, November 2014. doi: 10.1088/0004-637X/795/2/161.
- S. T. Douglas, M. A. Ag eros, K. R. Covey, P. A. Cargile, T. Barclay, A. Cody, S. B. Howell, and T. Kopytova. K2 Rotation Periods for Low-mass Hyads and the Implications for Gyrochronology. *ApJ*, 822:47, May 2016. doi: 10.3847/0004-637X/822/1/47.
- S. T. Douglas, M. A. Ag eros, K. R. Covey, and A. Kraus. Poking the Beehive from Space: K2 Rotation Periods for Praesepe. *ApJ*, 842:83, June 2017. doi: 10.3847/1538-4357/aa6e52.
- C. D. Dressing and D. Charbonneau. The Occurrence of Potentially Habitable Planets Orbiting M Dwarfs Estimated from the Full Kepler Dataset and an Empirical Measurement of the Detection Sensitivity. *ApJ*, 807:45, July 2015. doi: 10.1088/0004-637X/807/1/45.
- G. Duch ene and A. Kraus. Stellar Multiplicity. *ARA&A*, 51:269–310, August 2013. doi: 10.1146/annurev-astro-081710-102602.
- P. Duggan, B. McBreen, L. Hanlon, L. Metcalfe, A. Kvick, and G. Vaughan. The Effects of a Gamma-Ray Burst on Nearby Preplanetary Systems. In E. Costa, F. Frontera, and J. Hjorth, editors, *Gamma-ray Bursts in the Afterglow Era*, page 294, 2001. doi:

10.1007/10853853\_78.

- T. J. Dupuy and M. C. Liu. The Hawaii Infrared Parallax Program. I. Ultracool Binaries and the L/T Transition. *ApJS*, 201:19, August 2012. doi: 10.1088/0067-0049/201/2/19.
- A. G. Emslie, B. R. Dennis, A. Y. Shih, P. C. Chamberlin, R. A. Mewaldt, C. S. Moore, G. H. Share, A. Vourlidas, and B. T. Welsch. Global Energetics of Thirty-eight Large Solar Eruptive Events. *ApJ*, 759:71, November 2012. doi: 10.1088/0004-637X/759/1/71.
- N. Epchtein, B. de Batz, L. Capoani, L. Chevallier, E. Copet, P. Fouqué, P. Lacombe, T. Le Bertre, S. Pau, D. Rouan, S. Ruphy, G. Simon, D. Tiphène, W. B. Burton, E. Bertin, E. Deul, H. Habing, J. Borsenberger, M. Dennefeld, F. Guglielmo, C. Loup, G. Mamon, Y. Ng, A. Omont, L. Provost, J.-C. Renault, F. Tanguy, S. Kimeswenger, C. Kienel, F. Garzon, P. Persi, M. Ferrari-Toniolo, A. Robin, G. Paturel, I. Vauglin, T. Forveille, X. Delfosse, J. Hron, M. Schultheis, I. Appenzeller, S. Wagner, L. Balázs, A. Holl, J. Lépine, P. Boscolo, E. Picazzio, P.-A. Duc, and M.-O. Mennessier. The deep near-infrared southern sky survey (DENIS). *The Messenger*, 87:27–34, March 1997.
- N. Epchtein, E. Deul, S. Derriere, J. Borsenberger, D. Egret, G. Simon, C. Alard, L. G. Balázs, B. de Batz, M.-R. Cioni, E. Copet, M. Dennefeld, T. Forveille, P. Fouqué, F. Garzón, H. J. Habing, A. Holl, J. Hron, S. Kimeswenger, F. Lacombe, T. Le Bertre, C. Loup, G. A. Mamon, A. Omont, G. Paturel, P. Persi, A. C. Robin, D. Rouan, D. Tiphène, I. Vauglin, and S. J. Wagner. A preliminary database of DENIS point sources. *A&A*, 349:236–242, September 1999.
- E. D. Feigelson. X-rays, pre-main sequence stars and planet formation. In F. Favata, G. A. J. Hussain, and B. Battrick, editors, *13th Cambridge Workshop on Cool Stars, Stellar Systems and the Sun*, volume 560 of *ESA Special Publication*, page 175, March 2005.
- E. D. Feigelson. X-ray insights into star and planet formation. *Proceedings of the National Academy of Science*, 107:7153–7157, April 2010. doi: 10.1073/pnas.0913952107.
- E. D. Feigelson, G. P. Garmire, and S. H. Pravdo. Magnetic Flaring in the Pre-Main-Sequence Sun and Implications for the Early Solar System. *ApJ*, 572:335–349, June 2002. doi: 10.1086/340340.
- D. Foreman-Mackey, D. W. Hogg, D. Lang, and J. Goodman. emcee: The MCMC Hammer. *PASP*, 125:306–312, March 2013. doi: 10.1086/670067.
- A. Fruscione, J. C. McDowell, G. E. Allen, N. S. Brickhouse, D. J. Burke, J. E. Davis, N. Durham, M. Elvis, E. C. Galle, D. E. Harris, D. P. Huenemoerder, J. C. Houck, B. Ishibashi, M. Karovska, F. Nicastro, M. S. Noble, M. A. Nowak, F. A. Primini, A. Siemiginowska, R. K. Smith, and M. Wise. CIAO: Chandra’s data analysis system. In *Society of Photo-Optical Instrumentation Engineers (SPIE) Conference Series*, volume 6270 of *Society of Photo-Optical Instrumentation Engineers (SPIE) Conference Series*, page 1, June 2006. doi: 10.1117/12.671760.
- J. Gagné, J. K. Faherty, K. L. Cruz, D. Lafrenière, R. Doyon, L. Malo, A. J. Burgasser,

- M.-E. Naud, É. Artigau, S. Bouchard, J. E. Gizis, and L. Albert. BANYAN. VII. A New Population of Young Substellar Candidate Members of Nearby Moving Groups from the BASS Survey. *ApJS*, 219:33, August 2015. doi: 10.1088/0067-0049/219/2/33.
- J. Gagné, E. E. Mamajek, L. Malo, A. Riedel, D. Rodriguez, D. Lafrenière, J. K. Faherty, O. Roy-Loubier, L. Pueyo, A. C. Robin, and R. Doyon. BANYAN. XI. The BANYAN  $\Sigma$  Multivariate Bayesian Algorithm to Identify Members of Young Associations with 150 pc. *ApJ*, 856:23, March 2018. doi: 10.3847/1538-4357/aaae09.
- G. F. Gahm. Flares on T Tauri stars. In L. V. Mirzorian, B. R. Pettersen, and M. K. Tsvetkov, editors, *Flare Stars in Star Clusters, Associations and the Solar Vicinity*, volume 137 of *IAU Symposium*, pages 193–206, 1990.
- Gaia Collaboration, T. Prusti, J. H. J. de Bruijne, A. G. A. Brown, A. Vallenari, C. Babusiaux, C. A. L. Bailer-Jones, U. Bastian, M. Biermann, D. W. Evans, and et al. The Gaia mission. *A&A*, 595:A1, November 2016. doi: 10.1051/0004-6361/201629272.
- Gaia Collaboration, C. Babusiaux, F. van Leeuwen, M. A. Barstow, C. Jordi, A. Vallenari, D. Bossini, A. Bressan, T. Cantat-Gaudin, M. van Leeuwen, and et al. Gaia Data Release 2. Observational Hertzsprung-Russell diagrams. *A&A*, 616:A10, August 2018a. doi: 10.1051/0004-6361/201832843.
- Gaia Collaboration, A. G. A. Brown, A. Vallenari, T. Prusti, J. H. J. de Bruijne, C. Babusiaux, and C. A. L. Bailer-Jones. Gaia Data Release 2. Summary of the contents and survey properties. *ArXiv e-prints*, April 2018b.
- R. E. Gershberg. Some results of the cooperative photometric observations of the UV Cet-type flare stars in the years 1967–71. *Ap&SS*, 19:75–92, November 1972. doi: 10.1007/BF00643168.
- R. E. Gershberg. *Solar-Type Activity in Main-Sequence Stars*. 2005. doi: 10.1007/3-540-28243-2.
- R. E. Gershberg and N. I. Shakhovskaia. Characteristics of activity energetics of the UV Cet-type flare stars. *Ap&SS*, 95:235–253, September 1983. doi: 10.1007/BF00653631.
- K. V. Getman, E. D. Feigelson, P. S. Broos, G. Micela, and G. P. Garmire. X-Ray Flares in Orion Young Stars. I. Flare Characteristics. *ApJ*, 688:418–436, November 2008a. doi: 10.1086/592033.
- K. V. Getman, E. D. Feigelson, G. Micela, M. M. Jardine, S. G. Gregory, and G. P. Garmire. X-Ray Flares in Orion Young Stars. II. Flares, Magnetospheres, and Protoplanetary Disks. *ApJ*, 688:437–455, November 2008b. doi: 10.1086/592034.
- R. L. Gilliland, J. M. Jenkins, W. J. Borucki, S. T. Bryson, D. A. Caldwell, B. D. Clarke, J. L. Dotson, M. R. Haas, J. Hall, T. Klaus, D. Koch, S. McCauliff, E. V. Quintana, J. D. Twicken, and J. E. van Cleve. Initial Characteristics of Kepler Short Cadence Data. *ApJL*, 713:L160–L163, April 2010. doi: 10.1088/2041-8205/713/2/L160.
- M. Gillon, E. Jehin, S. M. Lederer, L. Delrez, J. de Wit, A. Burdanov, V. Van Grootel, A. J. Burgasser, A. H. M. J. Triaud, C. Opitom, B.-O. Demory, D. K. Sahu,

- D. Bardalez Gagliuffi, P. Magain, and D. Queloz. Temperate Earth-sized planets transiting a nearby ultracool dwarf star. *Nature*, 533:221–224, May 2016. doi: 10.1038/nature17448.
- M. Gillon, A. H. M. J. Triaud, B.-O. Demory, E. Jehin, E. Agol, K. M. Deck, S. M. Lederer, J. de Wit, A. Burdanov, J. G. Ingalls, E. Bolmont, J. Leconte, S. N. Raymond, F. Selsis, M. Turbet, K. Barkaoui, A. Burgasser, M. R. Burleigh, S. J. Carey, A. Chaushev, C. M. Copperwheat, L. Delrez, C. S. Fernandes, D. L. Holdsworth, E. J. Kotze, V. Van Grootel, Y. Almleaky, Z. Benkhaldoun, P. Magain, and D. Queloz. Seven temperate terrestrial planets around the nearby ultracool dwarf star TRAPPIST-1. *Nature*, 542:456–460, February 2017. doi: 10.1038/nature21360.
- J. E. Gizis, D. G. Monet, I. N. Reid, J. D. Kirkpatrick, J. Liebert, and R. J. Williams. New Neighbors from 2MASS: Activity and Kinematics at the Bottom of the Main Sequence. *AJ*, 120:1085–1099, August 2000. doi: 10.1086/301456.
- J. E. Gizis, I. N. Reid, and S. L. Hawley. The Palomar/MSU Nearby Star Spectroscopic Survey. III. Chromospheric Activity, M Dwarf Ages, and the Local Star Formation History. *AJ*, 123:3356–3369, June 2002. doi: 10.1086/340465.
- J. E. Gizis, A. J. Burgasser, E. Berger, P. K. G. Williams, F. J. Vrba, K. L. Cruz, and S. Metchev. Kepler Monitoring of an L Dwarf I. The Photometric Period and White Light Flares. *ApJ*, 779:172, December 2013. doi: 10.1088/0004-637X/779/2/172.
- J. E. Gizis, K. G. Dettman, A. J. Burgasser, S. Camnasio, M. Alam, J. C. Filippazzo, K. L. Cruz, S. Metchev, E. Berger, and P. K. G. Williams. Kepler Monitoring of an L Dwarf. II. Clouds with Multi-year Lifetimes. *ApJ*, 813:104, November 2015. doi: 10.1088/0004-637X/813/2/104.
- J. E. Gizis, R. R. Paudel, D. Mullan, S. J. Schmidt, A. J. Burgasser, and P. K. G. Williams. K2 Ultracool Dwarfs Survey. II. The White Light Flare Rate of Young Brown Dwarfs. *ApJ*, 845:33, August 2017a. doi: 10.3847/1538-4357/aa7da0.
- J. E. Gizis, R. R. Paudel, S. J. Schmidt, P. K. G. Williams, and A. J. Burgasser. K2 Ultracool Dwarfs Survey. I. Photometry of an L Dwarf Superflare. *ApJ*, 838:22, March 2017b. doi: 10.3847/1538-4357/aa6197.
- N. Gopalswamy. Coronal Mass Ejections of Solar Cycle 23. *Journal of Astrophysics and Astronomy*, 27:243–254, September 2006. doi: 10.1007/BF02702527.
- R. L. Griffith, J. D. Kirkpatrick, P. R. M. Eisenhardt, C. R. Gelino, M. C. Cushing, D. Benford, A. Blain, C. R. Bridge, M. Cohen, R. M. Cutri, E. Donoso, T. H. Jarrett, C. Lonsdale, G. Mace, A. Mainzer, K. Marsh, D. Padgett, S. Petty, M. E. Ressler, M. F. Skrutskie, S. A. Stanford, D. Stern, C.-W. Tsai, E. L. Wright, J. Wu, and L. Yan. Spitzer Photometry of WISE-selected Brown Dwarf and Hyper-luminous Infrared Galaxy Candidates. *AJ*, 144:148, November 2012. doi: 10.1088/0004-6256/144/5/148.
- N. Grosso, K. R. Briggs, M. Güdel, S. Guieu, E. Franciosini, F. Palla, C. Dougados, J.-L. Monin, F. Ménard, J. Bouvier, M. Audard, and A. Telleschi. X-ray emission from the young brown dwarfs of the Taurus molecular cloud. *A&A*, 468:391–403, June 2007. doi: 10.1051/0004-6361:20065559.

- M. Güdel, J. H. M. M. Schmitt, J. A. Bookbinder, and T. A. Fleming. A tight correlation between radio and X-ray luminosities of M dwarfs. *ApJ*, 415:236–239, September 1993. doi: 10.1086/173158.
- M. Güdel, M. Audard, F. Reale, S. L. Skinner, and J. L. Linsky. Flares from small to large: X-ray spectroscopy of Proxima Centauri with XMM-Newton. *A&A*, 416:713–732, March 2004. doi: 10.1051/0004-6361:20031471.
- M. Güdel, K. R. Briggs, K. Arzner, M. Audard, J. Bouvier, E. D. Feigelson, E. Franciosini, A. Glauser, N. Grosso, G. Micela, J.-L. Monin, T. Montmerle, D. L. Padgett, F. Palla, I. Pillitteri, L. Rebull, L. Scelsi, B. Silva, S. L. Skinner, B. Stelzer, and A. Telleschi. The XMM-Newton extended survey of the Taurus molecular cloud (XEST). *A&A*, 468:353–377, June 2007. doi: 10.1051/0004-6361:20065724.
- M. Guedel and A. O. Benz. X-ray/microwave relation of different types of active stars. *ApJL*, 405:L63–L66, March 1993. doi: 10.1086/186766.
- E. Gullbring, L. Hartmann, C. Briceño, and N. Calvet. Disk Accretion Rates for T Tauri Stars. *ApJ*, 492:323–341, January 1998. doi: 10.1086/305032.
- M. N. Günther, Z. Zhan, S. Seager, P. B. Rimmer, S. Ranjan, K. G. Stassun, R. J. Oelkers, T. Daylan, E. Newton, E. Gillen, S. Rappaport, G. R. Ricker, D. W. Latham, J. N. Winn, J. M. Jenkins, A. Glidden, M. Fausnaugh, A. M. Levine, J. A. Dittmann, S. N. Quinn, A. Krishnamurthy, and E. B. Ting. Stellar Flares from the First Tess Data Release: Exploring a New Sample of M-dwarfs. *arXiv e-prints*, January 2019.
- G. Hallinan, A. Antonova, J. G. Doyle, S. Bourke, C. Lane, and A. Golden. Confirmation of the Electron Cyclotron Maser Instability as the Dominant Source of Radio Emission from Very Low Mass Stars and Brown Dwarfs. *ApJ*, 684:644–653, September 2008. doi: 10.1086/590360.
- R. Handberg and M. N. Lund. Automated preparation of Kepler time series of planet hosts for asteroseismic analysis. *MNRAS*, 445:2698–2709, December 2014. doi: 10.1093/mnras/stu1823.
- S. L. Hawley and B. R. Pettersen. The great flare of 1985 April 12 on AD Leonis. *ApJ*, 378:725–741, September 1991. doi: 10.1086/170474.
- S. L. Hawley, J. E. Gizis, and I. N. Reid. The Palomar/MSU Nearby Star Spectroscopic Survey.II.The Southern M Dwarfs and Investigation of Magnetic Activity. *AJ*, 112:2799, December 1996. doi: 10.1086/118222.
- S. L. Hawley, J. R. A. Davenport, A. F. Kowalski, J. P. Wisniewski, L. Hebb, R. Deitrick, and E. J. Hilton. Kepler Flares. I. Active and Inactive M Dwarfs. *ApJ*, 797:121, December 2014. doi: 10.1088/0004-637X/797/2/121.
- K. Herbst, A. Papaioannou, S. Banjac, and B. Heber. From solar to stellar flare characteristics. On a new peak size distribution for G-, K-, and M-dwarf star flares. *A&A*, 621:A67, January 2019. doi: 10.1051/0004-6361/201832789.
- E. J. Hilton. *The Galactic M Dwarf Flare Rate*. PhD thesis, University of Washington, 2011.
- D. W. Hogg, J. Bovy, and D. Lang. Data analysis recipes: Fitting a model to data. *ArXiv e-prints*, August 2010.

- E. R. Houdebine, D. J. Mullan, B. Bercu, F. Paletou, and M. Gebran. The Rotation-Activity Correlations in K and M Dwarfs. II. New Constraints on the Dynamo Mechanisms in Late-K and M Dwarfs Before and At the Transition to Complete Convection. *ApJ*, 837:96, March 2017. doi: 10.3847/1538-4357/aa5cad.
- W. S. Howard, M. A. Tilley, H. Corbett, A. Youngblood, R. O. P. Loyd, J. K. Ratzloff, N. M. Law, O. Fors, D. del Ser, E. L. Shkolnik, C. Ziegler, E. E. Goeke, A. D. Pietraallo, and J. Haislip. The First Naked-eye Superflare Detected from Proxima Centauri. *ApJL*, 860:L30, June 2018. doi: 10.3847/2041-8213/aacaf3.
- S. B. Howell, C. Sobeck, M. Haas, M. Still, T. Barclay, F. Mullally, J. Troeltzsch, S. Aigrain, S. T. Bryson, D. Caldwell, W. J. Chaplin, W. D. Cochran, D. Huber, G. W. Marcy, A. Miglio, J. R. Najita, M. Smith, J. D. Twicken, and J. J. Fortney. The K2 Mission: Characterization and Early Results. *PASP*, 126:398, April 2014. doi: 10.1086/676406.
- D. Huber, S. T. Bryson, and et al. VizieR Online Data Catalog: K2 Ecliptic Plane Input Catalog (EPIC) (Huber+, 2017). *VizieR Online Data Catalog*, 4034, September 2017.
- J. A. G. Jackman, P. J. Wheatley, D. Bayliss, M. R. Burleigh, S. L. Casewell, P. Eigmüller, M. R. Goad, D. Pollacco, L. Raynard, C. A. Watson, and R. G. West. Detection of a giant white-light flare on an L2.5 dwarf with the Next Generation Transit Survey. *MNRAS*, March 2019. doi: 10.1093/mnras/slz039.
- B. V. Jackson and R. A. Howard. A CME Mass Distribution Derived from SOLWIND Coronagraph Observations. *Sol. Phys.*, 148:359–370, December 1993. doi: 10.1007/BF00645095.
- D. J. James, M. M. Jardine, R. D. Jeffries, S. Randich, A. Collier Cameron, and M. Ferreira. X-ray emission from nearby M-dwarfs: the super-saturation phenomenon. *MNRAS*, 318:1217–1226, November 2000. doi: 10.1046/j.1365-8711.2000.03838.x.
- M. Jardine and Y. C. Unruh. Coronal emission and dynamo saturation. *A&A*, 346: 883–891, June 1999.
- R. Jayawardhana, S. Mohanty, and G. Basri. Evidence for a T Tauri Phase in Young Brown Dwarfs. *ApJ*, 592:282–287, July 2003. doi: 10.1086/375573.
- J. M. Jenkins, D. A. Caldwell, H. Chandrasekaran, J. D. Twicken, S. T. Bryson, E. V. Quintana, B. D. Clarke, J. Li, C. Allen, P. Tenenbaum, H. Wu, T. C. Klaus, J. Van Cleve, J. A. Dotson, M. R. Haas, R. L. Gilliland, D. G. Koch, and W. J. Borucki. Initial Characteristics of Kepler Long Cadence Data for Detecting Transiting Planets. *ApJL*, 713:L120–L125, April 2010. doi: 10.1088/2041-8205/713/2/L120.
- J. S. Jenkins, L. W. Ramsey, H. R. A. Jones, Y. Pavlenko, J. Gallardo, J. R. Barnes, and D. J. Pinfield. Rotational Velocities for M Dwarfs. *ApJ*, 704:975–988, October 2009. doi: 10.1088/0004-637X/704/2/975.
- A. H. Joy and M. L. Humason. Observations of the Faint Dwarf Star L 726-8. *PASP*, 61:133–134, June 1949. doi: 10.1086/126150.
- S. Kahler. Injection profiles of solar energetic particles as functions of coronal mass ejection heights. *ApJ*, 428:837–842, June 1994. doi: 10.1086/174292.
- M. M. Kao, G. Hallinan, J. S. Pineda, I. Escala, A. Burgasser, S. Bourke, and

- D. Stevenson. Auroral Radio Emission from Late L and T Dwarfs: A New Constraint on Dynamo Theory in the Substellar Regime. *ApJ*, 818:24, February 2016. doi: 10.3847/0004-637X/818/1/24.
- H. Karttunen, P. Kröger, H. Oja, M. Poutanen, and K. J. Donner. *Fundamental Astronomy*. 2017. doi: 10.1007/978-3-662-53045-0.
- V. V. Kasinsky and R. T. Sotnicova. Integral Energy Spectra of Solar Soft X-Ray Flares in the Three Solar Activity Cycles (1972-2001). *Astronomical and Astrophysical Transactions*, 22:325–333, March 2003. doi: 10.1080/1055679031000079665.
- J. D. Kirkpatrick, T. J. Henry, and D. W. McCarthy, Jr. A standard stellar spectral sequence in the red/near-infrared - Classes K5 to M9. *ApJS*, 77:417–440, November 1991. doi: 10.1086/191611.
- J. D. Kirkpatrick, T. J. Henry, and D. A. Simons. The solar neighborhood. 2: The first list of dwarfs with spectral types of M7 and cooler. *AJ*, 109:797–807, February 1995. doi: 10.1086/117323.
- J. D. Kirkpatrick, I. N. Reid, J. Liebert, R. M. Cutri, B. Nelson, C. A. Beichman, C. C. Dahn, D. G. Monet, J. E. Gizis, and M. F. Skrutskie. Dwarfs Cooler than “M”: The Definition of Spectral Type “L” Using Discoveries from the 2 Micron All-Sky Survey (2MASS). *ApJ*, 519:802–833, July 1999. doi: 10.1086/307414.
- J. D. Kirkpatrick, I. N. Reid, J. Liebert, J. E. Gizis, A. J. Burgasser, D. G. Monet, C. C. Dahn, B. Nelson, and R. J. Williams. 67 Additional L Dwarfs Discovered by the Two Micron All Sky Survey. *AJ*, 120:447–472, July 2000. doi: 10.1086/301427.
- J. D. Kirkpatrick, K. L. Cruz, T. S. Barman, A. J. Burgasser, D. L.Looper, C. G. Tinney, C. R. Gelino, P. J. Lowrance, J. Liebert, J. M. Carpenter, L. A. Hillenbrand, and J. R. Stauffer. A Sample of Very Young Field L Dwarfs and Implications for the Brown Dwarf “Lithium Test” at Early Ages. *ApJ*, 689:1295–1326, December 2008. doi: 10.1086/592768.
- R. Klein, D. Apai, I. Pascucci, T. Henning, and L. B. F. M. Waters. First Detection of Millimeter Dust Emission from Brown Dwarf Disks. *ApJL*, 593:L57–L60, August 2003. doi: 10.1086/377729.
- D. G. Koch, W. J. Borucki, G. Basri, N. M. Batalha, T. M. Brown, D. Caldwell, J. Christensen-Dalsgaard, W. D. Cochran, E. DeVore, E. W. Dunham, T. N. Gautier, III, J. C. Geary, R. L. Gilliland, A. Gould, J. Jenkins, Y. Kondo, D. W. Latham, J. J. Lissauer, G. Marcy, D. Monet, D. Sasselov, A. Boss, D. Brownlee, J. Caldwell, A. K. Dupree, S. B. Howell, H. Kjeldsen, S. Meibom, D. Morrison, T. Owen, H. Reitsema, J. Tarter, S. T. Bryson, J. L. Dotson, P. Gazis, M. R. Haas, J. Kolodziejczak, J. F. Rowe, J. E. Van Cleve, C. Allen, H. Chandrasekaran, B. D. Clarke, J. Li, E. V. Quintana, P. Tenenbaum, J. D. Twicken, and H. Wu. Kepler Mission Design, Realized Photometric Performance, and Early Science. *ApJL*, 713:L79–L86, April 2010. doi: 10.1088/2041-8205/713/2/L79.
- C. Koen. An extensive search for rapid optical variability in ultracool dwarfs. *MNRAS*, 428:2824–2839, February 2013. doi: 10.1093/mnras/sts208.
- C. Koen, B. Miszalski, P. Väisänen, and T. Koen. Optical spectra of ultracool dwarfs with the Southern African Large Telescope. *MNRAS*, 465:4723–4734, March 2017.

- doi: 10.1093/mnras/stw3106.
- G. Kopp, G. Lawrence, and G. Rottman. The Total Irradiance Monitor (TIM): Science Results. *Sol. Phys.*, 230:129–139, August 2005. doi: 10.1007/s11207-005-7433-9.
- A. F. Kowalski, S. L. Hawley, E. J. Hilton, A. C. Becker, A. A. West, J. J. Bochanski, and B. Sesar. M Dwarfs in Sloan Digital Sky Survey Stripe 82: Photometric Light Curves and Flare Rate Analysis. *AJ*, 138:633–648, August 2009. doi: 10.1088/0004-6256/138/2/633.
- A. F. Kowalski, S. L. Hawley, J. A. Holtzman, J. P. Wisniewski, and E. J. Hilton. A White Light Megaflare on the dM4.5e Star YZ CMi. *ApJL*, 714:L98–L102, May 2010. doi: 10.1088/2041-8205/714/1/L98.
- A. F. Kowalski, S. L. Hawley, J. P. Wisniewski, R. A. Osten, E. J. Hilton, J. A. Holtzman, S. J. Schmidt, and J. R. A. Davenport. Time-resolved Properties and Global Trends in dMe Flares from Simultaneous Photometry and Spectra. *ApJS*, 207:15, July 2013. doi: 10.1088/0067-0049/207/1/15.
- A. F. Kowalski, S. L. Hawley, M. Carlsson, J. C. Allred, H. Uitenbroek, R. A. Osten, and G. Holman. New Insights into White-Light Flare Emission from Radiative-Hydrodynamic Modeling of a Chromospheric Condensation. *Sol. Phys.*, 290:3487–3523, December 2015. doi: 10.1007/s11207-015-0708-x.
- A. L. Kraus, R. J. White, and L. A. Hillenbrand. Multiplicity and Optical Excess across the Substellar Boundary in Taurus. *ApJ*, 649:306–318, September 2006. doi: 10.1086/503665.
- A. L. Kraus, E. L. Shkolnik, K. N. Allers, and M. C. Liu. A Stellar Census of the Tucana-Horologium Moving Group. *AJ*, 147:146, June 2014. doi: 10.1088/0004-6256/147/6/146.
- S. S. Kumar. Models for Stars of Very Low Mass. Technical report, October 1962.
- L. N. Kurochka. Energy Distribution of 15000 Solar Flares. *Soviet Ast.*, 31:231, April 1987.
- C. H. Lacy, T. J. Moffett, and D. S. Evans. UV Ceti stars - Statistical analysis of observational data. *ApJS*, 30:85–96, January 1976. doi: 10.1086/190358.
- H. Lammer, F. Selsis, I. Ribas, E. F. Guinan, S. J. Bauer, and W. W. Weiss. Atmospheric Loss of Exoplanets Resulting from Stellar X-Ray and Extreme-Ultraviolet Heating. *ApJL*, 598:L121–L124, December 2003. doi: 10.1086/380815.
- K. Lee, Y.-J. Moon, and V. M. Nakariakov. Dependence of Occurrence Rates of Solar Flares and Coronal Mass Ejections on the Solar Cycle Phase and the Importance of Large-scale Connectivity. *ApJ*, 831:131, November 2016. doi: 10.3847/0004-637X/831/2/131.
- J. Liebert and J. E. Gizis. RI Photometry of 2MASS-selected Late M and L Dwarfs. *PASP*, 118:659–670, May 2006. doi: 10.1086/503333.
- J. Liebert, J. D. Kirkpatrick, I. N. Reid, and M. D. Fisher. A 2MASS Ultracool M Dwarf Observed in a Spectacular Flare. *ApJ*, 519:345–353, July 1999. doi: 10.1086/307349.
- J. Liebert, J. D. Kirkpatrick, K. L. Cruz, I. N. Reid, A. Burgasser, C. G. Tinney, and J. E. Gizis. A Flaring L5 Dwarf: The Nature of H $\alpha$  Emission in Very Low Mass (Sub)Stellar Objects. *AJ*, 125:343–347, January 2003. doi: 10.1086/345514.

- D. N. Limber. The Structure of the M Dwarf Stars. II. *ApJ*, 127:387, March 1958. doi: 10.1086/146469.
- M. C. Liu and S. K. Leggett. Kelu-1 Is a Binary L Dwarf: First Brown Dwarf Science from Laser Guide Star Adaptive Optics. *ApJ*, 634:616–624, November 2005. doi: 10.1086/496915.
- M. C. Liu, J. Najita, and A. T. Tokunaga. A Survey for Circumstellar Disks around Young Substellar Objects. *ApJ*, 585:372–391, March 2003. doi: 10.1086/345895.
- R. O. P. Loyd, E. L. Shkolnik, A. C. Schneider, T. S. Barman, V. S. Meadows, I. Pagano, and S. Peacock. HAZMAT. IV. Flares and Superflares on Young M Stars in the Far Ultraviolet. *ApJ*, 867:70, November 2018. doi: 10.3847/1538-4357/aae2ae.
- R. Luger, E. Agol, E. Kruse, R. Barnes, A. Becker, D. Foreman-Mackey, and D. Deming. EVEREST: Pixel Level Decorrelation of K2 Light Curves. *AJ*, 152:100, October 2016. doi: 10.3847/0004-6256/152/4/100.
- R. Luger, M. Sestovic, E. Kruse, S. L. Grimm, B.-O. Demory, E. Agol, E. Bolmont, D. Fabrycky, C. S. Fernandes, V. Van Grootel, A. Burgasser, M. Gillon, J. G. Ingalls, E. Jehin, S. N. Raymond, F. Selsis, A. H. M. J. Triaud, T. Barclay, G. Barentsen, S. B. Howell, L. Delrez, J. de Wit, D. Foreman-Mackey, D. L. Holdsworth, J. Leconte, S. Lederer, M. Turbet, Y. Almleaky, Z. Benkhaldoun, P. Magain, B. M. Morris, K. Heng, and D. Queloz. A seven-planet resonant chain in TRAPPIST-1. *Nature Astronomy*, 1:0129, June 2017. doi: 10.1038/s41550-017-0129.
- K. L. Luhman, E. E. Mamajek, S. J. Shukla, and N. P. Loutrel. A Survey for New Members of the Taurus Star-forming Region with the Sloan Digital Sky Survey. *AJ*, 153:46, January 2017. doi: 10.3847/1538-3881/153/1/46.
- M. N. Lund, R. Handberg, G. R. Davies, W. J. Chaplin, and C. D. Jones. K2P<sup>2</sup> A Photometry Pipeline for the K2 Mission. *ApJ*, 806:30, June 2015. doi: 10.1088/0004-637X/806/1/30.
- W. J. Luyten. A Third Flare of L 726-8B. *PASP*, 61:179, August 1949. doi: 10.1086/126169.
- G. N. Mace. VizieR Online Data Catalog: Near-IR spectroscopy of low-mass binaries and brown dwarfs (Mace, 2014). *VizieR Online Data Catalog*, 5144, May 2014.
- M. A. MacGregor, A. J. Weinberger, D. J. Wilner, A. F. Kowalski, and S. R. Cranmer. Detection of a Millimeter Flare from Proxima Centauri. *ApJL*, 855:L2, March 2018. doi: 10.3847/2041-8213/aaad6b.
- H. Maehara, T. Shibayama, S. Notsu, Y. Notsu, T. Nagao, S. Kusaba, S. Honda, D. Nogami, and K. Shibata. Superflares on solar-type stars. *Nature*, 485:478–481, May 2012. doi: 10.1038/nature11063.
- H. Maehara, T. Shibayama, Y. Notsu, S. Notsu, S. Honda, D. Nogami, and K. Shibata. Statistical properties of superflares on solar-type stars based on 1-min cadence data. *Earth, Planets, and Space*, 67:59, April 2015. doi: 10.1186/s40623-015-0217-z.
- E. A. Magnier, E. F. Schlafly, D. P. Finkbeiner, J. L. Tonry, B. Goldman, S. Röser, E. Schilbach, K. C. Chambers, H. A. Flewelling, M. E. Huber, P. A. Price, W. E. Sweeney, C. Z. Waters, L. Denneau, P. Draper, K. W. Hodapp, R. Jedicke, R.-P. Kudritzki, N. Metcalfe, C. W. Stubbs, and R. J. Wainscoat. Pan-STARRS

- Photometric and Astrometric Calibration. *ArXiv e-prints*, December 2016.
- E. L. Martín and D. R. Ardila. Flares at the Cool End of the M Dwarfs: The Case of LHS 2065. *AJ*, 121:2758–2760, May 2001. doi: 10.1086/320412.
- E. L. Martín, X. Delfosse, G. Basri, B. Goldman, T. Forveille, and M. R. Zapatero Osorio. Spectroscopic Classification of Late-M and L Field Dwarfs. *AJ*, 118:2466–2482, November 1999. doi: 10.1086/301107.
- E. L. Martín, C. Dougados, E. Magnier, F. Ménard, A. Magazzù, J.-C. Cuillandre, and X. Delfosse. Four Brown Dwarfs in the Taurus Star-Forming Region. *ApJL*, 561:L195–L198, November 2001. doi: 10.1086/324754.
- E. L. Martín, J. Cabrera, E. Martioli, E. Solano, and R. Tata. Kepler observations of very low-mass stars. *A&A*, 555:A108, July 2013. doi: 10.1051/0004-6361/201321186.
- B. McBreen and L. Hanlon. Gamma-ray bursts and the origin of chondrules and planets. *A&A*, 351:759–765, November 1999.
- Wes McKinney. Data structures for statistical computing in python. In Stéfan van der Walt and Jarrod Millman, editors, *Proceedings of the 9th Python in Science Conference*, pages 51 – 56, 2010.
- I. S. McLean, J. R. Graham, E. E. Becklin, D. F. Figer, J. E. Larkin, N. A. Levenson, and H. I. Teplitz. Performance and results with the NIRSPEC echelle spectrograph on the Keck II telescope. In M. Iye and A. F. Moorwood, editors, *Optical and IR Telescope Instrumentation and Detectors*, volume 4008 of Proc. SPIE, pages 1048–1055, August 2000. doi: 10.1117/12.395422.
- M. McLean, E. Berger, and A. Reiners. The Radio Activity-Rotation Relation of Ultracool Dwarfs. *ApJ*, 746:23, February 2012. doi: 10.1088/0004-637X/746/1/23.
- A. McQuillan, S. Aigrain, and T. Mazeh. Measuring the rotation period distribution of field M dwarfs with Kepler. *MNRAS*, 432:1203–1216, June 2013. doi: 10.1093/mnras/stt536.
- G. Micela, S. Sciortino, S. Serio, G. S. Vaiana, J. Bookbinder, L. Golub, F. R. Harnden, Jr., and R. Rosner. Einstein X-ray survey of the Pleiades - The dependence of X-ray emission on stellar age. *ApJ*, 292:172–180, May 1985. doi: 10.1086/163143.
- K. J. Mighell and P. Plavchan. Period Error Estimation for the Kepler Eclipsing Binary Catalog. *AJ*, 145:148, June 2013. doi: 10.1088/0004-6256/145/6/148.
- C. J. Miller, C. Genovese, R. C. Nichol, L. Wasserman, A. Connolly, D. Reichart, A. Hopkins, J. Schneider, and A. Moore. Controlling the False-Discovery Rate in Astrophysical Data Analysis. *AJ*, 122:3492–3505, December 2001. doi: 10.1086/324109.
- D. Minniti, P. W. Lucas, J. P. Emerson, R. K. Saito, M. Hempel, P. Pietrukowicz, A. V. Ahumada, M. V. Alonso, J. Alonso-García, J. I. Arias, R. M. Bandyopadhyay, R. H. Barbá, B. Barbuy, L. R. Bedin, E. Bica, J. Borissova, L. Bronfman, G. Carraro, M. Catelan, J. J. Clariá, N. Cross, R. de Grijs, I. Dékány, J. E. Drew, C. Fariña, C. Feinstein, E. Fernández Lajús, R. C. Gamen, D. Geisler, W. Gieren, B. Goldman, O. A. Gonzalez, G. Gunthardt, S. Gurovich, N. C. Hambly, M. J. Irwin, V. D. Ivanov, A. Jordán, E. Kerins, K. Kinemuchi, R. Kurtev, M. López-Corredoira, T. Maccarone, N. Masetti, D. Merlo, M. Messineo, I. F. Mirabel, L. Monaco, L. Morelli, N. Padilla,

- T. Palma, M. C. Parisi, G. Pignata, M. Rejkuba, A. Roman-Lopes, S. E. Sale, M. R. Schreiber, A. C. Schröder, M. Smith, L. S. , Jr., M. Soto, M. Tamura, C. Tappert, M. A. Thompson, I. Toledo, M. Zoccali, and G. Pietrzynski. VISTA Variables in the Via Lactea (VVV): The public ESO near-IR variability survey of the Milky Way. *New A*, 15:433–443, July 2010. doi: 10.1016/j.newast.2009.12.002.
- T. J. Moffett. UV Ceti flare stars - Observational data. *ApJS*, 29:1–42, December 1974. doi: 10.1086/190330.
- S. Mohanty and G. Basri. Rotation and Activity in Mid-M to L Field Dwarfs. *ApJ*, 583:451–472, January 2003. doi: 10.1086/345097.
- S. Mohanty, G. Basri, F. Shu, F. Allard, and G. Chabrier. Activity in Very Cool Stars: Magnetic Dissipation in Late M and L Dwarf Atmospheres. *ApJ*, 571:469–486, May 2002. doi: 10.1086/339911.
- N. Mondrik, E. Newton, and D. C. J. Irwin. An increased rate of large flares at intermediate rotation periods for mid-to-late M dwarfs. *ArXiv e-prints*, September 2018.
- N. Mondrik, E. Newton, D. Charbonneau, and J. Irwin. An Increased Rate of Large Flares at Intermediate Rotation Periods for Mid-to-late M Dwarfs. *ApJ*, 870:10, January 2019. doi: 10.3847/1538-4357/aace64.
- J.-L. Monin, S. Guieu, C. Pinte, L. Rebull, P. Goldsmith, M. Fukagawa, F. Ménard, D. Padgett, K. Stappelfeld, C. McCabe, S. Carey, A. Noriega-Crespo, T. Brooke, T. Huard, S. Terebey, L. Hillenbrand, and M. Guedel. The large-scale disk fraction of brown dwarfs in the Taurus cloud as measured with Spitzer. *A&A*, 515:A91, June 2010. doi: 10.1051/0004-6361/200912338.
- P. S. Muirhead, C. D. Dressing, A. W. Mann, B. Rojas-Ayala, S. Lépine, M. Paegert, N. De Lee, and R. Oelkers. A Catalog of Cool Dwarf Targets for the Transiting Exoplanet Survey Satellite. *AJ*, 155:180, April 2018. doi: 10.3847/1538-3881/aab710.
- D. J. Mullan. Solar and stellar flares. *Sol. Phys.*, 54:183–206, September 1977. doi: 10.1007/BF00146436.
- D. J. Mullan. On the possibility of resonant electrodynamic coupling in the coronae of red dwarfs. *ApJ*, 282:603–611, July 1984. doi: 10.1086/162239.
- D. J. Mullan. Patterns of X-ray, Chromospheric, and Radio Emission in Low-mass Stars: Fast and Slow Magnetic Reconnection. *ApJ*, 721:1034–1043, October 2010. doi: 10.1088/0004-637X/721/2/1034.
- D. J. Mullan and H. P. Bais. Photosynthesis on a Planet Orbiting an M Dwarf: Enhanced Effectiveness during Flares. *ApJ*, 865:101, October 2018. doi: 10.3847/1538-4357/aadfd1.
- D. J. Mullan and M. Mathioudakis. Extreme-Ultraviolet Flares in an F2 Star. *ApJ*, 544:475–480, November 2000. doi: 10.1086/317202.
- D. J. Mullan and R. R. Paudel. Frequencies of Flare Occurrence: Interaction between Convection and Coronal Loops. *ApJ*, 854:14, February 2018. doi: 10.3847/1538-4357/aaa960.
- D. J. Mullan and R. R. Paudel. Origin of Radio-quiet Coronal Mass Ejections in Flare Stars. *ApJ*, 873:1, March 2019. doi: 10.3847/1538-4357/ab041b.

- D. J. Mullan, E. R. Houdebine, and J. MacDonald. A Model for Interface Dynamos in Late K and Early M Dwarfs. *ApJL*, 810:L18, September 2015. doi: 10.1088/2041-8205/810/2/L18.
- D. J. Mullan, J. MacDonald, S. Dieterich, and H. Fausey. Magnetic Fields on the Flare Star Trappist-1: Consequences for Radius Inflation and Planetary Habitability. *ArXiv e-prints*, November 2018.
- T. Nakajima, B. R. Oppenheimer, S. R. Kulkarni, D. A. Golimowski, K. Matthews, and S. T. Durrance. Discovery of a cool brown dwarf. *Nature*, 378:463–465, November 1995. doi: 10.1038/378463a0.
- K. Namekata, T. Sakaue, K. Watanabe, A. Asai, H. Maehara, Y. Notsu, S. Notsu, S. Honda, T. T. Ishii, K. Ikuta, D. Nogami, and K. Shibata. Statistical Studies of Solar White-light Flares and Comparisons with Superflares on Solar-type Stars. *ApJ*, 851:91, December 2017. doi: 10.3847/1538-4357/aa9b34.
- D. F. Neidig and E. W. Cliver. The occurrence frequency of white-light flares. *Sol. Phys.*, 88:275–280, October 1983. doi: 10.1007/BF00196192.
- E. R. Newton, J. Irwin, D. Charbonneau, Z. K. Berta-Thompson, J. A. Dittmann, and A. A. West. The Rotation and Galactic Kinematics of Mid M Dwarfs in the Solar Neighborhood. *ApJ*, 821:93, April 2016. doi: 10.3847/0004-637X/821/2/93.
- E. R. Newton, J. Irwin, D. Charbonneau, P. Berlind, M. L. Calkins, and J. Mink. The H $\alpha$  Emission of Nearby M Dwarfs and its Relation to Stellar Rotation. *ApJ*, 834:85, January 2017. doi: 10.3847/1538-4357/834/1/85.
- Elisabeth R. Newton, David Charbonneau, Jonathan Irwin, and Andrew W. Mann. An Empirical Calibration to Estimate Cool Dwarf Fundamental Parameters from H-band Spectra. *ApJ*, 800:85, February 2015. doi: 10.1088/0004-637X/800/2/85.
- Y. Notsu, T. Shibayama, H. Maehara, S. Notsu, T. Nagao, S. Honda, T. T. Ishii, D. Nogami, and K. Shibata. Superflares on Solar-type Stars Observed with Kepler II. Photometric Variability of Superflare-generating Stars: A Signature of Stellar Rotation and Starspots. *ApJ*, 771:127, July 2013. doi: 10.1088/0004-637X/771/2/127.
- Y. Notsu, H. Maehara, S. Honda, S. L. Hawley, J. R. A. Davenport, K. Namekata, S. Notsu, K. Ikuta, D. Nogami, and K. Shibata. Do Kepler Superflare Stars Really Include Slowly Rotating Sun-like Stars? Results Using APO 3.5 m Telescope Spectroscopic Observations and Gaia-DR2 Data. *ApJ*, 876:58, May 2019. doi: 10.3847/1538-4357/ab14e6.
- R. W. Noyes, L. W. Hartmann, S. L. Baliunas, D. K. Duncan, and A. H. Vaughan. Rotation, convection, and magnetic activity in lower main-sequence stars. *ApJ*, 279:763–777, April 1984. doi: 10.1086/161945.
- R. A. Osten and S. J. Wolk. Connecting Flares and Transient Mass-loss Events in Magnetically Active Stars. *ApJ*, 809:79, August 2015. doi: 10.1088/0004-637X/809/1/79.
- R. A. Osten, S. L. Hawley, J. C. Allred, C. M. Johns-Krull, and C. Roark. From Radio to X-Ray: Flares on the dMe Flare Star EV Lacertae. *ApJ*, 621:398–416, March 2005. doi: 10.1086/427275.

- R. A. Osten, S. L. Hawley, J. Allred, C. M. Johns-Krull, A. Brown, and G. M. Harper. From Radio to X-Ray: The Quiescent Atmosphere of the dMe Flare Star EV Lacertae. *ApJ*, 647:1349–1374, August 2006. doi: 10.1086/504889.
- R. A. Osten, O. Godet, S. Drake, J. Tueller, J. Cummings, H. Krimm, J. Pye, V. Pal’shin, S. Golenetskii, F. Reale, S. R. Oates, M. J. Page, and A. Melandri. The Mouse That Roared: A Superflare from the dMe Flare Star EV Lac Detected by Swift and Konus-Wind. *ApJ*, 721:785–801, September 2010. doi: 10.1088/0004-637X/721/1/785.
- R. A. Osten, A. Kowalski, K. Sahu, and S. L. Hawley. DRAFTS: A Deep, Rapid Archival Flare Transient Search in the Galactic Bulge. *ApJ*, 754:4, July 2012. doi: 10.1088/0004-637X/754/1/4.
- R. A. Osten, A. Kowalski, S. A. Drake, H. Krimm, K. Page, K. Gazeas, J. Kennea, S. Oates, M. Page, E. de Miguel, R. Novák, T. Apeltauer, and N. Gehrels. A Very Bright, Very Hot, and Very Long Flaring Event from the M Dwarf Binary System DG CVn. *ApJ*, 832:174, December 2016. doi: 10.3847/0004-637X/832/2/174.
- J. E. Owen and S. Mohanty. Habitability of terrestrial-mass planets in the HZ of M Dwarfs - I. H/He-dominated atmospheres. *MNRAS*, 459:4088–4108, July 2016. doi: 10.1093/mnras/stw959.
- J. E. Owen, B. Ercolano, and C. J. Clarke. Protoplanetary disc evolution and dispersal: the implications of X-ray photoevaporation. *MNRAS*, 412:13–25, March 2011. doi: 10.1111/j.1365-2966.2010.17818.x.
- E. N. Parker. Hydromagnetic Dynamo Models. *ApJ*, 122:293, September 1955. doi: 10.1086/146087.
- I. Pascucci, D. Apai, T. Henning, and C. P. Dullemond. The First Detailed Look at a Brown Dwarf Disk. *ApJL*, 590:L111–L114, June 2003. doi: 10.1086/376773.
- I. Pascucci, G. Laughlin, B. S. Gaudi, G. Kennedy, K. Luhman, S. Mohanty, J. Birkby, B. Ercolano, P. Plavchan, and A. Skemer. Planet Formation Around M-dwarf Stars: From Young Disks to Planets. In C. Johns-Krull, M. K. Browning, and A. A. West, editors, *16th Cambridge Workshop on Cool Stars, Stellar Systems, and the Sun*, volume 448 of *Astronomical Society of the Pacific Conference Series*, page 469, December 2011.
- R. R. Paudel, J. E. Gizis, D. J. Mullan, S. J. Schmidt, A. J. Burgasser, P. K. G. Williams, and E. Berger. K2 Ultracool Dwarfs Survey. III. White Light Flares Are Ubiquitous in M6-L0 Dwarfs. *ApJ*, 858:55, May 2018a. doi: 10.3847/1538-4357/aab8fe.
- R. R. Paudel, J. E. Gizis, D. J. Mullan, S. J. Schmidt, A. J. Burgasser, P. K. G. Williams, and E. Berger. K 2 Ultracool Dwarfs Survey. IV. Monster Flares Observed on the Young Brown Dwarf CFHT-BD-Tau 4. *ApJ*, 861:76, July 2018b. doi: 10.3847/1538-4357/aac8e0.
- M. J. Pecaut and E. E. Mamajek. Intrinsic Colors, Temperatures, and Bolometric Corrections of Pre-main-sequence Stars. *ApJS*, 208:9, September 2013. doi: 10.1088/0067-0049/208/1/9.
- J. S. Pineda, G. Hallinan, J. D. Kirkpatrick, G. Cotter, M. M. Kao, and K. Mooley. A

- Survey for H $\alpha$  Emission from Late L Dwarfs and T Dwarfs. *ApJ*, 826:73, July 2016. doi: 10.3847/0004-637X/826/1/73.
- J. S. Pineda, G. Hallinan, and M. M. Kao. A Panchromatic View of Brown Dwarf Aurorae. *ApJ*, 846:75, September 2017. doi: 10.3847/1538-4357/aa8596.
- N. Pizzolato, A. Maggio, G. Micela, S. Sciortino, and P. Ventura. The stellar activity-rotation relationship revisited: Dependence of saturated and non-saturated X-ray emission regimes on stellar mass for late-type dwarfs. *A&A*, 397:147–157, January 2003. doi: 10.1051/0004-6361:20021560.
- T. Preibisch, M. J. McCaughrean, N. Grosso, E. D. Feigelson, E. Flaccomio, K. Getman, L. A. Hillenbrand, G. Meeus, G. Micela, S. Sciortino, and B. Stelzer. X-Ray Emission from Young Brown Dwarfs in the Orion Nebula Cluster. *ApJS*, 160:582–593, October 2005. doi: 10.1086/432098.
- A. S. Rajpurohit, F. Allard, S. Rajpurohit, R. Sharma, G. D. C. Teixeira, O. Mousis, and R. Kamlesh. Exploring the stellar properties of M dwarfs with high-resolution spectroscopy from the optical to the near-infrared. *A&A*, 620:A180, December 2018. doi: 10.1051/0004-6361/201833500.
- G. Ramsay, J. G. Doyle, P. Hakala, D. Garcia-Alvarez, A. Brooks, T. Barclay, and M. Still. Short-duration high-amplitude flares detected on the M dwarf star KIC 5474065. *MNRAS*, 434:2451–2457, September 2013. doi: 10.1093/mnras/stt1182.
- G. Ramsay, P. Hakala, and J. G. Doyle. Searching for I-band variability in stars in the M/L spectral transition region. *MNRAS*, 453:1484–1488, October 2015. doi: 10.1093/mnras/stv1742.
- S. Ranjan, R. Wordsworth, and D. D. Sasselov. The Surface UV Environment on Planets Orbiting M Dwarfs: Implications for Prebiotic Chemistry and the Need for Experimental Follow-up. *ApJ*, 843:110, July 2017. doi: 10.3847/1538-4357/aa773e.
- S. Rappaport, J. Swift, A. Levine, M. Joss, R. Sanchis-Ojeda, T. Barclay, M. Still, G. Handler, K. Oláh, P. S. Muirhead, D. Huber, and K. Vida. M-dwarf Rapid Rotators and the Detection of Relatively Young Multiple M-Star Systems. *ApJ*, 788:114, June 2014. doi: 10.1088/0004-637X/788/2/114.
- R. Rebolo, M. R. Zapatero Osorio, and E. L. Martín. Discovery of a brown dwarf in the Pleiades star cluster. *Nature*, 377:129–131, September 1995. doi: 10.1038/377129a0.
- L. M. Rebull, J. R. Stauffer, L. A. Hillenbrand, A. M. Cody, J. Bouvier, D. R. Soderblom, M. Pinsonneault, and L. Hebb. Rotation of Late-type Stars in Praesepe with K2. *ApJ*, 839:92, April 2017. doi: 10.3847/1538-4357/aa6aa4.
- I. N. Reid, S. L. Hawley, and J. E. Gizis. The Palomar/MSU Nearby-Star Spectroscopic Survey. I. The Northern M Dwarfs -Bandstrengths and Kinematics. *AJ*, 110:1838, October 1995. doi: 10.1086/117655.
- A. Reiners and G. Basri. Chromospheric Activity, Rotation, and Rotational Braking in M and L Dwarfs. *ApJ*, 684:1390–1403, September 2008. doi: 10.1086/590073.
- A. Reiners and G. Basri. A Volume-Limited Sample of 63 M7-M9.5 Dwarfs. I. Space Motion, Kinematic Age, and Lithium. *ApJ*, 705:1416–1424, November 2009. doi: 10.1088/0004-637X/705/2/1416.
- A. Reiners and G. Basri. A Volume-Limited Sample of 63 M7-M9.5 Dwarfs. II. Activity,

- Magnetism, and the Fade of the Rotation-Dominated Dynamo. *ApJ*, 710:924–935, February 2010. doi: 10.1088/0004-637X/710/2/924.
- A. Reiners and U. R. Christensen. A magnetic field evolution scenario for brown dwarfs and giant planets. *A&A*, 522:A13, November 2010. doi: 10.1051/0004-6361/201014251.
- A. Reiners, G. Basri, and M. Browning. Evidence for Magnetic Flux Saturation in Rapidly Rotating M Stars. *ApJ*, 692:538–545, February 2009a. doi: 10.1088/0004-637X/692/1/538.
- A. Reiners, G. Basri, and U. R. Christensen. Surprisingly Weak Magnetism on Young Accreting Brown Dwarfs. *ApJ*, 697:373–379, May 2009b. doi: 10.1088/0004-637X/697/1/373.
- A. Reiners, M. Zechmeister, J. A. Caballero, I. Ribas, J. C. Morales, S. V. Jeffers, P. Schöfer, L. Tal-Or, A. Quirrenbach, P. J. Amado, A. Kaminski, W. Seifert, M. Abril, J. Aceituno, F. J. Alonso-Floriano, M. Ammler-von Eiff, R. Antona, G. Anglada-Escudé, H. Anwand-Heerwart, B. Arroyo-Torres, M. Azzaro, D. Baroch, D. Barrado, F. F. Bauer, S. Becerril, V. J. S. Béjar, D. Benítez, Z. M. Berdiñas, G. Bergond, M. Blümcke, M. Brinkmüller, C. del Burgo, J. Cano, M. C. Cárdenas Vázquez, E. Casal, C. Cifuentes, A. Claret, J. Colomé, M. Cortés-Contreras, S. Czesla, E. Díez-Alonso, S. Dreizler, C. Feiz, M. Fernández, I. M. Ferro, B. Fuhrmeister, D. Galadí-Enríquez, A. Garcia-Piquer, M. L. García Vargas, L. Gesa, V. Gómez Galera, J. I. González Hernández, R. González-Peinado, U. Grözinger, S. Grohnert, J. Guàrdia, E. W. Guenther, A. Guijarro, E. de Guindos, J. Gutiérrez-Soto, H.-J. Hagen, A. P. Hatzes, P. H. Hauschildt, R. P. Hedrosa, J. Helmling, T. Henning, I. Hermelo, R. Hernández Arabí, L. Hernández Castaño, F. Hernández Hernando, E. Herrero, A. Huber, P. Huke, E. N. Johnson, E. de Juan, M. Kim, R. Klein, J. Klüter, A. Klutsch, M. Kürster, M. Lafarga, A. Lamert, M. Lampón, L. M. Lara, W. Laun, U. Lemke, R. Lenzen, R. Launhardt, M. López del Fresno, J. López-González, M. López-Puertas, J. F. López Salas, J. López-Santiago, R. Luque, H. Magán Madinabeitia, U. Mall, L. Mancini, H. Mandel, E. Marfil, J. A. Marín Molina, D. Maroto Fernández, E. L. Martín, S. Martín-Ruiz, C. J. Marvin, R. J. Mathar, E. Mirabet, D. Montes, M. E. Moreno-Raya, A. Moya, R. Mundt, E. Nagel, V. Naranjo, L. Nortmann, G. Nowak, A. Ofir, R. Oreiro, E. Pallé, J. Panduro, J. Pascual, V. M. Passegger, A. Pavlov, S. Pedraz, A. Pérez-Calpena, D. Pérez Medialdea, M. Perger, M. A. C. Perryman, M. Pluto, O. Rabaza, A. Ramón, R. Rebolo, P. Redondo, S. Reffert, S. Reinhard, P. Rhode, H.-W. Rix, F. Rodler, E. Rodríguez, C. Rodríguez-López, A. Rodríguez Trinidad, R.-R. Rohloff, A. Rosich, S. Sadegi, E. Sánchez-Blanco, M. A. Sánchez Carrasco, A. Sánchez-López, J. Sanz-Forcada, P. Sarkis, L. F. Sarmiento, S. Schäfer, J. H. M. M. Schmitt, J. Schiller, A. Schweitzer, E. Solano, O. Stahl, J. B. P. Strachan, J. Stürmer, J. C. Suárez, H. M. Taberner, M. Tala, T. Trifonov, S. M. Tulloch, R. G. Ulbrich, G. Veredas, J. I. Vico Linares, F. Vilardell, K. Wagner, J. Winkler, V. Wolthoff, W. Xu, F. Yan, and M. R. Zapatero Osorio. The CARMENES search for exoplanets around M dwarfs. High-resolution optical and near-infrared spectroscopy of 324 survey stars.

- A&A, 612:A49, April 2018. doi: 10.1051/0004-6361/201732054.
- T. Reinhold, A. Reiners, and G. Basri. Rotation and differential rotation of active Kepler stars. A&A, 560:A4, December 2013. doi: 10.1051/0004-6361/201321970.
- I. Ribas, E. Bolmont, F. Selsis, A. Reiners, J. Leconte, S. N. Raymond, S. G. Engle, E. F. Guinan, J. Morin, M. Turbet, F. Forget, and G. Anglada-Escudé. The habitability of Proxima Centauri b. I. Irradiation, rotation and volatile inventory from formation to the present. A&A, 596:A111, December 2016. doi: 10.1051/0004-6361/201629576.
- L. Ricci, L. Testi, A. Natta, A. Scholz, I. de Gregorio-Monsalvo, and A. Isella. Brown Dwarf Disks with ALMA. ApJ, 791:20, August 2014. doi: 10.1088/0004-637X/791/1/20.
- G. R. Ricker. The Transiting Exoplanet Survey Satellite Mission. *Journal of the American Association of Variable Star Observers (JAAVSO)*, 42:234, June 2014.
- G. H. Rieke and M. J. Lebofsky. The interstellar extinction law from 1 to 13 microns. ApJ, 288:618–621, January 1985. doi: 10.1086/162827.
- E. Rigliaco, A. Natta, S. Randich, L. Testi, E. Covino, G. Herczeg, and J. M. Alcalá. X-shooter observations of the accreting brown dwarf J053825.4-024241. A&A, 526:L6, February 2011. doi: 10.1051/0004-6361/201016002.
- B. Rockenfeller, C. A. L. Bailer-Jones, R. Mundt, and M. A. Ibrahimov. Multiband photometric detection of a huge flare on the M9 dwarf 2MASSW J1707183+643933. MNRAS, 367:407–411, March 2006. doi: 10.1111/j.1365-2966.2006.09961.x.
- C. Rodríguez-López, J. MacDonald, and A. Moya. Pulsations in M dwarf stars. MNRAS, 419:L44–L48, January 2012. doi: 10.1111/j.1745-3933.2011.01174.x.
- M. Route. The Discovery of Solar-like Activity Cycles Beyond the End of the Main Sequence? ApJL, 830:L27, October 2016. doi: 10.3847/2041-8205/830/2/L27.
- M. Route and A. Wolszczan. The Arecibo Detection of the Coolest Radio-flaring Brown Dwarf. ApJL, 747:L22, March 2012. doi: 10.1088/2041-8205/747/2/L22.
- M. Route and A. Wolszczan. The Second Arecibo Search for 5 GHz Radio Flares from Ultracool Dwarfs. ApJ, 830:85, October 2016. doi: 10.3847/0004-637X/830/2/85.
- R. E. Rutledge, G. Basri, E. L. Martín, and L. Bildsten. Chandra Detection of an X-Ray Flare from the Brown Dwarf LP 944-20. ApJL, 538:L141–L144, August 2000. doi: 10.1086/312817.
- S. H. Saar. Recent magnetic fields measurements of stellar. In K. G. Strassmeier and J. L. Linsky, editors, *Stellar Surface Structure*, volume 176 of *IAU Symposium*, page 237, 1996.
- R. K. Saito, M. Hempel, D. Minniti, P. W. Lucas, M. Rejkuba, I. Toledo, O. A. Gonzalez, J. Alonso-García, M. J. Irwin, E. Gonzalez-Solares, S. T. Hodgkin, J. R. Lewis, N. Cross, V. D. Ivanov, E. Kerins, J. P. Emerson, M. Soto, E. B. Amôres, S. Gurovich, I. Dékány, R. Angeloni, J. C. Beamin, M. Catelan, N. Padilla, M. Zoccali, P. Pietrukowicz, C. Moni Bidin, F. Mauro, D. Geisler, S. L. Folkes, S. E. Sale, J. Borissova, R. Kurtev, A. V. Ahumada, M. V. Alonso, A. Adamson, J. I. Arias, R. M. Bandyopadhyay, R. H. Barbá, B. Barbuy, G. L. Baume, L. R. Bedin, A. Bellini, R. Benjamin, E. Bica, C. Bonatto, L. Bronfman, G. Carraro, A. N. Chenè, J. J.

- Clariá, J. R. A. Clarke, C. Contreras, A. Corvillón, R. de Grijs, B. Dias, J. E. Drew, C. Fariña, C. Feinstein, E. Fernández-Lajús, R. C. Gamen, W. Gieren, B. Goldman, C. González-Fernández, R. J. J. Grand, G. Gunthardt, N. C. Hambly, M. M. Hanson, K. G. Helminiak, M. G. Hoare, L. Huckvale, A. Jordán, K. Kinemuchi, A. Longmore, M. López-Corredoira, T. Maccarone, D. Majaess, E. L. Martín, N. Masetti, R. E. Mennickent, I. F. Mirabel, L. Monaco, L. Morelli, V. Motta, T. Palma, M. C. Parisi, Q. Parker, F. Peñaloza, G. Pietrzyński, G. Pignata, B. Popescu, M. A. Read, A. Rojas, A. Roman-Lopes, M. T. Ruiz, I. Saviane, M. R. Schreiber, A. C. Schröder, S. Sharma, M. D. Smith, L. Sodr , J. Stead, A. W. Stephens, M. Tamura, C. Tapert, M. A. Thompson, E. Valenti, L. Vanzi, N. A. Walton, W. Weidmann, and A. Zijlstra. VVV DR1: The first data release of the Milky Way bulge and southern plane from the near-infrared ESO public survey VISTA variables in the Vía Láctea. *A&A*, 537:A107, January 2012. doi: 10.1051/0004-6361/201118407.
- D. Saumon and M. S. Marley. The Evolution of L and T Dwarfs in Color-Magnitude Diagrams. *ApJ*, 689:1327–1344, December 2008. doi: 10.1086/592734.
- D. Saumon, P. Bergeron, J. I. Lunine, W. B. Hubbard, and A. Burrows. Cool zero-metallicity stellar atmospheres. *ApJ*, 424:333–344, March 1994. doi: 10.1086/173892.
- J. T. Schmelz, G. D. Holman, J. W. Brosius, and R. F. Willson. Coronal Magnetic Structures Observing Campaign. 3: Coronal plasma and magnetic field diagnostics derived from multiwaveband active region observations. *ApJ*, 434:786–794, October 1994. doi: 10.1086/174781.
- S. J. Schmidt, K. L. Cruz, B. J. Bongiorno, J. Liebert, and I. N. Reid. Activity and Kinematics of Ultracool Dwarfs, Including an Amazing Flare Observation. *AJ*, 133: 2258–2273, May 2007. doi: 10.1086/512158.
- S. J. Schmidt, A. A. West, S. L. Hawley, and J. S. Pineda. Colors and Kinematics of L Dwarfs from the Sloan Digital Sky Survey. *AJ*, 139:1808–1821, May 2010. doi: 10.1088/0004-6256/139/5/1808.
- S. J. Schmidt, A. A. West, J. J. Bochanski, S. L. Hawley, and C. Kielty. Calibrating Ultracool Dwarfs: Optical Template Spectra, Bolometric Corrections, and  $\chi$  Values. *PASP*, 126:642, July 2014. doi: 10.1086/677403.
- S. J. Schmidt, S. L. Hawley, A. A. West, J. J. Bochanski, J. R. A. Davenport, J. Ge, and D. P. Schneider. BOSS Ultracool Dwarfs. I. Colors and Magnetic Activity of M and L Dwarfs. *AJ*, 149:158, May 2015. doi: 10.1088/0004-6256/149/5/158.
- S. J. Schmidt, B. J. Shappee, J. Gagné, K. Z. Stanek, J. L. Prieto, T. W.-S. Holoien, C. S. Kochanek, L. Chomiuk, S. Dong, M. Seibert, and J. Strader. ASASSN-16ae: A Powerful White-light Flare on an Early-L Dwarf. *ApJL*, 828:L22, September 2016. doi: 10.3847/2041-8205/828/2/L22.
- J. H. M. M. Schmitt and C. Liefke. NEXXUS: A comprehensive ROSAT survey of coronal X-ray emission among nearby solar-like stars. *A&A*, 417:651–665, April 2004. doi: 10.1051/0004-6361:20030495.
- A. Scholz and R. Jayawardhana. Variable Accretion and Outflow in Young Brown Dwarfs. *ApJ*, 638:1056–1069, February 2006. doi: 10.1086/498973.
- A. Scholz, K. Moore, R. Jayawardhana, S. Aigrain, D. Peterson, and B. Stelzer. A

- universal spin-mass relation for brown dwarfs and planets. *ArXiv e-prints*, April 2018.
- A. Segura, L. M. Walkowicz, V. Meadows, J. Kasting, and S. Hawley. The Effect of a Strong Stellar Flare on the Atmospheric Chemistry of an Earth-like Planet Orbiting an M Dwarf. *Astrobiology*, 10:751–771, September 2010. doi: 10.1089/ast.2009.0376.
- T. Shibayama, H. Maehara, S. Notsu, Y. Notsu, T. Nagao, S. Honda, T. T. Ishii, D. Nogami, and K. Shibata. Superflares on Solar-type Stars Observed with Kepler. I. Statistical Properties of Superflares. *ApJS*, 209:5, November 2013. doi: 10.1088/0067-0049/209/1/5.
- D. Shulyak, A. Reiners, A. Engeln, L. Malo, R. Yadav, J. Morin, and O. Kochukhov. Strong dipole magnetic fields in fast rotating fully convective stars. *Nature Astronomy*, 1:0184, August 2017. doi: 10.1038/s41550-017-0184.
- M. F. Skrutskie, R. M. Cutri, R. Stiening, M. D. Weinberg, S. Schneider, J. M. Carpenter, C. Beichman, R. Capps, T. Chester, J. Elias, J. Huchra, J. Liebert, C. Lonsdale, D. G. Monet, S. Price, P. Seitzer, T. Jarrett, J. D. Kirkpatrick, J. E. Gizis, E. Howard, T. Evans, J. Fowler, L. Fullmer, R. Hurt, R. Light, E. L. Kopan, K. A. Marsh, H. L. McCallon, R. Tam, S. Van Dyk, and S. Wheelock. The Two Micron All Sky Survey (2MASS). *AJ*, 131:1163–1183, February 2006. doi: 10.1086/498708.
- D. S. Spiegel, A. Burrows, and J. A. Milsom. The Deuterium-burning Mass Limit for Brown Dwarfs and Giant Planets. *ApJ*, 727:57, January 2011. doi: 10.1088/0004-637X/727/1/57.
- J. Stauffer, L. Rebull, J. Bouvier, L. A. Hillenbrand, A. Collier-Cameron, M. Pinsonneault, S. Aigrain, D. Barrado, H. Bouy, D. Ciardi, A. M. Cody, T. David, G. Micela, D. Soderblom, G. Somers, K. G. Stassun, J. Valenti, and F. J. Vrba. Rotation in the Pleiades with K2. III. Speculations on Origins and Evolution. *AJ*, 152:115, November 2016. doi: 10.3847/0004-6256/152/5/115.
- B. Stelzer, R. Neuhäuser, and V. Hambaryan. X-ray flares on zero-age- and pre-main sequence stars in Taurus-Auriga-Perseus. *A&A*, 356:949–971, April 2000.
- B. Stelzer, G. Micela, E. Flaccomio, R. Neuhäuser, and R. Jayawardhana. X-ray emission of brown dwarfs: towards constraining the dependence on age, luminosity, and temperature. *A&A*, 448:293–304, March 2006. doi: 10.1051/0004-6361:20053677.
- B. Stelzer, A. Scholz, and R. Jayawardhana. Emission Line Variability of the Accreting Young Brown Dwarf 2MASSW J1207334-393254: From Hours to Years. *ApJ*, 671:842–852, December 2007. doi: 10.1086/521431.
- P. B. Stetson. On the Automatic Determination of Light-Curve Parameters for Cepheid Variables. *PASP*, 108:851, October 1996. doi: 10.1086/133808.
- T. Takahashi, Y. Mizuno, and K. Shibata. Scaling Relations in Coronal Mass Ejections and Energetic Proton Events Associated with Solar Superflares. *ApJL*, 833:L8, December 2016. doi: 10.3847/2041-8205/833/1/L8.
- J. C. Tarter. Brown Dwarfs, Lilliputian Stars, Giant Planets and Missing Mass Problems. In *Bulletin of the American Astronomical Society*, volume 8 of BAAS, page 517, September 1976.
- A. Telleschi, M. Güdel, K. Briggs, M. Audard, J.-U. Ness, and S. L. Skinner. Coronal

- Evolution of the Sun in Time: High-Resolution X-Ray Spectroscopy of Solar Analogs with Different Ages. *ApJ*, 622:653–679, March 2005. doi: 10.1086/428109.
- C. A. Theissen. Parallaxes of Cool Objects with WISE: Filling in for Gaia. *ApJ*, 862:173, August 2018. doi: 10.3847/1538-4357/aaccfa.
- C. A. Theissen, A. A. West, G. Shippee, A. J. Burgasser, and S. J. Schmidt. The Late-Type Extension to MoVeRS (LaTE-MoVeRS): Proper Motion Verified Low-mass Stars and Brown Dwarfs from SDSS, 2MASS, and WISE. *AJ*, 153:92, March 2017. doi: 10.3847/1538-3881/153/3/92.
- M. A. Tilley, A. Segura, V. S. Meadows, S. Hawley, and J. Davenport. Modeling Repeated M-dwarf Flaring at an Earth-like Planet in the Habitable Zone: I. Atmospheric Effects for an Unmagnetized Planet. *ArXiv e-prints*, November 2017.
- J. L. Tonry, C. W. Stubbs, K. R. Lykke, P. Doherty, I. S. Shivvers, W. S. Burgett, K. C. Chambers, K. W. Hodapp, N. Kaiser, R.-P. Kudritzki, E. A. Magnier, J. S. Morgan, P. A. Price, and R. J. Wainscoat. The Pan-STARRS1 Photometric System. *ApJ*, 750:99, May 2012. doi: 10.1088/0004-637X/750/2/99.
- V. Van Grootel, C. S. Fernandes, M. Gillon, E. Jehin, J. Manfroid, R. Scudlaire, A. J. Burgasser, K. Barkaoui, Z. Benkhaldoun, A. Burdanov, L. Delrez, B.-O. Demory, J. de Wit, D. Queloz, and A. H. M. J. Triaud. Stellar Parameters for Trappist-1. *ApJ*, 853:30, January 2018. doi: 10.3847/1538-4357/aaa023.
- A. van Maanen. The Photographic Determination of Stellar Parallaxes with the 60- and 100-INCH Reflectors. Seventeenth Series. *ApJ*, 91:503, June 1940. doi: 10.1086/144192.
- A. van Maanen. Variable Star with Faint Absolute Magnitude. *PASP*, 57:216, August 1945. doi: 10.1086/125730.
- K. Vida, Z. Kóvári, A. Pál, K. Oláh, and L. Kriskovics. Frequent Flaring in the TRAPPIST-1 System Unsuitable for Life? *ApJ*, 841:124, June 2017. doi: 10.3847/1538-4357/aa6f05.
- O. Vilhu. The nature of magnetic activity in lower main sequence stars. *A&A*, 133:117–126, April 1984.
- Zé Vinícius, Geert Barentsen, Christina Hedges, Michael Gully-Santiago, and Ann Marie Cody. Keplergo/lightkurve, February 2018. URL <http://doi.org/10.5281/zenodo.1181928>.
- L. M. Walkowicz, G. Basri, N. Batalha, R. L. Gilliland, J. Jenkins, W. J. Borucki, D. Koch, D. Caldwell, A. K. Dupree, D. W. Latham, S. Meibom, S. Howell, T. M. Brown, and S. Bryson. White-light Flares on Cool Stars in the Kepler Quarter 1 Data. *AJ*, 141:50, February 2011. doi: 10.1088/0004-6256/141/2/50.
- A. J. Weinberger, A. P. Boss, S. A. Keiser, G. Anglada-Escudé, I. B. Thompson, and G. Burley. Trigonometric Parallaxes and Proper Motions of 134 Southern Late M, L, and T Dwarfs from the Carnegie Astrometric Planet Search Program. *AJ*, 152:24, July 2016. doi: 10.3847/0004-6256/152/1/24.
- M. C. Weisskopf, B. Brinkman, C. Canizares, G. Garmire, S. Murray, and L. P. Van Speybroeck. An Overview of the Performance and Scientific Results from the Chandra X-Ray Observatory. *PASP*, 114:1–24, January 2002. doi: 10.1086/338108.

- D. L. Welch and P. B. Stetson. Robust variable star detection techniques suitable for automated searches - New results for NGC 1866. *AJ*, 105:1813–1821, May 1993. doi: 10.1086/116556.
- A. A. West and S. L. Hawley.  $\chi$  Values for Blue Emission Lines in M Dwarfs. *PASP*, 120:1161, November 2008. doi: 10.1086/593024.
- A. A. West, S. L. Hawley, L. M. Walkowicz, K. R. Covey, N. M. Silvestri, S. N. Raymond, H. C. Harris, J. A. Munn, P. M. McGehee, Ž. Ivezić, and J. Brinkmann. Spectroscopic Properties of Cool Stars in the Sloan Digital Sky Survey: An Analysis of Magnetic Activity and a Search for Subdwarfs. *AJ*, 128:426–436, July 2004. doi: 10.1086/421364.
- A. A. West, D. P. Morgan, J. J. Bochanski, J. M. Andersen, K. J. Bell, A. F. Kowalski, J. R. A. Davenport, S. L. Hawley, S. J. Schmidt, D. Bernat, E. J. Hilton, P. Muirhead, K. R. Covey, B. Rojas-Ayala, E. Schlawin, M. Gooding, K. Schluns, S. Dhital, J. S. Pineda, and D. O. Jones. The Sloan Digital Sky Survey Data Release 7 Spectroscopic M Dwarf Catalog. I. Data. *AJ*, 141:97, March 2011. doi: 10.1088/0004-6256/141/3/97.
- Andrew A. West, Suzanne L. Hawley, John J. Bochanski, Kevin R. Covey, I. Neill Reid, Saurav Dhital, Eric J. Hilton, and Michael Masuda. Constraining the Age-Activity Relation for Cool Stars: The Sloan Digital Sky Survey Data Release 5 Low-Mass Star Spectroscopic Sample. *AJ*, 135:785–795, Mar 2008. doi: 10.1088/0004-6256/135/3/785.
- P. J. Wheatley, T. Louden, V. Bourrier, D. Ehrenreich, and M. Gillon. Strong XUV irradiation of the Earth-sized exoplanets orbiting the ultracool dwarf TRAPPIST-1. *MNRAS*, 465:L74–L78, February 2017. doi: 10.1093/mnrasl/slw192.
- J. P. Williams and L. A. Cieza. Protoplanetary Disks and Their Evolution. *ARA&A*, 49:67–117, September 2011. doi: 10.1146/annurev-astro-081710-102548.
- P. K. G. Williams. *Radio Emission from Ultracool Dwarfs*, page 171. 2018. doi: 10.1007/978-3-319-55333-7\_171.
- P. K. G. Williams and E. Berger. The Rotation Period and Magnetic Field of the T Dwarf 2MASS J1047539+212423 Measured from Periodic Radio Bursts. *ApJ*, 808:189, August 2015. doi: 10.1088/0004-637X/808/2/189.
- P. K. G. Williams, B. A. Cook, and E. Berger. Trends in Ultracool Dwarf Magnetism. I. X-Ray Suppression and Radio Enhancement. *ApJ*, 785:9, April 2014. doi: 10.1088/0004-637X/785/1/9.
- S. J. Wolk, F. R. Harnden, Jr., E. Flaccomio, G. Micela, F. Favata, H. Shang, and E. D. Feigelson. Stellar Activity on the Young Suns of Orion: COUP Observations of K5-7 Pre-Main-Sequence Stars. *ApJS*, 160:423–449, October 2005. doi: 10.1086/432099.
- N. J. Wright, J. J. Drake, E. E. Mamajek, and G. W. Henry. The Stellar-activity-Rotation Relationship and the Evolution of Stellar Dynamos. *ApJ*, 743:48, December 2011. doi: 10.1088/0004-637X/743/1/48.
- R. K. Yadav, U. R. Christensen, J. Morin, T. Gastine, A. Reiners, K. Poppenhaeger, and S. J. Wolk. Explaining the Coexistence of Large-scale and Small-scale Magnetic Fields in Fully Convective Stars. *ApJL*, 813:L31, November 2015. doi: 10.1088/

2041-8205/813/2/L31.

- S. Yashiro, S. Akiyama, N. Gopalswamy, and R. A. Howard. Different Power-Law Indices in the Frequency Distributions of Flares with and without Coronal Mass Ejections. *ApJL*, 650:L143–L146, October 2006. doi: 10.1086/508876.
- D. G. York, J. Adelman, J. E. Anderson, Jr., S. F. Anderson, J. Annis, N. A. Bahcall, J. A. Bakken, R. Barkhouser, S. Bastian, E. Berman, W. N. Boroski, S. Bracker, C. Briegel, J. W. Briggs, J. Brinkmann, R. Brunner, S. Burles, L. Carey, M. A. Carr, F. J. Castander, B. Chen, P. L. Colestock, A. J. Connolly, J. H. Crocker, I. Csabai, P. C. Czarapata, J. E. Davis, M. Doi, T. Dombeck, D. Eisenstein, N. Ellman, B. R. Elms, M. L. Evans, X. Fan, G. R. Federwitz, L. Fiscelli, S. Friedman, J. A. Frieman, M. Fukugita, B. Gillespie, J. E. Gunn, V. K. Gurbani, E. de Haas, M. Haldeman, F. H. Harris, J. Hayes, T. M. Heckman, G. S. Hennessy, R. B. Hindley, S. Holm, D. J. Holmgren, C.-h. Huang, C. Hull, D. Husby, S.-I. Ichikawa, T. Ichikawa, Ž. Ivezić, S. Kent, R. S. J. Kim, E. Kinney, M. Klaene, A. N. Kleinman, S. Kleinman, G. R. Knapp, J. Korienek, R. G. Kron, P. Z. Kunszt, D. Q. Lamb, B. Lee, R. F. Leger, S. Limmongkol, C. Lindenmeyer, D. C. Long, C. Loomis, J. Loveday, R. Lucinio, R. H. Lupton, B. MacKinnon, E. J. Mannery, P. M. Mantsch, B. Margon, P. McGehee, T. A. McKay, A. Meiksin, A. Merelli, D. G. Monet, J. A. Munn, V. K. Narayanan, T. Nash, E. Neilsen, R. Neswold, H. J. Newberg, R. C. Nichol, T. Nicinski, M. Nonino, N. Okada, S. Okamura, J. P. Ostriker, R. Owen, A. G. Pauls, J. Peoples, R. L. Peterson, D. Petravick, J. R. Pier, A. Pope, R. Pordes, A. Prosapio, R. Rechenmacher, T. R. Quinn, G. T. Richards, M. W. Richmond, C. H. Rivetta, C. M. Rockosi, K. Ruthmansdorfer, D. Sandford, D. J. Schlegel, D. P. Schneider, M. Sekiguchi, G. Sergey, K. Shimasaku, W. A. Siegmund, S. Smee, J. A. Smith, S. Snedden, R. Stone, C. Stoughton, M. A. Strauss, C. Stubbs, M. SubbaRao, A. S. Szalay, I. Szapudi, G. P. Szokoly, A. R. Thakar, C. Tremonti, D. L. Tucker, A. Uomoto, D. Vanden Berk, M. S. Vogeley, P. Waddell, S.-i. Wang, M. Watanabe, D. H. Weinberg, B. Yanny, N. Yasuda, and SDSS Collaboration. The Sloan Digital Sky Survey: Technical Summary. *AJ*, 120:1579–1587, September 2000. doi: 10.1086/301513.
- A. Youngblood, K. France, R. O. P. Loyd, A. Brown, J. P. Mason, P. C. Schneider, M. A. Tilley, Z. K. Berta-Thompson, A. Buccino, C. S. Froning, S. L. Hawley, J. Linsky, P. J. D. Mauas, S. Redfield, A. Kowalski, Y. Miguel, E. R. Newton, S. Rugheimer, A. Segura, A. Roberge, and M. Vieytes. The MUSCLES Treasury Survey. IV. Scaling Relations for Ultraviolet, Ca II K, and Energetic Particle Fluxes from M Dwarfs. *ApJ*, 843:31, July 2017. doi: 10.3847/1538-4357/aa76dd.
- N. Zacharias, C. T. Finch, T. M. Girard, A. Henden, J. L. Bartlett, D. G. Monet, and M. I. Zacharias. *VizieR Online Data Catalog: UCAC4 Catalogue (Zacharias+, 2012)*. *VizieR Online Data Catalog*, art. I/322A, July 2012.
- Z. Zhang, M. C. Liu, W. M. J. Best, E. A. Magnier, K. M. Aller, K. C. Chambers, P. W. Draper, H. Flewelling, K. W. Hodapp, N. Kaiser, R.-P. Kudritzki, N. Metcalfe, R. J. Wainscoat, and C. Waters. The Pan-STARRS1 Proper-motion Survey for Young Brown Dwarfs in Nearby Star-forming Regions. I. Taurus Discoveries and a

Reddening-free Classification Method for Ultracool Dwarfs. *ArXiv e-prints*, April 2018.

Z. Zhu, L. Hartmann, and C. Gammie. Nonsteady Accretion in Protostars. *ApJ*, 694: 1045–1055, April 2009. doi: 10.1088/0004-637X/694/2/1045.

## Appendix A

### PROPERTIES OF FLARES IDENTIFIED USING *K2* SHORT CADENCE DATA

Table A.1: Flare properties of GJ 3631

$T_{\text{peak}}$ (BJD - 2454833)	ED (s)	$\log E$ (erg)
3074.0285	11.5	31.7
3074.1675	825.3	33.6
3074.3166	7.2	31.5
3075.1741	7.2	31.5
3075.8668	23.2	32.0
3076.2359	2.1	31.0
3076.7072	32.1	32.2
3076.8516	2.4	31.0
3076.8584	4.9	31.3
3076.9122	4.2	31.3
3077.1615	18.0	31.9
3077.5790	5.0	31.4
3077.7724	22.2	32.0
3078.3323	5.4	31.4
3078.6639	104.5	32.7
3078.9936	305.8	33.1
3079.0937	38.3	32.2
3079.1312	19.9	32.0
3080.6329	30.6	32.1
3081.1758	906.9	33.6
3081.3488	7.0	31.5
3081.4904	152.1	32.8
3082.4473	11.8	31.7
3082.5141	59.8	32.4
3083.2844	67.0	32.5
3083.6399	16.1	31.9
3084.2842	8.2	31.6
3085.0123	31.8	32.2
3085.6286	9.9	31.6
3085.7056	32.3	32.2
3085.7710	9.4	31.6
3085.8009	9.5	31.6
3086.0053	14.3	31.8
3087.1352	54.0	32.4
3087.1849	14.8	31.8
3087.2680	86.5	32.6
3088.1711	79.5	32.6
3088.6921	3.7	31.2
3088.9516	7.8	31.5
3088.9693	21.6	32.0
3089.2335	37.6	32.2
3089.3234	9.2	31.6
3089.3888	12.7	31.8
3089.4535	16.9	31.9

Continued on next page

**Table A.1 – continued from previous page**

$T_{\text{peak}}$ (BJD - 2454833)	ED (s)	$\log E$ (erg)
3089.5325	11.5	31.7
3090.3566	392.3	33.2
3090.7196	4.0	31.3
3091.3973	8.2	31.6
3091.5512	609.4	33.4
3093.0748	14.0	31.8
3093.4923	6.9	31.5
3093.7259	9.5	31.6
3094.0678	5.1	31.4
3094.2299	16.0	31.9
3094.8885	7.7	31.5
3095.4210	8.3	31.6
3096.4188	7.5	31.5
3096.5121	30.7	32.1
3096.7491	24.9	32.0
3096.8043	789.4	33.6
3096.9160	655.7	33.5
3096.9671	15.6	31.8
3097.1353	23.4	32.0
3098.0302	28.2	32.1
3098.3081	16.0	31.9
3098.3510	3.2	31.2
3098.6806	60.3	32.4
3098.9891	5.4	31.4
3099.2663	13.8	31.8
3099.9985	6.2	31.4
3101.8401	10.2	31.7
3101.8959	20.8	32.0
3102.3495	20.5	32.0
3102.4496	3.0	31.1
3102.6866	16.1	31.9
3102.7827	81.9	32.6
3103.0054	10.5	31.7
3103.2444	194.2	32.9
3103.4590	5.8	31.4
3104.6304	4.0	31.3
3105.1153	47.8	32.3
3105.2549	4.2	31.3
3105.9094	12.0	31.7
3106.6143	4.7	31.3
3106.6382	4.7	31.3
3107.9288	25.7	32.1
3108.3170	5.6	31.4
3109.3079	81.7	32.6
3110.7238	53.5	32.4
3110.7797	3.1	31.2
3111.3640	42.5	32.3
3112.1084	8.8	31.6
3112.5171	34.7	32.2
3113.0279	18.5	31.9
3114.6379	152.2	32.8
3114.9832	28.1	32.1
3115.0540	121.7	32.7
3115.0962	2.3	31.0
3115.6602	3.1	31.1
3115.9169	22.3	32.0
3116.1178	14.0	31.8
3116.2983	75.1	32.5
3116.3289	80.2	32.6
3116.3896	8.6	31.6
3116.4270	55.6	32.4
3117.7408	1293.6	33.8

Continued on next page

**Table A.1 – continued from previous page**

$T_{\text{peak}}$ (BJD - 2454833)	ED (s)	$\log E$ (erg)
3118.1208	158.6	32.9
3118.8809	23.7	32.0
3118.9694	13.6	31.8
3118.9926	4.3	31.3
3119.1267	39.4	32.2
3119.2132	16.6	31.9
3119.4993	84.1	32.6
3119.8568	3.3	31.2
3120.8798	20.0	32.0
3121.1277	5.7	31.4
3122.1731	9.5	31.6
3122.3366	77.0	32.5
3122.4516	24.2	32.0
3122.6042	3.2	31.2
3122.6383	7.7	31.5
3122.7969	76.2	32.5
3122.9107	8.7	31.6
3123.4746	16.3	31.9
3123.5951	609.0	33.4
3123.6925	6.1	31.4
3123.7811	8.4	31.6
3124.3150	3906.5	34.2
3124.9382	34.7	32.2
3125.0465	6.0	31.4
3125.1486	9.4	31.6
3125.3557	9.6	31.6
3126.3235	1338.8	33.8
3126.7702	120.8	32.7
3128.0404	34.0	32.2
3128.4252	9.6	31.6
3128.6915	33.6	32.2
3128.9864	18.2	31.9
3129.0633	7.4	31.5
3129.1709	12.3	31.7
3129.4870	22.6	32.0
3129.6327	271.9	33.1
3130.1721	16.0	31.9
3130.6740	15.1	31.8
3131.3122	46.7	32.3
3132.1233	11.3	31.7
3132.1499	20.2	32.0
3132.3310	15.8	31.9
3136.0019	22.8	32.0
3136.4937	34.4	32.2
3137.5881	44.5	32.3
3138.1180	38.6	32.2
3138.5797	19.2	31.9
3138.6723	70.0	32.5
3139.5611	13.3	31.8
3139.7355	12.5	31.7
3139.8301	68.6	32.5
3141.5267	7.8	31.5
3141.5811	55.8	32.4
3141.9939	20.7	32.0
3142.6020	7.9	31.5
3142.7614	11.4	31.7
3142.9589	23.5	32.0
3143.2599	40.0	32.3
3143.7925	221.0	33.0
3143.9791	17.8	31.9
3144.7154	4.2	31.3
3145.1969	105.2	32.7

Continued on next page

**Table A.1 – continued from previous page**

$T_{\text{peak}}$ (BJD - 2454833)	ED (s)	$\log E$ (erg)
3147.6207	550.6	33.4
3148.0416	22.6	32.0
3148.2017	461.5	33.3
3149.6244	10.5	31.7
3149.8063	16.8	31.9
3151.6594	12.2	31.7
3152.3057	27.7	32.1

**Table A.2: Flare properties of GJ 3636**

$T_{\text{peak}}$ (BJD - 2454833)	ED (s)	$\log E$ (erg)
3077.1696	2.8	31.1
3077.8480	7.9	31.5
3079.5009	25.2	32.0
3079.5772	3.2	31.1
3080.3652	0.7	30.5
3080.7657	8.2	31.6
3081.3882	8.5	31.6
3082.6291	4.2	31.3
3082.6530	3.2	31.1
3082.8614	15.3	31.8
3083.0773	15.8	31.8
3083.8339	6.5	31.5
3083.9347	11.4	31.7
3084.9952	9.1	31.6
3085.4168	312.8	33.1
3085.9119	258.1	33.1
3086.2041	3.8	31.2
3086.9553	32.0	32.1
3088.6941	5.1	31.3
3088.9706	7.9	31.5
3089.1470	4.0	31.2
3089.9840	3.9	31.2
3090.5241	9.0	31.6
3090.5827	8.0	31.5
3091.5600	0.7	30.5
3091.5920	9.9	31.6
3092.2145	4.9	31.3
3092.6021	8.9	31.6
3092.8697	6.4	31.5
3093.0958	18.2	31.9
3095.2644	9.0	31.6
3095.4768	6.1	31.4
3096.1688	10.6	31.7
3096.4106	16.7	31.9
3096.4283	4.2	31.3
3096.5591	17.8	31.9
3097.4513	2.5	31.0
3098.4483	42.9	32.3
3098.6663	8.5	31.6
3099.8690	2.8	31.1
3100.6407	2.8	31.1
3101.2870	21.0	32.0
3101.4838	5.0	31.3
3101.7004	20.3	32.0
3102.5981	137.0	32.8
3104.0051	9.5	31.6
3104.1645	12.1	31.7
3104.3729	5.6	31.4
3104.3824	6.0	31.4

Continued on next page

**Table A.2 – continued from previous page**

$T_{\text{peak}}$ (BJD - 2454833)	ED (s)	$\log E$ (erg)
3104.7659	10.3	31.7
3106.3098	9.3	31.6
3107.5630	49.8	32.3
3108.7576	11.1	31.7
3109.3072	3.5	31.2
3109.6143	10.7	31.7
3110.8225	12.4	31.7
3111.2019	2.9	31.1
3113.6094	32.6	32.2
3113.6741	10.3	31.7
3114.5180	43.4	32.3
3114.6399	5.5	31.4
3115.7371	2.9	31.1
3116.2070	38.6	32.2
3117.1795	8.7	31.6
3118.6486	3.0	31.1
3118.9796	8.2	31.6
3119.9528	6.2	31.4
3120.5249	5.8	31.4
3120.8634	9.8	31.6
3122.0477	6.0	31.4
3122.3031	2.5	31.0
3122.8602	23.4	32.0
3123.1831	17.3	31.9
3123.7790	36.5	32.2
3124.6357	3.9	31.2
3124.7515	8.2	31.6
3126.1865	5.9	31.4
3127.6848	13.3	31.8
3128.8542	3.3	31.2
3129.2022	61.7	32.4
3129.2710	2.4	31.0
3129.6994	10.1	31.6
3129.9405	10.6	31.7
3130.0849	2.7	31.1
3131.2018	9.2	31.6
3131.7616	5.3	31.4
3132.1110	3.5	31.2
3133.6182	2.7	31.1
3133.7421	4.0	31.2
3135.1022	25.7	32.1
3135.2125	3.6	31.2
3135.5395	1.2	30.7
3135.6069	1.7	30.9
3136.3159	15.1	31.8
3136.5031	7.2	31.5
3136.6795	6.9	31.5
3138.3924	3.8	31.2
3138.7963	6.5	31.5
3139.2219	23.3	32.0
3139.2887	3.9	31.2
3139.7089	5.5	31.4
3139.7456	60.2	32.4
3141.2426	2.7	31.1
3141.9713	232.4	33.0
3142.8016	54.8	32.4
3143.2545	8.3	31.6
3144.3707	48.6	32.3
3146.3900	8.7	31.6
3146.7421	3.5	31.2
3147.0799	46.6	32.3
3149.2566	7.4	31.5

Continued on next page

**Table A.2 – continued from previous page**

$T_{\text{peak}}$ (BJD - 2454833)	ED (s)	$\log E$ (erg)
3149.4098	1.9	30.9
3149.8348	20.1	31.9

**Table A.3: Flare properties of Wolf 359**

$T_{\text{peak}}$ (BJD - 2454833)	ED (s)	$\log E$ (erg)
3073.5572	14.8	31.1
3073.6962	8.0	30.8
3073.7214	5.2	30.6
3073.7731	130.2	32.0
3074.1900	4.6	30.6
3074.4774	34.9	31.5
3074.8166	8.4	30.8
3074.8840	8.4	30.8
3075.1864	4.2	30.5
3075.7694	6.9	30.7
3076.1365	35.9	31.5
3076.9245	7.6	30.8
3077.7064	2.2	30.3
3078.1409	34.8	31.4
3078.2785	57.7	31.7
3078.3139	2.7	30.3
3078.5278	253.5	32.3
3078.6238	7.8	30.8
3078.7008	2.4	30.3
3078.7920	4.9	30.6
3079.2783	5.7	30.7
3079.5419	2.3	30.3
3079.5582	14.7	31.1
3080.2924	2.7	30.3
3081.0219	3.8	30.5
3081.3209	7.1	30.8
3082.5958	101.8	31.9
3082.7341	12.2	31.0
3082.8601	60.9	31.7
3082.9241	3.3	30.4
3084.2188	34.3	31.4
3084.3775	3.4	30.4
3084.5567	17.6	31.2
3084.7017	6.3	30.7
3085.8098	4.8	30.6
3087.0855	6.3	30.7
3087.9927	2.9	30.4
3088.4538	3.3	30.4
3088.7609	353.3	32.5
3089.7539	4.2	30.5
3089.8125	120.5	32.0
3090.2790	10.8	30.9
3090.4391	4.7	30.6
3091.6064	2.6	30.3
3091.7678	6.5	30.7
3091.7835	2.6	30.3
3092.3556	2.1	30.2
3093.1300	8.4	30.8
3094.1911	12.3	31.0
3096.4740	2.3	30.3
3096.4890	2.0	30.2
3096.6436	2.7	30.3
3096.8152	8.5	30.8
3097.5167	32.7	31.4

Continued on next page

**Table A.3 – continued from previous page**

$T_{\text{peak}}$ (BJD - 2454833)	ED (s)	$\log E$ (erg)
3097.7285	3.4	30.4
3098.3640	5.8	30.7
3098.7842	182.6	32.2
3098.9061	16.2	31.1
3099.1547	5.5	30.6
3099.3434	4.8	30.6
3099.5797	17.9	31.2
3099.7561	5.7	30.7
3099.9992	3.8	30.5
3100.3214	7.1	30.8
3100.5727	3.2	30.4
3100.7354	125.7	32.0
3101.3770	33.5	31.4
3101.3934	3.3	30.4
3101.4683	63.2	31.7
3101.5112	3.6	30.5
3101.8401	2.9	30.4
3101.9968	17.1	31.1
3102.7453	1.1	30.0
3103.1553	3.4	30.4
3103.5421	5.7	30.7
3103.9201	11.5	31.0
3104.4023	1.7	30.1
3104.4765	15.3	31.1
3104.4765	17.2	31.1
3105.2250	5.9	30.7
3106.7778	6.2	30.7
3106.8507	3.8	30.5
3107.6339	7.1	30.8
3108.0153	3.9	30.5
3108.0991	3.5	30.5
3108.1447	8.0	30.8
3108.6072	12.5	31.0
3108.8101	2.3	30.3
3109.1506	6.1	30.7
3109.6328	31.5	31.4
3109.8310	4.3	30.5
3110.1981	19.2	31.2
3110.3977	2.3	30.3
3110.4072	6.7	30.7
3111.0842	6.1	30.7
3111.8660	4.4	30.6
3112.5641	8.6	30.8
3113.2615	66.6	31.7
3114.7694	10.6	30.9
3115.4082	2.8	30.4
3116.4659	47.2	31.6
3116.6920	10.0	30.9
3116.7227	1.9	30.2
3117.6768	3.9	30.5
3117.8198	37.9	31.5
3118.2346	5.4	30.6
3118.5281	6.2	30.7
3118.8550	15.2	31.1
3119.9325	2.4	30.3
3120.0333	4.9	30.6
3120.2049	19.2	31.2
3120.8328	20.7	31.2
3121.1141	3.5	30.5
3121.1277	2.3	30.3
3121.4029	29.4	31.4
3121.5813	4.5	30.6

Continued on next page

**Table A.3 – continued from previous page**

$T_{\text{peak}}$ (BJD - 2454833)	ED (s)	$\log E$ (erg)
3122.0499	27.5	31.3
3122.1255	2.8	30.4
3123.4161	3.5	30.5
3124.4390	11.4	31.0
3124.5895	6.0	30.7
3124.6971	13.5	31.0
3124.9777	4.1	30.5
3125.0172	2.3	30.3
3125.4661	3.4	30.4
3126.0095	8.7	30.8
3126.1941	96.2	31.9
3126.4842	6.7	30.7
3126.8125	20.0	31.2
3126.9222	42.7	31.5
3127.4813	9.7	30.9
3127.7129	26.9	31.3
3128.0336	13.3	31.0
3128.2679	14.6	31.1
3128.4307	22.1	31.3
3129.2561	10.3	30.9
3129.3849	146.4	32.1
3129.4993	8.3	30.8
3129.6879	6.8	30.7
3130.0169	4.5	30.6
3130.2886	43.5	31.5
3130.4766	351.2	32.5
3130.5474	72.6	31.8
3130.6979	10.2	30.9
3132.6907	16.2	31.1
3132.7520	37.0	31.5
3132.8480	88.3	31.9
3133.1382	7.5	30.8
3133.2151	9.2	30.9
3133.5468	3.9	30.5
3133.8730	8.5	30.8
3134.7175	22.8	31.3
3135.2726	62.1	31.7
3136.3807	59.3	31.7
3136.5714	3.7	30.5
3136.5891	6.1	30.7
3136.9418	4.2	30.5
3136.9643	3.0	30.4
3137.1067	114.1	32.0
3138.0057	24.4	31.3
3138.6888	14.5	31.1
3139.0422	6.8	30.7
3139.2390	4.4	30.6
3139.4154	16.6	31.1
3139.5019	3.4	30.4
3139.7056	5.3	30.6
3140.6985	6.8	30.7
3140.7823	15.4	31.1
3141.1685	21.5	31.2
3141.8591	84.1	31.8
3142.8085	1.6	30.1
3142.8616	12.4	31.0
3142.9787	6.3	30.7
3143.4895	4.7	30.6
3143.6291	18.6	31.2
3144.1379	11.2	31.0
3144.3878	70.3	31.8
3144.4859	3.9	30.5

Continued on next page

**Table A.3 – continued from previous page**

$T_{\text{peak}}$ (BJD - 2454833)	ED (s)	$\log E$ (erg)
3144.7011	7.2	30.8
3145.5913	19.5	31.2
3145.6512	10.2	30.9
3145.8351	12.5	31.0
3145.9931	31.7	31.4
3146.7647	7.2	30.8
3146.8662	4.9	30.6
3146.9922	3.5	30.5
3147.7843	7.4	30.8
3147.9818	51.9	31.6
3148.7350	8.0	30.8
3149.0102	16.5	31.1
3149.7995	3.4	30.4
3149.9412	9.0	30.9
3151.0036	9.0	30.9
3151.2890	3.8	30.5
3151.5539	49.5	31.6
3151.5975	10.0	30.9
3151.9768	77.7	31.8
3152.3507	6.8	30.7

**Table A.4: Flare properties of LHS 2090**

$T_{\text{peak}}$ (BJD - 2454833)	ED (s)	$\log E$ (erg)
3264.9262	27.1	31.2
3264.9603	96.4	31.8
3265.0583	17.7	31.0
3265.1605	5.0	30.5
3265.2463	19.4	31.1
3265.6353	4.1	30.4
3266.0147	235.6	32.2
3266.0318	4.5	30.4
3266.9820	4.6	30.4
3267.1319	2.1	30.1
3267.2116	7.6	30.7
3267.2259	2.0	30.1
3268.4779	3.6	30.3
3268.5371	5.5	30.5
3268.7095	3.4	30.3
3269.1918	1.8	30.0
3269.1924	1.9	30.0
3269.5487	4.7	30.5
3269.9533	18.8	31.1
3270.9914	13.3	30.9
3271.2605	5.6	30.5
3271.3607	3.1	30.3
3271.4901	14.3	30.9
3271.7360	9.5	30.8
3272.0160	2.5	30.2
3272.8266	2.9	30.2
3272.8668	17.2	31.0
3272.9778	16.5	31.0
3273.1985	10.6	30.8
3273.6644	7.8	30.7
3274.4294	29.9	31.3
3274.8892	48.6	31.5
3275.3701	32.4	31.3
3275.6460	21.6	31.1
3275.6950	1.9	30.0
3276.0302	1.9	30.0

Continued on next page

**Table A.4 – continued from previous page**

$T_{\text{peak}}$ (BJD - 2454833)	ED (s)	$\log E$ (erg)
3276.0370	4.7	30.5
3276.0894	12.9	30.9
3276.4607	16.6	31.0
3277.0513	3.4	30.3
3277.1344	1.1	29.8
3277.2400	10.0	30.8
3277.2638	5.6	30.5
3277.5186	2.6	30.2
3277.7154	32.6	31.3
3277.9239	13.0	30.9
3278.1889	1.3	29.9
3278.2454	168.5	32.0
3278.7617	3.1	30.3
3279.3264	1.3	29.9
3279.3271	1.3	29.9
3279.5240	2.7	30.2
3280.9409	2.1	30.1
3281.0206	10.0	30.8
3281.6016	79.0	31.7
3281.9007	38.6	31.4
3282.1289	5.5	30.5
3283.1513	5.0	30.5
3283.9006	2.4	30.1
3284.0505	3.8	30.4
3284.1874	35.4	31.3
3284.3802	5.0	30.5
3284.4067	2.9	30.2
3284.6022	1.4	29.9
3285.0437	5.8	30.5
3285.2194	9.7	30.8
3285.8631	68.9	31.6
3286.2460	2.6	30.2
3286.2684	13.1	30.9
3286.2814	23.5	31.1
3286.8774	14.4	30.9
3287.2521	10.4	30.8
3287.7078	2.9	30.2
3288.0824	3.9	30.4
3288.7956	19.0	31.1
3288.8202	13.9	30.9
3289.1328	5.3	30.5
3289.2350	5.9	30.5
3289.6948	8.0	30.7
3289.9864	3.1	30.3
3290.7581	16.5	31.0
3291.0994	61.2	31.6
3291.3433	14.0	30.9
3291.4720	3.4	30.3
3291.5504	2.6	30.2
3292.4945	1.9	30.0
3292.6123	7.3	30.6
3292.8181	66.9	31.6
3293.1396	8.1	30.7
3293.4502	369.1	32.3
3293.6300	18.6	31.0
3294.0612	179.5	32.0
3294.4597	5.7	30.5
3295.6940	4.2	30.4
3296.2731	1.4	29.9
3296.5053	8.2	30.7
3296.7717	2.0	30.1
3297.6238	13.4	30.9

Continued on next page

**Table A.4 – continued from previous page**

$T_{\text{peak}}$ (BJD - 2454833)	ED (s)	$\log E$ (erg)
3299.2253	7.2	30.6
3299.2900	2.0	30.1
3299.3173	10.7	30.8
3300.9378	21.4	31.1
3301.0918	8.9	30.7
3301.2123	153.2	32.0
3301.8295	3.0	30.3
3301.8615	6.3	30.6
3303.0379	6.6	30.6
3303.3901	5.5	30.5
3303.5025	4.4	30.4
3304.2416	7.4	30.6
3304.9275	28.1	31.2
3305.3764	10.4	30.8
3305.4146	2.6	30.2
3306.0474	2.4	30.1
3306.2204	25.3	31.2
3306.3975	1.9	30.0
3308.4861	53.3	31.5
3309.0010	2.4	30.1
3309.0215	19.1	31.1
3309.0392	1.6	30.0
3309.3546	4.4	30.4
3309.4561	28.2	31.2
3310.4676	28.5	31.2
3310.7810	122.7	31.9
3311.5432	4.2	30.4
3312.2230	3.6	30.3
3312.2591	2.7	30.2
3312.3048	3.4	30.3
3312.4403	17.1	31.0
3312.6188	21.1	31.1
3313.0820	5.2	30.5
3313.1113	45.1	31.4
3313.2714	7.0	30.6
3314.1290	22.5	31.1
3314.6767	2.0	30.1
3315.2509	2.3	30.1
3315.2598	2.6	30.2
3315.4988	2.2	30.1
3316.4035	1.0	29.8
3316.6875	2.7	30.2
3317.5404	2.6	30.2
3317.5458	5.7	30.5
3317.9797	3.1	30.3
3318.2270	9.7	30.8
3319.0546	17.3	31.0
3319.5546	6.9	30.6
3319.9585	3.5	30.3
3320.1922	8.6	30.7
3320.2133	7.8	30.7
3320.5982	15.1	31.0
3320.6145	3.0	30.3
3320.8393	10.7	30.8
3320.9354	66.3	31.6
3321.1479	7.0	30.6
3321.9108	40.7	31.4
3321.9728	2.8	30.2
3322.1083	7.2	30.6
3322.3992	3.9	30.4
3322.4455	52.1	31.5
3322.8774	12.2	30.9

Continued on next page

**Table A.4 – continued from previous page**

$T_{\text{peak}}$ (BJD - 2454833)	ED (s)	$\log E$ (erg)
3324.1444	6.2	30.6
3324.3051	2.4	30.1
3324.3794	3.3	30.3
3324.4169	1.8	30.0
3325.4100	10.0	30.8
3325.8684	7.3	30.6
3326.2410	49.9	31.5
3326.3759	16.8	31.0
3326.5932	15.6	31.0
3326.7015	6.6	30.6
3327.7621	12.0	30.9
3327.8963	11.7	30.8
3328.0257	7.7	30.7
3328.2301	3.3	30.3
3329.1728	1.7	30.0
3329.9705	7.5	30.7
3330.4514	13.0	30.9
3330.4882	22.9	31.1
3330.5883	10.3	30.8
3331.1530	15.5	31.0
3331.2082	23.6	31.2
3331.7981	7.1	30.6
3332.8668	1.3	29.9
3332.9949	29.7	31.3
3333.9015	5.3	30.5
3334.8749	4.0	30.4
3334.9682	4.3	30.4
3335.0166	22.9	31.1
3335.1508	2.7	30.2
3335.6555	240.8	32.2
3335.9362	2540.7	33.2
3336.1037	29.6	31.2
3336.4675	2.1	30.1
3337.0751	8.1	30.7
3337.1337	53.7	31.5
3337.7283	7.2	30.6
3337.9340	17.1	31.0
3338.1684	12.6	30.9
3339.9700	5.2	30.5
3340.0906	13.1	30.9

**Table A.5: Flare properties of 2M1507-2000**

$T_{\text{peak}}$ (BJD - 2454833)	ED (s)	$\log E$ (erg)
3158.2457	158.1	32.1
3170.0099	43.6	31.5
3175.8663	45.4	31.6
3176.5597	37.0	31.5
3179.6149	720.3	32.8
3179.8253	7.2	30.8
3185.2439	3.6	30.5
3185.3017	15.8	31.1
3187.0957	11.4	31.0
3187.2421	2.6	30.3
3187.9075	6.0	30.7
3193.6188	16.1	31.1
3195.3705	54.7	31.6
3203.6269	46.7	31.6
3204.3570	72.0	31.8
3207.6254	103.9	31.9

Continued on next page

**Table A.5 – continued from previous page**

$T_{\text{peak}}$ (BJD - 2454833)	ED (s)	$\log E$ (erg)
3212.3819	13.3	31.0
3221.6006	128.0	32.0
3222.2027	6.1	30.7
3226.5029	16.0	31.1
3227.3631	22.7	31.3
3227.3964	3161.1	33.4
3232.1257	4.3	30.5
3232.9702	5.2	30.6
3235.0842	12.8	31.0
3238.9377	14.8	31.1
3239.6760	22.2	31.3
3243.7426	5.2	30.6

**Table A.6: Flare properties of 2M0825+2021**

$T_{\text{peak}}$ (BJD - 2454833)	ED (s)	$\log E$ (erg)
3425.0226	106.1	32.5
3425.2283	231.3	32.9
3427.7121	176.8	32.8
3431.4416	252.4	32.9
3432.6417	169.3	32.7
3433.0857	194.7	32.8
3440.6285	264.5	32.9
3441.4730	685.5	33.4
3458.1575	684.4	33.4
3465.3971	252.9	32.9
3465.4434	100.2	32.5

**Table A.7: Flare properties of 2M1330-0453**

$T_{\text{peak}}$ (BJD - 2454833)	ED (s)	$\log E$ (erg)
2392.4503	23.0	30.8
2394.0862	48.6	31.2
2403.7056	148.2	31.6
2415.5084	27.7	30.9
2422.5975	58.8	31.2
2435.5607	29.6	30.9
2436.6020	114.1	31.5
3366.6703	402.7	32.1
3368.1764	42.0	31.1
3376.2280	115.1	31.5
3379.2103	65.2	31.3
3386.7108	129.9	31.6
3399.4148	77.1	31.4

**Table A.8: Flare properties of 2M2353-0833**

$T_{\text{peak}}$ (BJD - 2454833)	ED (s)	$\log E$ (erg)
2914.5145	40.1	30.8
2916.3241	22.8	30.5
2924.4465	68.8	31.0
2932.1125	211.7	31.5
2938.7345	142.3	31.3
2945.0989	135.5	31.3

Continued on next page

**Table A.8 – continued from previous page**

$T_{\text{peak}}$ (BJD - 2454833)	ED (s)	$\log E$ (erg)
2946.8567	167.8	31.4
2961.6825	46.5	30.8
2981.7988	67.0	31.0
2982.2612	45.0	30.8

**Table A.9: Flare properties of 2M1055+0808**

$T_{\text{peak}}$ (BJD - 2454833)	ED (s)	$\log E$ (erg)
3076.3776	12.3	30.3
3078.0142	20.4	30.5
3081.3460	10.2	30.2
3082.2165	10.7	30.2
3085.6777	7.9	30.1
3095.3761	5.3	29.9
3111.9845	4.7	29.9
3114.6420	13.0	30.3
3120.1238	8.9	30.1
3120.3656	18.2	30.5
3120.6809	11.2	30.2
3121.3572	752.0	32.1
3123.4984	16.3	30.4
3123.9500	19.6	30.5
3126.5714	19.5	30.5
3133.8893	106.6	31.2
3137.5282	22.1	30.5
3137.8667	5.6	29.9
3138.0839	24.8	30.6
3140.3668	16.7	30.4
3143.1598	268.3	31.6

**Table A.10: Flare properties of 2M1048+0111**

$T_{\text{peak}}$ (BJD - 2454833)	ED (s)	$\log E$ (erg)
3075.0509	43.3	30.4
3076.5029	39.2	30.4
3084.1358	178.4	31.0
3087.0869	24.0	30.1
3114.8334	119.4	30.8
3125.4933	21.2	30.1
3140.4214	252.6	31.2
3144.7774	48.9	30.5
3148.8686	93.9	30.7
3151.8795	87.5	30.7

**Table A.11: Flare properties of 2M2228-1325**

$T_{\text{peak}}$ (BJD - 2454833)	ED (s)	$\log E$ (erg)
2145.4316	1.1	30.3
2145.5278	0.6	30.0
2146.7530	239.6	32.6
2147.2441	30.3	31.7
2147.7570	1.5	30.4
2148.0304	53.1	32.0
2149.7279	22.6	31.6

Continued on next page

**Table A.11 – continued from previous page**

$T_{\text{peak}}$ (BJD - 2454833)	ED (s)	$\log E$ (erg)
2150.5321	16.4	31.4
2151.8034	14.5	31.4
2152.4019	5.8	31.0
2153.0392	101.1	32.2
2153.2133	13.8	31.4
2155.5389	1.2	30.3
2156.2957	40.5	31.8
2156.5088	2.5	30.6
2157.0641	35.2	31.8
2157.1270	76.9	32.1
2160.8812	1.5	30.4
2161.6706	2.4	30.6
2162.7380	31.2	31.7
2173.2718	1.0	30.2
2174.9069	5.6	31.0
2175.9981	5.6	31.0
2179.1037	11.9	31.3
2181.1503	9.6	31.2
2182.1199	1.6	30.4
2184.1766	1.1	30.3
2184.9962	6.0	31.0
2187.5795	34.2	31.8
2188.9153	8.2	31.1
2189.0867	24.9	31.6
2191.5079	1.7	30.5
2192.9842	4.2	30.9
2193.7177	4.0	30.8
2195.3758	10.2	31.2
2196.0187	37.2	31.8
2197.2331	105.7	32.3
2197.4422	68.7	32.1
2199.7102	1.4	30.4
2200.0509	6.4	31.0
2200.7708	9.4	31.2
2201.6024	13.0	31.3
2204.6049	7.4	31.1
2204.6692	23.0	31.6
2205.1944	6.3	31.0
2206.0605	21.8	31.6
2206.5389	24.3	31.6
2206.8726	43.2	31.9
2210.9375	16.6	31.5
2212.1003	13.0	31.3

**Table A.12: Flare properties of 2M2202-1109**

$T_{\text{peak}}$ (BJD - 2454833)	ED (s)	$\log E$ (erg)
2144.8352	7.7	30.7
2147.4002	8.6	30.8
2147.5155	7.3	30.7
2149.9502	8.2	30.8
2150.1343	32.5	31.4
2150.1667	41.0	31.5
2152.5107	5.3	30.6
2153.1794	7.5	30.7
2153.6131	5.0	30.5
2154.4757	46.4	31.5
2154.5422	14.5	31.0
2155.0098	15.6	31.0
2156.6671	27.6	31.3

Continued on next page

**Table A.12 – continued from previous page**

$T_{\text{peak}}$ (BJD - 2454833)	<b>ED</b> (s)	<b>log E</b> (erg)
2157.4049	4.2	30.5
2158.2444	38.6	31.4
2158.5388	8.9	30.8
2158.8966	5.1	30.6
2159.1818	681.0	32.7
2161.9861	43.7	31.5
2162.2759	119.1	31.9
2162.8276	11.2	30.9
2163.9409	22.8	31.2
2166.4971	195.6	32.1
2166.9856	37.1	31.4
2167.2407	6.1	30.6
2168.5393	21.4	31.2
2171.2043	6.2	30.6
2172.7186	1994.0	33.1
2174.5368	26.0	31.3
2177.8521	27.6	31.3
2178.3239	17.9	31.1
2178.3462	31.0	31.3
2180.0101	24.8	31.2
2181.6909	45.3	31.5
2184.5248	8.5	30.8
2185.5130	37.2	31.4
2187.8212	100.9	31.8
2188.6505	56.4	31.6
2190.4253	469.4	32.5
2198.6648	36.2	31.4
2199.6864	167.8	32.1
2201.6704	26.3	31.3
2201.9148	25.7	31.3
2202.6609	23.2	31.2
2204.7965	45.3	31.5
2208.5398	15.5	31.0
2208.8992	129.4	32.0
2209.3064	19.8	31.1
2210.5130	366.6	32.4
2212.9586	57.9	31.6

**Table A.13: Flare properties of 2M0835+1029**

$T_{\text{peak}}$ (BJD - 2454833)	<b>ED</b> (s)	<b>log E</b> (erg)
2315.8371	37.7	30.9
2328.2400	78.4	31.2
2330.0303	19.9	30.6
2331.9130	145.3	31.5
2333.9439	105.2	31.4
2344.3019	10.3	30.4
2345.6774	19.2	30.6
2350.9757	22.9	30.7
2372.4915	41.0	31.0
2379.8826	27236.4	33.8
2381.2464	26.9	30.8

**Table A.14: Flare properties of 2M2214-1319**

$T_{\text{peak}}$ (BJD - 2454833)	<b>ED</b> (s)	<b>log E</b> (erg)
2146.7290	34.3	31.2

Continued on next page

**Table A.14 – continued from previous page**

$T_{\text{peak}}$ (BJD - 2454833)	ED (s)	$\log E$ (erg)
2154.8862	35.5	31.2
2158.8522	183.9	32.0
2159.4159	37.8	31.3
2161.1016	65.8	31.5
2162.4426	134.2	31.8
2162.8551	1275.9	32.8
2165.8338	504.7	32.4
2171.5198	78.1	31.6
2173.7128	18.0	30.9
2187.3768	33.6	31.2
2187.6903	76.2	31.6
2188.1009	132.8	31.8
2193.8231	83.4	31.6
2195.1214	66.8	31.5
2198.2233	87.7	31.6
2199.7099	53.5	31.4
2199.8133	33.7	31.2
2204.6701	44.4	31.3
2205.6107	255.2	32.1
2205.8970	2888.3	33.2
2206.2446	31.9	31.2
2206.8442	113.7	31.7
2210.8474	35.5	31.2
2211.6343	258.8	32.1
2212.6362	41.9	31.3

**Table A.15: Flare properties of 2M1332-0441**

$T_{\text{peak}}$ (BJD - 2454833)	ED (s)	$\log E$ (erg)
2384.9954	11.0	30.4
2389.0276	379.4	32.0
2391.0706	7.7	30.3
2395.8815	41.5	31.0
2400.1190	194.4	31.7
2405.3001	22.0	30.7
2406.1120	11.6	30.5
2413.0500	9.7	30.4
2417.6567	16.6	30.6
2419.2466	237.2	31.8
2419.2763	344.0	31.9
2420.5197	188.3	31.7
2425.8723	7.7	30.3
2427.0553	63.0	31.2
2428.6803	13.2	30.5
2430.6328	852.3	32.3
2431.1226	44.5	31.0
2437.6107	40.6	31.0
2439.0514	18.0	30.7
2444.4024	31.2	30.9
2447.0652	238.8	31.8
2449.9006	24.6	30.8
2451.2583	52.8	31.1
2453.0232	9.4	30.4
2453.5987	74.7	31.3
2453.7290	74.5	31.3
2459.3101	6.9	30.2
2460.1269	83.0	31.3
2460.2546	22.1	30.7
2461.8496	8.6	30.3
2462.3502	71.5	31.3

Table A.16: Flare properties of TRAPPIST-1

$T_{\text{peak}}$ (BJD - 2454833)	ED (s)	$\log E$ (erg)
2906.1132	6.4	30.2
2912.1249	102.2	31.4
2912.9066	15.2	30.6
2916.0324	14.8	30.6
2916.0933	5.3	30.1
2916.3000	14.2	30.6
2919.8897	36.7	31.0
2922.0807	10.2	30.4
2922.1486	3.2	29.9
2923.6377	3.2	29.9
2923.7645	8.8	30.4
2924.5278	2.7	29.8
2926.9682	22.3	30.8
2932.6106	3.3	29.9
2934.5026	63.1	31.2
2938.2947	46.3	31.1
2940.4482	149.1	31.6
2943.4982	91.4	31.4
2950.9779	20.4	30.7
2959.0948	9.6	30.4
2959.6040	2.7	29.8
2959.8056	2.4	29.8
2960.3503	9.0	30.4
2960.3626	6.6	30.2
2964.8134	4.1	30.0
2966.7367	11.3	30.5
2967.5109	9.1	30.4
2967.6178	15.6	30.6
2969.0906	13.4	30.5
2969.6094	26.3	30.8
2970.3802	84.1	31.3
2972.5410	31.2	30.9
2973.3600	6.4	30.2
2973.5176	200.7	31.7
2974.6890	7.8	30.3
2979.8355	12.5	30.5
2979.9511	2598.5	32.8
2981.8732	15.0	30.6
2981.9720	50.5	31.1

Table A.17: Flare properties of 2M1221-0843

$T_{\text{peak}}$ (BJD - 2454833)	ED (s)	$\log E$ (erg)
2751.5620	55.3	31.6
2754.9956	303.6	32.4
2771.5915	97.5	31.9
2772.1872	40.5	31.5
2773.7407	20.9	31.2
2776.5896	19.8	31.2
2776.9729	160.5	32.1
2778.4633	47.7	31.6
2781.8195	29.2	31.4
2783.8164	37.2	31.5
2784.8417	1469.9	33.1
2784.9262	23.2	31.3
2785.5129	110.5	31.9
2786.6326	53.4	31.6
2786.7083	497.1	32.6
2788.1226	62.3	31.7

Continued on next page

**Table A.17 – continued from previous page**

$T_{\text{peak}}$ (BJD - 2454833)	ED (s)	$\log E$ (erg)
2789.0377	20.4	31.2
2789.4079	20.8	31.2
2789.4684	35.9	31.4
2792.0682	239.9	32.3
2793.3817	73.2	31.8
2794.9394	51.3	31.6
2795.2787	54.6	31.6
2799.5751	17.8	31.1
2801.8855	43.5	31.5
2803.2329	83.0	31.8
2803.3851	28.4	31.3
2804.3787	76.5	31.8
2804.8240	16.0	31.1
2807.3241	1469.9	33.1
2808.5400	67.7	31.7
2808.9569	58.8	31.7
2813.1739	13.7	31.0
2814.4040	17.7	31.1
2816.6892	143.7	32.0
2818.1534	33.3	31.4

**Table A.18: Flare properties of 2M0326+1919**

$T_{\text{peak}}$ (BJD - 2454833)	ED (s)	$\log E$ (erg)
2235.9401	50.8	31.1
2236.0150	14.0	30.5
2236.4862	54.1	31.1
2238.8718	997.7	32.4
2240.1374	796.5	32.3
2247.8987	12.1	30.4
2247.9459	19.9	30.7
2248.3242	384.8	31.9
2249.3563	23.0	30.7
2253.2909	73.9	31.2
2254.0567	60.3	31.1
2258.6868	276.4	31.8
2263.5381	124.1	31.5
2266.7949	319.7	31.9
2267.6417	709.0	32.2
2284.0439	158.0	31.6
2284.6184	19.4	30.6
2298.1398	218.5	31.7

**Table A.19: Flare properties of 2M1221-0257**

$T_{\text{peak}}$ (BJD - 2454833)	ED (s)	$\log E$ (erg)
2750.3254	24.6	30.3
2755.2032	33.8	30.4
2756.3360	83.7	30.8
2771.9580	45.4	30.5
2772.1863	71.7	30.7
2786.2816	25.6	30.3
2795.7802	26.6	30.3
2797.6173	31.9	30.4
2799.9371	915.1	31.8
2801.8849	61.2	30.7
2803.9084	17.4	30.1

Table A.20: Flare properties of 2M1232-0951

$T_{\text{peak}}$ (BJD - 2454833)	ED (s)	$\log E$ (erg)
2755.0598	4400.9	32.6
2772.1873	77.0	30.8
2778.3452	562.8	31.7
2782.9361	97.5	30.9
2789.5562	137.9	31.1
2792.2461	34.1	30.5
2801.1353	28.8	30.4
2801.8858	130.3	31.1
2808.7771	31.9	30.4
2810.5028	46.5	30.6
2811.7661	40278.7	33.5

## Appendix B

### M6-M8 DWARFS OBSERVED IN *K2* LONG CADENCE MODE

Table B.1: List of M6 dwarfs

EPIC	2MASS name	Campaign #	$i$ (mag)	$z$ (mag)	$M_i$ (mag)	parallax (mas)
206050032	J22285440-1325178 (LHS 523)	3	12.80 <sup>a</sup>		12.54	88.81
206135809	J22021125-1109461	3	15.83	14.61	13.62	36.06
206173821	J22512196-1014225	3	18.31	17.38	13.25	9.72
206194689	J22511224-0950559	3	18.23	17.33	12.51	7.17
206235652	J22361609-0912233	3	19.47	18.48	11.32	2.34
206296292	J22360552-0817523	3	18.6	17.59	11.7	4.18
206494490	J22151717-0459197	3	16.36	15.37	12.17	14.48
212402103	J13401152-1451591	6	16.68	15.59	13.19	20.07
220195996	J00540990-0009160	8	17.28	16.35	11.81	8.08
245995471	J23361422-0936065	12	16.80	15.64	13.67	23.64
246322698	J23172072-0236323	12	15.33	14.28	12.99	34.04
246403896	J23084293-0052292	12	18.71	17.78	12.02	4.58
246404848	J23145940-0050364	12	16.83	15.9	12.64	14.57
246405614	J23113982-0049120	12	17.16	16.22	11.90	8.87
247051861	J04321606+1812464	13	14.48	13.4	8.68	6.91
248015397	J04411078+2555116	13	17.90	16.31	11.92	6.38
248019863	J04380186+2557112	13	12.76	11.88	3.69	1.54
201693239	J11014472+0331331	14	18.19	17.17	12.32	6.68
201705352	J11012507+0343454	14	18.89	18.01	12.29	4.79
201744267	J11000170+0423056	14	17.84	16.86	12.58	8.85
248455574	J10304305+0140008	14	19.32	18.29	11.95	3.35
248456554	J10313185+0142187	14	18.98	17.93	12.73	5.62
248519036	J10164247+0342577	14	17.97	17.03	12.95	9.93 <sup>b</sup>
248525204	J10194963+0353224	14	18.95	18.01	12.02	4.10
248609711	J10144278+0607029	14	18.63	17.77	11.17	3.21
248615433	J10380862+0615418	14	18.99	18.05	12.57	5.20
248621243	J10375820+0624395	14	19.37	18.42	11.54	2.72
248624299	J10274572+0629104	14	17.03	16.03	12.06	10.11
248631849	J10202167+0640362	14	18.54	17.55	11.97	4.85
248648532	J10322597+0705176	14	18.95	18.05	12.43	4.97
248655562	J10551663+0715313	14	15.94	15.04	12.75	23.04 <sup>c</sup>
248666674	J10340004+0732074	14	19.03	18.11	12.48	4.89
248671305	J10401164+0739006	14	19.40	18.43	10.72	1.84
248744078	J10470045+0920145	14	19.44	18.46	13.00	5.16
248750733	J10435088+0929353	14	17.51	16.56	12.71	11.00
248751905	J10423183+0931131	14	19.77	18.71	12.03	2.83
212117236	J08342822+2221414	16	18.38	17.5	11.98	5.25
212130922	J08300140+2238125	16	19.15	18.21	12.63	4.97
212162487	J08392846+2318366	16	19.46	18.47	10.05	1.31
212402103	J13401152-1451591	17	16.68	15.59	13.19	20.07

Continued on next page

Table B.1 – continued from previous page

EPIC	2MASS name	Campaign #	$i$ (mag)	$z$ (mag)	$M_i$ (mag)	parallax (mas)
212130922	J08300140+2238125	18	19.15	18.21	12.63	4.97
212162470	J08392900+2318355	18	16.78	16.20	8.75	2.47
212162487	J08392846+2318366	18	19.46	18.47	10.05	1.31

Note: <sup>a</sup>Epchtein et al. [1997]; <sup>b</sup>Best et al. [2018]; <sup>c</sup>West et al. [2011]

Table B.2: List of M7 dwarfs

EPIC	2MASS name	Campaign #	$i$ (mag)	$z$ (mag)	$M_i$ (mag)	parallax (mas)
206053352	J22145070-1319590	3	16.94	15.71	13.42	25.33
206181579	J22544137-1005195	3	17.42	16.37	13.22	14.48
206184645	J22542382-1001454	3	18.91	17.91	12.6	5.47
206185256	J22564217-1001028	3	19.54	18.67	12.60	4.08
206213997	J22333001-0932110	3	19.41	18.22	14.37	9.80
206244023	J22520015-0904463	3	19.12	18.09	12.79	5.43 <sup>a</sup>
206262805	J22383015-0847469	3	19.11	18.09	13.34	6.99
206284791	J22344229-0828192	3	18.13	17.08	12.61	7.86
211073549	J03455065+2409037	4	19.50	18.19	14.02	8.02
212287292	J13392651-1755053	6	17.24	15.88	14.72	31.38
212826600	J13322442-0441126	6	16.08	14.78	14.70	52.91 <sup>b</sup>
220195098	J00480864-0011182	8	18.16	17.15	13.23	10.34
220197688	J00465574-0005192	8	18.59	17.44	13.52	9.69
201425001	J12132877-0034453	10	16.69	15.62	13.17	19.82
229052381	J12280469-0022412	10	16.97	16.02	12.41	12.25
245953430	J23124761-1044502	12	18.17	17.03	12.99	9.20
245970317	J23332702-1016159	12	17.63	16.64	11.50	5.96
246015548	J23430665-0905098	12	18.27	17.33	11.67	4.80
246016138	J23412019-0904126	12	18.14	17.20	12.41	7.14
246034587	J23223296-0836389	12	17.54	16.55	12.14	8.34
246393886	J23322973-0110377	12	16.35	15.43	11.59	11.19
246395463	J23140106-0107587	12	19.28	18.30	12.33	4.08
246395512	J23274585-0107531	12	18.01	17.02	12.00	6.29
246401499	J23320833-0057062	12	18.56	17.41	13.66	10.48
246407066	J23231027-0046362	12	17.51	16.51	11.92	7.63
246414315	J23310852-0033116	12	18.24	17.33	12.39	6.76
246416841	J23124351-0028281	12	18.72	17.81	11.87	4.28
246420090	J23205795-0022167	12	17.81	16.88	10.75	3.88
246452199	J23212507+0038526	12	18.78	17.84	12.29	5.03
246468225	J23225253+0112054	12	18.63	17.51	13.22	8.28
248051303	J04381486+2611399	13	18.98	17.66	13.17	6.88
247991214	J04390396+2544264	13	16.74	15.29	10.95	6.94
248029954	J04394748+2601407	13	17.54	15.79	11.70	6.80
201573260	J10554616+0138036	14	19.12	18.13	13.05	6.12
201575762	J10502404+0140197	14	19.51	18.52	12.43	3.84
201581268	J10542846+0145153	14	19.41	18.43	10.74	1.84
201801587	J10564295+0523446	14	19.33	18.19	13.63	7.26
248440677	J10230742+0107532	14	17.39	16.42	11.97	8.25
248452093	J10313961+0132451	14	17.92	16.82	13.55	13.33
248484484	J10311572+0238389	14	18.34	17.35	12.99	8.51
248525367	J10163213+0353399	14	18.96	17.93	13.22	7.13 <sup>a</sup>

Continued on next page

Table B.2 – continued from previous page

EPIC	2MASS name	Campaign #	$i$ (mag)	$z$ (mag)	$M_i$ (mag)	parallax (mas)
248551923	J10170533+0435457	14	18.84	17.91	12.55	5.51
248561247	J10162377+0451054	14	19.10	18.03	12.84	5.59
248565564	J10150953+0458087	14	17.36	16.37	12.5	10.67
248580531	J10210278+0521223	14	18.42	17.31	13.51	10.41
248597458	J10391617+0548357	14	19.36	18.42	11.93	3.27
248604738	J10514015+0559340	14	19.17	18.22	12.3	4.23
248622974	J10224553+0627111	14	18.95	18.05	12.47	5.06
248638618	J10445415+0650487	14	19.49	18.57	12.33	3.71
248651399	J10202457+0709249	14	18.84	17.74	12.57	5.57
248655628	J10152510+0715383	14	18.20	17.14	14.03	14.66 <sup>c</sup>
248656573	J10533711+0716594	14	19.21	18.17	11.66	3.09
248658559	J10342027+0719581	14	19.21	18.21	12.09	3.77
248659481	J10180577+0721206	14	18.92	17.90	12.04	4.21
248659647	J10503930+0721348	14	15.98	14.97	12.96	24.91
248659722	J10542720+0721424	14	18.34	17.35	12.88	8.10
248660752	J10393158+0723169	14	19.40	18.37	12.07	3.42
248676218	J10455204+0746195	14	18.72	17.67	13.22	7.95
248682489	J10354429+0755246	14	18.26	17.03	13.9	13.46
248718280	J10430207+0845114	14	18.93	17.86	13.57	8.46
248755514	J10564831+0936160	14	18.22	17.26	12.63	7.60
248766826	J10455229+0952344	14	19.27	18.25	12.66	4.77
248777799	J10173284+1008463	14	18.89	17.84	13.28	7.55
204407831	J15594802-2227162	16	17.80	16.56	11.81	6.33
249639465	J15072779-2000431	16	15.32	14.04	13.42	41.8
211411366	J08402621+1148442	16	18.81	17.9	11.28	3.12
211439338	J08555883+1214095	16	17.83	16.91	11.74	6.04
211458709	J08503449+1231593	16	18.62	17.63	12.39	5.66
211460625	J08534015+1233405	16	18.31	17.32	12.44	6.69
211478560	J08432901+1249461	16	17.99	17.02	12.12	6.70
211493031	J08453007+1302215	16	18.44	17.43	12.98	8.10
211563696	J08434983+1402053	16	18.60	17.54	12.98	7.49
211631830	J08472827+1458578	16	18.17	17.22	12.8	8.45
211707676	J08405443+1601007	16	18.18	17.24	11.75	5.18
211738457	J08414994+1626415	16	18.53	17.64	12.28	5.62
211740609	J08382850+1628301	16	17.36	16.43	12.69	11.67
211742071	J08414120+1629468	16	18.33	17.41	11.95	5.30
211758584	J08533829+1643431	16	18.41	17.32	12.8	7.54
211759353	J08444549+1644218	16	17.88	16.98	12.24	7.46 <sup>c</sup>
211770368	J08402941+1653432	16	18.94	18.03	11.52	3.29
211845911	J08522663+1757430	16	17.69	16.75	12.67	9.88
211847385	J08391297+1758541	16	18.01	16.93	13.14	10.62
211869078	J09024330+1816512	16	17.38	16.46	12.43	10.27

Continued on next page

Table B.2 – continued from previous page

EPIC	2MASS name	Campaign #	$i$ (mag)	$z$ (mag)	$M_i$ (mag)	parallax (mas)
211877519	J08575696+1824037	16	18.28	17.34	12.74	7.78 <sup>a</sup>
211892842	J08420732+1837169	16	18.30	17.42	11.69	4.76
211908843	J08533351+1851304	16	18.17	17.23	12.42	7.08
211912744	J09145284+1854591	16	18.00	16.99	11.19	4.34
211916047	J08574941+1857583	16	18.20	17.24	12.64	7.70
211917847	J08514388+1859346	16	18.12	17.15	11.92	5.76
211928727	J08410950+1909205	16	17.62	16.68	12.09	7.81
211934172	J08405890+1914167	16	17.63	16.71	11.32	5.48
211947924	J08560483+1926313	16	17.82	16.93	12.00	6.85
211964067	J08541663+1941146	16	18.56	17.65	12.59	6.40
211969262	J08471141+1945551	16	18.74	17.87	11.99	4.47
211996000	J09030311+2011190	16	16.66	15.74	12.70	16.12
212002661	J08285410+2017539	16	18.99	18.07	12.50	5.03
212008870	J08310840+2024042	16	18.87	17.92	11.43	3.25
212013999	J08571777+2029125	16	18.72	17.83	12.13	4.81
212019105	J08260971+2034154	16	17.30	16.33	12.32	10.09
212022763	J08262900+2037578	16	18.58	17.62	11.87	4.55
212027121	J08315742+2042213	16	18.51	17.53	11.86	4.67
212032430	J09035006+2047425	16	18.82	17.92	12.10	4.51
212044515	J08325345+2100114	16	18.31	17.31	12.94	8.41
212059071	J08263441+2115314	16	18.83	17.88	12.76	6.12
212066577	J09070364+2123379	16	17.93	16.98	12.76	9.27
212067906	J08272584+2125038	16	19.53	18.42	13.22	5.45
212067916	J08353644+2125040	16	18.68	17.65	12.82	6.73
212072712	J08280190+2130204	16	19.20	18.26	12.66	4.94
212075399	J08523489+2133182	16	17.87	16.92	12.98	10.48
212077206	J08554770+2135202	16	18.03	17.05	12.85	9.20
212078253	J08594100+2136260	16	18.77	17.85	12.60	5.85
212080001	J08335765+2138296	16	18.17	17.24	12.69	8.03
212081772	J09104395+2140225	16	18.45	17.49	12.70	7.08
212089454	J08342159+2148585	16	18.70	17.74	12.63	6.11
212098179	J09092911+2159088	16	18.67	17.73	12.63	6.19
212111539	J09001010+2214567	16	18.55	17.56	12.67	6.68
212117165	J09061058+2221361	16	18.89	18.01	11.92	4.04
212155930	J08503464+2309504	16	19.03	18.05	10.34	1.83
212156288	J08574487+2310168	16	18.26	17.32	12.09	5.85
212162176	J08542632+2318079	16	17.81	16.84	11.87	6.49
212170651	J08390595+2330106	16	19.16	18.18	10.69	2.03
212183917	J08523260+2350335	16	18.49	17.63	12.45	6.18
251287438	J09182409+1514342	16	18.00	17.06	12.48	7.87
251314012	J09231747+1759473	16	17.77	16.80	12.57	9.13
251317744	J09172163+1819293	16	17.79	16.80	11.58	5.74

Continued on next page

Table B.2 – continued from previous page

EPIC	2MASS name	Campaign #	$i$ (mag)	$z$ (mag)	$M_i$ (mag)	parallax (mas)
251340486	J09174589+2017361	16	18.00	17.10	12.54	8.11
251347715	J09241907+2053124	16	18.64	17.73	12.66	6.37 <sup>a</sup>
251358654	J09215755+2148237	16	19.00	18.07	11.03	2.54
251364084	J09121559+2214189	16	18.39	17.51	12.45	6.48
251365679	J09090474+2221274	16	18.08	17.03	13.13	10.23
251394211	J09124523+2425493	16	17.04	15.79	14.12	26.0
251394863	J09055747+2428182	16	19.21	18.31	10.88	2.17
251396437	J08593897+2434260	16	18.14	17.21	12.52	7.49
251397724	J09124005+2439019	16	18.28	17.28	12.97	8.66
251406926	J08593647+2511090	16	19.35	18.46	12.68	4.64
251407310	J09062462+2512380	16	18.43	17.45	13.08	8.53
251408963	J08531166+2518061	16	19.37	18.34	13.71	7.37
212826600	J13322442-0441126	17	16.08	14.78	14.70	52.91
212872421	J13295634-0304232	17	19.33	18.36	12.68	4.69
212876200	J13292260-0255184	17	19.09	18.14	12.10	4.00
212878661	J13432034-0248599	17	19.11	18.07	13.39	7.18
212878986	J13423359-0248104	17	18.87	17.95	10.54	2.16
212880174	J13435186-0244489	17	19.05	18.15	12.17	4.22
212883317	J13303046-0235019	17	18.99	17.99	13.05	6.47
212884029	J13312568-0232051	17	18.25	17.30	12.84	8.29 <sup>a</sup>
251547634	J13314483-0226119	17	17.64	16.70	12.39	8.92
251554277	J13173577-0216551	17	20.67	19.46	14.30	5.32 <sup>d</sup>
251557288	J13492757-0213183	17	19.11	18.12	12.90	5.74
251558388	J13325189-0211585	17	19.03	18.08	12.90	5.94
251583509	J13301745-0141050	17	17.51	16.48	12.38	9.43
251596433	J13485922-0124144	17	19.38	18.42	11.55	2.72
251599629	J13354750-0120068	17	18.05	17.16	13.02	9.85
251556648	J13314737-0214059	17	20.57	19.22	14.95	7.53 <sup>c</sup>
251593967	J13175740-0127257	17	20.41	19.04	14.46	6.45 <sup>d</sup>
211303420	J08500542+0955004	18	18.08	17.91	7.67	0.83
211311813	J08510475+1005210	18	18.93	17.92	14.01	10.38 <sup>c</sup>
211893584	J08135406+1837559	18	18.12	17.17	12.52	7.57
211896791	J08132764+1840480	18	19.34	18.41	12.90	5.15
211910449	J08150831+1852580	18	19.41	18.53	12.58	4.31
211942125	J08211628+1921246	18	19.21	18.22	12.49	4.52
211953626	J08173975+1931381	18	18.71	17.81	12.36	5.37
211974835	J08261262+1951080	18	18.45	17.47	12.87	7.67
211994941	J08324426+2010171	18	19.13	18.16	13.13	6.30
212003005	J08253864+2018165	18	19.17	18.22	12.44	4.50
212006725	J08252223+2021567	18	18.19	17.19	11.91	5.53
212013823	J08175969+2029003	18	19.44	18.51	12.41	3.92
212017281	J08320196+2032301	18	19.35	18.37	12.73	4.75

Continued on next page

Table B.2 – continued from previous page

EPIC	2MASS name	Campaign #	$i$ (mag)	$z$ (mag)	$M_i$ (mag)	parallax (mas)
212019105	J08260971+2034154	18	17.30	16.33	12.32	10.09
212022763	J08262900+2037578	18	18.58	17.62	11.87	4.55
212026054	J08131463+2041141	18	17.44	16.47	13.60	17.10 <sup>c</sup>
212027121	J08315742+2042213	18	18.51	17.53	11.86	4.67
212067906	J08272584+2125038	18	19.53	18.42	13.22	5.45
212071306	J08415177+2128461	18	19.13	18.21	11.79	3.41
212072251	J08361437+2129492	18	19.38	18.34	12.33	3.89
212072712	J08280190+2130204	18	19.20	18.26	12.66	4.94
212078008	J08381637+2136112	18	19.43	18.45	13.44	6.34
212080001	J08335765+2138296	18	18.17	17.24	12.69	8.03
212080305	J08374471+2138487	18	18.37	17.50	12.09	5.53
212085465	J08443381+2144323	18	19.35	18.32	13.18	5.84
212090825	J08400926+2150393	18	18.17	17.2	12.02	5.88
212091105	J08421796+2150576	18	19.15	18.21	12.77	5.30
212106472	J08420488+2208540	18	18.50	17.58	12.19	5.49
212108940	J08383012+2211498	18	18.76	17.79	12.68	6.09
212109980	J08435384+2213065	18	18.77	17.88	12.76	6.29
212110421	J08492109+2213375	18	18.19	17.18	12.72	8.08
212113915	J08361401+2217469	18	19.49	18.50	12.34	3.73
212123277	J08405877+2228499	18	18.46	17.56	12.17	5.54
212135209	J08415185+2243199	18	19.00	18.10	12.76	5.65
212136180	J08481517+2244322	18	18.73	17.79	12.47	5.59
212144120	J08372040+2254280	18	17.35	16.36	12.90	12.84
212150766	J08552314+2302545	18	18.55	17.49	11.93	4.76
212153751	J08295948+2306545	18	18.56	17.60	12.83	7.17
212155930	J08503464+2309504	18	19.03	18.05	10.34	1.83
212156288	J08574487+2310168	18	18.26	17.32	12.09	5.85
212162176	J08542632+2318079	18	17.81	16.84	11.87	6.49
212170953	J08264724+2330367	18	19.40	18.34	12.11	3.48
212176032	J08290300+2338034	18	19.21	18.23	12.69	4.97
212178513	J08313594+2341508	18	16.92	15.81	13.59	21.55

Note: <sup>a</sup>West et al. [2011]; <sup>b</sup>Reiners and Basri [2009]; <sup>c</sup>Ahmed and Warren [2019]; <sup>d</sup>West et al. [2008]

Table B.3: List of M8 dwarfs

EPIC	2MASS name	Campaign #	$i$ (mag)	$z$ (mag)	$M_i$ (mag)	parallax (mas)
206215073	J22531563-0931113	3	19.38	18.05	13.95	8.21
210457230	J03552014+1439297	4	17.78	16.38	14.95	27.17
210764183	J03264453+1919309	4	17.13	15.71	14.8	34.12
211046195	J03350208+2342356	4	15.68	14.48	12.14	19.53
212411722	13571497-1438529	6	16.55	15.28	14.15	33.16
212820594	J13300232-0453202	6	17.16	15.79	14.55	29.99
220170497	J00545910-0111150	8	19.19	18.00	14.01	9.22
201217402	J12162679-0342201	10	19.07	17.89	13.78	8.76
201250232	J12050387-0312128	10	18.48	17.25	13.97	12.58
201295866	J12164386-0230475	10	19.69	18.49	13.54	5.88
201317801	J12080641-0211127	10	19.24	17.92	13.9	8.54
201422946	J12154938-0036387	10	18.42	17.16	14.29	14.90
201484170	J12034963+0016573	10	18.94	17.61	14.37	12.24
228754562	J12215066-0843197	10	17.07	15.81	13.52	19.48
228876276	J12302520-0340441	10	19.11	17.74	14.67	12.93
228884768	J12303586-0332183	10	18.89	17.57	14.54	13.48
228971161	J12323184-0200391	10	19.51	18.20	14.26	8.89
229102518	J12285538+0050440	10	20.11	18.54	15.52	12.05
245985652	J23384491-0951192	12	18.53	17.24	14.56	16.09
246013537	J23421858-0908207	12	18.11	17.02	13.55	12.22
246036729	J23535946-0833311	12	17.04	15.59	15.35	45.87
247581233	J04355143+2249119	13	20.23	18.55	14.18	6.18
248018652	J04305718+2556394	13	18.55	17.10	13.11	8.14
248044306	J04300724+2608207	13	19.24	17.70	13.92	8.62
247566033	J04324059+2242108	13	14.94	14.4	5.61	1.36
201580841	J10502087+0144523	14	18.88	17.71	13.61	8.82
201800829	J10541027+0522526	14	18.01	16.82	13.8	14.37
248413181	J10425127+0004221	14	20.09	18.86	14.0	6.05
248433880	J0303169+0052303	14	19.95	18.61	14.93	9.90 <sup>a</sup>
248445614	J10490112+0119106	14	19.29	17.99	14.18	9.48
248450332	J10250505+0129091	14	19.67	18.42	14.01	7.39
248463831	J10304379+0157099	14	18.92	17.73	13.95	10.13
248567554	J10321706+0501032	14	17.53	16.15	14.99	31.05
248574498	J10173207+0511509	14	18.62	17.48	13.54	9.65
248592301	J10501487+0540278	14	18.49	17.29	13.81	11.6
248623263	J10471320+0627389	14	20.13	18.81	14.12	6.29 <sup>b</sup>
248680268	J10151763+0752121	14	19.91	18.44	14.55	8.45
248779449	J10360188+1011148	14	20.12	18.77	13.89	5.67
248849283	J10361013+1153150	14	19.51	18.26	14.4	9.49
249472713	J15330937-2205069	16	17.60	16.28	14.52	24.23
211464826	J08525003+1237347	16	18.35	17.30	13.12	8.99

Continued on next page

Table B.3 – continued from previous page

EPIC	2MASS name	Campaign #	$i$ (mag)	$z$ (mag)	$M_i$ (mag)	parallax (mas)
211616100	J08513910+1445328	16	17.71	16.5	13.12	12.1
212051014	J08295299+2107031	16	20.12	18.86	14.37	7.07 <sup>c</sup>
212083796	J08352239+2142418	16	20.09	18.62	15.26	10.83
212158934	J08403780+2313507	16	18.63	17.41	13.9	11.34
212184948	J08513466+2352155	16	19.04	17.82	14.09	10.26
212216110	J08392938+2448283	16	19.42	18.05	14.28	9.37
251385331	J09101018+2349478	16	18.09	16.79	14.44	18.65
251394129	J09085508+2425306	16	20.12	18.73	14.42	7.25 <sup>c</sup>
251404208	J09104976+2501538	16	19.10	18.04	13.45	7.43
251405376	J09032690+2505522	16	19.23	18.21	12.68	4.91
212820594	J13300232-0453202	17	17.16	15.79	14.55	29.99
251550196	J13283141-0222213	17	20.12	18.73	14.28	6.80 <sup>c</sup>
251581842	J13441109-0143110	17	17.98	16.74	12.64	15.16
251605563	J13363416-0111354	17	19.58	18.3	14.97	11.97
211301854	J08553808+0952584	18	18.91	17.83	13.11	6.90
211981759	J08243082+1957344	18	19.28	18.22	12.01	3.51
212035340	J08371832+2050349	18	18.80	17.78	11.61	3.65
212140336	J08335103+2249400	18	18.95	17.84	12.82	5.93
212141692	J08560474+2251237	18	19.94	18.67	13.87	6.12
212158934	J08403780+2313507	18	18.63	17.41	13.90	11.34
212165192	J08330052+2322285	18	19.32	18.28	12.88	5.17

Note: <sup>a</sup>Ahmed and Warren [2019]; <sup>b</sup>West et al. [2008]; <sup>c</sup>West et al. [2011]

Table B.4: List of M9 dwarfs observed by *K2*

EPIC	2MASS/other name	Campaign #	<i>i</i> (mag)	<i>z</i> (mag)	$M_i$ (mag)	parallax mas
201103788	J12022564-0629026	10	17.93	16.45	15.12	27.37
201345209	J12153971-0146422	10	19.84	18.51	14.28	7.72
201453319	J10524701-0010174	14	19.58	18.32	14.17	8.27
203912136	J16110360-2426429	2	18.98	17.46	13.25	7.15
204354278	J16104714-2239492	2	19.75	18.14	14.20	7.78
211329075	J08315598+1025417	5, 18	17.69	16.24	15.19	31.56
211978086	J08252301+1954093	5,18	19.17	18.00	13.77	8.31
212021699	J08312842+2036548	5,16,18	18.92	17.63	14.15	11.09
212022056	J08274526+2037162	5, 16, 18	19.18	18.02	13.60	7.63
212130380	J08452732+2237335	5,18	18.68	17.37	14.52	14.72
212136544	J08312608+2244586	5, 18	18.77	17.43	14.43	13.52
220181289	J01031145-0044170	8	18.43	16.94	15.66	27.90
220220365	J00522335+0043108	8	18.64	17.44	12.89	7.09
228803953	J12271545-0636458	10	18.21	16.74	15.18	24.82
229100074	J12372771+0046422	10	18.82	17.56	14.54	13.92
229146028	J12444661+0154154	10	19.46	18.18	14.08	8.38
245997252	J23371663-0933251	12	17.11	15.79	14.48	29.85
246404954	J23322437-0050251	12	17.11	15.86	14.07	24.71
248600681	J10191120+0553297	14	20.36	19.10	14.34	6.25 <sup>a</sup>
248604083	J10503886+0558333	14	19.13	17.69	15.93	22.95
248663141	J10315635+0726460	14	20.51	19.09	14.44	6.10 <sup>b</sup>
248691809	J10554733+0808427	14	16.62	15.18	15.25	53.33
248864625	J10330903+1216265	14	19.39	17.95	18.02	53.34
248908851	J10495444+1331047	14	19.90	18.45	14.58	8.62 <sup>b</sup>
251357067	J09161504+2139512	16	17.37	15.87	15.81	48.81
251552213	J13245630-0219353	17	19.38	18.22	13.58	6.93

Note:<sup>a</sup>West et al. [2008]; <sup>b</sup>West et al. [2011]

## Appendix C

### PROPERTIES OF WL FLARES OBSERVED ON M6 - M9 DWARFS BY *K2*

Table C.1: Flare properties of M6 dwarfs

EPIC	$T_{peak}$ (BJD - 2454833)	ED (hr)	$\log E$ (erg)
206050032	2146.7593	0.07	32.7
206050032	2148.0261	0.03	32.2
206050032	2153.0933	0.03	32.3
206050032	2157.8539	0.07	32.6
206050032	2165.5567	0.02	32.1
206050032	2185.6615	0.02	32.0
206050032	2187.5821	0.06	32.6
206050032	2200.1066	0.03	32.3
206135809	2159.1816	0.22	32.7
206135809	2160.8978	0.11	32.4
206135809	2210.5058	0.10	32.4
206296292	2166.4152	0.43	33.8
206494490	2148.9660	0.07	32.8
206494490	2160.1627	0.06	32.7
206494490	2166.8031	0.08	32.9
206494490	2180.2880	0.04	32.6
206494490	2185.5185	0.07	32.8
206494490	2189.8704	0.08	32.9
206494490	2190.6672	0.11	33.0
206494490	2191.0554	0.12	33.0
206494490	2194.4266	0.08	32.9
206494490	2195.2234	0.15	33.1
206494490	2198.4108	0.13	33.1
206494490	2209.3417	0.07	32.8
212402103	2389.4898	0.27	33.0
220195996	2559.8242	0.59	33.9
220195996	2605.9591	0.53	33.8
245995471	2915.1643	0.67	33.2
245995471	2949.7756	0.22	32.7
245995471	2959.3376	0.09	32.3
245995471	2960.8495	0.28	32.8
245995471	2971.1470	0.13	32.5
246322698	2962.4021	0.07	32.5
246403896	2925.4413	0.18	33.3
246403896	2949.3463	0.53	33.8
246404848	2936.1067	0.83	33.7
246404848	2982.6907	0.24	33.2
247051861	3049.3872	0.22	34.7
247051861	3061.6258	0.21	34.7
201744267	3085.4991	0.09	32.8
201744267	3088.6456	0.11	32.8
248456554	3094.8974	0.79	33.6
248525204	3119.6195	0.22	33.4
248525204	3148.6120	1.02	34.0

Continued on next page

**Table C.1 – continued from previous page**

<b>EPIC</b>	$T_{peak}$ (BJD - 2454833)	<b>ED</b> (hr)	<b>log <math>E</math></b> (erg)
248609711	3135.1065	1.01	34.4
248624299	3080.8808	0.27	33.5
248624299	3088.4406	0.03	32.5
248624299	3091.1172	0.50	33.7
248624299	3110.8544	0.37	33.6
248631849	3141.5017	0.82	34.0
248744078	3088.6657	1.51	33.8
248750733	3082.3725	0.52	33.5
248750733	3141.2774	0.28	33.2
248751905	3099.9645	0.95	34.0
248751905	3127.3021	0.55	33.8
248751905	3137.3545	0.78	33.9
212402103	3369.1135	0.05	32.3
212402103	3386.5655	0.11	32.6

**Table C.2: Energies of flares on M7 dwarfs**

<b>EPIC</b>	$T_{peak}$ (BJD - 2454833)	<b>ED</b> (hr)	<b>log <math>E</math></b> (erg)
206053352	2165.8425	0.32	32.8
206053352	2205.8884	0.67	33.1
206181579	2153.0529	1.48	33.7
206181579	2170.5632	0.25	33.0
206181579	2173.5258	0.08	32.5
206213997	2169.4186	1.11	33.1
206213997	2169.3164	1.45	33.2
206213997	2184.6197	1.19	33.2
212826600	2389.0399	0.15	32.2
212826600	2389.0399	0.15	32.2
212826600	2427.1248	0.02	31.4
212826600	2430.6391	0.28	32.5
212826600	2433.5200	0.05	31.7
212826600	2453.6043	0.10	32.0
212826600	2455.2389	0.05	31.7
201425001	2777.0911	0.04	32.2
201425001	2787.3274	0.09	32.5
201425001	2793.4160	0.19	32.8
246015548	2907.5023	0.78	34.1
246015548	2923.5006	0.79	34.1
246015548	2927.7300	1.55	34.4
246015548	2938.7019	0.81	34.1
246015548	2947.8552	0.55	33.9
246015548	2969.9009	1.36	34.3
246034587	2942.1952	0.08	32.9
246393886	2933.8188	0.23	33.6
246393886	2947.8962	0.05	32.9
246393886	2962.5660	0.57	34.0
246393886	2965.4673	0.29	33.7
246393886	2966.9179	0.26	33.6
246395512	2943.9936	0.42	33.7
246401499	2912.7535	1.36	33.5
246401499	2937.2513	0.48	33.1
246401499	2937.2513	0.49	33.1
246401499	2951.1652	1.67	33.6
246468225	2936.5565	1.29	33.7
246468225	2976.9905	0.47	33.2
248029954	2998.1652	107.00	36.3
248029954	3058.4182	2.40	34.6
201581268	3086.2550	0.32	34.0
201581268	3140.3585	1.16	34.6
248452093	3131.2863	0.27	32.8

Continued on next page

**Table C.2 – continued from previous page**

<b>EPIC</b>	$T_{\text{peak}}$ (BJD - 2454833)	<b>ED</b> (hr)	<b>log <math>E</math></b> (erg)
248565564	3111.4058	0.43	33.5
248565564	3111.4058	0.43	33.5
248580531	3075.5070	0.22	32.8
248659481	3077.0189	0.26	33.4
248682489	3092.2411	0.18	32.5
248718280	3111.6924	0.48	33.1
248718280	3119.6607	0.27	32.8
248718280	3119.9263	0.18	32.7
248718280	3128.4259	0.19	32.7
248718280	3149.4705	0.09	32.4
248755514	3112.0195	0.61	33.6
249639465	3198.8612	0.16	32.7
249639465	3227.4043	0.86	33.4
211411366	3267.3722	0.51	34.0
211478560	3292.8349	0.20	33.3
211742071	3268.5984	0.28	33.5
211758584	3270.6621	5.10	34.4
211758584	3339.7954	1.08	33.7
211770368	3265.5331	0.52	33.9
211770368	3317.4395	0.46	33.9
211770368	3325.2049	1.82	34.5
211892842	3274.4839	1.65	34.4
211892842	3306.2204	0.17	33.4
211892842	3327.6367	0.42	33.8
211892842	3330.5794	0.80	34.1
211917847	3277.7738	0.95	34.0
211917847	3292.3444	2.96	34.5
211947924	3275.9550	1.43	34.2
211964067	3303.5227	0.49	33.5
212019105	3271.1533	0.18	33.2
212019105	3287.2157	0.31	33.4
212019105	3302.0724	0.29	33.4
212019105	3320.9547	0.76	33.8
212075399	3283.5367	0.72	33.5
212075399	3290.2192	1.06	33.7
212075399	3293.2232	0.33	33.2
212075399	3293.7341	0.35	33.2
212075399	3298.6795	5.50	34.4
212075399	3301.2748	0.17	32.9
212075399	3301.3975	0.32	33.1
212075399	3325.3683	0.29	33.1
212075399	3339.7954	0.47	33.3
212156288	3269.0887	0.39	33.6
251314012	3265.0009	0.37	33.4
251314012	3318.0517	0.09	32.8
251317744	3275.3210	0.71	34.1
251317744	3292.4665	0.14	33.3
251358654	3264.9806	1.55	34.6
251365679	3264.6130	0.16	32.8
251394863	3341.1849	0.81	34.4
212826600	3360.3267	0.07	31.9
212826600	3362.7176	0.88	33.0
212826600	3380.9667	0.07	31.9
212826600	3382.1928	0.11	32.1
212826600	3383.3167	0.03	31.6
212826600	3393.9636	0.17	32.2
251558388	3378.6167	0.91	33.6
251558388	3378.6371	0.16	32.9
211910449	3436.7303	0.42	33.4
211910449	3458.8782	2.22	34.1
212006725	3468.0522	0.86	34.0
212019105	3424.2057	0.17	33.1

Continued on next page

**Table C.2 – continued from previous page**

<b>EPIC</b>	$T_{\text{peak}}$ (BJD - 2454833)	<b>ED</b> (hr)	<b>log <math>E</math></b> (erg)
212019105	3426.2080	0.15	33.1
212019105	3434.8099	0.75	33.8
212019105	3435.3411	2.41	34.3
212019105	3455.7728	2.75	34.3
212019105	3468.6447	0.20	33.2
212027121	3444.1064	13.70	35.1
212071306	3436.1178	0.93	34.1
212080305	3446.7218	0.44	33.6
212080305	3460.3906	1.01	34.0
212091105	3451.1556	0.24	33.1
212106472	3447.7435	0.31	33.4
212108940	3437.6297	1.77	34.0
212123277	3444.7400	0.34	33.5
212123277	3462.7812	0.16	33.2
212156288	3461.8212	0.97	34.0
212170953	3462.1883	2.74	34.4
212176032	3442.3288	0.29	33.2

**Table C.3: Energies of flares on M8 dwarfs**

<b>EPIC</b>	$T_{\text{peak}}$ (BJD - 2454833)	<b>ED</b> (hr)	<b>log <math>E</math></b> (erg)
210764183	2238.8728	0.36	32.5
210764183	2240.1396	0.26	32.4
210764183	2266.5374	0.21	32.3
210764183	2267.6407	0.32	32.4
210764183	2272.7281	0.08	31.8
211046195	2240.0377	0.16	33.2
211046195	2253.6657	0.07	32.8
211046195	2268.8668	0.03	32.4
211046195	2287.9091	0.08	32.9
220170497	2633.9300	0.53	33.0
228754562	2784.8557	0.56	33.2
228754562	2786.7150	0.20	32.7
228754562	2813.5010	0.06	32.2
246013537	2940.2138	0.62	33.2
248044306	3040.6016	5.23	34.0
201580841	3137.1915	0.41	33.0
201800829	3133.8202	0.16	32.5
248413181	3126.0357	0.57	33.0
248445614	3083.0879	0.39	32.8
248445614	3093.7127	1.03	33.2
248445614	3100.7208	1.95	33.5
248445614	3103.7448	5.51	33.9
248445614	3104.5825	0.42	32.8
248445614	3121.7860	1.07	33.2
248445614	3129.0597	9.82	34.2
248445614	3141.3596	0.38	32.8
248567554	3078.8377	0.15	32.0
248567554	3101.6806	0.10	31.9
248592301	3084.2934	0.56	33.1
248592301	3106.1965	0.30	32.8
249472713	3157.9570	0.59	31.7
249472713	3210.3445	0.40	31.5
211616100	3263.0397	4.53	34.3
211616100	3286.0093	5.55	34.3
211616100	3307.5893	0.30	33.1
211616100	3327.2482	1.07	33.6
212184948	3279.7766	3.46	33.8
212184948	3293.2029	0.26	32.6
212184948	3298.8022	2.11	33.5

Continued on next page

**Table C.3 – continued from previous page**

<b>EPIC</b>	$T_{\text{peak}}$ (BJD - 2454833)	<b>ED</b> (hr)	<b>log <math>E</math></b> (erg)
212184948	3305.1577	1.90	33.5
212184948	3338.2220	11.10	34.3
212820594	3396.6815	0.10	32.0
211301854	3442.8404	0.42	33.2
211981759	3439.6522	0.83	34.0
212035340	3437.8545	46.36	35.5
212035340	2378.0196	1.70	34.1
212035340	2312.3112	1.30	34.0
212035340	2377.7744	1.00	33.9
212035340	2380.2058	0.70	33.7

**Table C.4: Energies of flares on M9 dwarfs**

<b>EPIC</b>	$T_{\text{peak}}$ (BJD - 2454833)	<b>ED</b> (hr)	<b>log <math>E</math></b> (erg)
201453319	3100.9457	1.7	33.4
203912136	2077.4059	0.9	33.5
203912136	2087.9691	4.2	34.2
212022056	2330.0662	2.5	33.8
212022056	3328.6996	0.7	33.3
212022056	3454.0565	2.9	33.9
212136544	3426.7801	1.6	33.3
212136544	3440.8373	1.2	33.2
212136544	3449.0100	12.6	34.2
212136544	3456.9579	1.3	33.2
212136544	3457.9386	50.2	34.8
246404954	2942.5022	1.0	33.2
246404954	2977.1541	0.7	33.1
248600681	3089.8094	10.6	34.2
248600681	3137.1293	6.6	33.9
248691809	3121.3568	0.24	32.2
248691809	3133.8814	0.04	31.3

## Appendix D

### COPYRIGHT POLICY OF JOURNALS

Some of the results presented in this dissertation were published in the *Astrophysical Journal* (ApJ) and the *Monthly Notices of the Royal Astronomical Society* (MNRAS). Here, I mention the copyright policy of these journals.

#### **i) Copyright policy of the Astrophysical Journal:**

Before your article can be published in an American Astronomical Society (AAS) journal, we require you to grant and assign the entire copyright in it to the AAS. The copyright consists of all rights protected by the copyright laws of the United States and of all foreign countries, in all languages and forms of communication, including the right to furnish the article or the abstracts to abstracting and indexing services, and the right to republish the entire article in any format or medium.

In return, the AAS grants to you the non-exclusive right of republication, subject only to your giving appropriate credit to the journal in which your article is published. This non-exclusive right of republication includes your right to allow reproduction of parts of your article wherever you wish, and permits you to post the published (PDF) version of your article on your personal website. To protect the copyright in your article, the original copyright notice as it appears in the journal should be included in the credit.

If your article is accepted for publication we require you to read, sign, and return the Copyright Agreement to us. We cannot publish your article without this approval. In the event that your article is not accepted for publication, you will be notified in writing and the copyright and all rights conferred by copyright shall revert to you. Copies of these agreements can be downloaded from this website for standard and Gold Open Access basis.

The agreement should be signed by at least one of the authors (who agrees to inform the others, if any) or, in the case of a work made for hire, by the employer.

An author who is a U.S. Government officer or employee and who prepared the article as part of his or her official duties does not own any copyright in it. If at least one of the authors is not a U.S. Government employee, one of those non-government authors should sign the Copyright Agreement.

#### **ii) Copyright Policy of the Monthly Notices of the Royal Astronomical Society (MNRAS):**

It is the responsibility of the authors to ensure they have the necessary copyright permissions for any material (including, but not limited to, figures and text) used in their paper. Any re-use of material which has previously been published even by the same authors, and/or in the same journal must be accompanied by a citation to the original source and the necessary copyright permissions obtained. Quotation marks should be used around any text which has been reproduced from elsewhere, in addition to a citation.

Dear Rishi,

RE. R R Paudel et al. 2MASS J10274572+0629104: the very short period young M6 dwarf binary system identified in K2 data. *MNRAS* (2019) 486 (3): 4144-4148, doi: 10.1093/mnras/stz1067

R R Paudel et al. K2 Ultracool Dwarfs Survey – V. High superflare rates on rapidly rotating late-M dwarfs. *MNRAS* (2019) 486 (1): 1438-1447, doi: 10.1093/mnras/stz886

Thank you for your email requesting permission to reuse all of your article in a thesis/dissertation.

As part of your copyright agreement with Oxford University Press you have retained the right, after publication, to use all or part of the article and abstract, in the preparation of derivative works, extension of the article into a booklength work, in a thesis/dissertation, or in another works collection, provided that a full acknowledgement is made to the original publication in the journal. As a result, you should not require direct permission from Oxford University Press to reuse your article.

Authors may upload a PDF of the accepted manuscript to institutional and/or centrally organized repositories and/or in free public servers, upon acceptance for publication in the journal. Authors may upload the version of record to institutional and/or centrally organized repositories and/or in free public servers, upon publication in the journal.

**Please Note: Inclusion under a Creative Commons License or any other Open-Access License allowing onward reuse is prohibited.**

For full details of our publication and rights policy, including **credit-lines**, please see the attached link to our website:

[https://academic.oup.com/journals/pages/access\\_purchase/rights\\_and\\_permissions/self\\_archiving\\_policy\\_p](https://academic.oup.com/journals/pages/access_purchase/rights_and_permissions/self_archiving_policy_p)

If you have any other queries, please feel free to contact us.

## Figure D.1: Permission from Oxford University Press.

Failure to properly cite material which has previously been published constitutes plagiarism and is a serious breach of scientific ethics. Papers which are found to contain plagiarized (including self-plagiarized) material will be rejected. All submissions are screened for originality using the iThenticate plagiarism detection system.

Note that the copyright for previously published material may rest with its publisher not its author, so it is not sufficient to merely obtain the original authors permission. This also applies in the case of the authors own previous publications. Please refer to the relevant journal or publisher websites for instructions.

Authors who wish to re-use material previously published in MNRAS should refer to the instructions at [https://academic.oup.com/mnras/pages/rights\\_and\\_new\\_business\\_development](https://academic.oup.com/mnras/pages/rights_and_new_business_development).

### Third-Party Content in Open Access papers

If you will be publishing your paper under an Open Access licence but it contains material for which you do not have Open Access re-use permissions, please state this clearly by supplying the following credit line alongside the material:

*Title of content, Author, Original publication, year of original publication, by permission of [rights holder] This image/content is not covered by the terms of the Creative Commons licence of this publication. For permission to reuse, please contact the rights holder.*

The screen shot of email regarding permission obtained from Oxford University Press about the use of the results from two articles published in MNRAS is given in Figure D.1.